STUDIA UNIVERSITATIS
BABEŞ-BOLYAI

UNIVERSITATEA BABEŞ-BOLYAI
BABEŞ-BOLYAI TUDOMÁNYEGYETEM
BABEŞ-BOLYAI UNIVERSITÄT
BABEŞ-BOLYAI UNIVERSITY
TRADITIO ET EXCELLENTIA

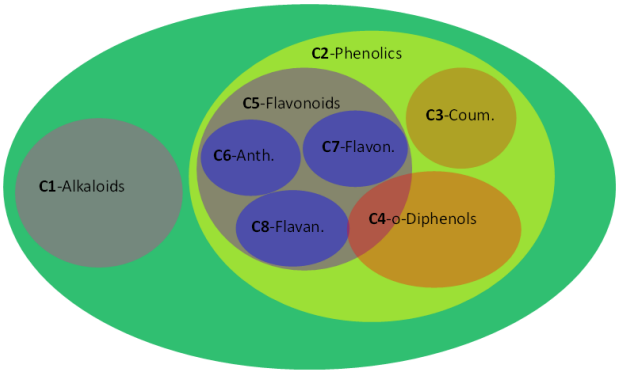

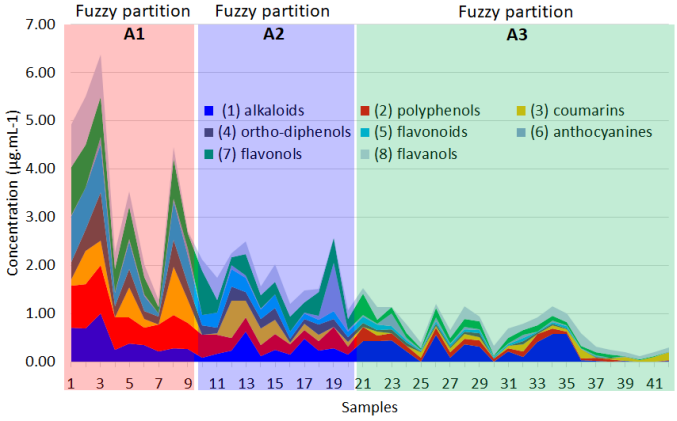

CHEMIA

3/2023

STUDIA UNIVERSITATIS BABEŞ-BOLYAI CHEMIA

3/2023

ISSN (print): 1224-7154;
ISSN (online): 2065-9520; ISSN-L: 2065-9520

Published by Babeş-Bolyai University

http://chem.ubbcluj.ro/~studiachemia/;
http://www.studia.ubbcluj.ro/serii/chemia/index_en.html

YEAR **Volume 68 (LXVIII) 2023**
MONTH **SEPTEMBER**
ISSUE **3**

PUBLISHED ONLINE: 2023-09-30
PUBLISHED PRINT: 2023-09-30
ISSUE DOI: 10.24193/subbchem.2023.3

S T U D I A
UNIVERSITATIS BABEŞ–BOLYAI
CHEMIA

3

CONTENT/ SOMMAIRE/ INHALT/ CUPRINS

Studia Universitatis Babes-Bolyai Chemia has been selected for coverage in Thomson Reuters products and custom information services. Beginning with V. 53 (1) 2008, this publication is indexed and abstracted in the following:

- Science Citation Index Expanded (also known as SciSearch®)
- Chemistry Citation Index®
- Journal Citation Reports/Science Edition

STUDIA UBB CHEMIA, LXVIII, 3, 2023 (p. 7-18)
(RECOMMENDED CITATION)
DOI:10.24193/subbchem.2023.3.01

NANOCOMPOSITE BASED ON HYDROXYAPATITE AND SILVER WITH ANTIBACTERIAL ACTIVITY

Aurora MOCANU[a], Diana Alexandra FLOREA[a], Gheorghe TOMOAIA[b,c], Lucian-Cristian POP[a,*], Ancuta DANISTEAN[a], Sorin RAPUNTEAN[d], Ossi HOROVITZ[a] and Maria TOMOAIA-COTISEL[a,c,*]

ABSTRACT. A nanocomposite made from hydroxyapatite (HAP) and silver nanoparticles (AgNPs), namely HAP-4.5 wt% AgNPs, is reported. HAP was prepared using a wet precipitation technique, and AgNPs were made by reducing silver nitrate with glucose in basic medium. HAP, AgNPs and HAP-4.5 wt% AgNPs composite were characterized by X-ray diffraction (XRD), SEM - energy dispersive X-ray spectroscopy (EDS) and different imagistic methods: TEM and AFM. The antibacterial effect of the HAP-4.5 wt% AgNPs nanocomposite was tested using diffusion technique in nutritive agar on two pathogenic species, one Gram-negative (*Salmonella typhimurium*) and one Gram-positive (*Bacillus cereus*) and promising results were obtained. This hydroxyapatite-silver nanocomposite can be employed as a potential antimicrobial coating for dental and orthopedic implants, or they can be utilized such as bone cements in clinical procedures.

Keywords: *hydroxyapatite, silver nanoparticles, nanocomposite, antibacterial activity, pathogens*

[a] *Babes-Bolyai University of Cluj-Napoca, Faculty of Chemistry and Chemical Engineering, Research Centre of Physical Chemistry, 11 Arany Janos Str., Cluj-Napoca, 400084, Romania*
[b] *Iuliu Hatieganu University of Medicine and Pharmacy, Orthopedics and Traumatology, 47 Gen. Traian Mosoiu Str., Cluj-Napoca, 400132, Romania*
[c] *Academy of Romanian Scientists, 3 Ilfov Str., RO-400132, Bucharest, Romania*
[d] *University of Agricultural Sciences and Veterinary Medicine of Cluj-Napoca, 3-5 Manastur Str., Cluj-Napoca, 400372, Romania*
* *Corresponding authors: Lucian-Cristian Pop lucian.pop@ubbcluj.ro; Maria Tomoaia-Cotisel maria.tomoaia@ubbcluj.ro*

INTRODUCTION

The finding of the earliest antibiotic, penicillin, by Alexander Fleming in 1928 revolutionized medicine and saved countless lives by providing a way to effectively treat bacterial infections [1]. Since then, almost a century has passed and bacteria, due to misuse, have evolved resistance to antibiotics through mutations that led to drug-resistant bacteria, which are a foremost threat to public health [2, 3]. Although some metal ions, like Ag, Cu, Zn, and Au, have long been acknowledged to have antibacterial characteristics, they were "forgotten" during the successful era of antibiotics. Silver nanoparticles, known for their antimicrobial properties for centuries, have been proposed as a potential solution to combat drug-resistant bacteria. Due to their insignificant dimension and huge surface area, AgNPs can interfere with bacterial cell walls by disrupting the cellular processes leading to bacterial death [4, 5].

Silver nanoparticles (AgNPs) produced *via* a variety of techniques, including chemical, physical, photochemical and biological, were found to have an antibacterial effect [6-14]. AgNPs produced in various formulations, with diverse shapes and sizes, show variable antimicrobial activity, while the mechanism of antimicrobial effect of Ag ions and AgNPs, as well as their toxicity on tissues, are not fully elucidated [15-20]. The antibacterial effect of AgNPs was associated with their shape, with triangular particles presenting a more intense effect compared to spherical ones [21-23]. Compared to other metals, silver has a high toxicity against microorganisms and a much lower toxicity against mammalian cells [24-26].

The human body contains nanosize hydroxyapatite (HAP), an inorganic mineral ($Ca_{10}(PO_4)_6(OH)_2$) having a Ca to P mole ratio of 5/3 (cca 1.67). It is found within the bone as a bioactive ceramic that covers about 70% of bone weight and in teeth that covers up to 80% of dentin and enamel.

Crystallographic and chemical studies revealed that synthetic HAP is comparable to natural HAP. Due to this fact, synthetic HAP is also considered a great option for bone or dental reconstruction because it is osteoconductive, stable at physiological pH, biocompatible, and readily adsorbed with bioorganic substances (proteins, amino acids, etc.).

As a support and carrier for AgNPs, both pure hydroxyapatite (HAP) and doped HAP with various cations or anions, were also used as nanomaterials of choice [27-35]. As an alternative, HAP doped with silver ions was also used as antimicrobial material [36-41]. HAP-AgNPs composites with organic polymers were also used [42-47], to ensure a retarded silver ion release.

Here we intended to synthesize a hydroxyapatite with a low degree of crystallization and high porosity, able to assure a good adsorption and release of silver nanoparticles. For the synthesis of HAP with the desired characteristics, we use a chemical precipitation method developed by us [39, 48-55]. By reducing silver nitrate with glucose, silver nanoparticles are obtained [49]. In addition, some microbiological tests were performed having in mind to assess the antimicrobial properties of the newly synthetized nanocomposite.

RESULTS AND DISCUSSION

Characterization of AgNPs

The UV-Vis spectrum of the dispersion containing AgNPs presents the specific SPR absorption band of Ag, with the maximum at 405 nm (Fig. 1A). The spectrum did not change in time for 1 year, thus evidencing the high stability of the AgNPs dispersion.

TEM image for AgNPs is depicted in Fig. 1. The mean diameter of the AgNPs was found to be 13.0 ± 2 nm.

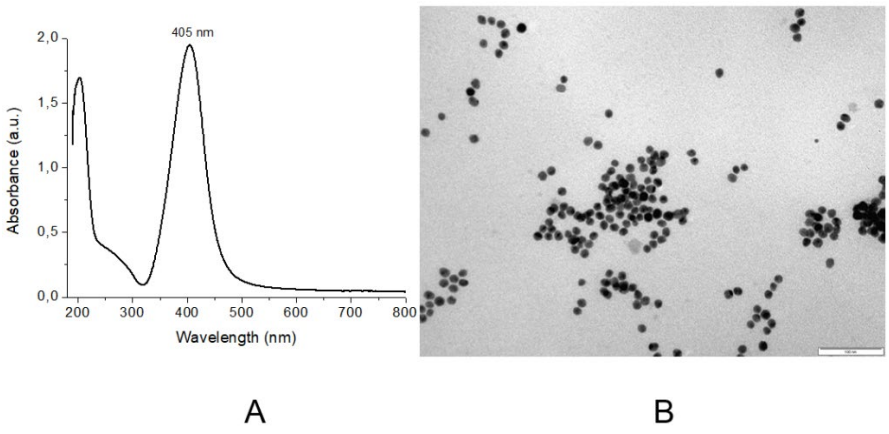

Fig. 1. UV-Vis spectrum for AgNPs aqueous dispersion (A) and TEM image for AgNPs (B); the scale bar is 100 nm. The average diameter of AgNPs is around 13 nm. The zeta potential value for AgNPs is negative, -39 mV, ensuring a high electrostatic stability of the AgNPs dispersion.

Characterization of HAP-4.5 wt% Ag composite

The samples do not differ significantly from each other. The HAP nanoparticles present a rather low degree of crystallinity, as wanted by the synthesis. The presence of crystalline silver is evidenced in Fig. 2 for HAP-4.5 wt% Ag where the lines for silver from PDF 89-3722 are shown. Their position is in good agreement with that found for nanosilver particles [56] for the (111), (200), (220), (311) and (222) planes of Ag, corresponding to the peaks at 2θ values of 38.32, 44.50, 64.61, 77.54 and 81.68° respectively. In Figure 2, the most intense diffraction of silver [(111) plane] in HAP-4.5 wt% Ag appears distinctly, while the other Ag diffraction lines are partially superposed on the diffraction peaks of HAP.

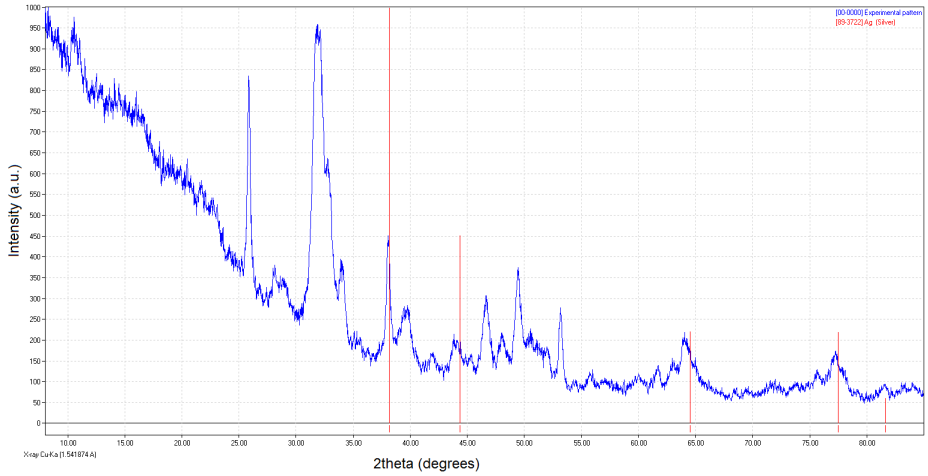

Fig. 2. XRD pattern for HAP-4.5 wt% Ag compared with PDF 89-3722 for Ag (vertical red lines)

The typical crystallite dimensions and the crystallinity amount of the samples are given in Table 1.

Table 1. Average crystallite size and crystallinity degree of HAP and HAP-4.5 wt% Ag composite, from XRD data; NPs average diameter of composite from AFM investigation

Sample	HAP [57]	HAP-4.5 wt% Ag	HAP-4.5 wt% Ag (AFM Fig. 4)
Crystallites size (nm)	47.6	45.3	-
Crystallinity (%)	36	37	-
Average diameter of NPs (nm)	-	-	54 ± 8nm

The average diameter of HAP-4.5 wt% AgNPs is 54 ± 8nm, as obtained from AFM measurements (Fig. 4), which is somewhat higher than about 45 nm obtained from XRD measurements (Fig. 2) and to about 48 nm found for pure HAP. Thus, the average diameter of HAP-4.5 wt% AgNPs composite is only slightly increased by mixing HAP NPs with AgNPs for this composition.

In the SEM-EDS (EDX) spectrum, fig. 3, the presence of Ag is revealed, along with the elements which enter in the composition of HAP (Ca, P, O), as shown in Fig. 3B. Cu and C also appear in the spectrum, since the grids on which the particles were adsorbed are made from carbon coated copper. The uniform distribution of AgNPs in the sample is also evident in Fig. 3A and Fig. 4A.

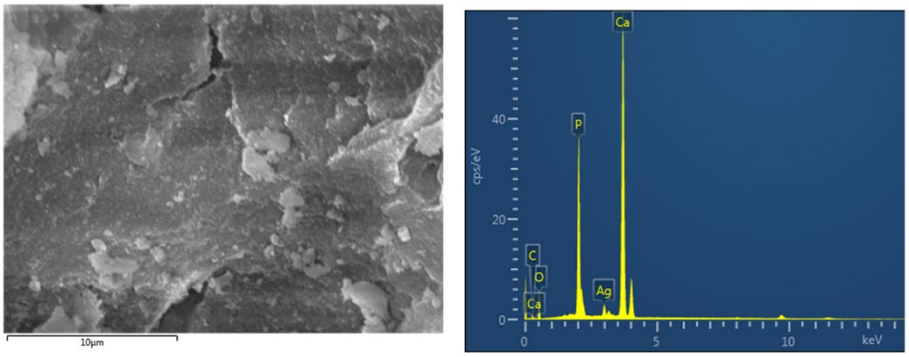

Fig. 3. SEM image (A) and EDX spectrum (B) for HAP-4.5 wt% AgNPs.

AFM images for the HAP-4.5% Ag nanocomposite, on sample obtained by adsorption on glass plate, are presented in Fig. 4. As shown in AFM images (A, B and C) and from the cross-section profile (D), the average particle size is 54 nm ± 8nm in this nanocomposite.

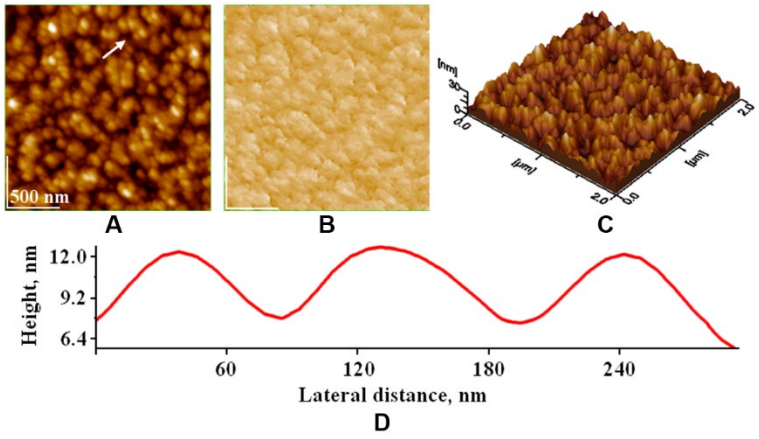

Fig. 4. AFM images of HAP-4.5 wt% AgNPs adsorbed on glass plate**:** A) topographic image, B) amplitude image, C) 3D image, and D) profile on the white arrow in panel (A). Scanned area 2 µm x 2 µm. Maximum height 30 nm, surface roughness evaluated as root mean square, Rrms = 4.8 nm. Average particle diameter is determined from many profiles (at least 10) as 54 nm ± 8nm.

Zeta potential measurements for HAP dispersions gave a slightly negative value: -6.5 mV.

Antimicrobial effect

After the incubation period, the plates were examined and the diameters of the inhibition zones (in mm) were determined. Values of 13 mm was found for *Salmonella typhimurium (*ATCC 14028) and 12 mm for *Bacillus cereus (*ATCC 14579).

The results evidence a clear inhibitory effect of HAP-Ag composite on the verified bacterial strains, whereas no inhibition zone is detected for the witness sample (pure HAP). The silver content in a well corresponding to the HAP-4.5 wt% Ag composite is 32 µg.

When comparing the different bacterial strains, we find only small differences. The most sensible appears to be *Salmonella typhimurium* followed by *Bacillus cereus*.

CONCLUSIONS

In conclusion, a straightforward technique for synthesizing HAP-AgNPs with a silver content of 4.5 wt% was effectively developed. Using the XRD, SEM-EDS, TEM, and AFM, the morphological and compositional characteristics of the as-prepared nanocomposite were verified. TEM, SEM, and AFM images showed the dimension and form of HAP particles, both with and without AgNPs, and XRD and EDS measurements confirmed the presence of silver.

Equally Gram-negative and Gram-positive isolates were effectively killed by the HAP-4.5wt%AgNPs that was under investigation. These findings imply that our composite could be regarded as antibacterial materials and that they could be utilized in dentistry and orthopedic implants.

EXPERIMENTAL SECTION

Materials and methods

Materials: As precursors were used: calcium nitrate tetrahydrate, $Ca(NO_3)_2 \cdot 4H_2O$ (p.a., Poch S.A., Poland), alongside with diammonium hydrogen phosphate, $(NH_4)_2HPO_4$ (p.a., Nordic Invest, Romania); glucose (10% solution, Hemofarm, Braun Pharmaceuticals S.A., Timisoara, Romania), silver nitrate, $AgNO_3$ (analytical purity, Merck, Germany) and NaOH (10% solution, Sigma-Aldrich, Germany).

Preparation of HAP-Ag samples

Synthesis of low crystallinity hydroxyapatite (HAP). Low crystallinity nano hydroxyapatite (HAP) was synthetized *via* a wet chemical process, with $Ca(NO_3)_2 \cdot 4H_2O$ and $(NH_4)_2HPO_4$ as starting materials [57]. A 250 mM $Ca(NO_3)_2$ solution was obtained in bidistilled water with added 25% ammonia solution (pH 8.5), and another 150 mM $(NH_4)_2HPO_4$ solution in bidistilled water, containing ammonia solution (pH 11). These solutions were quickly mixed at 0 °C. The dispersion, as obtained in the mother liquor was allowed to mature 10 h at 22 °C (under intermittent stirring), then filtered and rinsed with bidistilled water until no NO_3^- is found. For further characterization, a portion of the watery precipitate was desiccated by lyophilization. The wet precipitate separated by filtration (containing 80% water) was used as scaffold for AgNPs.

Preparation of AgNPs. A method using the reduction of Ag^+ ions by glucose, in a basic solution was used. This implied the reduction of silver nitrate, $AgNO_3$ (analytical purity, Merck, Germany) in a very diluted aqueous solution (final concentration $0.25 \cdot 10^{-3}$ M, silver content 27 mg/L) with glucose (10 % aqueous solution), the glucose being in large excess: 0.5 ml glucose solution / 1 mg Ag (molar ratio glucose/Ag = 30) in alkaline medium (pH cca. 12, obtained with the help of a 10% NaOH solution) at room temperature (22 °C). Silver nanoparticles were dispersed, giving off a light yellowish-brown tint.

Preparation of HAP-4.5% Ag composite. The AgNPs aqueous dispersion is added under continuous magnetic stirring to the wet HAP precipitate in the ratio needed for an Ag content in the HAP-Ag composite of 4.5 %. (For instance, to 1 g wet HAP precipitate (80% water) 350 mL AgNPs dispersion were added). The stirring continues for 2h, and the mixture is let to stay for 24 h at 22 °C. Then the HAP-Ag precipitate is filtered and desiccated at ambient temperature.

Characterization methods

X-ray diffraction (XRD) patterns have been produced employing a DRON-3 diffractometer (Bragg–Brentano geometry) fitted with an X-ray tube with copper K_α radiation, λ = 1.541874 Å, in the domain between 5° and 85° 2θ.

Comparing the peaks of the diffraction images with PDF allowed the identification of phases [58-63]. The peak locations of the diffraction patterns were compared to PDF (Powder Diffraction File) 74-0566 belonging to stoichiometric HAP and PDF 89-3722 for silver to determine the phases.

UV-Vis absorption spectra were measured between 190 and 900 nm by means of a Jasco UV/Vis V-650 spectrophotometer and 1 cm quartz cuvettes, at ambient temperature. HAP water dispersions required for TEM and AFM imaging were obtained by ultra-sonification (Sonics Vibra-Cell, VCX 750), for 5 min, at room temperature.

TEM images acquired with TEM, JEOL – JEM 1010 equipment were captured with JEOL typical software. *SEM* images were obtained with a scanning transmission electron microscope, STEM Hitachi HD-2700. Also, energy-dispersive *X-ray* spectrum (*EDS* or *EDX*) of the distribution and relative proportion of elements was obtained over the scanned areas.

The AFM JEOL 4210 apparatus was run in tapping mode [64-69] using conventional silicon nitride-tipped cantilevers (resonant frequency: 200–300 kHz; spring constant: 17.5 N/m). The particles were adsorbed from their ultrapure water dispersion for 10 s on glass plates. On the same adsorbed film, various regions ranging in size from 10 μm x 10 μm to 0.5 μm x 0.5 μm were scanned. The various obtained images have been managed by usual AFM JEOL procedures.

On aqueous dispersions of the AgNPs, zeta potential readings were made with a Malvern Zetasizer Nano-ZS90 apparatus.

Antibacterial assays

The bacterial strains tested were: *Bacillus cereus* ATCC 14579 and *Salmonella typhimurium* ATCC 14028. The microbial strains were inseminated in glucose medium (nutrient broth and nutrient agar) (TM Media, Titan Biotech, India), and incubated in a thermostat (37 °C), under aerobic conditions, for a period of 18-24 h. The microbial strains have been verified by bacteriological examination. The tested microbial strains are checked every time by a bacteriological test, to appreciate the culture characteristics, both in liquid and solid medium, as well as the morphological characters, on smears stained by Gram's method. This is done in order to have a pure culture and to use a young culture of 24 h.

The inhibiting effect is assessed by the antibiogram technique of diffusion in nutritive agar gel, adapted for testing products treated as suspensions. For this, nutritive agar, supplemented with glucose and NaCl, was liquefied by warming in a water bath and transferred to 90 mm diameter Petri dishes in a volume of 25 ml, giving a 3 mm thick even layer of 3 mm thick. Flood inoculation was applied, using a 1 ml suspension made from the tested strain at density 0.5, according to McFarland standards. The uniform dispersion on the entire surface is done using a Drigalski spate. After drying of the agar surface (20 minutes in the thermostat with half-open lid), the wells (diameter 0.6 cm) are cut out in the agar gel in a circular shape. Amounts of 0.2 g of HAP-4.5 wt% Ag sample and pure HAP (as a witness) were dispersed in 2 ml of water and then an amounts of 35 µl were distributed in the wells. For 18-24 hours, the dishes were incubated at 37 °C in a thermostat. The plates were read in order to identify the existence or non-existence of culture growth around the wells. The span of the inhibition zone (expressed in millimetres) was determined if an inhibitory effect was seen. The dishes were monitored for an additional 5 days to spot any variations over time.

ACKNOWLEDGMENTS

This work was supported by grants from the Ministry of Research, Innovation and Digitization, CNCS/CCCDI-UEFISCDI, project number 186, within PNCDI III.

REFERENCES

1. R. Gaynes, *Emerg. Infect. Dis.,* **2017**, *23*(*5*), 849-853.
2. R. Urban-Chmiel; A. Marek; D. Stępień-Pyśniak; K. Wieczorek; M. Dec; A. Nowaczek; J. Osek; *Antibiotics (Basel, Switzerland),* **2022**, *11*(*8*), 1079.
3. D.G.J. Larsson; C.-F. Flach; *Nat. Rev. Microbiol.,* **2022**, *20*(*5*), 257-269.

4. E. Urnukhsaikhan; B.-E Bold; A. Gunbileg; N. Sukhbaatar; T. Mishig-Ochir; *Sci. Rep.,* **2021**, *11*(*1*), 21047.
5. S.A. Ahmad; S.S. Das; A. Khatoon; M.T. Ansari; M. Afzal; M.S. Hasnain; A.K. Nayak; *Mater. Sci. Technol.,* **2020**, *3*, 756-769.
6. S. Rajeshkumar; C. Malarkodi; M.Vanaja; G. Annadurai; *J. Mol. Struct.,* **2016**, *1116,* 165-173.
7. M. Bhat; B. Chakraborty; R.S. Kumar; A.I. Almansou; N. Arumugam; D.Kotresha; S. Pallavi, S. Dhanyakumara; K. Shashiraj; S. Nayaka; *J. King Saud Univ. Sci*., **2021**, *33*, 101296.
8. M.M.N. El-Dein; Z.A.M. Baka; M.I. Abou-Dobara; A.K. El-Sayed; M.M. El-Zahed; *J. Microbiol. Biotechnol. Food Sci*., **2021**, *10*, 648–656.
9. J.S. Gabriel; V.A.M. Gonzaga; A.L. Poli; C.C. Schmitt; *Carbohydr. Polym.*, **2017**, *171*, 202-210.
10. G.A. Bhaduri; R. Little; R.B. Khomane; S.U. Lokhande; B.D. Kulkarni; B.G. Mendis; L. Šiller; *J. Photochem. Photobiol. A: Chemistry,* **2013***, 258*, 1-9.
11. M. Mohammadlou; Maghsoudi H; H. Jafarizadeh-Malmiri; *Int. Food. Res. J.*, **2016**, *23*(*2*), 446-463.
12. S. Kaviya; J. Santhanalakshmi; B. Viswanathan; J. Muthumary; K. Srinivasan; *Spectrochim. Acta A Mol. Biomol. Spectrosc.,* **2011**, *79*(*3*), 594-598.
13. N.G. Mlalila; H.S. Swai; A. Hilonga; D.M. Kadam; *Nanotechnol. Sci. Appl.,* **2017**, *10*, 1-9.
14. S. Ullah Khan; T.A. Saleh; A. Wahab; M.H. Ullah Khan; D. Khan; W. Ullah Khan; A. Rahim; S. Kamal; F. Ullah Khan; S. Fahad; *Int. J. Nanomed.*, **2018**, *13*, 733-762.
15. M. Zahoor; N. Nazir; M. Iftikhar; S. Naz; I. Zekker; J. Burlakovs; F. Uddin; A.W. Kamran; A. Kallistova; N. Pimenov; F.A. Khan; *Water,* **2021**, 1*3*(*16*), 2216.
16. P.R. More; S. Pandit; A. Filippis; G. Franci; I. Mijakovic; M. Galdiero; *Microorganisms*, **2023,***11*(*2*), 369.
17. Y. Yang; X. Chen; N. Zhang; B. Sun; K. Wang; Y. Zhang; L. Zhu; *Water Research*, **2022**, *218*, 118452.
18. A. Luceri; R. Francese; D. Lembo; M. Ferraris; C. Balagna; *Microorganisms*, **2023**,*11*(*3*), 629.
19. T. Bruna; F. Maldonado-Bravo; P. Jara; N. Caro; *Int. J. Mol. Sci.*, **2021**, *22*(*13*), 7202.
20. H.A. Hemeg; *Int. J. Nanomed.*, **2017**, *12*, 8211-8225.
21. P. Sukdeb; Y.K. Tak; J.M. Song; *Appl. Environ. Microbiol.*, **2007**, *73*(*6*),1712-1720.
22. M.F. Anwar; D. Yadav; S. Jain; S. Kapoor; S. Rastogi; I. Arora; M. Samim; *Int. J. Nanomed.,* **2016**, *11*, 147-158.
23. J.Y. Cheon; S.J. Kim; Y.H. Rhee; O.H. Kwon, W.H. Park; *Int. J. Nanomed.,* **2019**, *14,* 2773-2780.
24. G. Zhao; S.E. Stevens; *Biometals*, **1998**, *11*, 27-32.
25. M. Ema, H. Okuda, M. Gamo, K. Honda; *Reprod. Toxicol.,* **2017**, *67*,149-164.
26. F.J. Osonga; A. Akgul; I. Yazgan; A. Akgul; G.B. Eshun; L. Sakhaee; O.A. Sadik; *Molecules,* **2020**, *25*(*11*), 2682.
27. P. Phatai; N. Prachumrak; S. Kamonwannasit; A. Kamcharoen; W. Roschat; S. Phewphong; C.M. Futalan; P. Khemthong; T. Butburee; S. Youngjan; J.C. Millare; O. Prasitnok; *Sustainability,* **2022**, *14*, 11756.

28. A. Nenen; M. Maureira; M. Neira; S.L. Orellana; C. Covarrubias; I. Moreno-Villoslada; *Ceram. Int.*, **2022**, *48*(*23*), A, 34750-34759.
29. V. Stanić; S. Dimitrijević; J. Antić-Stanković; M. Mitrić; B Jokić; I. B. Plećaš; S. Raičević; *Appl. Surf. Sci.*, **2010**, *256*(*20*), 6083-6089.
30. S. Kamonwannasit; C.M. Futalan; P. Khemthong; T. Butburee; A. Karaphun; P. Phatai; *J. Sol-Gel Sci. Technol.*, **2020**, *96***,** 452-463.
31. T. Tithito; S. Sillapaprayoon; W. Pimtong; J. Thongbunchoo; N. Charoenphandhu; N. Krishnamra; A. Lert-Itthiporn; W. Maneeprakorn; W. Pon-On; *Nanomaterials (Basel)*, **2023**, *13*(*2*), 255.
32. S. Sprio; M. Dapporto; L. Preti; E. Mazzoni; M.R. Iaquinta; F. Martini; M. Tognon; N.M. Pugno; E. Revisto; L. Visai; A. Tampieri; *Front. Mater.*, **2020**, *7*, 224.
33. A. Z. Alshemary; A. E. Pazarceviren; T. Aysen; E. Zafer; *RSC Advances*, **2016**, *6*(*72*), 68058-68071.
34. P.N. Lim; L. Chang; E.S. Thian; *Nanomedicine*, **2015**, *11*(*6*) 1331-1344.
35. R. Ahmadi; S. Izanloo; *J. Mech. Behav. Biomed. Mater.*, **2022**, *126*, 105075.
36. F.A.C. Andrade; L.C. de Oliveira Vercik; F.J. Monteiro; E.C. da Silva Rigo; *Ceram. Int.*, **2016**, *42*(*2*), 2271-2280.
37. P.N. Silva-Holguín; S.Y. Reyes-López; *Dose-Response*, **2020**,*18*(*3*).
38. S. Jadalanagan; K. Deshmukh; S.R. Ramanan; M. Kowshik; *Appl. Nanosci.*, **2014**, *4*(*2*), 133-141.
39. A. Mocanu; G. Furtos; S. Rapuntean; O. Horovitz; C. Flore; C. Garbo; A. Danisteanu; G. Rapuntean; C. Prejemrean; M. Tomoaia-Cotisel; *Appl. Surf. Sci.*, **2014**, *298*, 225-235.
40. S. Elbasuney; G.S. El-Sayyad; S.M. Radwan; M. A. Correa-Duarte; *J. Inorg. Organomet. Polym.*, **2022**, *32*, 4559-4575.
41. S. L. Iconaru; D. Predoi; C.S. Ciobanu; M. Motelica-Heino; R. Guegan; C. Bleotu; *Coatings*, **2022**, *12*, 341.
42. L.F.B. Nogueira; M.A. Eufrásio Cruz; G.J. Aguilar; D.R. Tapia-Blácido; M.E. da Silva Ferreira; B.C. Maniglia; M. Bottini; P. Ciancaglini; A.P. Ramos; *Int. J. Mol. Sci.*, **2022**, *23*(*13*), 7277.
43. Y. Zhang; V.J. Reddy; S.Y. Wong; X. Li; B. Su; S. Ramakrishna; C.T. Lim; *Tissue Eng. Part A.*, **2010**, *16*(*6*), 1949-1960.
44. J. P. Monte; A. Fontes; S. Beate; S. Santos; G.A.L. Pereira; G. Pereira; *Mater. Lett.*, **2023**, *338*, 134027.
45. R. Choubey; R. Chouhan; A.K. Bajpai; J. Bajpai; S.K. Singh, *Int. J. Polym. Mater. Polym.*; **2021**, *70* (*11*), 782-796.
46. F. Liu; X. Wang; T. Chen; N. Zhang; Q. Wei; J. Tian; Y. Wang; C. Ma; Y. Lu, *J. Adv. Res.*; **2020**, *21*, 91-102.
47. R.K. Saini; L.P. Bagri; A.K. Bajpa; *Colloids Surf. B*, **2019**, *177*, 211-218.
48. C. Garbo; M. Sindilaru; A. Carlea; Gh. Tomoaia; V. Almasan; I. Petean; A. Mocanu; O. Horovitz; M. Tomoaia-Cotisel; *Part. Sci. Technol.*, **2017,** *35*(*1*), 29.
49. Gh. Tomoaia; A. Mocanu; I. Vida-Simiti; N. Jumate; L.-D. Bobos; O. Soritau; M. Tomoaia-Cotisel; *Mater. Sci. Eng. C*, **2014**, *37*(*1*), 37- 47.

50. D. Oltean-Dan; G.-B. Dogaru; M. Tomoaia-Cotisel; D. Apostu; A. Mester; H.-R.-C. Benea; M.-Gh. Paiusan; E.-M. Jianu; A. Mocanu; R. Balint; C.-O. Popa; C. Berce; G.-I. Bodizs; A.-M. Toader; Gh. Tomoaia; *Int. J. of Nanomed.*, **2019**, *14*, 5799-5816.
51. Gh. Tomoaia; O. Soritau; M. Tomoaia-Cotisel; L.-B. Pop; A. Mocanu; O. Horovitz; L.-D. Bobos; *Powder Technol.*, **2013**, *107*, 23899.
52. A. Mocanu; R.D. Pasca; Gh. Tomoaia; C. Garbo; P.T. Frangopol; O. Horovitz; M. Tomoaia-Cotisel; *Int. J. Nanomed.*, **2013**, *8*, 3867-3874.
53. D. Oltean-Dan; G.-B. Dogaru; E.-M. Jianu; S. Riga; M. Tomoaia-Cotisel; A. Mocanu; L. Barbu-Tudoran; Gh. Tomoaia; *Micromachines*; **2021**, *12*, 1352.
54. A. Mocanu; O. Cadar; P.T. Frangopol; I. Petean; Gh. Tomoaia, G.-A. Paltinean; Cs.P. Racz, O. Horovitz; M. Tomoaia-Cotisel; *R. Soc. Open. Sci.*, **2021**, *8*(*1*), 201785.
55. A. Avram; T. Frentiu; O. Horovitz; A. Mocanu; F. Goga; M. Tomoaia-Cotisel; *STUDIA UBB Chemia*, **2017**, *62*(*4*), 93-104.
56. T. Theivasanthi; M. Alagar; *Nano Biomed. Eng.*, **2012**, *4*, 58-65.
57. A. Mocanu; R. Balint; C. Garbo; I. Timis; I. Petean; O. Horovitz; M. Tomoaia-Cotisel, *STUDIA UBB Chemia*, **2017**, 62, *2*(*1*), 95-103.
58. Zs. Pap; E. Karácsonyi; L. Baia; L.-C. Pop; V. Danciu; K. Hernádi; K. Mogyorósi; A. Dombi; *Phys. Status Solidi B*, **2012**, *12*, 2592-2595.
59. E. Karácsonyi; L. Baia; A. Dombi; V. Danciu; K. Mogyorósi; L.-C. Pop; G. Kovács; V. Coșoveanu; A. Vulpoi; S. Simon; Zs. Pap; *Catal. Today*, **2013**, *208*, 19-27.
60. S. Sfaelou; L.-C. Pop; O. Monfort; V. Dracopoulos; P. Lianos; *Int. J. Hydrog. Energy.*, **2016**, *41*, 5902–5907.
61. M. Popa; L.C. Pop; G. Schmerber; C. Bouillet; O. Ersen; *Appl. Surf. Sci.*, **2021**, *562*, 150159.
62. A.I. Cadiş; L.E. Mureșan; I. Perhaița; L. C. Pop; K. Saszet; L. Barbu-Tudoran; G. Borodi; *J. Nanopart. Res.*, **2022**, *24*, 74.
63. E.-Z.Kedves; C. Fodor; Á. Fazekas; I. Székely; Á. Szamosvölgyi; A. Sápi; Z. Kónya; L.C. Pop; L. Baia; Z. Pap; *Appl. Surf. Sci.*, **2023**, *624*,156914.
64. U.V. Zdrenghea; Gh. Tomoaia; D.-V. Pop-Toader; A. Mocanu; O. Horovitz; M. Tomoaia-Cotisel; *Comb. Chem. High Throughput Screen.*, **2011**, *14*(*4*), 237-247.
65. L.Z. Racz; G.-A. Paltinean; I. Petean; Gh. Tomoaia; L. C. Pop; G. Arghir; E. Levei; A. Mocanu; Cs.-P. Racz; M. Tomoaia-Cotisel; *STUDIA UBB Chemia*, **2022**, *67*(*3*), 61-74.
66. Cs.-P. Racz; L.Z. Racz; C.G. Floare; Gh. Tomoaia; O. Horovitz; S. Riga; I. Kacso; Gh. Borodi; M. Sarkozi; A. Mocanu; C. Roman; M. Tomoaia-Cotisel; *Food. Hydrocoll.*, **2023**, *139*, 1088547.
67. M. Tomoaia-Cotisel; A. Tomoaia-Cotisel; T. Yupsanis; Gh. Tomoaia; I. Balea; A. Mocanu; Cs-P. Racz; *Rev. Roum. Chim.*, **2006**, *51*(*12*), 1181-1185.
68. O. Horovitz; Gh. Tomoaia; A. Mocanu; T. Yupsanis; M. Tomoaia-Cotisel; *Gold Bull.*, **2007**, *40*(*4*), 295-304.
69. O. Monfort; L.-C. Pop; S. Sfaelou; T. Plecenik; T. Roch; V. Dracopoulos; E. Stathatos; G. Plesch; P. Lianos; *Chem. Eng. J.*, **2016**, *286*, 91-97.

STUDIA UBB CHEMIA, LXVIII, 3, 2023 (p. 19-34)
(RECOMMENDED CITATION)
DOI:10.24193/subbchem.2023.3.02

FUZZY DISCRIMINANT ANALYSIS OF MEDICINAL PLANT EXTRACTS ACCORDING TO THEIR TOTAL CONTENT OF PHYTOCHEMICALS AND THE ANTIOXIDANT CAPACITY

Augustin Cătalin MOŢ[a], Cezara ZĂGREAN-TUZA[a], Costel SÂRBU[a,*]

ABSTRACT. Fuzzy linear discriminant analysis, a robust supervised method, has been successfully applied for characterization and classification of 42 Romanian medicinal plant extracts according to the total content of eight phytochemical compounds (alkaloids, polyphenols, coumarins, o-diphenols, flavonoids, anthocyanins, flavonols, flavanols) estimated by dedicated molecular absorption spectrophotometry-based methods, and their antioxidant capacity determined by DPPH* method. The obtained results (fuzzy partitions) and parameters of the class centers (robust fuzzy means) clearly demonstrated the efficiency and information power of the advanced fuzzy method in plants characterization and classification, and allow a rationale choice of a medicinal plant extract with a specified phytochemical composition and/or antioxidant activity. Previous studies have investigated the association of certain classes of phytochemicals with the antioxidant activity in plant extracts. However, most of them are limited either in the number of the plants extracts they have analyzed or in the number of the employed phytochemical classes. The distinctness of this work is the application of a fuzzy multivariate analysis on data obtained for high number of plant extracts—42 widespread medicinal plants form various plant taxa—and a high number of ubiquitous phytochemical classes in plants. The methodology developed in this paper might be also extended in the authenticity and origin control of other fruits, herbs or derived products.

Keywords: *Fuzzy discriminant analysis, chemometrics, medicinal plants, phytochemical composition*

[a] *Faculty of Chemistry and Chemical Engineering, Department of Chemistry, Babeş-Bolyai University, 400028, Cluj-Napoca, Romania*
* *Corresponding author: costel.sarbu@ubbcluj.ro*

INTRODUCTION

Human beings, over the ages, used herbal and mineral drugs provided by nature for their ailments and treatments of disease. Being a rich source of natural antioxidants, medicinal plants—Romania is among the top three countries in Europe for the number of natural medicinal plants—fruits and vegetables have always been considered as part of a healthy and balanced diet, which more and more people are trying to achieve. According to World Health Organization (WHO) in many developing countries the main system used by the people to treat or to prevent diseases is traditional medicine, based on medicinal herbs, even though the modern medicine is available [1,2]. The complex chemical composition proved to be responsible for their curative properties [3-9] and for this reason they have begun to be used also in the food, beverage and cosmetics industry and more important to prevent lipid oxidation and food preservation.

Because of their complex composition, the development of a suitable analytical procedure to separate and evaluate all the constituents of herbal medicines is difficult, impractical and not to mention, time consuming. Therefore, the global evaluation of these samples seems more suitable, instead of focusing on individual compounds and fingerprinting methods fit this challenge by emphasizing and comprehensively characterizing the analyzed samples [10]. The Food and Drug Administration [11] and the European Medicines Agency [12] recommend that the chromatographic and spectroscopic techniques are the most appropriate for analytical procedures. Thus, in the last decades, many methods have been developed for analyzing different plant samples, including thin layer chromatography/high performance thin layer chromatography [10, 13, 14], high performance liquid chromatography and gas chromatography [15, 16], highly speed counter current chromatography [17], capillary zone electrophoresis [10-12]. These techniques are successfully completed by spectroscopic techniques, such as: nuclear magnetic resonance or mass spectrometry and representative results, comparable to those obtained by chromatography, were also obtained using also IR or UV-Vis spectroscopy [18]. The huge amount of spectrophotometric and chromatographic data can be efficiently processed and realistic interpreted using multivariate analysis methods as Cluster Analysis (CA), Principal Component Analysis (PCA) and Linear Discriminant Analysis (LDA) [3-5, 13-15].

At a first sight it seems like these methods are able to solve all problems, but often they may lead to confusing results, because traditional chemometric methods have, indeed, difficulty in identifying outliers in large datasets, and in

finding real patterns. In this case these methodologies have to be improved, by hyphenation or by using more performant methods of discrimination such as fuzzy methods [19]. The applications of fuzzy techniques for characterization and classification of the analytical results are much broader and have significant potential in the authenticity and origin control of fruits, herbs or derived products [20].

The goal of the present study is to propose a new fuzzy classification method [21-23] for medicinal plants according to the total concentration of some classes of phytochemical compounds and their total radical scavenging capacity (RSC %) estimated by DPPH* method [20].

RESULTS AND DISCUSSION

The data used in this study are summarized in **Table 1** and **Figure 1 (a, b)**. It can be easily observed that in all cases, outliers and extremes values are highlighted and the distributions seem to be quite asymmetric. The mean concentration ($\mu g.mL^{-1}$) of anthocyanins and flavanols are the highest and the mean concentration of flavonols and coumarins are the lowest. The mean concentrations of alkaloids, polyphenols, o-diphenols, flavonoids, flavanols are more or less similar. These assertions are also supported by the matrix of correlation depicted in **Table 2**. The results of the correlation analysis also reveal that the phytochemical class most responsible of the antioxidant activity is by far the polyphenols and more specifically, its subclasses, flavonoids, o-diphenols and flavonols. Coumarins and alkaloids contribute to a much less extent to the antioxidant activity, at least to this antiradical ability that was tested via the DPPH bleaching assay in this current study. However, these compounds do have important contribution to other activities such as anti-inflammatory or other pharmacological activities.

According to the profile of antioxidant capacity of plant extract samples, the number of classes for FLDA was chosen to be 3. FLDA produced three fuzzy partitions, which were well represented by a prototype (a cluster center with the parameters corresponding to the fuzzy robust means [24] of the original phytochemical concentrations ($\mu g.mL^{-1}$) for the 42 samples weighted by DOMs corresponding to each partition) depicted in **Table 3**.

Table 1. The statistics of data discussed in this study (μg.mL^{-1})

Variable	Valid N	Mean	Minimum	Maximum	Range	Quartile Range	SD
DPPH (RSC* %)	42	11.18	0.220	46.71	46.49	17.04	12.15
Alkaloids	42	1.16	0.000	4.14	4.14	1.43	0.97
Polyphenols	42	1.03	0.008	3.78	3.77	1.13	0.98
Coumarins	42	0.25	0.000	1.45	1.45	0.25	0.34
o-Diphenols	42	0.78	0.000	5.35	5.35	0.96	1.02
Flavonoids	42	1.08	0.004	5.28	5.28	1.36	1.44
Anthocyanins	42	3.97	0.000	67.56	67.56	2.94	10.61
Flavonols	42	0.19	0.002	0.69	0.69	0.25	0.19
Flavanols	42	3.00	0.000	13.22	13.22	1.97	2.87

*relative total radical scavenging capacity

Table 2. Matrix of correlation concerning the concentration of phytochemicals

Variable	(1)	(2)	(3)	(4)	(5)	(6)	(7)	(8)	DPPH
Alkaloids (1)	1.000	0.577	0.278	0.582	0.591	0.119	0.533	0.598	0.468
Polyphenols (2)		1.000	0.544	0.871	0.912	0.143	0.878	0.735	0.936
Coumarins (3)			1.000	0.713	0.723	-0.030	0.489	0.357	0.529
o-Diphenols (4)				1.000	0.896	0.141	0.773	0.634	0.759
Flavonoids (5)					1.000	0.047	0.834	0.771	0.879
Anthocyanins (6)						1.000	0.167	-0.193	0.005
Flavonols (7)							1.000	0.655	0.824
Flavanols (8)								1.000	0.691
DPPH									1.000

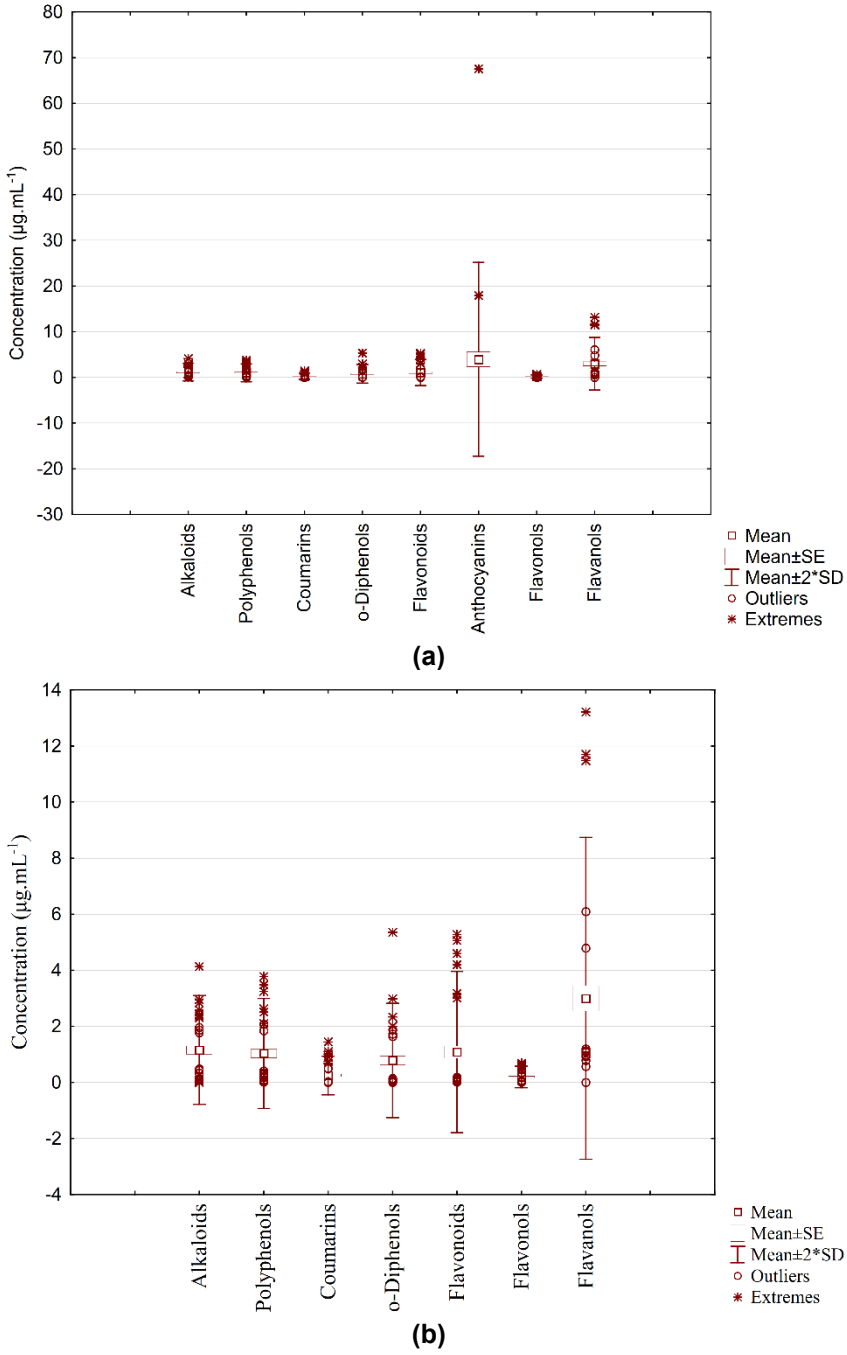

Figure 1. Box and whiskers plot of all data (**a**) and data without anthocyanins (**b**)

Table 3. The results obtained applying fuzzy linear discriminant analysis

Fuzzy partition (class)	Parameters of partition centers (fuzzy mean) ($\mu g.mL^{-1}$)	Plant extract	Name of medicinal plant	RSC* %	DOM
A1	(1) 1.81 (2) 2.52 (3) 0.58 (4) 2.05 (5) 3.09 (6) 3.18 (7) 0.41 (8) 5.70	1-9	1.Blueberry 2.Lingon berry 3.Rosemary 4.Hoary willowherb 5.Lady's mantel 6.Quaking aspen 7.Lemon balm 8.Sage 9.Silver birch	46.71 36.58 31.01 29.82 29.61 27.97 27.36 27.36 26.27	0.934 0.821 0.921 0.999 0.874 0.168 0.976 0.842 0.623
A2	(1) 1.03 (2) 1.05 (3) 0.32 (4) 0.89 (5) 1.13 (6) 1.99 (7) 0.25 (8) 3.04	10-20	10.Saint John's wort 11.Hawthorn 12.Breckland thyme 13.Burdock 14.Great celandine 15.Lady's bedstraw 16.Common juniper 17.Yarrow 18.Spinycockle-bur 19.Lavender 20.Artichoke	21.12 18.74 15.48 13.98 12.86 11.16 10.13 9.45 9.44 8.93 7.42	0.848 0.718 0.796 0.880 0.916 0.662 0.784 0.712 0.168 0.342 0.261
A3	(1) 0.87 (2) 0.36 (3) 0.09 (4) 0.16 (5) 0.20 (6) 1.79 (7) 0.07 (8) 1.95	21-42	21.Liquorice 22.Gentian 23.Echinacea 24.Comfrey 25.Milk thistle 26.Nettle 27.Heart's ease 28.Motherwort 29.Ginger 30.Valerian 31.Shepherd's purse 32.Horsetail 33.Dill 34.Garlic 35.Mistletoe 36.Elder 37.Chili pepper 38.Sweet flag 39.Hogweed 40.Wolf's-foot clubmoss 41.Celery 42.Ramson	4.93 4.46 4.38 4.32 3.75 3.69 3.06 2.78 2.26 2.09 1.78 1.70 1.62 1.45 1.20 1.19 1.05 1.00 0.68 0.37 0.25 0.22	0.090 0.356 0.491 0.944 0.827 0.983 0.915 0.834 0.163 0.906 0.928 0.812 0.242 0.626 0.726 0.768 0.937 0.951 0.974 0.978 0.993 0.989

(1) alkaloids, (2) polyphenols, (3) coumarins, (4) ortho-diphenols,
(5) flavonoids, (6) anthocyanins, (7) flavonols, (8) flavanols
*relative total radical scavenging capacity [13]

To compare the fuzzy partitions (fuzzy classes) and the similarity and differences of the investigated medicinal plant extracts, we have to analyze both the characteristics of the prototypes (centers) corresponding to the three fuzzy partitions (**A1**-**A3**) obtained by applying FLDA and DOMs of samples corresponding to all fuzzy partitions, including also the canonical scores used usually in classical linear discriminant analysis [25].

The results presented in **Table 3** clearly illustrate the most specific characteristics of each fuzzy partition and their similarity and differences.

The mean values of prototype corresponding to the first partition (**A1**), including the medicinal plant extracts with the highest RSC (46.71-26.27%), are the highest for all phytochemicals. The blueberry extract (*a supper fruit*) has the strongest antioxidant capacity (46.71%). In addition, all the samples assigned to this group have a high DOM (0.821-0.999) except Silver birch (0.623) and Quaking aspen sample (0.168). This situation is well illustrated in **Figure 2**; Quaking aspen has a relatively high RSC, but in accordance with the total concentration of all phytochemical compounds is closer to the center of partition **A2**.

The partition **A2** contains plant extracts samples with moderate RSC (21.12-7.42%) and also quite different DOMs (0.916-0.168). All the concentrations obtained for the center of this partition are between the values corresponding to partition **A1** and **A3 (Figure 2)**.

The partition **A3** includes the medicinal plant extracts with the smallest RSC (4.93-0.22%) which is in good agreement with the concentration of phytochemical compounds (see center concentrations in **Table 3** and **Figure 2**). The 2D scatterplot of DOMs corresponding to the three partitions confirmed in a good way the results discussed above (**Figure 3a**).

The efficiency of the robust Fuzzy Linear Discriminant Analysis (FLDA) applied was measured by the correct classification rate of original data and by the values of quality performance features obtained applying leave-one-out (LOO) cross-validation approach including also relevant graphs obtained by scatterplot of degrees of freedom (DOMs) and fuzzy canonical scores on the plan defined by Root1-Root2 (**Figure 3b**) and the values of quality performance features obtained for the correct classification rate of the original data and by applying the leave-one-out (LOO) cross-validation approach (**Table 4**).

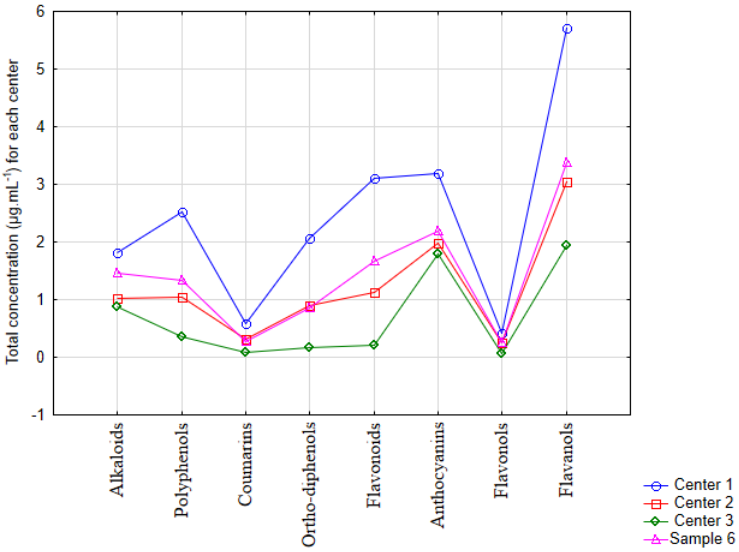

Figure 2. The concentration profile corresponding to all centers and the sample 6

Table 4. Matrix classification of medicinal plants

Class	Total	Classification matrix					
		Samples			%		
		A1	A2	A3	A1	A2	A3
A1	**9**	**8**	1	0	**88.89**	11.11	0.00
A2	**11**	0	**8**	3	0.00	**72.73**	27.27
A3	**22**	0	4	**18**	0.00	18.18	**81.82**
Leave-one-out cross-validation							
A1	**9**	**7**	1	1	**77.78**	11.11	11.11
A2	**11**	0	**8**	3	0.00	**72.73**	27.27
A3	**22**	0	4	**18**	0.00	18.18	**81.82**

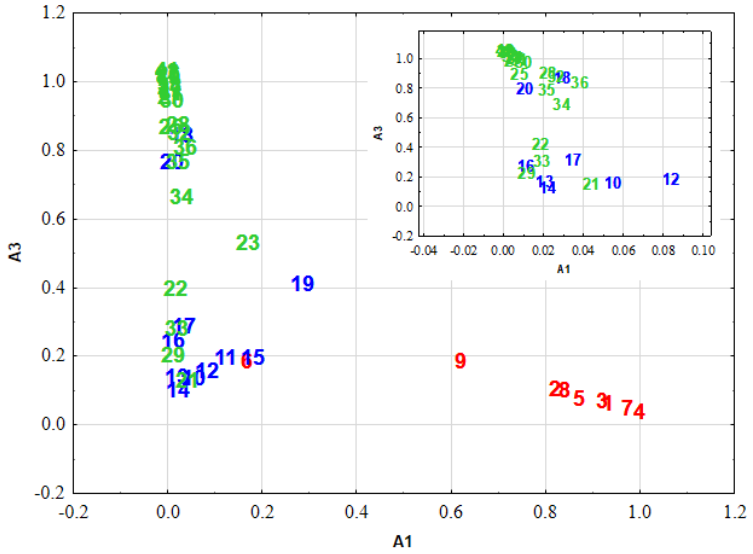

(**a**)

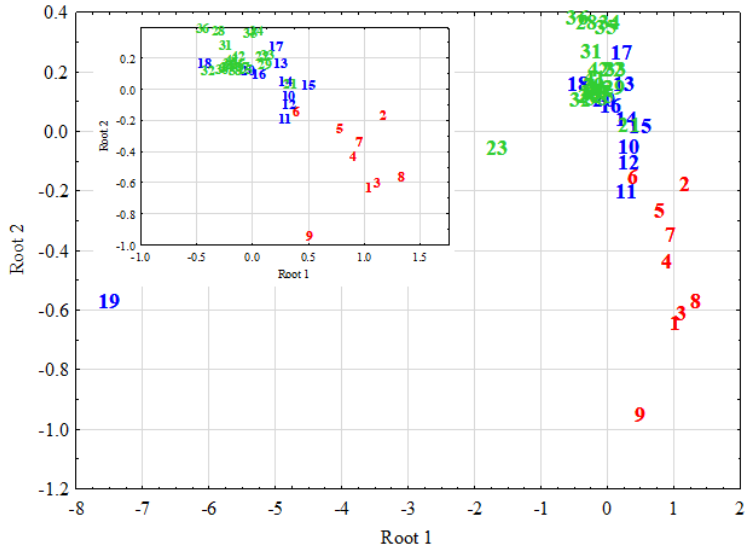

(**b**)

Figure 3. Scatterplot of DOMs corresponding to partition **A1** and **A3** (**a**) and scatterplot of fuzzy canonical scores on the plan defined by root 1 and root 2. Inserts contain zoomed in regions, for heavily packed intervals, for better clarity.

Whereas the multivariate approach applied in this study allows for a fuzzy classification of the plant extracts in three main groups, mostly related to the antioxidant activity level, it also supports the expected finding that only to a limited extent their content and the diversity of the phytochemical classes are responsible for this activity but rather the chemical structure of the compounds (Figure 1, Table 3, Figure 2). For example, despite their small content compared to the other classes, flavonols do exhibit a significant positive correlation with the determined antioxidant activity ($r = 0.824$, $p < 0.05$). On the other hand, one might be aware that the determined phytochemical classes are chemically hierarchized, as indicated in Figure 4.

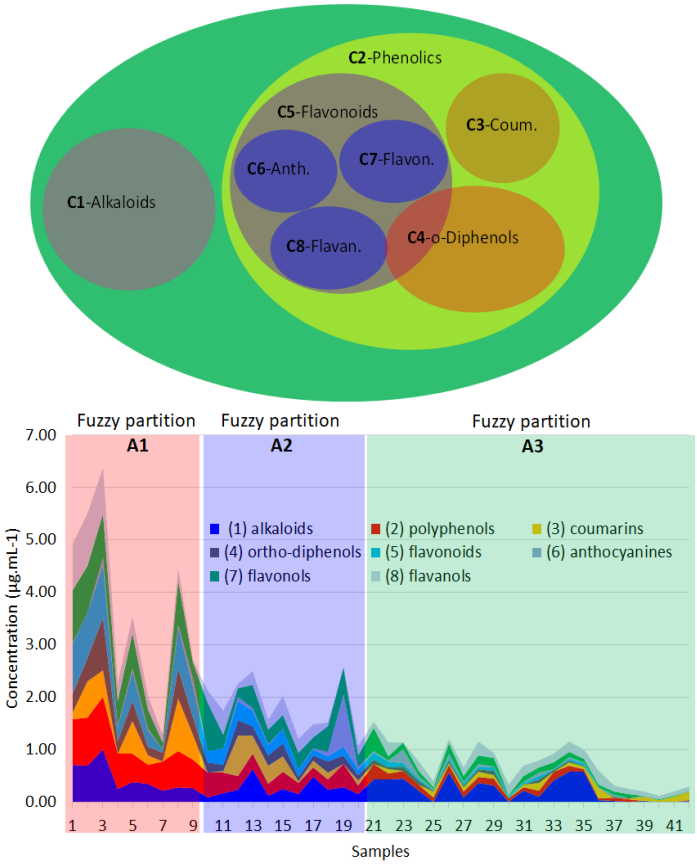

Figure 4. **Top**: Ven diagram of the analyzed phytochemical classes, according to their chemical relationships. **Bottom**: Concentration profile for the determined phytochemical classes for all the 42 plant extract samples.

Following the identification of the three fuzzy partitions by the FLDA, one might observe not only the strong association of the concentration profiles for certain phytochemical classes—polyphenols, o-diphenols, flavonoids, flavonols—with the antioxidant activity, but also the phytochemical groups responsible for the generation of the outliers/extremes and thus production of the significant variation within/between classes (Figure 4). Such systems could only be efficiently investigated using fuzzy analysis. One inconvenience of this work is that FLDA was applied only on DPPH antioxidant activity which is based mainly on electron transfer mechanism but possible more or less different plant classification might be observed if other types of antioxidant assays would be investigated.

CONCLUSIONS

In this study, the advantages of the fuzzy linear discriminant analysis for the characterization and classification of various medicinal plant extracts on the basis of their phytochemical composition and antioxidant capacity have been explored. The informative potential of this robust fuzzy method is clearly demonstrated. The new classification approach allows more relevant conclusions to be drawn, finding more specific groups. The parameters of the prototype (class center) illustrate much better than, for example, arithmetic mean the specific characteristics of each class. In addition, the 2D scatterplot of DOMs and fuzzy canonical scores allow a rationale comparison of the similarities and differences of medicinal plant extract samples investigated. This procedure can be successfully extended to other similar studies in different scientific and technical fields.

EXPERIMENTAL SECTION

Medicinal plant samples and analytical methods

The plant samples consisted of 42 hydroalcoholic extracts commercially available (**Table 2**), distributed by Dacia Plant manufacturer (Brasov, Romania).

Analytical methods

Total alkaloids content. This assay is a modified version of the analysis with the Dragendorff reagent [26]. Basically, the plant extract is treated with a mixture of bismuth nitrate and potassium iodide when a yellowish bismuth-nitrogen complex forms. Instead of separating and resuspending this precipitate, the turbidity of the reaction mixture was measured which was then correlated to the berberine equivalent from the calibration function. A 0.035 mM solution of $Bi(NO_3)_3$ was prepared, the solvent being mixture of water: acetic acid ratio of 4:1 v/v. The other prepared solution was one of KI of 50% (w/v). Vigorous shaking is required for dissolving both salts. The reagent was prepared by mixing 5 ml of $Bi(NO_3)_3$ with 2 ml of KI. A volume of 20 µl of extract were mixed with 200 µl of this solution along with 80 µl 50% ethanol in a 96 wells plate. The turbidity was measured using a Tecan spectrophotometer at 530 nm. The calibration function was done by using berberine as standard in concentrations ranging from 0.11 to 32.2 $\mu g.mL^{-1}$. The final values were expressed as berberine equivalents and were calculated by using the calibration function. All samples were analysed in duplicates.

Total polyphenolics content (*Folin-Ciocâlteu reducing capacity assay*). The basis of this method is the capacity of some phenolate anions to be oxidized by a molybdenum-based complex which changes color from yellow to blue. The polyphenols are exposed to a basic medium ensured by a saturated carbonate solution which deprotonates the compounds; as a result, phenolate ions are obtained. They are capable to react with the so-called Folin-Ciocâlteu reagent which contains a combination of phospho- tungsten and molybdenum compounds along with lithium sulfate as bromine. As a result of the chemical reaction, the polyphenols are oxidized, whereas the molybdenum is reduced, obtaining the metallic complex $(PMoW_{11}O_4)^{4-}$ which has a bluish shade. The main disadvantage of this assay is that not only polyphenols react with this reagent, but also other compounds with reducing abilities. In order to measure the antioxidant activity using this method, 2 µL of each extract was mixed with 236 µL water and 17 µL Folin-Ciocâlteu reagent in a 96 wells Tecan microplate. This solution was incubated in the dark for about 5 minutes. Then 45 µL of 20% sodium carbonate solution was added and the whole mixture was incubated for 30 minutes. After the time passed, the microplate was placed in a Tecan spectrophotometer and the absorbance was measured at 725 nm. All extracts were analysed in duplicates. In the meantime, a signal on concentration dependence was all performed, with values of concentration

varying from 0 to 40 $\mu g.mL^{-1}$ Gallic acid. The Gallic acid equivalents (GAE) of each extract were determined by calculating the concentration value from the calibration function by means of absorbance [27].

Total coumarins content. When exposed to pH variations coumarin phenolic hydroxyl moieties can suffer ionization which appears as a bathochromic effect in UV-vis spectrophotometry. A volume of 5 µL of extract were mixed with 295 µL 50% ethanol in ultrapure water along with 2 µL of 20 mM sodium carbonate solution in a 96 wells plate [28]. The absorbance was measured before and after the addition of the carbonate solution: first at 320 nm and then at 370 nm. The final absorbance value was calculated by adding up both values. A calibration function was built using coumarin as standard by plotting the absorbance values against the concentrations ranging from 1.65 to 33.11 $\mu g.mL^{-1}$. The final results were expressed as coumarin equivalents. All experiments have been performed in duplicates.

Total ortho-diphenols content. This method is based on the fact that the hydroxyl group of ortho-dipehnols can react with sodium molybdate thus producing a yellowish metallic complex in an aqueous medium [29]. In order to perform this analysis, 3 µL of extract were mixed with 97 µL 50% ethanol in ultrapure water, then 200 µL of 5 g/100 mL sodium molybdate was added in a 96 wells plate. The samples were incubated for 25 minutes and the absorbance was measured at 370 nm with the help of a Tecan spectrophotometer. A calibration function was built by using caffeic acid as standard in concentrations from 0.91 to 91.6 $\mu g.mL^{-1}$ by plotting the measured absorbance against the values of concentration. The final results were given as caffeic acid equivalents and they were obtained by applying the equation of the calibration function to each measurement. Each extract was analysed in duplicate.

Total flavonoids content. This method is based on the fact that flavonoids react with sodium nitrite, a potent nitration reagent, and aluminum chloride to form an adduct that in a strong basic media turns a bright red [30]. Basically, the aluminum ion is chelated toward a catechol moiety by reacting with its hydroxyls, fact that makes this analysis highly specific. A volume of 120 µL of ultrapure water were mixed with 5 µL extract and 80 µL of 5% $NaNO_2$ solution in a 96 wells plate and allowed to react for 5 minutes. Afterward 50 µL of 2% AlCl3 were added. After another 5 minutes 50 µL of 1M NaOH to increase the pH. Finally, after further 5 minutes while the compounds were left to react, the absorbance was measured at 510 nm using a Tecan spectrophotometer. The experiments were performed in duplicates and the calibration function was built by use of rutin solution varying from 1.1 to

110 μg.mL^{-1} by plotting the values of absorbance against the quantities of standard. The final results were showed as rutin equivalents and they were calculated by applying the equation of the calibration function.

Total anthocyanins content. A pH differential method is used for quantifying anthocyanins. This assay is based on the fact that these compounds exhibit different species at various pHs: at a low pH the flavylium cation is dominant, thus the anthocyanins having a bright powerful color [26]. If the pH is increased, a conversion to a pseudo base carbinol takes place with loss of color. Reading the absorbance at 700 nm is essential in order to correct the possible haze. In order to make this assay, 2 buffering solutions were prepared: one of pH=1 of 0.025 M KCl and another of pH=4.5 of 0.4 M sodium acetate. A volume of 270 μL of each buffer was separately mixed with 30 μL extract and the absorbance was read after 5 minutes at 520 nm. The absorbance values were obtained by subtracting the value of pH=4.5 from the value of pH=1 and then it was corrected with the 700 nm absorbance. The experiments were performed in duplicates for each pH value. The final cyaniding-3-glucoside-equivalents expressed results were calculated using the following formula:

Total anthocyanins (TA) = (absorbance at 520 * dilution factor)/ 98.2
where 98.2 is the extinction coefficient of the standard.

Total flavonols content. The basis of this method is the complexation reaction between aluminium and the hydroxyl groups of flavonols in slightly acidic pH, ensured by the presence of sodium acetate buffer [26]. For this purpose, 75 μL of 50% ethanol in ultrapure water was mixed with 5 μL extract and incubated for 5 minutes in the presence of 80 μL of 2% $AlCl_3$ solution in a 96 wells plate. Afterwards, 120 μL of 1M sodium acetate was added and the absorbance was recorded at 430 nm using a Tecan spectrophotometer in duplicates for each sample. The standard used to build the calibration function was quercetin in concentration range between 0.55 to 26.57 μg.mL^{-1}. The absorbance read for standard containing samples was then plotted against the values and concentration and the resulting equation was used to calculate the quercetin equivalents for each extract.

Total flavanols content. At low pH vanillin is protonated, one of its carbons becoming an electrophilic carbocation that can react with a flavonoid ring at the 6th or 8th carbon atom, giving rise to a reddish complex [26]. Even though, chemically speaking, the reaction is very selective towards flavanols, interferences with anthocyanins might occur when measuring the absorbance. In order to make this assay, 30 μL of extract were diluted in 70 μL 50% ethanol in ultrapure water in a 96 wells plate. A volume of 150 μL of 4% vanillin

solution was added, along with 75 µL of 35% H_2SO_4 and the mixture was left to react for 15 minutes at room temperature. Afterwards, the absorbance was recorded at 520 nm on a Tecan spectrophotometer for each extract in duplicates. Meanwhile, a calibration function was built by plotting the read absorbance against various concentrations of catechin (from 0.71 to 1146 $\mu g.mL^{-1}$). The final results were presented as equivalents of catechin obtained by applying the curve equation for each extract.

Fuzzy Linear Discriminant Analysis

Linear discriminant analysis (LDA) is a supervised classification technique based on the linear discriminant functions, which maximizes the ratio of between-class variance and minimizes the ratio of within-class variance. LDA selects directions, which accomplish maximum separation among the given classes. The Euclidean distance is used in the LDA algorithms in order to classify unknown samples and the stepwise algorithm to extract the most important variables. It is also possible to visualize how the functions discriminate between groups by plotting the individual scores for the discriminant functions. In addition, FLDA may offer some remarkable information for classification and discrimination of the considered samples according to DOMs and fuzzy canonical scores. The robust FLDA has been clearly described and efficiently applied in some interesting works [21-23].

All the graphs and some statistics were performed using Statistica 8.0 (StatSoft, Inc. 1984–2007, Tulsa, USA) software. All the other results were obtained using our own fuzzy software package.

REFERENCES

1. WHO monographs on selected medicinal plants, Volume 1-4, **2009**.
2. M.A. Motaleb; Selected medicinal plants of Chittagong hill tracts, IUCN, Dhaka, **2011**.
3. M.I. Simion; D. Casoni; C. Sârbu; *J. Liq. Chrom. Relat. Tech*., **2018**, *41*, 342–348.
4. M.I. Simion; H.F. Pop; C. Sârbu; *Rev. Roum. Chim*. **2018**, *63*, 489–496.
5. M.I. Simion; D. Casoni; C. Sârbu; *J. Pharm. Biomed. Anal*. **2019**, *163*, 137–143.
6. D. Komes; A. Belščak-Cvitanović; D. Horžić; G. Rusak; S. Likić; M. Berendika; *Phytochem. Anal*., **2011**, 22, 172-180.
7. M. Alexan; O. Bojor; F. Crăciun; Flora Medicinală a României, Vol. 1, Ceres, Bucureşti, **1988**.

8. O. Bojor; Ghidul plantelor medicinale şi aromatice de la A la Z, Dharana, Bucuresti, **2018**.
9. A. Vasilica-Mozaceni; Ghidul plantelor medicinale, Polirom, Iasi, **2003**.
10. Y. Ni; Y. Lai; S. Brandes; S. Kokot; *Anal. Chim. Acta*, **2009**, *647*, 149–158.
11. FDA, Guidance for Industry—Botanical Drug Products (Draft Guidance), US Food and Drug Administration, Rockville **2000**, pp. 4.
12. Note for Guidance on Quality, of Herbal Medicinal Products, European Medicines Agency, London **2001**, pp. 6.
13. I.A. Sima; C. Sârbu; R.D. Naşcu-Briciu; *Chromatographia*, **2015**, *78*, 929–935.
14. I.A. Sima; M. Andrási; C. Sârbu; *J. Chromatogr. Sci*., **2018**, *56*, 49–55.
15. C. Sârbu; R.D. Naşcu-Briciu; A. Kot-Wasik; S. Gorinstein; A. Wasik, J. Namiesnik; *Food Chem*., **2012**, *130*, 994–1002.
16. M. Costas-Rodriguez; I. Lavilla; C. Bendicho; *Anal. Chim. Acta*, **2010**, *664*, 121–128.
17. L. Cuadros-Rodríguez; C. Ruiz-Samblas; L. Valverde-Som; E. Perez-Castano; A. Gonzalez-Casado; *Anal. Chim. Acta*, **2016**, *909*, 9-23.
18. Z.L. Cardeal; P.P. de Souza; M.D.R. Gomes da Silva; P.J. Marriott; *Talanta*, **2008**, *74*, 793-799.
19. C. Sârbu; Fuzzy Clustering of Environmental Data in Current Applications of Chemometrics, Mohammadreza Khanmohammadi (ed.), NOVA Science Publishers, **2015**, Chapt. 3., p. 33-56.
20. M.I. Simion; A.C. Moț; C. Sârbu; *Anal. Methods*, **2020**, *12*, 3260–3267.
21. H.F. Pop; C. Sârbu; *MATCH Commun. Math. Comput. Chem*., **2013**, *69*, 391-412.
22. A. Guidea; C. Sârbu; *J. Liq. Chrom. Relat. Tech*., **2020**, *43*, 1−8.
23. A. Guidea; R. Găceanu; H.F.Pop; C. Sârbu; *STUDIA UBB CHEMIA*, **2020**, *LXV*, *2*, 45−56.
24. C. Sârbu; H.F. Pop; *Talanta*, **2001**, *54*, 125-130.
25. G. J. McLachlan; Discriminant Analysis and Statistical Pattern Recognition, John Wiley & Sons, Inc., **2004**.
26. S. Garba; *J. Microbiol. Antimicrob*., **2012** *4*, 60–63.
27. D. Granato; J.S. Santos; L.G. Maciel; D.S. Nunes; *TrAC Trends Anal. Chem*., **2016**, *80*, 266–279.
28. E.LC. Amorim; V.T.N. Castro; J.G. Melo; T.J. Sobrinho; World's Largest Science, Technology & Medicine, Open Access Book Publisher, Standard Operating Procedures (SOP) for the Spectrophotometric Determination of Phenolic Compounds Contained in Plant Samples, **2012**.
29. C. Gerdemann; C. Eicken; B. Krebs; *Acc. Chem. Res*., **2002**, *35*, 183–191.
30. A. Pękal; K. Pyrzynska; *Food Anal. Methods*, **2014**, *7*, 1776–1782.

STUDIA UBB CHEMIA, LXVIII, 3, 2023 (p. 35-49)
(RECOMMENDED CITATION)
DOI:10.24193/subbchem.2023.3.03

ANALYSIS OF THE MINERAL PROFILE OF MILK AND SWISS CHEESE FROM ŢARA DORNELOR IN RELATION TO SEASONAL AND TECHNOLOGICAL FACTORS

Doru NECULA[a,b], Mădălina UNGUREANU-IUGA[b,c,*], Sorin Daniel DAN[a], Octavia TAMAS-KRUMPE[a], Laurenț OGNEAN[a]

ABSTRACT. Milk and cheese are important sources of macro and microelements, their amounts depend on the feeding method of the animal, the climatic and environmental conditions, the state of health and the lactation period, as well as the technology of milk processing. The purpose of this paper is to evaluate the mineral profile of raw milk and Swiss cheese produced in Ţara Dornelor in different seasons and obtained by different technologies. The results showed that during the summer season, milk is richer in K and Ca and poorer in Cu. Swiss cheese presented a lower content of Na, Ca and Mg in the summer period compared to the winter one, a similar trend being observed for Mn and Fe. The processing technology also determined significant variations ($p < 0.05$) in the content of micro and macro elements. The processing of Swiss cheese in a copper boiler determined an increase in the Cu content of up to 6 times compared to the product obtained in a stainless-steel boiler. These results are important both for processors interested in increasing the quality of their products, and for consumers aware of the importance of food with high nutritional value.

Keywords: *micro and macroelements, dairy products technology, season, Emmental cheese*

[a] *University of Agricultural Sciences and Veterinary Medicine, 3-5 Mănăştur street, 400037, Cluj-Napoca, Romania.*
[b] *Mountain Economy Center (CE-MONT), National Institute of Economic Research (INCE), Romanian Academy, 49 Petreni street, 725700, Vatra Dornei, Romania.*
[c] *Integrated Research, Development and Innovation Center for Advanced Materials, Nanotechnologies and Distributed Manufacturing and Control Systems (MANSiD), "Ştefan cel Mare" University of Suceava, 13 Universităţii street, 720229 Suceava, Romania.*
[*] *Corresponding author: madalina.iuga@ce-mont.ro*

INTRODUCTION

Dairy products are rich in micronutrients such as minerals that are implied in multiple vital processes for the body. Minerals from milk and dairy products are classified into macroelements (Ca, Mg, Na, K, P and Cl) and microelements (Fe, Cu, Zn and Se), being often found in various associations with other ions or organic molecules [1]. The distribution of minerals in milk takes place depending on the nature of the elements, for example K, Na and Cl being present in the aqueous phase, and Ca, P and Mg being bound to the casein micelles [1].

The content of micro- and macroelements in cheeses largely depends on the processing technology. Traditional Swiss cheese is made in copper boilers, but in countries such as Finland a practice is found that involves the manufacture of Emmental type cheeses in stainless steel boilers and the addition of copper sulfate solution in certain concentrations to ensure the copper level in the final product similar to traditional cheese [2]. Copper in the technological process can inhibit the activity of lactic and propionic bacteria depending on the amount present, large quantities leading to ripening defects of the final product due to the modification of propionic fermentation [3]. Studies have shown that the presence of copper could reduce the risk of defects caused by C. tyrobutyricum and other clostridial species, thus improving the overall quality of Emmental cheeses [3]. The amount of micro and macro elements in cheeses depends on a series of factors such as the mineral content of the raw milk, which in turn is influenced by the state of health of the animal, breed, lactation period, feed, and growing environment, climatic conditions; the technological process of cheese manufacturing, which differs depending on its type (fresh, matured); in the case of matured cheeses, the ripening conditions (temperature, humidity) that influence the microbial activity, as well as the salting procedures on the surface of the products, have a major contribution [4].

The consumption of adequate amounts of macroelements is essential for the proper functioning of the body. Milk and dairy products can contribute to the supply of macroelements such as Ca, Mg, K, Na. Ca is a structural element of bones and teeth and is responsible for regulating the functioning of the nervous and muscular system, the transformation of prothrombin into thrombin, ensuring the permeability of the cell membrane involved in muscle contraction, being also a constituent of enzymes such as adenosine triphosphatase (ATPase), succinic dehydrogenase, lipase [5]. Na is the cation found in the largest quantity in the extracellular fluid and has an essential role in maintaining its volume, in blood pressure, in the transport of nutrients to and from the cells [6]. K is the predominant cation in the intracellular fluid and is involved in the acid-base balance, the regulation of osmotic pressure, the proper functioning of the nervous

and muscular system and in glycogenesis [5]. Mg is a component of over 300 enzymes and has an important role in muscle contraction, the functioning of the nervous system, regulation of blood sugar and blood pressure, transmembrane transport of other ions, energy production and nucleic acid synthesis [7].

The microelements present in milk have an important role for human nutrition, as the consumption of dairy products can partially or totally cover the daily requirement. Se is part of the structure of the enzyme glutathione peroxidase and some selenoproteins, also participating in a series of biological processes such as the reduction of oxidative stress, the activity of the immune system and the synthesis of thyroid hormones [8]. Fe is essential for ensuring the good functioning of the body as it is involved in the synthesis of hemoglobin by erythroblastic cells, Fe absorption being dependent on the interaction with other elements (for example Cd, Pb, Mn and Zn are Fe antagonists) [9]. The importance of Cu derives from its involvement in cellular energy, the synthesis of some neurotransmitters, in the biochemical process of collagen and elastin production, as well as in the absorption, storage and metabolism of Fe [9]. The role of Mn in the human body is to modulate the synthesis and metabolism of carbohydrates, fats and cholesterol, being also of major importance for the correct functioning of the brain and muscle tissue, but also for the production of DNA and RNA molecules [5]. Zn is part of many enzymes, thus being involved in DNA and RNA synthesis, in protein synthesis, macronutrient metabolism, in cell replication, in the proper functioning of the immune system and in the inhibition of the oxidative processes of unsaturated fatty acids [5,9].

The purpose of this paper is to highlight the effects of season and processing technology on the mineral content of cow's milk and Swiss cheese from Ţara Dornelor, a region with a history of producing this variety of cheese. To the best of our knowledge, there are no studies on the mineral profile of these products from Ţara Dornelor region, and the results are of major importance for the support of the producers and for the certification of the Dorna Swiss cheese.

RESULTS AND DISCUSSION

Mineral profile of milk

The content of some of the macro and microelements in the raw milk studied showed differences both between seasons and between producers (Table 1). Thus, the amount of K and Ca for unit A was significantly higher ($p < 0.05$) in the summer season (increase by 9.88% and 10.65% respectively), the content of Mg and Na not being significantly influenced. Conversely, for the milk from unit B, significant increases ($p < 0.05$) were observed in the amounts of Na (increase by 462.44%), Mg (increase by 121.08%), K (increase by 371.96%)

and Ca (increase by 68.24%) in the summer season compared to the winter season. On the other hand, significant differences ($p < 0.05$) were observed between the two processors regarding the amount of macroelements in both seasons. Thus, in the winter season, higher amounts of Na (4.90 times), Mg (1.64 times), K (5.40 times) and Ca (1.18 times) were obtained in the milk from unit A compared to unit B. In the summer season, higher amounts of Na (1.18 times), Mg (1.38 times) and Ca (1.29 times) were observed in milk from unit B and K content (1.28 times) lower compared to unit A. The content of micro and macro elements in milk depends on a series of factors such as animal species, season, animal nutrition, soil nature and farm location [10]. Macroelements such as Ca and Mg are found in milk in the form of calcium phosphate, calcium phosphocaseinate and free magnesium, associated with the colloidal suspension of casein micelles [11]. The amount of Na in milk is influenced by the animals feeding, the practice of supplementing the diet with sodium salts being known [11]. The presence of lactose, ascorbate, citrate, phosphopeptides and lactoferrin can have a significant effect on the absorption of macro and micro elements from milk in the human body [9]. Król et al. [12] reported lower values of the content of Ca and Mg in milk in summer compared to winter, similar to Gulati et al. [13] who obtained higher Ca, Mg and Na values in the autumn-winter period compared to the summer season. The differences could be related to the different feeding: in summer the animals were grazed outside, while in winter they were fed with hay.

Table 1. Minerals content (expressed as mg/kg d.b.) of raw milk in different seasons

Element	Unit A		Unit B	
	ITCL	VTCL	ICAL	VCAL
Macroelements				
Na	369.90 ± 4.10^{aA}	360.90 ± 4.00^{aY}	75.50 ± 1.20^{yB}	425.40 ± 6.50^{xX}
Mg	75.60 ± 3.80^{aA}	73.50 ± 1.20^{aY}	46.00 ± 1.50^{yB}	101.70 ± 1.20^{xX}
K	1869.80 ± 28.0^{bA}	2105.60 ± 26.60^{aX}	346.00 ± 2.10^{yB}	1633.00 ± 18.80^{xY}
Ca	2424.40 ± 89.70^{bA}	2682.50 ± 31.90^{aY}	2058.60 ± 125.60^{yB}	3463.00 ± 41.50^{xX}
Microelements				
Mn	0.02 ± 0.00^{aB}	0.03 ± 0.00^{aY}	0.11 ± 0.00^{xA}	0.09 ± 0.00^{yX}
Zn	1.23 ± 0.02^{bB}	2.99 ± 0.10^{aY}	3.27 ± 0.04^{xA}	3.24 ± 0.11^{xX}
Se	0.01 ± 0.00^{aA}	0.02 ± 0.00^{aX}	0.02 ± 0.01^{xA}	0.01 ± 0.01^{xX}
Cu	0.27 ± 0.01^{bA}	0.09 ± 0.01^{aY}	0.26 ± 0.01^{xA}	0.11 ± 0.01^{yX}
Fe	0.53 ± 0.01^{bB}	0.78 ± 0.03^{aY}	4.43 ± 0.04^{xA}	1.01 ± 0.04^{yX}

ITCL - milk sample from unit A from the winter period, VTCL - milk sample from unit A from the summer period, ICAL - milk sample from unit B from the winter period, VCAL - milk sample from the unit B from the summer period; a-b (for unit A) and x-y (for unit B) mean values followed by distinct lowercase letters in the same row indicate significant differences ($p < 0.05$) between seasons, A-B (for the winter season) and X-Y (for the summer season) mean values followed by distinct capital letters in the same row indicate significant differences ($p < 0.05$) between the processing units in the same season.

Regarding the microelement content of raw milk, significant differences ($p < 0.05$) were observed between seasons in the case of unit A, where Zn, Cu and Fe were found in greater quantities in summer compared to winter (increase with 143.09, 66.66, respectively 47.17%), while Mn and Se had no significant variations ($p > 0.05$). The same trend of increasing the concentration of Mn (by 22.22%), Cu (by 136.36%) and Fe (by 338.61%) during summer compared to winter was obtained in the case of milk from unit B, while the Se and Zn did not vary significantly ($p > 0.05$). Sola-Larrañaga and Navarro-Blasco [11] reported differences in Fe, Mn, Zn and Cu content of cow's milk in different seasons probably due to feed and metabolic adaptation to climate change. The amount of Fe in milk depends on the presence of lactoferrin and xanthine oxidase transferase enzymes, Fe, Zn and Cu from ruminant milk being mostly related to the casein fraction [14]. Our results regarding the content of Zn, Fe, and Mn are comparable to those obtained by Król et al. [15] for milk from different areas of Poland. The same authors reported higher values for Cu and Zn content in summer compared to winter [15], while Górska and Oprządek [16] reported an opposite trend. According to the opinion of some authors, Zn from animal feed decreases Cu absorption due to the interaction with its absorption system [15]. The values reported by the literature for Fe, Cu, Zn and Se differ due to the sample preparation protocol and the quantification methodology, generally the amounts being around 0.5 mg/L for Fe, 0.1 mg/L for Cu, 3-4 mg/L for Zn and 0.03 mg/L for Se [1]. The results of the present study are close to these values (Table 1).

Mineral profile of Swiss Cheese

The macroelement content of the Swiss cheeses from unit A was significantly different ($p < 0.05$) between the winter and summer periods (Table 2). If in the case of Na, Mg and Ca, in the summer periods the quantities were significantly lower ($p < 0.05$), as for K, it was found in larger quantities in the summer products compared to the winter ones. The Swiss cheese produced by unit B showed higher amounts of Na and Ca in the winter periods, while Mg and K were found in higher proportions in the summer samples compared to the winter ones. The differences between seasons for unit A in terms of Mn and Se content were not significant ($p > 0.05$), while the amounts of Zn and Fe recorded higher values in the winter periods compared to the summer ones. A higher content of microelements in the winter samples, except Zn, was also observed in the samples from unit B, the differences being significant ($p < 0.05$). The most significant change was observed regarding the Fe content which was much higher (up to 8 times higher) in the winter samples compared to the summer samples from both producers. Król et al. [12]

reported higher values for Ca and Mg in the curd obtained in the winter period compared to the summer season, which is consistent with the results of the present study. Minerals are usually present in the aqueous phase of milk or in an insoluble state, bound to casein micelles, and a higher concentration of macroelements in cheese could be due to the dry matter content of milk and/or reduced losses during processing [12].

Table 2. Minerals content (expressed as mg/kg d.b.) Swiss cheese in different seasons

	Unit A				Unit B			
	ITC1	**ITC2**	**VTC1**	**VTC2**	**ICA1**	**ICA2**	**VCA1**	**VCA2**
Macroelements								
Na	2181.40± 30.50^{cB}	4359.10± 61.00^{aE}	2172.10± 25.60^{cH}	2941.60± 30.40^{bM}	9095.10± 63.70^{xA}	7055.2± 35.50^{yD}	5786.00± 77.90^{zG}	3410.10± 44.60^{wL}
Mg	361.70± 14.50^{bA}	413.80± 34.30^{aD}	339.60± 5.10^{cH}	358.40± 5.60^{bL}	378.90± 24.20^{xA}	288.00± 6.30^{yE}	405.10± 5.80^{xG}	281.40± 5.00^{yM}
K	933.80± 14.00^{cB}	1379.30± 26.20^{aD}	815.60± 9.50^{dH}	12690± 20.10^{bL}	1311.20± 15.70^{yA}	1049.60± 4.20^{zE}	1693.30± 17.90^{xG}	1029.00± 15.40^{zM}
Ca	41047.20± 738.80^{bB}	58352.00± 700.20^{aD}	18157.50± 177.40^{dG}	22125.50± 200.10^{cL}	51948.90 ±987.00^{xA}	22908.30± 778.90^{yE}	18519.50 ±197.30^{zG}	15865.00± 227.80^{wM}
Microelements								
Mn	0.76± 0.01^{bA}	1.63± 0.02^{aD}	0.78± 0.03^{bG}	0.67± 0.02^{cL}	0.64± 0.01^{xB}	0.64± 0.01^{xE}	0.40± 0.01^{yH}	0.32± 0.01^{zM}
Zn	29.89± 0.51^{cB}	43.83± 0.61^{aD}	30.30± 1.03^{cH}	32.64± 1.11^{bL}	33.14± 0.36^{yA}	26.33± 0.37^{wE}	36.47± 1.24^{xG}	29.52± 1.00^{zM}
Se	0.02± 0.00^{aA}	0.02± 0.00^{aD}	0.01± 0.00^{aG}	0.002± 0.00^{aL}	0.04± 0.00^{xA}	0.004± 0.00^{yE}	0.02± 0.00^{xyG}	0.02± 0.00^{xyL}
Cu	19.54± 0.27^{aA}	10.80± 0.15^{bD}	19.81± 1.46^{aG}	12.50± 0.92^{bL}	0.67± 0.01^{yB}	1.69± 0.03^{xE}	0.57± 0.04^{zH}	0.50± 0.04^{zM}
Fe	12.50± 0.14^{bA}	52.59± 0.58^{aD}	12.67± 0.55^{bG}	10.24± 0.44^{aL}	20.89± 0.50^{yB}	44.87± 0.01^{xE}	4.70± 0.20^{wH}	5.75± 0.25^{zM}

ITC1 - Swiss cheese sample from unit A from winter period I, ITC2 – Swiss cheese sample from unit A from winter period II, VTC1 – Swiss cheese sample from unit A from summer period I, VTC2 - Swiss sample from unit A from the summer period II, ICA1 – Swiss cheese sample from unit B from the winter period I, ICA2 – Swiss cheese sample from unit B from the winter period II, VCA1 - Swiss cheese sample from unit B from the summer period I, VCA2 - Swiss cheese sample from unit B from the summer period II; a-d (for unit A) and x-w (for unit B) mean values followed by distinct lowercase letters in the same row indicate significant differences ($p < 0.05$) between seasons, A-B (for the winter period I) / D-E (for the winter period II) / G-H (for the summer period I) and L-M (for the summer period II) mean values followed by distinct capital letters in the same row indicate significant differences ($p < 0.05$) between the processing units in the same season.

The results presented by Kirdar et al. [4] for Çanak cheese (a type of Turkish semi-hard cheese) showed a decrease in the content of Ca, Mg, K and Zn in the summer season compared to the winter season, while for Cu,

Fe and Mn the trend was opposite. These differences could be due to variations in the chemical composition of raw milk due to different metabolic rates and feed characteristics offered in the two seasons [4]. This finding can be confirmed in the present study since in summer the cows were grazed, while in winter they were feed with hay. On the one hand, Cu and Fe have an essential role in the nutritional and biological value of cheeses. On the other hand, they can create problems due to their catalytic effect on the oxidation processes of lipoproteins and proteins supporting the membrane of fat globules that generate unpleasant odor [4].

Regarding the comparison between the two producers, Swiss cheese from unit A presented a lower Na content in all the studied periods, compared to the samples from unit B. The amounts of Mg, Ca and K in Swiss cheese were significantly different between the two producers, the Ca content being higher in the samples from unit B due to the exogenous addition of calcium chloride. The Swiss cheese from unit A showed a higher content of Mn and Fe, significant variations ($p < 0.05$) being also observed in the case of Zn. There was no large variation in Se content between samples, while Cu was observed in up to 35 times higher amounts (Table 2) in the products from unit A due to the manufacturing technology involving the use of the copper boiler. The results obtained for Mg and Zn are comparable to those reported by Manuelian et al. [17] for Emmentaler type cheese, while the amounts of Ca, K, Na, Fe and Cu were higher compared to the mentioned work. Ca represents an important macroelement present in hard cheeses and indispensable in human nutrition. Walther et al. [18] state that this macroelement can be found in amounts of 6 to 11 g/kg in semi-hard and hard cheeses, a 50g portion of cheese providing a daily intake of about 1200 mg of calcium in the human nutrition. The results of the present study show a much higher Ca content of the Swiss cheeses which can ensure the necessary Ca by consuming a smaller portion. In general, the amount of Ca in cheeses is much higher compared to milk and it is found in the form of precipitates of calcium phosphate, calcium lactate and calcium carbonate [1]. It has been shown that phosphopeptides and free fatty acids in hard cheeses can form phosphopeptide-Ca or soap complexes [1]. The Na content correlates with brining and salting of the wheels in the ripening technology, which may explain its presence in Swiss cheese [19]. Mn content together with other rare elements has been shown to be an important predictor for traditional cheeses, and Mn itself can represent a geographic marker [20], a correlation that we can consider a geographic footprint considering that most of the Ţara Dornelor area is located on a rock rich in Mn associated with other elements. Another study showed that elements such as Cu, Mg, Mn, Ca, K and Na can be used as markers for authenticating the origin area of Emmental and Edam cheeses [21]. The

transfer of mineral elements from the soil to the plants used as animal feed occurs only if they are found in inorganic form. If the minerals are found in organic form, the respective compounds must go through biochemical processes generated by the soil microflora that transform them into inorganic compounds to be absorbed by plants, especially through the roots [22].

Relationships between variables

The analysis of the relationships between the variables considered in the winter period (Table 3) highlighted significant direct correlations ($p < 0.05$) of the Na content with the content of Ca, Zn, Mg and Fe ($0.61 < r < 0.70$). Mg content was directly correlated with Ca, Zn, Mn, Cu and Fe ($0.57 < r < 0.98$, $p < 0.05$), while Ca content was directly correlated with Mn, Zn, Se, Cu and Fe ($0.51 < r < 0.96$, $p < 0.05$). Significant correlations ($p < 0.05$) were observed between some of the microelements studied, as follows: Mn directly correlated with Zn, Cu and Fe ($0.56 < r < 0.92$) and Zn directly correlated with Cu and Fe ($0.53 < r < 0.79$). Kirdar et al. [4] also reported significant correlations between Zn and Mn, Mg and Zn, Ca and Zn, Mn and Mg, Mn and Ca, Mg and Ca, Fe and Mn in the winter season.

Table 3. Pearson correlations coefficients for the winter season

Variable	Na	Mg	K	Ca	Mn	Zn	Se	Cu	Fe
Na	1.00								
Mg	0.70**	1.00							
K	0.16	0.17	1.00						
Ca	0.65**	0.96***	0.18	1.00					
Mn	0.42	0.85***	0.12	0.87***	1.00				
Zn	0.68**	0.98***	0.11	0.96***	0.92***	1.00			
Se	0.37	0.37	-0.06	0.51*	0.16	0.33	1.00		
Cu	-0.14	0.57*	-0.09	0.53*	0.56*	0.53*	0.03*	1.00	
Fe	0.61**	0.69**	0.10	0.63**	0.84***	0.79***	-0.12***	0.18	1.00

* significant at $p < 0.05$, ** * significant at $p < 0.01$, *** * significant at $p < 0.001$.

The Principal Components Analysis (Figure 1) for the winter period showed that the first component (PC1) explains 58.51% of the data variation, while PC2 explains 14.80% of it. Thus, K, Se and Cu variables and the ITC1 sample were associated with PC2, while Mn, Fe, Zn, Mg, and Ca and the rest of the analyzed samples were associated with PC1. A grouping of the milk

samples is observed in the left quadrants, while the Swiss cheese samples are grouped in the right side, depending on the manufacturer (those from unit A in the upper quadrant, and those from unit B in the lower quadrant).

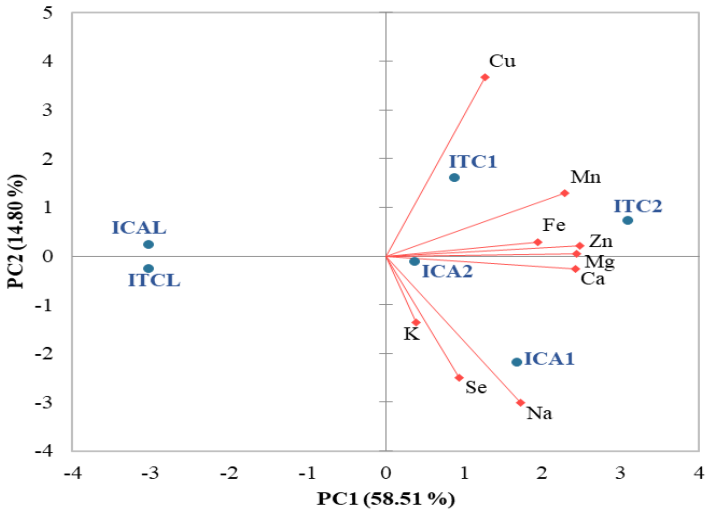

Figure 1. Principal Component Analysis bi-plot for the winter season

For the summer period, significant direct correlations ($p < 0.05$) were observed between the content of Na and Mg, Ca, and Zn ($0.77 < r < 0.87$), as shown in Table 4. The Mg content correlates directly with Ca, Mn, Zn, Cu ($0.75 < r < 0.99$, $p < 0.05$) and indirectly with K ($r = -0.58$, $p < 0.05$). Significant inverse correlations ($p < 0.05$) were also obtained for the content of K with Ca, Mn, Zn, Cu and Fe ($-0.83 < r < -0.62$).

Ca was directly correlated with Mn, Zn, Cu and Fe ($0.57 < r < 0.97$, $p < 0.05$), while Mn was directly correlated with Zn, Cu and Fe ($0.80 < r < 0.99$, $p < 0.05$) . Fe was significantly correlated with Cu, respectively Zn ($r = 0.92$, respectively $r = 0.74$, $p < 0.05$). Similar to our results, significant correlations were reported between Fe and Mn, Mg, Zn, respectively K, between Zn and Mn, Mg, Ca and K, between Mn and Mg, Ca, respectively K, between Mg and K, respectively K, as well as between Ca and K by Kirdar et al. [4] for cheese in the summer season.

The relationships between the studied variables during the summer period were highlighted through the Principal Components Analysis (Figure 2). The first component (PC1) explains 69.05% of the data variance, and the second one explains 22.13%. The PC1 component is associated with Fe, Mn, Ca, Mg, Zn and K content, while the PC2 component is associated with Na, Se and Cu. Regarding the analyzed samples, the milk samples (VTCL

and VCAL), and the Swiss cheese samples VTC1 and VTC2 are associated with PC1, while the VCA1 and VCA2 samples are associated with PC2. A grouping of milk samples is observed in the left half of the graph, and the Swiss cheese samples from unit A are positioned in the negative right quadrant, while the cheese samples from unit B are located in the positive right quadrant. The content of K is placed in opposition to the content of Cu, Fe and Mn, according to the graph presented in Figure 2.

Table 4. Pearson correlations coefficients for the summer season

Variable	Na	Mg	K	Ca	Mn	Zn	Se	Cu	Fe
Na	1								
Mg	0.87***	1.00							
K	-0.25	-0.58*	1.00						
Ca	0.77****	0.97***	-0.67**	1.00					
Mn	0.44	0.82***	-0.78***	0.88***	1.00				
Zn	0.87***	0.99***	-0.62**	0.97***	0.80***	1.00			
Se	0.24	-0.05	0.22	-0.16	-0.33	0.02	1.00		
Cu	0.01	0.48*	-0.69**	0.57*	0.89***	0.44	-0.44	1.00	
Fe	0.34	0.75***	-0.83***	0.83***	0.99***	0.74***	-0.32	0.92***	1.00

* significant at p < 0.05, ** * significant at p < 0.01, *** * significant at p < 0.001.

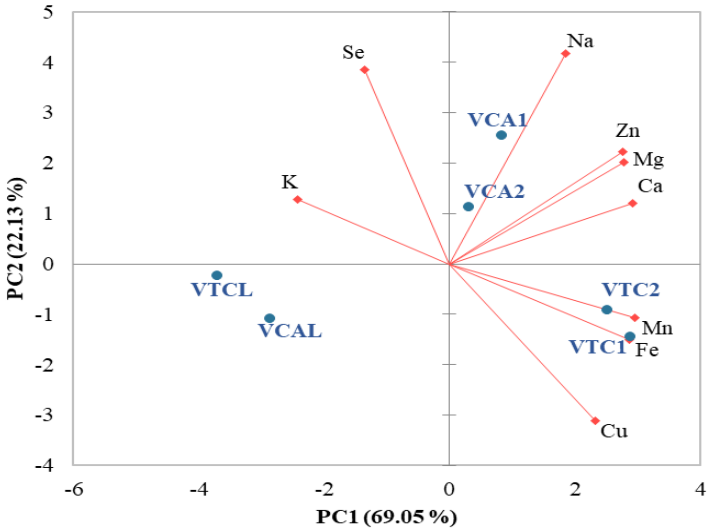

Figure 2. Principal Component Analysis bi-plot for the summer season

CONCLUSIONS

As the season and the milk processing technology to obtain Swiss cheese exhibited significant influences on the mineral profile of milk and Swiss cheese. The content of K and Ca in raw milk was higher in the summer period compared to the winter season in the case of both producers and with regard to the content of microelements, significant variations being observed for Zn and Fe. The season had a significant effect on the amounts of Na, Ca and Mg in Swiss cheese, which recorded lower values in summer compared to winter, with the content of Mn and Fe being also lower in the Swiss cheese samples from the summer season compared to the winter one. The influence of the processing technology was observed especially for the samples obtained in a copper boiler which presented more than 6 times higher content of Cu compared to the sample manufactured in a stainless-steel boiler. The obtained results highlight the rich nutritional value of the analyzed products and can be useful both to consumers for information and to producers to control the quality of the final product. As expected, our study presents some limitations regarding the variations regarding the quality of Swiss cheese samples due to the long ripening time and the spontaneous microflora that may not be constant, as well as to the limited study area since the Ţara Dornelor is the only area where Dorna Swiss cheese is produced. The results of our study are able to encourage the development of new research on the influence of season on the spontaneous microflora that outline the sensory and physico-chemical characteristics of Dorna dairy products.

EXPERIMENTAL SECTION

Sample collection and unit characteristics

To determine the mineral content of raw milk, samples were collected from two producers (UnitUnit A and UnitUnit B characterized in Table 5), in different seasons, winter and summer respectively (n=4). To determine the mineral content of Swiss cheese, the samples were collected from the same producers, in different seasons, namely two periods of winter 2022 and two periods of summer 2022 (n=8). The samples were investigated at a laboratory within the INCDTIM (National Research and Development Institute for Isotopic and Molecular Technologies) in Cluj-Napoca.

Table 5. Characteristics of the processing units

Characteristic	Unit A	Unit B
Production capacity	600 – 1000 L of which 420-840 L for Swiss cheese	2000 – 2400 L of which 500 L for Swiss cheese
Milk origin	The cooperative "Caşcaşaru Dornei"	Own farm, 40 micro farms and 4 commercial farms
Feeding type	Hay in winter and fresh grass in summer	Hay in winter and fresh grass in summer
Swiss cheese processing technology	Copper boiler and wood heating are used, lactic cultures are added	Double-walled stainless-steel boiler with water is used, no lactic cultures are used, calcium chloride is added

The stages of Swiss cheese production include: slow pasteurization of milk, addition of raw milk and homogenization, normalization, addition of lactic cultures (only in the case of unit A), coagulation, processing of the curd, scalding of the curd and draining of the whey, forming of the Swiss cheese wheel, pressing, brining, drying, maturation for 70-90 days and storage. Since the manufacturing period of the Swiss cheese exceeds 90 days, the data related to the atmospheric conditions were selected from the period prior to the processing of the analyzed milk (Table 6).

Table 6. Atmospheric conditions in 2022 (mean values) [23]

Period	Temperature* (°C)	Humidity* (%)	Rain* (L/m^2)	Air pressure* (mb)
Winter I	1.50	89.00	74.45	850.60
Winter II	-2.15	87.50	60.10	857.45
Summer I	12.55	86.00	61.15	850.35
Summer II	14.50	82.00	127.85	855.60

* mean value between the data reported at the Călimani meteorological station an those reported at the Poiana Stampei station.

Samples preparation

To determine the concentration of Na, Mg, K, Ca, Mn, Zn, Se, Cu and Fe, a closed microwave digestion unit (Speed ENTRY by Berghof) equipped with 10 Teflon containers was used to mineralize 0.1 g dry sample. Each sample was accurately weighed into a PTFE digestion vessel and 6 mL of

HNO_3 (60% v/v) and 2 mL of H_2O_2 (30% v/v) were added for sample digestion, according to the method of Lee et al. [24]. The microwave system was set as follows: step 1 (a ramp time of 3 min to reach a temperature of 145 °C and a hold time of 5 min), step 2 (a ramp time of 5 min to reach a temperature of 170 °C and a hold time of 10 min), step 3 (a ramp time of 2 min to reach a temperature of 190 °C and a hold time of 15 min) and step 4 (a ramp time of 1 min to reach a temperature of 75 °C and a hold time of 10 min). The obtained solution was allowed to cool to room temperature and was then diluted with ultrapure water to a final volume of 50 mL. Digestion of blank (6 mL of HNO_3 and 2 mL of H_2O_2) was done using the same preparation steps.

Determination of the concentration of macroelements by atomic absorption spectrometry (AAS)

The concentration of macroelements (Na, Mg, K and Ca) in milk and cheese samples was determined by atomic absorption spectrometry (AAS) with a Contra AA 800D spectrometer (Analytic Jena, Germany) equipped with a xenon lamp as a lamp with continuous supply for all elements. Mg, Na and K concentrations were measured by air-acetylene flame, while Ca was determined by nitrous oxide-acetylene flame. The samples were further properly diluted to analyze in the range of 0.1-0.5 mg/L for AAS analysis. The results were expressed in mg/kg of product on a dry basis.

Determination of trace elements concentration by inductively coupled plasma mass spectrometry (ICP-MS)

The concentrations of Mn, Zn, Se, Cu and Fe in cheese and milk samples were analyzed by inductively coupled plasma mass spectrometry (ICP-MS) using an ELAN DRC mass spectrometer (PerkinElmer SCIEX, Billerica, MA, USA) equipped with a Meinhart nebulizer. Operating conditions for ICP-MS were optimized daily using a 10µg/L solution of Ba, Cd, Ce, Cu, In, Mg, Pb, Rh and U. A certified multi-element standard solution composed of Ag, Al, As, Ba, Fi, Bi, Ca, Cd, Co, Cr, Cs, Cu, Fe, Ga, In, K, Li, Mg, Mn, Na, Ni, Pb, Rb, Se, Sr, Tl, U, V and Zn (10 µg/mL, PerkinElmer Pure Plus, Billerica, MA, USA) was used for the preparation of calibration solutions. The standard calibration solutions were prepared in the range of 0.1-100 µg/L (Zn, Fe and Cu) and 0.1-25 µg/L (Mn and Se), respectively. The results were expressed in mg/kg of product on dry basis.

Statistical analysis of the experimental data

Determinations were performed in triplicate for each sample. The evaluation of the differences between the mean values was carried out by applying the Fisher test and the t-test, the Analysis of Variance (ANOVA) with Tukey test, at a significance level of 95%. The relationships between the studied variables were evaluated by Principal Component Analysis (PCA). The statistical processing of the experimental data was performed using the XL STAT program, version 2022.

REFERENCES

1. F. Gaucheron; *J. Am. Coll. Nutr.*, **2011**, *30*, 400S-409S. https://doi.org/10.1080/07315724.2011.10719983.
2. L. Mato Rodriguez; T. Ritvanen; V. Joutsjoki; J. Rekonen; T. Alatossava; *J. Dairy Sci.,* **2011**, *94*, 4831–4842. https://doi.org/10.3168/jds.2011-4536.
3. L. Mato Rodriguez; T. Alatossava; *Food Microbiol.*, **2010**, *27*, 434–437. https://doi.org/10.1016/j.fm.2010.01.003.
4. S.S. Kirdar; E. Ocak; S. Köse; E. Özer; *Asian J. Chem.*, **2013**, *25*, 6177–6180. https://doi.org/10.14233/ajchem.2013.14304.
5. K.O. Soetan; C.O. Olaiya; O.E. Oyewole; *African J. Food Sci.*, **2010**, *4*, 200–222.
6. D. Miller; Amino Acids, Peptides, and Proteins. In: *Food Chemistry*, 4th ed.; S. Damodaran, K.L. Parkin, O. Fennema Eds.; , CRC Press: Boca Raton, USA, **2008**: Chapter 8, pp. 523–570. https://doi.org/10.1515/9783110793765-002.
7. A.M. Al Alawi; S.W. Majoni; H. Falhammar; *Int. J. Endocrinol.,* **2018**, *2018*, 1-17. https://doi.org/10.1155/2018/9041694.
8. H. Langauer-Lewowicka; K. Pawlas; *Environ. Med.,* **2016**, *19*, 9–16.
9. K. Konikowska; A. Mandecka; Trace elements in human nutrition. In *Recent Advances in Trace Elements*, first ed.; K. Chojnacka, A. Saeid Eds.; John Wiley & Sons Ltd: New Jersey, USA, **2018**, Chapter 17, pp. 663–701. https://doi.org/10.1108/eb058670.
10. D.A. Magdas; A. Dehelean; I. Feher; G. Cristea; R. Puscas; S.D. Dan; D.V. Cordea; *Int. Dairy J.*, **2016**, *61*, 135–141. https://doi.org/10.1016/j.idairyj.2016.06.003.
11. C. Sola-Larrañaga; I. Navarro-Blasco; *Food Chem.,* **2009**, *112*, 189–196. https://doi.org/10.1016/j.foodchem.2008.05.062.
12. J. Król; A. Wawryniuk; A. Brodziak; J. Barłowska, B. Kuczy; *Animals*, **2020**, *10*, 1–18. https://doi.org/10.3390/ani10101800.
13. A. Gulati; N. Galvin; E. Lewis; D. Hennessy; M.O. Donovan; J.J. Mcmanus; M.A. Fenelon; T.P. Guinee; *J. Dairy Sci.,* **2018**, *101*, 2710–2723. https://doi.org/10.3168/jds.2017-13338.
14. J. Barlowska; M. Szwajkowska; Z. Litwińczuk; J. Król; *Compr. Rev. Food Sci. Food Saf.,* **2011**, *10*, 291–302. https://doi.org/10.1111/j.1541-4337.2011.00163.x.

15. J. Król; Z. Litwińczuk; A. Brodziak; M. Kedzierska-Matysek; *J. Elem.,* **2012**, *17*, 597–608. https://doi.org/10.5601/jelem.2012.17.4.04.
16. A. Górska; K. Oprządek; *Polish J. Environ. Stud.*, **2006**, *15,* 269–272.
17. C.L. Manuelian; S. Currò; M. Penasa; M. Cassandro; M. De Marchi; *J. Dairy Sci.*, **2017**, *100*, 3384–3395. https://doi.org/10.3168/jds.2016-12059.
18. B. Walther; A. Schmid; R. Sieber; K. Wehrmüller; *Dairy Sci. Technol.,* **2008**, *88*, 389–405. https://doi.org/10.1051/dst:2008012.
19. L. Pillonel; R. Badertscher; P. Froidevaux; G. Haberhauer; S. Hölzl; P. Horn; A. Jakob; E. Pfammatter; U. Piantini; A. Rossmann; R. Tabacchi; J.O. Bosset; *LWT-Food Sci. Technol.*, **2003**, *366*, 15–623. https://doi.org/10.1016/S0023-6438(03)00081-1.
20. D.A. Magdas; I. Feher; G. Cristea; C. Voica; A. Tabaran; M. Mihaiu; D.V. Cordea; V.A. Bâlteanu; S.D. Dan; *Food Chem.*, **2019**, *277*, 307–313. https://doi.org/10.1016/j.foodchem.2018.10.103.
21. M. Suhaj; M. Kore; *Eur. Food Res. Technol.*, **2008**, *227*, 1419–1427. https://doi.org/10.1007/s00217-008-0861-7.
22. T.H. Jukes; *Photosynth. Res.,* **1995**, *46*, 13–15.
23. ANM; *Meteorological parameters*, **2023**. https://www.meteoromania.ro/ (accessed March 24, 2023).
24. J. Lee; Y. S. Park; H. J. Lee; Y. E. Koo; *Food chem.*, **2022**, *373*, 131483. https://doi.org/10.1016/j.foodchem.2021.131483

STUDIA UBB CHEMIA, LXVIII, 3, 2023 (p. 51-70)
(RECOMMENDED CITATION)
DOI:10.24193/subbchem.2023.3.04

COMPARISON OF MEMBRANE-BASED PRE-AND POST-COMBUSTION CO_2 CAPTURE OPTIONS APPLIED IN ENERGY-INTENSIVE INDUSTRIAL APPLICATIONS

Calin-Cristian CORMOS[a,*], Marius SANDRU[b], Cristian DINCA[c], Flavia-Maria ILEA[a], Alexandra DUDU[d], Mihaela Diana LAZAR[e], Nela SLAVU[c], Constantin SAVA[d], Letitia PETRESCU[a], Ana-Maria CORMOS[a], Ionela DUMBRAVA[a]

ABSTRACT. Deployment of decarbonization technologies in energy-intensive industrial applications (e.g., heat and power, metallurgy, cement, chemical sectors etc.) is of great importance for reducing CO_2 emission and achieving global climate neutrality. Membrane CO_2 removal systems gained relevant attention as possible energy and cost-efficient CO_2 capture technology. This paper is evaluating membrane-based pre- and post-combustion CO_2 capture to be applied in various industrial applications with high fossil CO_2 emissions. The evaluation was geared mainly towards quantification of ancillary energy consumptions of membrane systems as well as the specification of captured CO_2 in respect to its potential utilization and storage applications. As the assessment show, the membrane-based systems are promising CO_2 capture technology for both pre- and post-combustion capture configurations.

Keywords: *Energy-intensive industrial applications; Pre- and post-combustion CO_2 capture; Membrane; Ancillary energy consumptions; Technical performance indexes*

[a] *Babes-Bolyai University, Faculty of Chemistry and Chemical Engineering, 11 Arany Janos, RO-400028, Cluj-Napoca, Romania*
[b] *Sintef Industry, Sem Sælands vei 2 A, Trondheim, Norway*
[c] *University Politehnica of Bucharest, Faculty of Power Engineering, 313 Splaiul Independentei, RO-060042, Bucharest, Romania*
[d] *National Institute of Marine Geology and Geoecology - GeoEcoMar, 23-25 Dimitrie Onciul, RO-024053, Bucharest, Romania*
[e] *National Institute for Research and Development of Isotopic and Molecular Technologies – INCDTIM, 67-103 Donat Street, RO-400293, Cluj-Napoca, Romania*
[*] *Corresponding author: calin.cormos@ubbcluj.ro*

INTRODUCTION

Reduction of anthropogenic CO_2 emissions represents a key environmental target to achieve global climate neutrality and developing the future low carbon economy. Decoupling the global energy demand from fossil CO_2 emissions is one of the main elements to be considered [1]. Relevant sectors of our globalized society such as industry, transport, agriculture, residential systems are due to implement efficient decarbonization strategies for both reduction of the CO_2 emissions and fossil energy. Several possible conceptual methods can be applied for this purpose [2] e.g., replacement of fossil energy with renewable energy sources, boosting efficiency for both conversion and utilization stages, deployment of Carbon Capture, Utilization and Storage (CCUS) systems, reduction of overall energy consumption etc. In the last years, significant political, economic, social and technological strategies were developed and planned to be deployed in practice at national and international level. For instance, the European Union (EU) aims to achieve the climate neutrality by 2050 [3].

The CCUS technologies are predicted to play a crucial role in the coming decades to achieve the climate neutrality by facilitating the transition from fossil to renewable energy sources. The CO_2 capture can be done is a variety of options, the most promising systems being pre- and post-combustion capture [4]. In pre-combustion capture, the gaseous fuel (e.g., syngas produced from partial oxidation technologies such as catalytic reforming or gasification) is decarbonized prior to its utilization since, in the post-combustion capture, the CO_2 is removed from the flue gases resulted in total oxidation (burning) processes. In respect to captured CO_2 destinations, it can be either geologically stored in saline aquifers, depleted oil and gas fields, unmined coal beds or used for Enhanced Oil Recovery (EOR) purposes [5]. In addition, the CO_2 utilization technologies by its chemical transformations to various chemicals / energy carriers (e.g., synthetic natural gas, methanol, biofuels etc.) are predicted to use the captured CO_2 as a valuable raw material in respect to the circular economy principles [6].

This paper assessed the membrane technology as CO_2 removal option in both pre- and post-combustion arrangements. As targeted industrial processes, heat and power, iron and steel, cement production plants were evaluated considering their important share in global CO_2 emissions. It worth mention that the non-power energy-intensive industrial processes such as steel and cement production (responsible for more than 12% global CO_2 emissions [7]) are hard to decarbonize due to involvement of carbon-based materials in the production scheme rather than just as fuel. For instance, in

cement production, two thirds of CO_2 emissions are coming from the raw-materials (raw meal) decomposition and only one third from the fuel used for the thermal treatment in clincher production [8]. As targeted capacities, large scale plants were evaluated (e.g., 500-1000 MW net power, 1 Mt/y cement).

Membrane CO_2 capture has important features such as easy scalable technology, not requiring high energy consumptions as the chemical gas-liquid absorption [9]. All these advantages of membrane-based CO_2 removal systems are expected to give better techno-economic and environmental benefits. The evaluated pre- and post-combustion CO_2 capture systems using membrane technology were modeled and simulated using ChemCAD, the overall mass and energy balances being used for assessment of CO_2 capture energy penalty. In addition, the conceptual design of membrane system was chosen to satisfy the required CO_2 quality specification [10].

MATHEMATICAL MODELING OF MEMBRANE CO_2 SEPARATION

Mathematical modeling and simulation of pre- and post-combustion CO_2 capture by membrane systems integrated in energy-intensive industrial processes was done by process flow modeling using ChemCAD [11]. As thermodynamic package, the Soave-Redlich-Kwong (SRK) system was chosen for the membrane CO_2 removal systems based on operational parameters (temperature and pressure) and present chemical species. The captured CO_2 is further dried for moisture removal (using an absorption – desorption cycle with Tri-Ethylene-Glycol - TEG) and compressed to 120 bar for transport to the selected utilization / storage sites.

For the post-combustion CO_2 capture, two distinct energy-intensive industrial cases were evaluated as follow: Case 1 - Coal-based super-critical power plant [12] and Case 2 - Conventional cement plant [13]. Figure 1 presents the conceptual layout of 3-stage membrane unit for post-combustion CO_2 capture to be applied in various applications (e.g., heat and power generation, metallurgy, cement, petro-chemical etc.). The 3-stage configuration was chosen taking into consideration the two combined targeted performance indicators to be simultaneously accomplished by the membrane-based CO_2 removal unit: 90% carbon capture rate and min. 95% (vol.) CO_2 concentration in the captured stream. Since the CO_2 concentration in the flue gases is rather low (about 12 – 15% vol. for coal-based combustion systems), a 3-stage system is required for achieving these two targets [14].

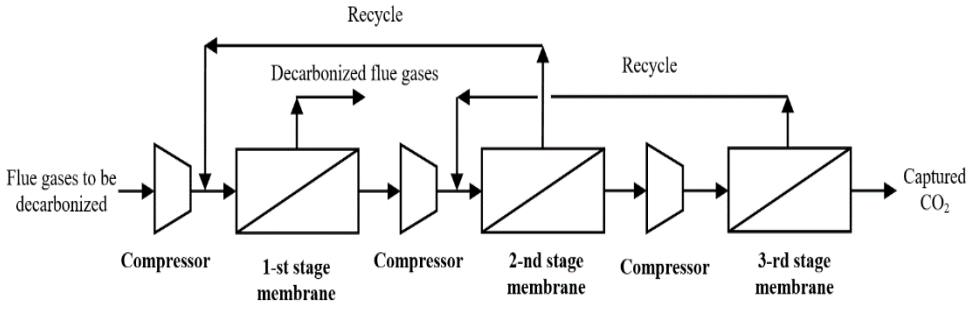

Figure 1. 3-stage membrane-based post-combustion CO_2 capture unit

For the pre-combustion CO_2 capture, one power generation system was evaluated as follow: Case 3 - Coal-based integrated gasification combined cycle (IGCC) power plant [15]. Figure 2 presents the conceptual layout of 2-stage membrane unit for pre-combustion CO_2 capture. In contrast to the post-combustion CO_2 capture unit which requires a 3-stage system, the pre-combustion unit requires only a 2-stage system because the CO_2 concentration in syngas to be decarbonize is significantly higher than for post-combustion systems (about 40% vol. for a coal-based gasification process). In addition, the pre-combustion CO_2 capture system uses a hydrogen selective membrane considering the differences in comparison to the post-combustion capture option [16].

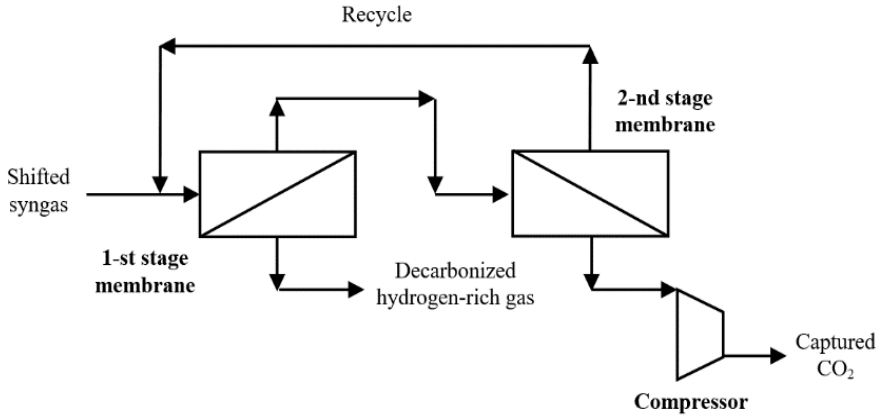

Figure 2. 2-stage membrane-based pre-combustion CO_2 capture unit

Table 1 presents the main design assumption of the investigated pre- and post-combustion CO_2 capture systems using membrane separation technology. In respect for the gas streams to be decarbonized (either by pre-combustion or post-combustion arrangements), the following plant capacities were used in the current analysis: Coal-based super-critical power plant (Case 1) - 1000 MW net power output [12]; Cement production plant (Case 2) - 1 Mt/y cement [17] and Coal-based Integrated Gasification Combined Cycle (IGCC) power plant (Case 3) - 450 MW net power output [18]. The evaluated pre- and post-combustion capture concepts were fully integrated in respect to mass and energy balances to give overall global performance indicators such as ancillary power consumption and cooling duties for the membrane unit and the specific primary energy consumption for CO_2 avoided (SPECCA) defined as follow:

- Ancillary power consumption for membrane unit was calculated as ratio of compressing work needed for flue gases and recycled gaseous streams and the mass flow of captured CO_2:

$$W_{Membrane\ unit} = \frac{W_{Flue\ gas\ \&\ recycle\ compression\ work}}{Captured\ CO_2\ flowrate} \quad (1)$$

- Cooling duty of membrane unit was calculated as ratio of cooling duties of the heat exchangers associated with flue gases and recycled gaseous streams and the mass flow of captured CO_2:

$$Cooling\ duty_{Membrane\ unit} = \frac{Q_{Flue\ gas\ \&\ recycle}}{Captured\ CO_2\ flowrate} \quad (2)$$

- Specific primary energy consumption for CO_2 avoided (SPECCA) was calculated for the whole decarbonized process (power plant or cement plant) as follow [19]:

$$SPECCA = \frac{3600 \cdot \left(\frac{1}{Efficiency_{\ CO2\ capture}} - \frac{1}{Efficiency_{\ No\ capture}}\right)}{CO_2\ emissions_{\ No\ capture} - CO_2\ emissions_{\ CO2\ Capture}} \quad (3)$$

Table 1. Main design assumptions of pre- and post-combustion CO_2 capture units

Plant sub-system	**Design parameter**
Super-critical power plant (Case 1) flue gases	Mass flow: 1650.10 kg/s Composition (vol. %): 77.11% N_2, 12.83% CO_2, 6.03% O_2, 3.11% H_2O, 0.92% Ar Temperature & pressure: 50°C / 1.03 bar
Cement plant (Case 2) flue gases	Mass flow: 81.04 kg/s Composition (vol. %): 64.80% N_2, 23.61% CO_2, 7.74% O_2, 3.08% H_2O, 0.76% Ar Temperature & pressure: 40°C / 1.03 bar
Gasification power plant (Case 3) syngas	Mass flow: 126.28 kg/s Composition (vol. %): 54.25% H_2, 39.84% CO_2, 3.25% N_2, 1.90% CO, 0.61% Ar, 0.15% other gases Temperature & pressure: 50°C / 31 bar
Membrane unit - Post-combustion CO_2 capture (Case 1: Super-critical power plant)	CO_2 selective membrane CO_2 capture rate: 90% Permeance data: CO_2 - 370, O_2 - 7.41, N_2 - 1.85 Operating temperature: 50°C Pressure ratio: 10 Compressor efficiency: 85%
Membrane unit - Post-combustion CO_2 capture (Case 2: Cement plant)	CO_2 selective membrane CO_2 capture rate: 90% Permeance data: CO_2 - 370, O_2 - 7.41, N_2 - 1.85 Operating temperature: 50°C Pressure ratio: 10 Compressor efficiency: 85%
Membrane unit - Pre-combustion CO_2 capture (Case 3: Gasification plant)	H_2 selective membrane CO_2 capture rate: 90% Permeance data: H_2 - 300, CO_2 - 10, CO - 4, N_2 - 2, Ar - 2, CH_4 - 2, H_2O - 10000 Pressure ratio: 5 – 10 Compressor efficiency: 85%
CO_2 conditioning unit (drying and compression)	Gas-liquid absorption - desorption cycle Drying solvent: Tri-Ethylene-Glycol (TEG) Absorber column: 4 stages Desorber column: 6 stages 4 stages with inter-cooling compressor Compressor efficiency: 85% Delivery pressure: 120 bar CO_2 composition (vol. %) [10]: >95% CO_2, <2000 ppm CO, <250 ppm H_2O, <100 ppm H_2S, <4% other gases (N_2, Ar, H_2)
Thermodynamic package	Membrane unit: Soave-Redlich-Kwong (SRK) CO_2 drying unit: TEG Dehydration
Heat exchanger network	Min. temperature difference $\Delta T_{min.}$ = 10°C Pressure drops: 2 – 3% from inlet pressure

ILLUSTRATIVE PRE- AND POST-COMBUSTION CO_2 CAPTURE CASES

1. Post-combustion decarbonization of fossil-based power plants

The investigated coal-based super-critical power plant is generating 1000 MW net power with 90% carbon capture rate. These key design assumptions were chosen to be in line with ongoing CO_2 capture projects in power generation sector. As main steam cycle parameters, the following design assumptions are used: 290 bar and 582°C for the live steam with two MP steam reheats at 75 and 20 bar [20]. The conceptual design of decarbonized coal-based super-critical power plant is presented in Figure 3 and the overall key performance indicators are presented in Table 2.

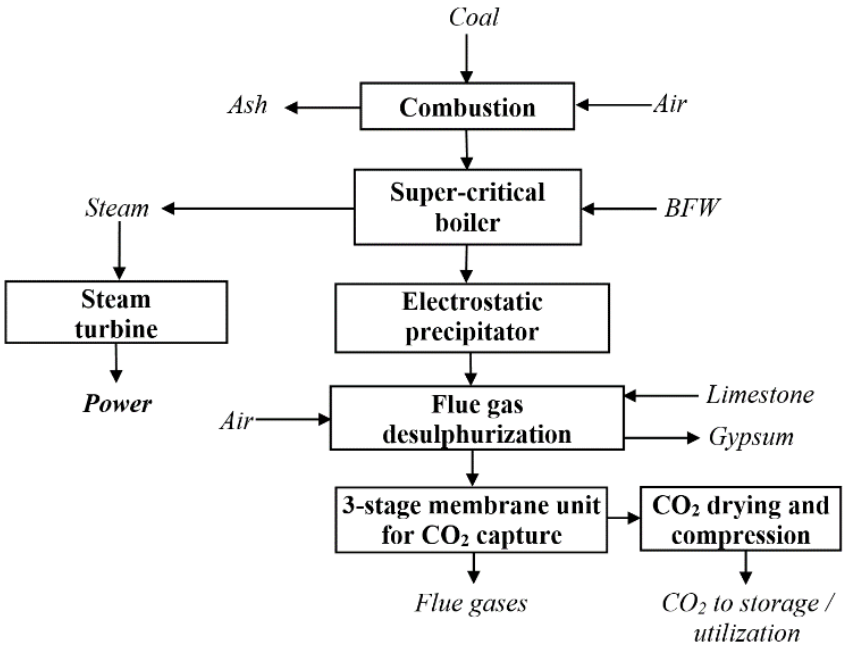

Figure 3. Super-critical plant with post-combustion membrane-based CO_2 capture

As benchmark super-critical power plant without CO_2 capture, a concept reported in [12] was used. One can be observed that the membrane-based CO_2 removal technology implies an important energy penalty for the capture (about 12 percentage points) due to the compressing large flow of flue gases. Also, the specific power consumption and cooling duty of the membrane unit are rather high as well as SPECCA indicator in comparison to the chemical scrubbing technology (3.25 vs. 2.43 GJ/t as SPECCA).

Table 2. Key performance indicators of decarbonized super-critical power plant

Main performance indicator	UM	Value
Coal flowrate (as received basis)	t/h	458.00
Coal LHV (as received basis)	MJ/kg	25.17
Coal thermal energy – LHV (A)	MW_{th}	3202.18
Steam turbine output	MW_e	1472.75
Gross power output (B)	MW_e	1472.75
Coal processing (0.5 % feedstock energy)	MW_e	16.00
CO_2 capture & compression (membrane)	MW_e	392.35
Power island consumption	MW_e	64.40
Ancillary power consumption (C)	MW_e	472.75
Net power output (D = B - C)	MW_e	1000.00
Gross power efficiency (B/A * 100)	%	46.00
Net power efficiency (D/A * 100)	%	31.22
Carbon capture rate	%	90.00
Specific CO_2 emissions	kg/MWh	110.80
SPECCA	GJ/t	3.25
Specific power consumption membrane unit	kWh/t	273.59
Cooling duty membrane unit	GJ/t	1.07

2. Post-combustion decarbonization of cement plants

The conceptual design of a decarbonized cement plant with membrane-based technology is presented in Figure 4. The overall performance indicators of the conventional cement production line as benchmark case (1 Mt/y production capacity without carbon capture) were taken from IEAGHG reports [13,21]. The additional flue gas desulphurization, membrane-based CO_2 capture unit and captured CO_2 conditioning units were simulated using ChemCAD software. The overall performance indicators of decarbonized cement plant are presented in Table 3 (the specific energy consumptions are reported on captured CO_2 flow while the specific CO_2 emission is reported on cement output).

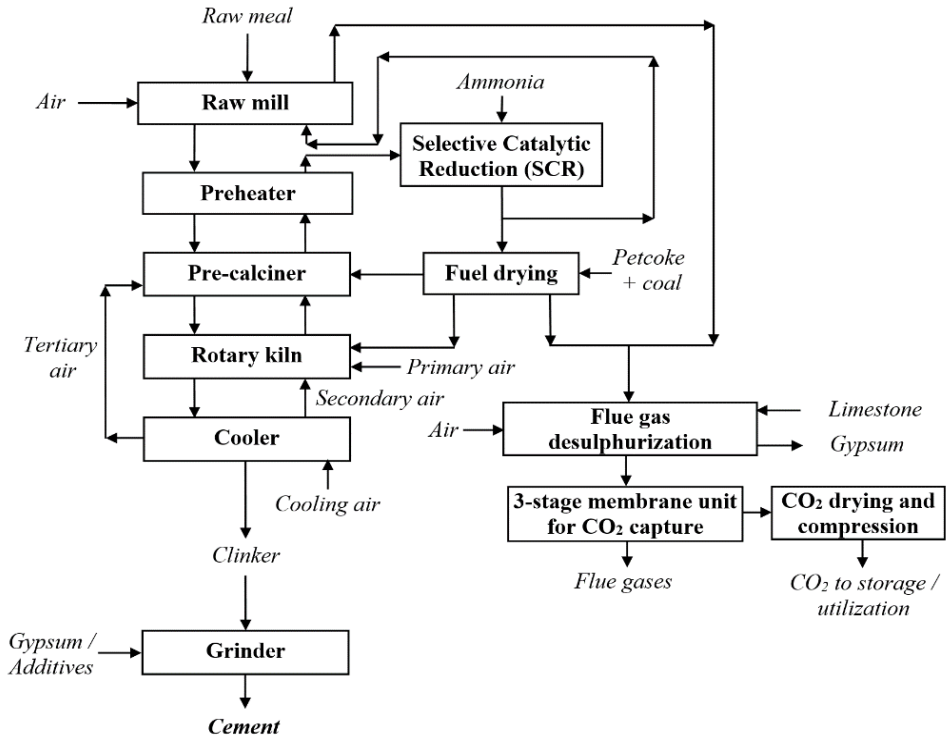

Figure 4. Cement plant with post-combustion membrane-based CO_2 capture

Table 3. Key performance indicators of decarbonized cement plant

Main performance indicator	UM	Value
Cement plant capacity	kt/y	1000
Coal and petcoke flowrate (cement line)	t/h	12.20
CO_2 capture & compression (membrane unit)	MW_e	31.20
Power consumption (cement line)	MW_e	10.20
Ancillary power consumption (whole plant)	MW_e	41.40
Carbon capture rate	%	90.00
Specific CO_2 emissions (incl. power import)	kg/t	233.60
SPECCA	GJ/t	2.65
Specific power consumption membrane unit	kWh/t	206.82
Cooling duty membrane unit	GJ/t	0.64

It can be observed that in comparison to super-critical power plant, the ancillary energy consumptions (both power and cooling duties) of the membrane unit is lowered for the cement plant. This can be explained by the fact that a lower flow of more CO_2 concentrated flue gases is to be treated for decarbonisation. Also, the SPECCA indicator is significantly reduced in comparison to chemical gas-liquid absorption (2.65 vs. 5.4 GJ/t).

3. Pre-combustion decarbonization of partial oxidation plants

The conceptual design of a decarbonized coal-based IGCC power plant with membrane-based technology is presented in Figure 5 [22].

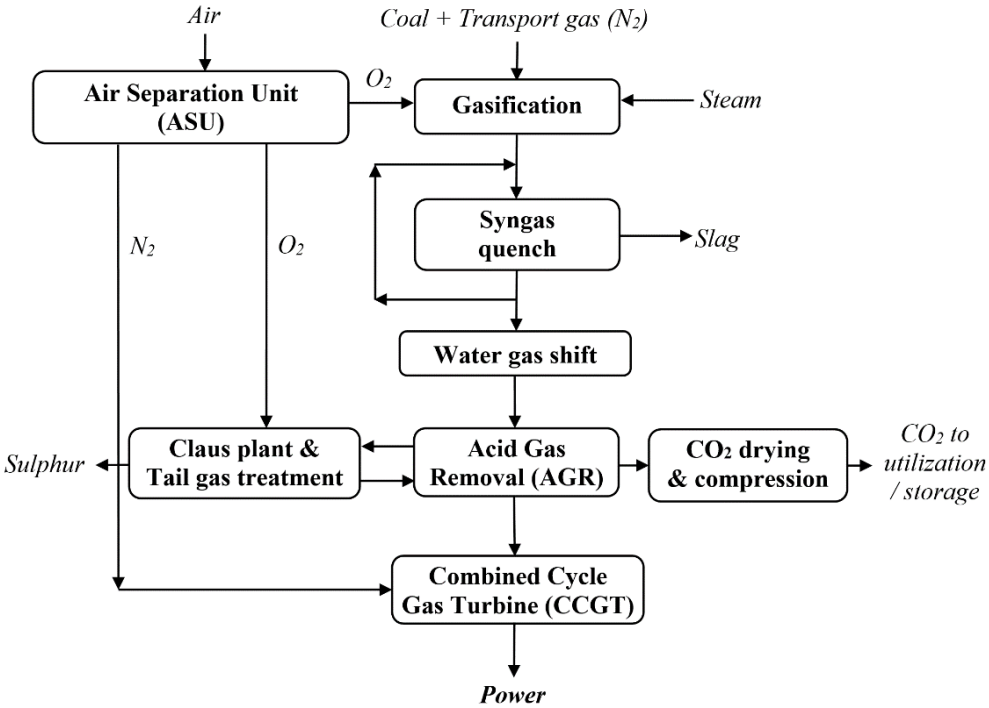

Figure 5. IGCC power plant with pre-combustion membrane-based CO_2 capture

The evaluated IGCC power plant was based on Shell gasification technology [23] and Mitsubishi gas turbine combine cycle unit [24]. Table 4 presents the overall performance indicators of decarbonized IGCC power plant using pre-combustion membrane-based CO_2 capture.

Table 4. Key performance indicators of decarbonized IGCC power plant

Main performance indicator	UM	Value
Coal flowrate (as received basis)	t/h	168.50
Coal LHV (as received basis)	MJ/kg	25.17
Coal thermal energy – LHV (A)	MW_{th}	1178.09
Gas turbine output	MW_e	334.00
Steam turbine output	MW_e	217.25
Gross power output (B)	MW_e	552.25
Air separation unit consumption	MW_e	43.12
Gasification island consumption	MW_e	10.00
CO_2 capture & compression (membrane)	MW_e	30.75
Power island power consumption	MW_e	19.80
Ancillary power consumption (C)	MW_e	103.67
Net power output (D = B - C)	MW_e	448.58
Gross power efficiency (B/A * 100)	%	46.87
Net power efficiency (D/A * 100)	%	38.07
Carbon capture rate	%	90.00
Specific CO_2 emissions	kg/MWh	91.50
SPECCA	GJ/t	2.46
Specific power consumption membrane unit	kWh/t	51.40
Cooling duty membrane unit	GJ/t	0.11

As can be noticed, the membrane-based pre-combustion CO_2 capture technology has lower ancillary energy consumption than the corresponded post-combustion capture options (due to high CO_2 partial pressure in the gas to be treated for decarbonization). For instance, the specific power consumption and cooling duty for the membrane CO_2 removal unit are significantly reduced by about 75 - 80%, respectively by about 83 - 90%. Also, the SPECCA indicator is lower for gasification-based power plants than for combustion-based power plants (2.46 vs. 3.25 GJ/t). As key conclusion from the evaluation is that the membrane-based decarbonization technology is more suitable for pre-combustion capture (applied in gasification and reforming processes) than for the post-combustion capture.

CAPTURED CO_2 PROPERTIES AND ITS UTILISATION & STORAGE

The quality specifications of the captured CO_2 streams from the three investigated decarbonized plant concepts using membrane-based pre- and post-combustion configurations in respect to the accepted literature specification [10] are presented in Table 5 together with their main characteristics (mass flows, pressure and temperature).

Table 5. Captured CO_2 streams characteristics

Parameter	Literature	Case 1	Case 2	Case 3
Mass flowrate (t/h)	NA	1031.38	83.13	374.38
Pressure (bar)	NA	120	120	120
Temperature (°C)	NA	40	40	40
Composition (vol. %)				
CO_2	Min. 95.00	96.34	97.10	98.02
CO (ppm)	Max. 2000	800	500	600
Water (ppm)	Max. 500	100	150	100
Sulphur species (ppm)	Max. 200	50	50	50
Other non-condensable components (N_2, Ar, H_2)	Max. 4.00	3.56	2.83	1.90

As can be noticed for all investigated cases, the quality specifications of the captured CO_2 are fully in line with literature references. After capture and conditioning, the captured CO_2 can be used for transformation into various chemicals / energy carriers (e.g., synthetic natural gas, methanol, synthetic fuels) or geologically stored (e.g., saline aquifers, depleted hydrocarbon fields or used for Enhanced Oil Recovery - EOR).

For instance, in term of CO_2 utilization possibilities, its transformation in value added products by catalytically hydrogenation is the most promising and straightforward option. In this regard several directions are investigated: (i) syngas production either by reverse water gas shift, by dry reforming or by combined steam and dry reforming; (ii) production of synthetic fuels such as methane, methanol etc. (iii) CO_2 involvement in chemical hydrogen storage cycles as $CO_2 + H_2 \leftrightarrow HCOOH$; (iv) CO_2 transformation in chemicals: ethylene, monomers/polymers, urea, fine chemicals etc.

From all these possibilities, the CO_2 methanation process (Sabatier process, see reaction 4) is the most studied due to its part in the Power-to-methane concepts to enhance renewable power utilization [25].

$$CO_2 + 4H_2 \leftrightarrow CH_4 + 2H_2O \qquad \Delta H = -165 \text{ kJ/mol (298K)} \qquad (4)$$

In this concept, the extra power obtained from renewable sources (e.g., solar and wind applications) at peak generation is chemically stored as synthetic methane, mitigating thus one of the most important problems of renewable power, which is its time unpredictable generation.

Although favorized from thermodynamically point of view, the reaction 4 is kinetically limited, as 8 electrons are needed in the reduction process of carbon dioxide. The main problem is the high stability of the CO_2 molecule making its chemical transformation highly unfavorable. In these conditions, the presence of an active catalyst is mandatory for the process to become energy- and cost-efficient [26]. Also, the selectivity of catalyst for methane formation is of main importance for overall process performance, as many other products can be formed from hydrogen and carbon dioxide.

The composition of captured CO_2, as presented in Table 8, is proper for its direct use in the CO_2 methanation reaction without other modifications. The reaction mixture tested in this work consists in CO_2, H_2 and Ar in molar ratio CO_2 / H_2 / Ar = 1 / 4.5 / 1. In these testing conditions, the sulphur species which can negatively intervene in catalyst activity and stability are in very low concentrations (at the ppm level due to previous cleaning). Water or CO are also in low proportion and the non-condensable gases does not interfere in the catalytic process. Using Ni as active metal and a combination of oxides as support, the CO_2 can be transformed in synthetic methane with good conversion and selectivity in relatively mild conditions. The best results were obtained using Ni(14wt.%)/La_2O_3(10wt.%)-SiO_2 catalyst for which a 72% CO_2 conversion rate and a total methane selectivity were obtained at 350°C, atmospheric pressure and 5500 h^{-1} Gas Hourly Space Velocity (GHSV) as experimental testing conditions.

The Combined Steam and Dry Reforming of Methane (CSDRM) represents the parallel and concomitant reformation reaction of methane with H_2O and CO_2 (see reactions 5 and 6) [27].

$$CH_4 + CO_2 \leftrightarrow 2CO + 2H_2 \qquad (5)$$

$$CH_4 + H_2O \leftrightarrow CO + 3H_2 \qquad (6)$$

As a way for CO_2 valorization, the CSDRM presents a series of advantages compared to both individually, dry reforming (reaction 5) and steam reforming (reaction 6) such as: (i) the composition of synthesis gas can be designed by adjusting the ratio of water in the mixture; it is thus possible to

design the experimental conditions which provide directly syngas with proper composition for the Fischer-Tropsch process for superior hydrocarbon synthesis (H_2 : CO molar ratio of 2 : 1); (ii) the catalysts' stability and lifetime are significantly improved compared to the dry reforming process due to less carbon formation.

Among the best catalysts for this reaction are Ni-based ones. When Ni is supported on alumina doped with basic or reducible oxides very good results are obtained at medium temperatures, as demonstrated by our group previous studies [28-29]. The Ni/La_2O_3-Al_2O_3 catalyst possess a very capacity to disperse and stabilize the Ni nanoparticles on the support, increasing thus significantly both the catalytic activity and catalyst stability against deactivation. Regarding the Ni/CeO_2-Al_2O_3 catalyst, the redox and oxygen storage properties of ceria positively intervene in the reaction mechanism, improving substantially the catalytic performances. In all mentioned cases, the produced synthesis gas is of good quality with H_2 : CO_2 molar ratio of 2.3 - 2.5 is obtained.

Both presented CO_2 utilization routes by catalytic processes, described above (methanation and CSDRM concepts) present real opportunities for up-scaling and large-scale deployment. In this respect, some pilot plants being already in function [25]. By developing new catalysts as those described above, the economic efficiency of the CO_2 hydrogenation processes can be improved, making the CO_2 utilization a viable option and contributing thus to the attractivity of general CCUS technologies.

In respect to the CO_2 transport and storage options, several targeted onshore geological locations within Romania (e.g., Oltenia and Galati regions) were considered within this study. As transport options, road truck / rail tanks and pipeline are the most promising technical options with a distinct advantage for the pipeline transport considering the high volumes of CO_2 to be transported (see Table 5). The CO_2 transportation costs can have a significant impact on the overall economics of a CO_2 storage project [30]. Therefore, it is important to carefully consider the transport parameter when selecting a suitable site for CO_2 storage and / or used for Enhanced Oil Recovery (EOR). This involves analyzing the transport distance between the source of CO_2 (e.g., energy-intensive industrial processes such as power plants, cement and steel mills) and the potential storage sites, as well as the available means of transport and their associated economic costs. By carefully considering these factors, the most cost-effective and feasible transport option for a given CO_2 storage project is chosen. As CO_2 transport costs, most of under-development large-scale CCUS projects consider an average value of 10 €/t [31].

In respect to the CO_2 geological storage, two onshore potential sites were evaluated by project partner GeoEcomar as follow: the Oltenia region is which both saline aquifers and depleted oil and gas reservoirs were identified and characterized in term of storage capacity and the Galati region is which both onshore and offshore storage were identified (using depleted oil and gas

fields as well as EOR). As the CO_2 storage costs, most of under-development large-scale CCUS projects consider an average value of 10-15 €/t [32]. In respect to the CO_2 storage capacities, the Oltenia region has a capacity of about 1.5 million tons per year in onshore deep saline aquifers in a radius of 50 km from the power plant as evaluated in the CCS Getica demo project which evaluated the potential decarbonization of Turceni power plant [33]. It worth also mention that the large-scale deployment of any decarbonization technologies implies a significant increase of power / cement production costs (starting from at least 30 - 50% [17,24,34]).

CONCLUSIONS

This paper presents the main experimental and numerical investigation devoted to the integration of membrane technology as pre- and post-combustion decarbonization option for various energy-intensive industrial applications (e.g., heat and power generation, cement etc.). Also, relevant aspects are evaluated in respect to the captured CO_2 utilization (for catalytic transformation to various energy carriers / chemicals) and geological storage. As key result of the experimental and numerical investigations, one can noticed the promising performances of membrane-based decarbonization technology applied to pre-combustion capture systems in comparison to the post-combustion capture systems e.g.: lower specific power consumption for the membrane unit (52 kWh/t vs. 206 - 274 kWh/t), lower specific primary energy consumption for CO_2 avoided (2.46 GJ/t vs. 3.25 GJ/t), lower cooling duty of the membrane unit (0.1 GJ/t vs. 0.64 - 1.1 GJ/t). The investigated membrane-based decarbonization systems (either pre-combustion or post-combustion cases) delivered the captured CO_2 stream within the quality specification considered for various CO_2 utilization (e.g., methanation process) and storage applications (e.g., saline aquifers or utilization for EOR purposes).

EXPERIMENTAL

Membrane-based CO_2 separation

The experimental analysis consisted of testing the durability of the membranes. The membranes were exposed to flue gases from the lignite combustion of the Circulating Fluidized Bed Combustion (CFBC) pilot plant at the University Politehnica of Bucharest, Power Engineering Faculty. The membranes analyzed were developed and produced by SINTEF, Trondheim, Norway. The following membranes were tested for durability:

Flat sheet membranes:

- Poly-dimethyl-siloxane on poly-acrylonitrile (PDMS/PAN);
- PSF coated with polyacrylamide (PAA/PSF);
- Mixed matrix membrane (RTI);

Hollow fibers membranes:

- Poly-p-phenylene oxide (PPO);
- Poly-sulfone (PSF).

Figure 6 shows the CFBC installation with pilot unit for assessing the durability membrane testing in real plant operating conditions. The evaluated membranes (up to 6 samples in the same time) are positioned on the sampler on the vessel bottom. The flue gases from CFBC unit are extracted with a compressor but because the flue gases temperature is higher than the temperature required by compressor a heat exchanger (air-flue gases) need to reduce the temperature around 80°C.

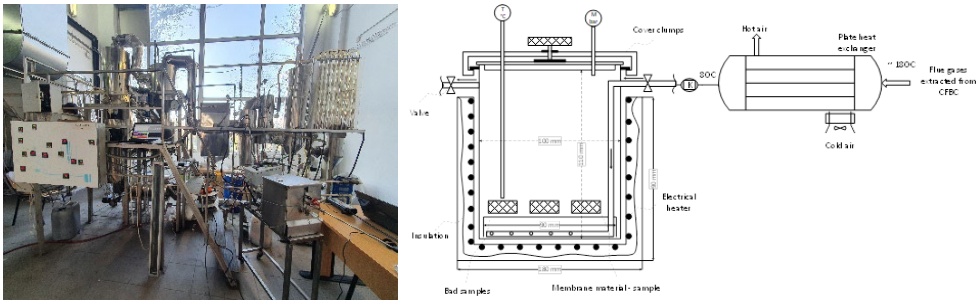

Figure 6. CFBC with pilot membrane testing installation (left).
Schematic diagram of the pilot membrane testing installation (right)

For beginning of membrane unit operation, the inlet and outlet valves are opened, and the flue gases enter the reactor, eliminating the air from the enclosure. This process takes several minutes. Further, the left valve is closed so that the flue gases introduced fill the entire volume of the reactor. The evaluated membranes are put on the bed provided inside the testing enclosure. After this step, the potentiometer of the electrical resistance is set at the desired testing temperature. When the desired pressure has been created, the right valve is closed. The evaluated membranes were exposed to flue gas with the composition shown in Table 6 for about 504 hours at a temperature between 50-60°C and atmospheric pressure. These testing conditions are similar to industrial processes such as CFBC power plants.

Table 6. Flue gas composition used for membrane testing

O_2 %	CO_2 %	NO ppm	NO_x ppm	SO_2 ppm	T_{gas}°C	λ
6.52	12.67	176	185	570	51.50	1.43

The evaluated membranes were characterized using the Fourier-transform infrared spectroscopy (FTIR) spectroscopy, water contact angle, scanning electron image and gas permeation properties before and after flue gas exposure at a specific temperature (similar to real power plant operation). From the appearance of membranes after flue gas exposure, it can be noted a small coloring (yellowish) and as well the presence of dust/carbon particles from flue gas (see Figure 7). No major changes in membrane structure were observed during the testing procedure.

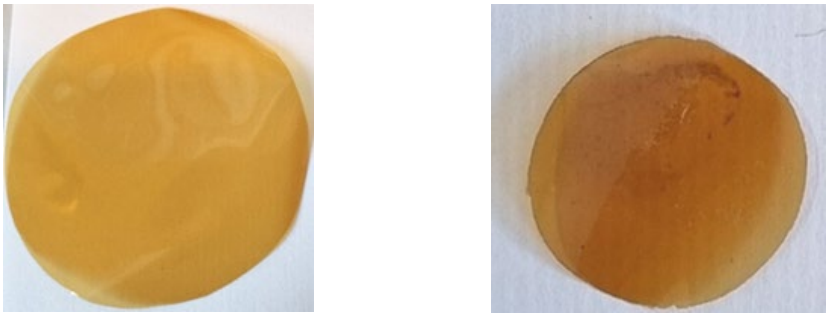

Figure 7. Images of tested membrane before (left) and after (right) the flue gas exposure for RTI case

The contact angle using water was performed in order to assess the deposition of dust / carbon or a change in membrane surface chemistry (e.g. oxidation) during its practical operation in a CO_2 capture process.

Table 7. Contact angle results before and after flue gas exposure

Polymer membrane	Contact angle	
	Before	After
PDMS-PAN	99.00	96.80
Polyacrylamide	70.00	64.00

The contact angle results presented in Table 2 show a small decrease indicating that exposure of membranes to flue gas hydrophilized the surface or some solid material was deposited on the surface. The changes are small and do not indicate a considerable change that needs to be addressed by

membrane optimization. The membranes were tested using a gas mixture of synthetic flue gas 10% CO_2 in N_2 at a pressure of 1.2 bar, at 25ºC and 100% relative humidity. The key results of the membrane gas permeation are presented in Table 8 for some illustrative cases.

Table 8. Summary of gas permeation before and after flue gas exposure

Type of membrane	**CO_2 Permeance [m^3(STP)/(m^2 bar h)]**		**CO_2/N_2 Selectivity**	
	Before	After	Before	After
Flat sheet membranes				
Mixed matrix membrane (RTI)	0.0029	0.0022	48.00	31.00
PDMS/PAN	1.20	0.23	11.00	12.00

After the experimental analysis for their durability, some changes were observed to the tested membranes. If for the RTI membranes, the CO_2 permeance remain practically unchanged before and after flue gas exposure, an about 35% decrease of selectivity was observed. For the PDMS/PAN membrane, the selectivity remained unchanged but the permeance decreased after exposure. For the PDMS/PAN membranes, the gas permeation reduction of the CO_2 permeance, indicated perhaps the deposition of an extra layer- this need to be investigated by FT-IR, EDX, etc.

ACKNOWLEDGMENTS

This work was supported by the NO Grants 2014 - 2021, under project contract no. 13/2020.

REFERENCES

1. Y. Wu; Q. Zhu; B. Zhu; *Energy Policy*, **2018**, *116*, 30-38
2. D. V. Quang; D. Milani; M. Abu Zahra; *Int. J. Greenh. Gas Control*, **2023**, *124*, 103862
3. European Commission, The European Green Deal, COM(2019) 640 final, Brussels, Belgium, **2019**
4. J. A. Garcia; M. Villen-Guzman; J. M. Rodriguez-Maroto; J. M. Paz-Garcia; *J. Environ. Chem. Eng.*, **2022**, *10*, 108470
5. M. Ali; N. K. Jha; N. Pal; A. Keshavarz; H. Hoteit; M. Sarmadivaleh; *Earth-Sci. Rev.*, **2022**, *225*, 103895
6. K. Zhi; Z. Li; B. Wang; J. J. Klemeš; L. Guo; *Process Saf. Environ. Prot.*, **2023**, *172*, 681-699

7. C. da Silveira Cachola; M. Ciotta; A. Azevedo dos Santos; D. Peyerl; *Carbon Capture Sci. Technol.*, **2023**, *7*, 100102
8. E. Benhelal; E. Shamsaei; M. I. Rashid; *J. Environ. Sci.*, **2021**, *104*, 84-101
9. P. Luis; T. van Gerven; B. van der Bruggen; *Prog. Energ. Combust.*, **2021**, *38*, 419-448
10. E. de Visser; C. Hendriks; M. Barrio, M. J. Mølnvik; G. Koeijer; S. Liljemark; Y. L. Gallo; *Int. J. Greenh. Gas Control*, **2008**, *2*, 478-84
11. Chemstations, ChemCAD - Chemical Process Simulation, http://www.chemstations.net/; 2023
12. C. C. Cormos; C. Dinca; *Energy*, **2021**, *220*, 119734
13. International Energy Agency - Greenhouse Gas R&D Programme (IEAGHG), CO_2 capture in the cement industry, Report 2008/3, Cheltenham, UK, 2008
14. H. Wu; Q. Li; M. Sheng; Z. Wang; S. Zhao; J. Wang; S. Mao; D. Wang; B. Guo; N. Ye; G. Kang; M. Li; Y. Cao; *J. Membr. Sci.*, **2021**, *624*, 119137
15. A. M. Cormos; S. Dragan; C. C. Cormos; *Appl. Therm. Eng.*, **2022**, *205*, 118078
16. L. Giordano; J. Gubis; G. Bierman; F. Kapteijn; *J. Membr. Sci.*, **2019**, *575*, 229-541
17. C. C. Cormos; *Fuel*, **2022**, 320, 123907
18. International Energy Agency - Greenhouse Gas R&D Programme (IEAGHG), Potential for improvement in gasification combined cycle power generation with CO_2 capture, Report PH4/19, Cheltenham, UK, 2003
19. G. Manzolini; A. Giuffrida; P. D. Cobden; H. A. J. van Dijk; F. Ruggeri; F. Consonni; Int. J. Greenh. Gas Control, **2020**, *94*, 102935
20. A. M. Cormos; C. C. Cormos; *Appl. Therm. Eng.*, **2017**, *127*, 106-115
21. International Energy Agency - Greenhouse Gas R&D Programme (IEAGHG), Deployment of CCS in the cement industry, Report 2013/19, Cheltenham, UK, 2008
22. U.S. Department of Energy - National Energy Technology Laboratory (NETL), Cost and performance baseline for fossil energy plants. Volume 1a: Bituminous coal (PC) and natural gas to electricity, Report DOE/NETL-2015/1723, USA, 2015
23. C. Higman; M. van der Burgt; *Gasification*, 2nd ed.; Oxford: Elsevier Science, Gulf Professional Publishing, 2008
24. C. C. Cormos; *Energy*, **2012**, *42*, 434-445
25. M. D. Lazar; M. Mihet; M. Dan; Hydrogen to Methane-An Important Step in the Power-to-Gas Concept. In: *Comprehensive Renewable Energy*, M. Letcher Trevor Eds.; 2nd edition, **2022**, vol. 4, pp. 553–565. Oxford: Elsevier. http://dx.doi.org/10.1016/B978-0-12-819727-1.00032-7
26. G. Torres-Sempere; L. Pastor-Perez; J. A. Odriozola; J. Yu; F. J. Duran-Olivencia; L. F. Bobadilla; T. R. Reina, *Curr. Opin. Green Sustain. Chem*. **2022**, *36*, 100647
27. A. S. Farooqi; M. Yusuf; N. A. Mohd Zabidi; R. Saidur; K. Sanaullah; A. S. Farooqi; A. Khan; B. Abdullah, *Int. J. Hydrog. Energy*, **2021**, *46*, 31024-31040
28. M. Dan, M. Mihet, G. Borodi, M. D. Lazar, *Catal. Today*, **2021**, *366*, 87-96
29. M. Dan, M. Mihet, L. Barbu-Tudoran, M. D. Lazar, *Microporous Mesoporous Mater.,* **2022,** *341*, 112082

30. E. Smith; J. Morris; H. Kheshgi; G. Teletzke; H. Herzog; S. Paltsev; *Int. J. Greenh. Gas Control*, **2021**, *109*, 103367
31. S. Roussanaly; G. Bureau-Cauchois; J. Husebye; *Int. J. Greenh. Gas Control*, **2013**, 12, 341-350
32. C. C. Cormos, *Energy*, **2023**, *170,* 126926
33. Global CCS Institute, Getica CCS project, Public report, https://www.globalccsinstitute.com/archive/hub/publications/25516/getica-251111v2.pdf, 2011
34. K. Storrs; I. Lyhne; R. Drustrup; *Int. J. Greenh. Gas Control*, **2023**, *125*, 103878

STUDIA UBB CHEMIA, LXVIII, 3, 2023 (p. 71-98)
(RECOMMENDED CITATION)
DOI:10.24193/subbchem.2023.3.05

HYDROGENOLYSIS OF PALM OIL DERIVED METHYL ESTERS OVER NIOBIUM AND TUNGSTEN BASE CATALYSTS

Mihai MARINESCU[a,*], Dragoș CIUPARU[a], Dorin BOMBOȘ[a], Cristina Maria DUȘESCU-VASILE[a], Roxana Daniela POPOVICI[a], Vasile MATEI[a,*]

ABSTRACT. Vegetable oils are widely available in nature and are one of the most important sustainable feedstocks for biofuel production. W/Pd/γ-Al_2O_3-ZnZSM-5 and Nb/Pd/γ-Al_2O_3-ZnZSM-5 catalysts where prepared, characterized and tested in the hydrogenolysis reaction of palm oil fatty acid esters. The catalysts were characterized by determining the textural characteristics, the thermal stability, and the nature of the acidic sites. The appearance of particle agglomerations was evaluated by scanning electron microscopy (SEM). The resulting reaction products were n-aliphatic hydrocarbons, iso-aliphatic hydrocarbons, cycloaliphatic hydrocarbons, and arenes. No oxygenated organic compounds were identified in the collected liquid phase. At lower pressures, the deoxygenation process occurs to approximately 33% through the hydrogenation of the carboxylic bond and to approximately 67% through decarboxylation/decarbonylation, while at higher pressure than 60 bar the deoxygenation process proceeds preferentially through decarboxylation/ decarbonylation.

Keywords: *fatty acids methyl esters, W/Pd/γ-Al_2O_3-ZnZSM-5, Nb/Pd/γ-Al_2O_3-ZnZSM-5, catalyst, hydrogenolysis*

INTRODUCTION

The world's population is increasing, leading to a higher worldwide energy consumption. One fifth of the total energy consumption is represented by the transportation sector and, the need for fuels will become even larger

[a] *Faculty of Petroleum Refining and Petrochemistry, Petroleum-Gas University of Ploiesti, 39 Bucuresti Blvd., 100680, Ploiesti, Romania*
* *Corresponding authors: mihaimarinescu23@gmail.com, vmatei@upg-ploiesti.ro*

in the future [1]. In this context, an effective and sustainable alternative to conventional fossil fuels are biofuels, obtained by the treatment of biomass. Beyond the obvious advantage of renewability, the development of biofuels from plant biomass can significantly reduce greenhouse gas emissions and can bring enormous benefits from both, economic and environmental point of view [2].

Vegetable oils (triglycerides) are widely available in nature and are one of the most important sustainable feedstocks for biofuel production. The biofuel based on fatty acid methyl esters (FAME), is produced by transesterification of triglycerides with methanol with an annual manufacture of more than 20 million tons [3,4]. However, FAME as a transportation fuel has several drawbacks, such as poor calorific value and high viscosity and oxygen content, which obviously limits its application [5].To overcome these limitations, alternative route such as hydrodeoxygenation (HDO) of bio-based feedstock to produce hydrocarbon fuels with high cetane number, low density and viscosity, and easy-blended with traditional fossil fuels was studied [6,7]. The HDO pathway of FAME consist in the hydrogenation of unsaturated fatty acid chains followed by deoxygenation through hydrodeoxygenation, decarbonylation and decarboxylation reactions into a mixture of paraffinic hydrocarbon with chain lengths between C15 and C18. During the reactions, gaseous by-products such as C1-C4 hydrocarbons and CO, CO_2, H_2O are produced [8].

Traditionally, transition metal sulfides catalysts such as Co-Mo and Ni-Mo on Al_2O_3 are used for the hydrotreating processing of triglycerides and fatty acids. However, using sulfide catalysts may lead to contamination of the final product with sulfur residue [9,10]. Another group of catalysts used for the HDO process are noble metal (non sulfided) catalysts, such as Pd, Pt, Rh and Ru, supported mainly on carbon, as well as on Al_2O_3, ZrO_2, CeO_2, TiO_2 have also exhibited high HDO activities [11]. A.R. Ardiyanti et al., [12], reported that Pt, Pd and Rh supported on ZrO_2, Pd/ZrO_2 catalysts exhibited the highest activity, followed by Rh/ZrO2 which however resulted in a product bio-oil with good properties[13]. Shao et al., [14] investigated the hydrodeoxygenation of fatty acid and triglycerides over Nb_2O_5-modified Pd/SiO_2. The results showed an excellent activity and stability for the hydrodeoxygenation of palmitic acid with almost no decrease in hexadecane yield (94–95 %). On the other hand, for hydrocracking reaction, catalysts such as nickel (Ni), niobium phosphate, zeolite, rhodium, platinum, and palladium were tested. Among them, noble metal catalysts (Pd and Pt) are the most favorable for hydrocracking reaction due to their high hydrogenation ability [15].In our previous work [16] a new bi-functional catalyst CuPd/ZSM-5 was developed and tested in the hydrodeoxygenation and hydrocracking reactions of fatty acid methyl esters.

The catalyst led to 100% FAME conversion into n-alkanes, iso-alkanes, saturated and aromatic cyclic hydrocarbons with 9 to 18 carbon atoms. There in order to continue our previous results, in this study, two new tungsten and niobium-based catalysts were prepared and tested for the HDO of fatty acids methyl esters derived from transesterification of palm oil. For better understanding of the reaction mechanisms, kinetic modelling for HDO of fatty acids methyl esters over the two catalysts was performed.

The novel aspects that this study brings refer to the improvement of the catalytic formula to increase the performance of the hydrogenolysis / isomerization / dehydrocyclization process of palm oil derived methyl esters by using ZnZSM5 zeolite in the presence of Nb or W oxides.

RESULTS AND DISCUSSIONS

Textural characteristics of catalysts

The adsorption/desorption isotherms and pore size distribution of the two supported catalysts are presented in Figure 1 and 2, respectively. The adsorption isotherms exhibit a type IV behavior with an H2 hysteresis loops [17-20]. This type of hysteresis loop is characteristic of mesoporous materials with slit-like pores having a narrow distribution of pore body size and a wide distribution of pore entrances.

The volume of nitrogen adsorbed is low up to relative pressures (p/p0) of 0.4, indicating monolayer adsorption at the surface of catalysts. At higher relative pressures, the volume of adsorbed nitrogen increases, and the appearance of the hysteresis loops suggests nitrogen condensation taking place in the interparticle spaces.

The total pore volume determined by the BJH method was 0.309 cm^3/g for the W/Pd/γ-Al_2O_3-ZnZSM5 catalyst with the average pore diameter of 4.2 nm and 0.309 cm^3/g for the Nb/Pd/γ-Al_2O_3-ZnZSM5catalyst with a pore diameter of 4.0 nm.

The surface area, pore volume and average pore diameters of the W/Pd/γ-Al_2O_3-ZnZSM5 and Nb/Pd/γ-Al_2O_3-ZnZSM5 catalysts and of the corresponding support are summarized in Table 1. Impregnation of tungsten, niobium and palladium metals on theγ Al_2O_3-ZnZSM5 support led to a decreased surface area, pore volume and pore diameter.

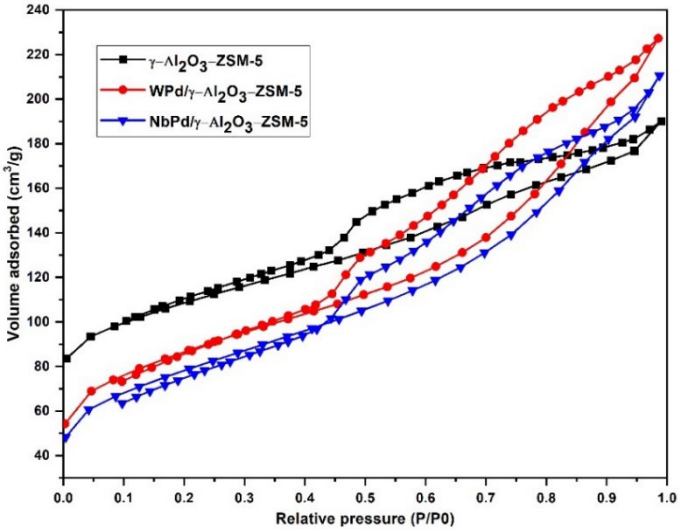

Figure 1. Experimental nitrogen adsorption/desorption isotherm for γ-Al_2O_3-ZnZSM5 support and W/Pd/γ-Al_2O_3-ZnZSM5, Nb/Pd/γ-Al_2O_3-ZnZSM5 catalyst

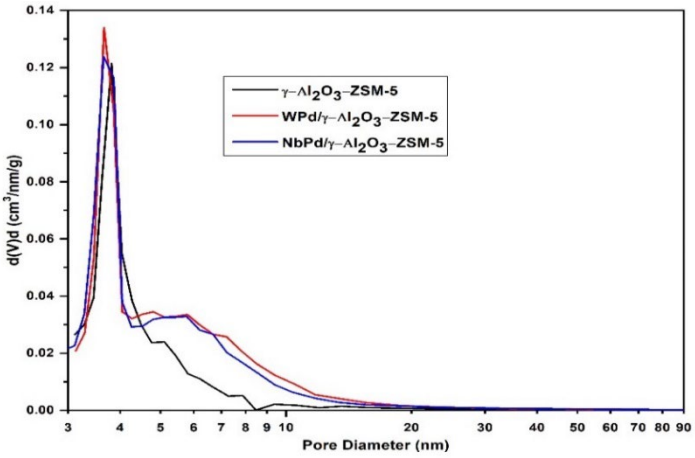

Figure 2. Pore size distribution for γ-Al_2O_3-ZnZSM5 support, W/Pd/γ-Al_2O_3-ZnZSM5 and Nb/Pd/γ-Al_2O_3-ZnZSM5 catalysts

Table 1. Textural characterization for γ-Al_2O_3-ZnZSM5 support and W/Pd/γ-Al_2O_3-ZnZSM5, Nb/Pd/γ-Al_2O_3-ZnZSM5 catalysts

	γ- Al_2O_3-ZnZSM5	W/Pd/γ-Al_2O_3-ZnZSM5	Nb/Pd/γ-Al_2O_3-ZnZSM5
Surface Area, m^2/g	193.38	185.708	184.685
Pore Volume, cm^3/g	0.309	0.283	0.275
Pore Diameter, nm	4.2	3.659	3.650

The Brønsted or Lewis nature of the acidic sites was determined by FTIR pyridine adsorption (Figure 3). The infrared spectra of pyridine at room temperature exhibits three absorption bands at 1540, 1488, and around 1450 cm^{-1}. The Brønsted acid sites correspond to the 1540 cm^{-1} band (pyridinium ion), and the Lewis acid sites to the 1450 cm^{-1} band, attributed to coordinatively bounded pyridine [21,22]. The peak around 1488 cm^{-1} corresponds to the overlapping vibrations of pyridine adsorbed on both Lewis and Brønsted acid sites. Hence, the concentration of both Brønsted and Lewis acid sites was calculated from their corresponding band intensities and extinction coefficients of each type of site using the equation reported by Zhang [21]. The results are presented in Table 2.

Table 2. The acidic properties of γ-Al_2O_3-ZnZSM5 support and W/Pd/γ-Al_2O_3-ZnZSM5, Nb/Pd/γ-Al_2O_3-ZnZSM5 catalysts

Support and catalysts	Lewis acid sites concentration (mmol/g)	Bronsted acid sites concentration (mmol/g)
γ-Al_2O_3-ZSM-5	70.05	15.7
Nb/Pd/γ-Al_2O_3-ZSM-5	90.51 (29.2%)	47.05 (200%)
W/Pd/γ-Al_2O_3-ZSM-5	125.42 (79%)	84.09

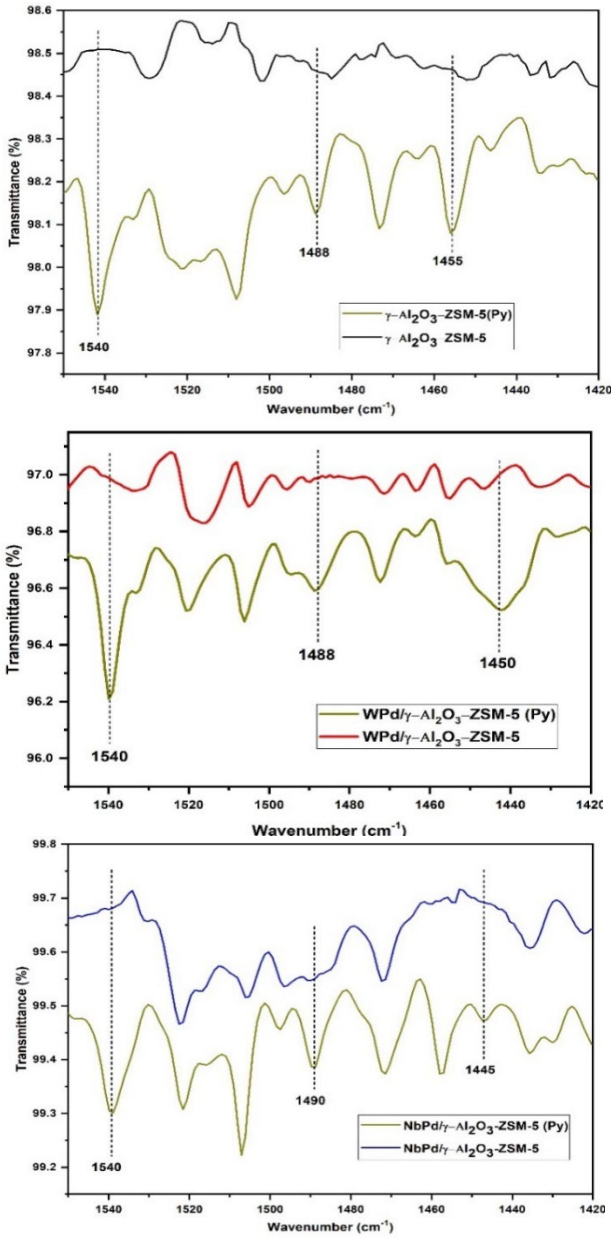

Figure 3. Pyridine-adsorbed FT-IR spectrum of the γ-Al_2O_3- ZnZSM5 support and W/Pd/γ-Al_2O_3- ZnZSM5, Nb/Pd/γ-Al_2O_3- ZnZSM5 catalysts

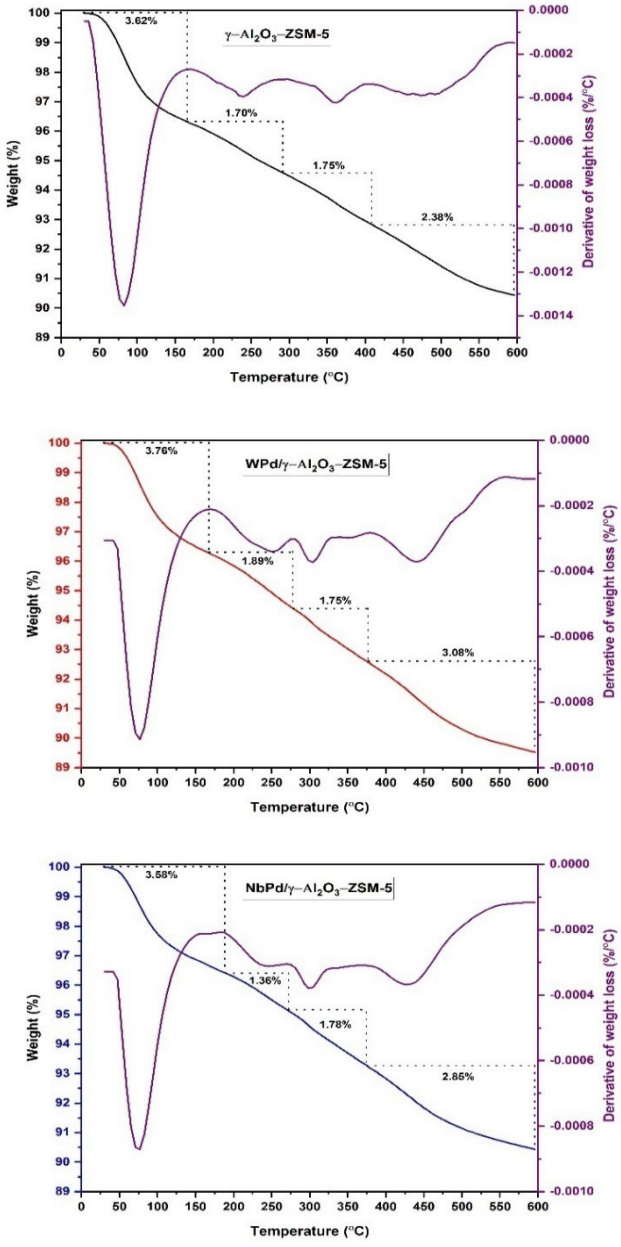

6.3

Figure 4. Thermogravimetric analysis (TGA) and derivative thermogravimetry (DTG) analysis of the support and catalysts

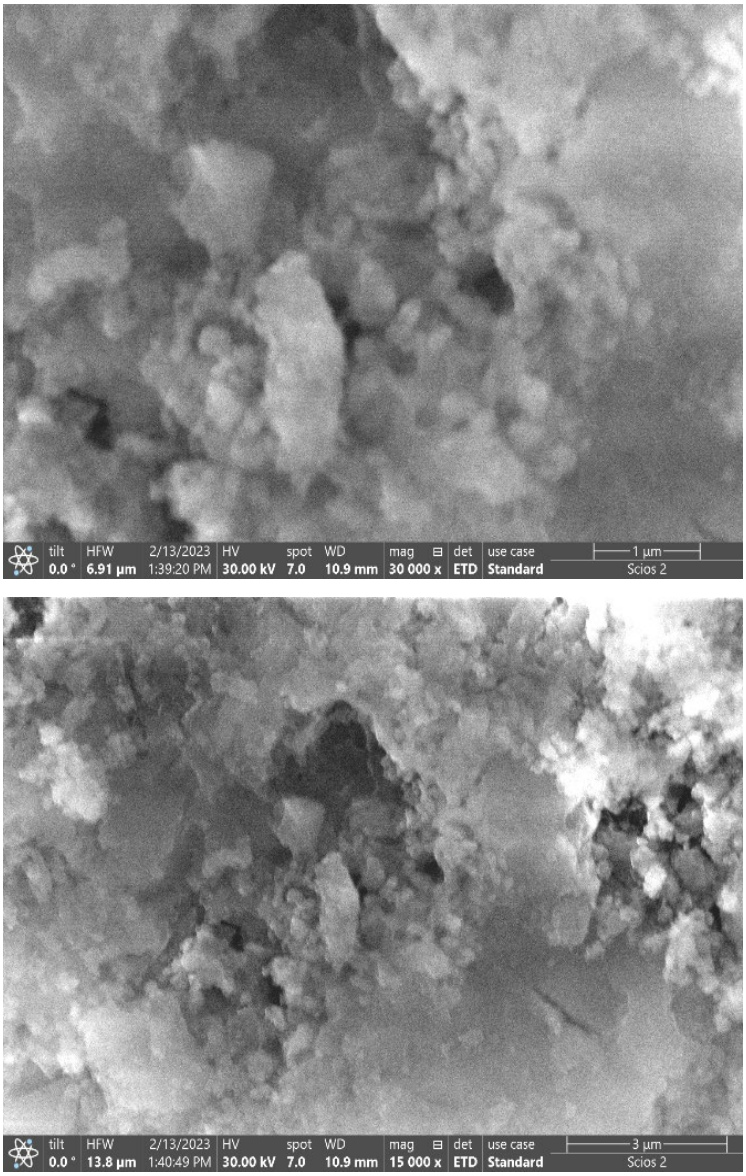

Figure 5. SEM images of the γ-Al_2O_3-ZnZSM5 support

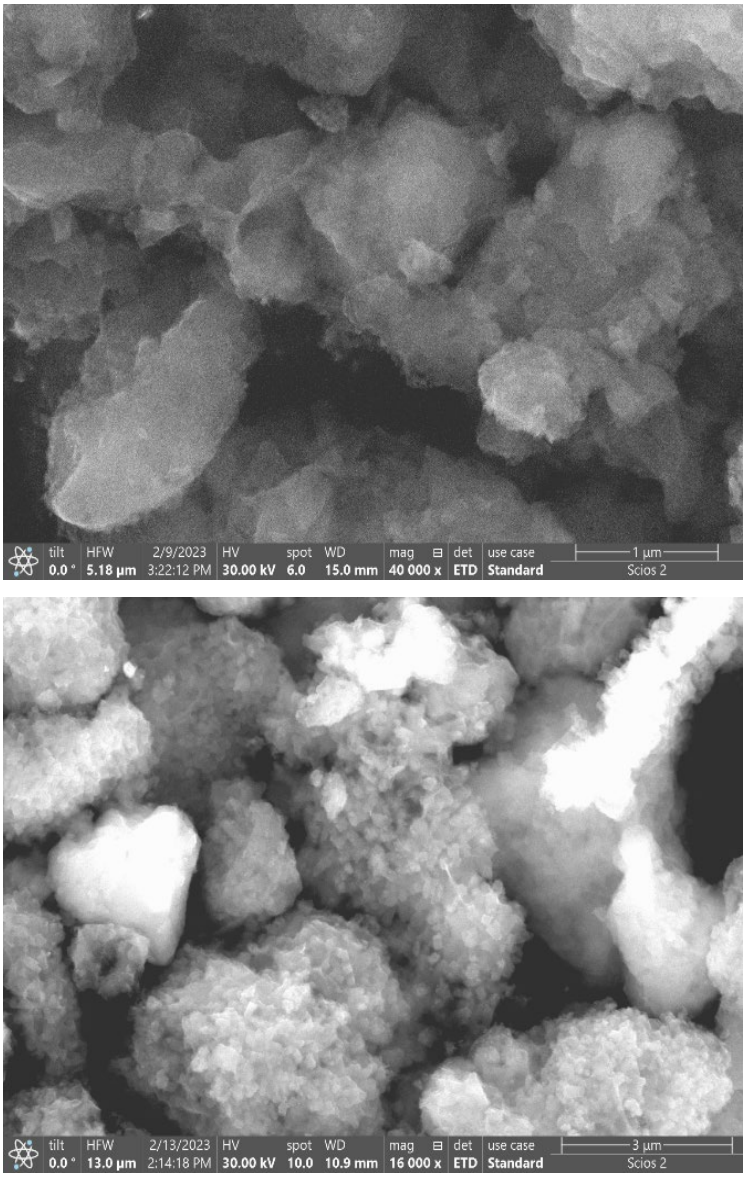

Figure 6. SEM images of the Nb/Pd/γ-Al_2O_3- ZnZSM5 catalyst

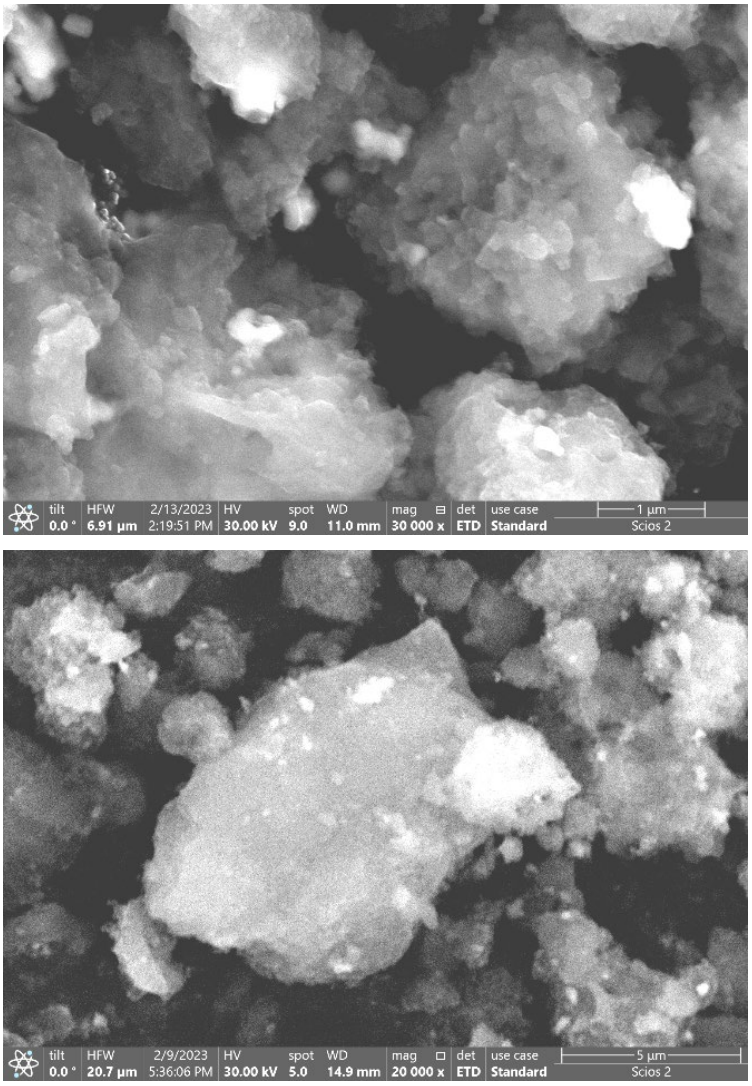

Figure 7. SEM images of the W/Pd/γ-Al_2O_3-ZnZSM5 catalyst

The thermal stability of the catalysts was evaluated to determine the mass losses of the catalytic precursors and their possible chemical changes. The initial weight loss observed in the temperature range of 50°C to 155°C corresponds to the desorption of water molecules [23,24] around 3.62% wt., both for the support and the catalysts (Figure 4). On the derivative thermogravimetric

curve (DTG), multiple mass loss peaks are observed. At higher temperatures, between approximately 200°C and 450°C, the weight loss was 3.45% wt. for the support, 3.64% wt. for the W/Pd/γ-Al_2O_3-ZnZSM5and 3.14% wt. for the Nb/Pd/γ-Al_2O_3- ZnZSM5. This loss can be attributed to the decomposition of the trapped nitrates in the narrow pores of the support and catalysts[25,26]. The slower weight loss of 2.38% wt. for the support, 3.08% wt. for the tungsten based catalyst and 2.85% wt. for the niobium based catalyst after 450°C indicates an extended process of gradual loss of hydroxyl groups from the crystalline structure of the metal/alumina/zeolite[27]. Based on the TGA/DTG profile, a temperature of 450°C was chosen for the calcination of the catalysts. The appearance of particle agglomerations was evaluated by scanning electron microscopy (SEM) as can be seen in the figures 5-7.

The scanning electron microscopy (SEM) images of the catalysts reveal that the particles are uniformly dispersed, at low concentrations, throughout the mass of γ-Al2O3-ZSM-5. SEM image analysis revealed that the average size of the agglomerates was usually between 900 and 2000.

Catalysts activity evaluation

The activity of W/Pd/γ-Al_2O_3-ZnZSM5 and Nb/Pd/γ-Al_2O_3-ZnZSM5 catalysts in the hydrodeoxygenation-hydrocracking of methyl esters of fatty acids was high in the range of temperatures and pressures studied. Thus, figure 8 shows the influence of temperature on the conversion of methyl esters at a pressure of 20 bar and the influence of pressure on the conversion of methyl esters at a temperature of 300°C. The process proceeded with the formation of different classes of compounds in the liquid phase, such as n-aliphatic hydrocarbons, iso-aliphatic hydrocarbons, cycloaliphatic hydrocarbons, and arenes. No oxygenated organic compounds were identified in the collected liquid phase. The high efficiency of the two catalysts in the deoxygenation process of methyl esters of fatty acids at relatively mild operating conditions (temperatures of 300-380°C and pressures of 20-60 bar) is probably attributed to the presence of ZnZSM5 type zeolite.

`The yield of n-aliphatic hydrocarbons showed relatively high values (up to 95%) within the studied temperature and pressure range. At a pressure of 20 bar and lower temperature values (300-325°C), the W/Pd/γ-Al_2O_3-ZnZSM5 catalyst favored higher yields of n-aliphatic hydrocarbons compared to the Nb/Pd/γ-Al_2O_3-ZnZSM5 catalyst. However, at higher temperature values (350-380°C), the Nb/Pd/γ-Al_2O_3-ZnZSM5 catalyst achieved higher yields of n-aliphatic hydrocarbons. Additionally, for the pressure of 20 bar, increasing the temperature led to a decrease in the yield of n-aliphatic

hydrocarbons for both catalysts. This decrease is attributed to the increased reactivity of n-aliphatic hydrocarbons in processes such as isomerization, cyclization, and dehydro-aromatization with rising temperature. N-aliphatic hydrocarbons act as intermediates in the production of these classes of organic compounds. The decrease in n-aliphatic hydrocarbons yield with increasing temperature is more pronounced for the W/Pd/γ-Al_2O_3-ZnZSM5 catalyst, likely due to the higher concentration of Bronsted acid centers in this catalyst, which catalyze the isomerization and cyclization reactions of n-aliphatic hydrocarbons.

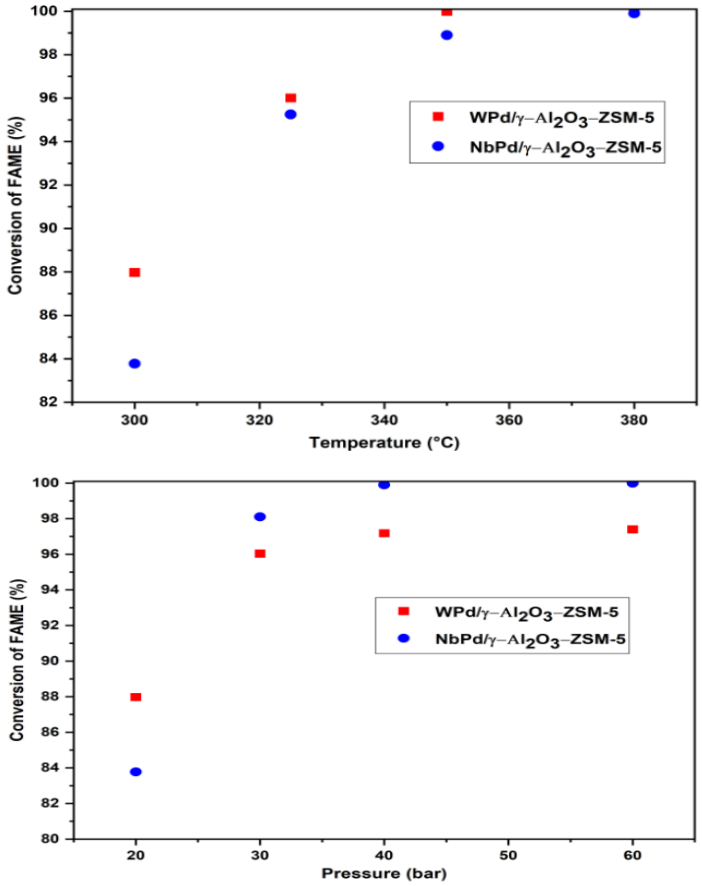

Figure 8. Conversion of fatty acid methyl esters (FAME) with temperature and pressure

The yield of n-aliphatic hydrocarbons with pressure at a temperature of 300°C varied following a curve with a minimum located at 30 atm for the Nb/Pd/γ-Al_2O_3-ZnZSM5 catalyst and at 40 atm for the W/Pd/γ-Al_2O_3-ZnZSM5 catalyst. This behavior is likely due to the fact that n-aliphatic hydrocarbons, as reaction intermediates, are formed through cracking reactions and are consumed in the isomerization-cyclization reaction at different rates at different pressures. At relatively low-pressure values (20-30 bar), the formation of n-aliphatic hydrocarbons is favored by improved adsorption on acidic centers. The increase in pressure above 40 bar disfavors the isomerization reactions of aliphatic hydrocarbons which are carried out by β-elimination reactions of carbocation type intermediates, thus reducing the consumption of such hydrocarbons.

In the studied temperature and pressure range, the yield of iso-aliphatic hydrocarbons, which are intermediates in the production of cycloaliphatic hydrocarbons, was lower compared to the yield of n-aliphatic hydrocarbons. At a pressure of 20 bar, the variation in iso-aliphatic hydrocarbons yield showed a maximum at 325°C for both studied catalysts. This behavior is likely due to the increased occurrence of pericyclic reactions of iso-aliphatic hydrocarbons at temperatures above 325°C, especially cycloaddition reactions, which proceed thermally and are favored by higher temperatures. As a result, the carboxyl group can activate any adjacent alkenic group (activated diene), promoting Diels-Alder reactions at relatively lower temperatures. The lower maximum yield of iso-aliphatic hydrocarbons on the W/Pd/γ-Al_2O_3-ZnZSM5 catalyst (26.1%) compared to the Nb/Pd/γ-Al_2O_3-ZnZSM5 catalyst (34.7%) is likely due to a more optimal distribution of Bronsted acid centers on the Nb/Pd/γ-Al_2O_3-ZnZSM5 catalyst. In this case, water formed during the deoxygenation process of the raw materials (methyl esters of fatty acids) reacts with WO_3type Lewis acids, favoring the formation of a larger quantity of Bronsted acids with lower strength, whose catalytic activity in isomerization reactions is reduced. Nb_2O_5-type Lewis acids do not react with the water formed in the deoxygenation process, and thus, the presence of water does not influence the concentration and strength of Bronsted acid centers and, consequently, the isomerization process for this catalyst.

The yield of iso-aliphatic hydrocarbons with pressure at a temperature of 300°C varied, with a maximum located at 30 atm for both catalysts, and a higher maximum value observed for the Nb/Pd/γ-Al_2O_3-ZnZSM5 catalyst (36.2%) compared to the W/Pd/γ-Al_2O_3-ZnZSM5 catalyst (31.6%). The decrease in iso-aliphatic hydrocarbons yield at pressure values higher than 30 bar is likely due to a reduction in β-elimination of the carbocation intermediates and the promotion of cycloaddition reactions of unsaturated intermediates

with increasing pressure. The higher yield of iso-aliphatic hydrocarbons on the Nb/Pd/γ-Al_2O_3-ZnZSM5 catalyst compared to the W/Pd/γ-Al_2O_3-ZnZSM5 catalyst is attributed to a more optimal distribution of Bronsted acid centers. Additionally, the abrupt drop to zero in the iso-aliphatic hydrocarbons yield at a pressure of 60 bar on the W/Pd/γ-Al_2O_3-ZnZSM5 catalyst is probably due to a reduction in the concentration of strong Bronsted acid centers resulting from the reaction of the WO_3Lewis acid with water formed during the deoxygenation of fatty acid esters. The adsorption of water on acid centers is favored by increasing pressure.

The yield of cycloaliphatic hydrocarbons showed average values (up to 29%) within the studied temperature and pressure range. On the W/Pd/γ-Al_2O_3-ZnZSM5 catalyst, cycloaliphatic hydrocarbons were not obtained at a pressure of 20 bar and lower temperature values (300°C). Increasing the temperature favored an increase in the yield of cycloaliphatic hydrocarbons, reaching up to 30% at a temperature of 380°C. Similarly, for the Nb/Pd/γ-Al_2O_3-ZnZSM5 catalyst, the yield of cycloaliphatic hydrocarbons increased with temperature within the studied temperature range, with the increase becoming less pronounced at higher temperatures (380°C). This increase is due to pericyclic reactions, such as cycloaddition reactions of dienes with activated dienes, which are compounds formed from the cracking of fatty acid esters; the exothermic nature of the cycloaddition reactions reduces this process at high temperatures.

For the Nb/Pd/γ-Al_2O_3-ZnZSM5 catalyst, at a temperature of 300°C, the yield of cycloaliphatic hydrocarbons increased with increasing pressure; however, the increase becomes insignificant at pressures above 30 bar. On the other hand, for the W/Pd/γ-Al_2O_3-ZnZSM5 catalyst, the increase followed a curve with a maximum, and as a result, cycloaliphatic hydrocarbons were not identified at pressures of 20 bar and 60 bar. The absence of cycloaliphatic hydrocarbons at a pressure of 20 bar is likely due to reduced accessibility in the pores that allow the occurrence of pericyclic reactions (shape selectivity). The absence of cycloaliphatic hydrocarbons at higher pressures (above 60 bar) is probably due to the negative influence of pressure on the β-elimination reactions of carbocations, which are intermediates in the cracking and isomerization process; the absence of iso-aliphatic hydrocarbons supports this conclusion. Pressure values of 30-40 bar favor the β-elimination reactions of carbocations, which lead to the formation of cycloaliphatic and iso-aliphatic hydrocarbons.

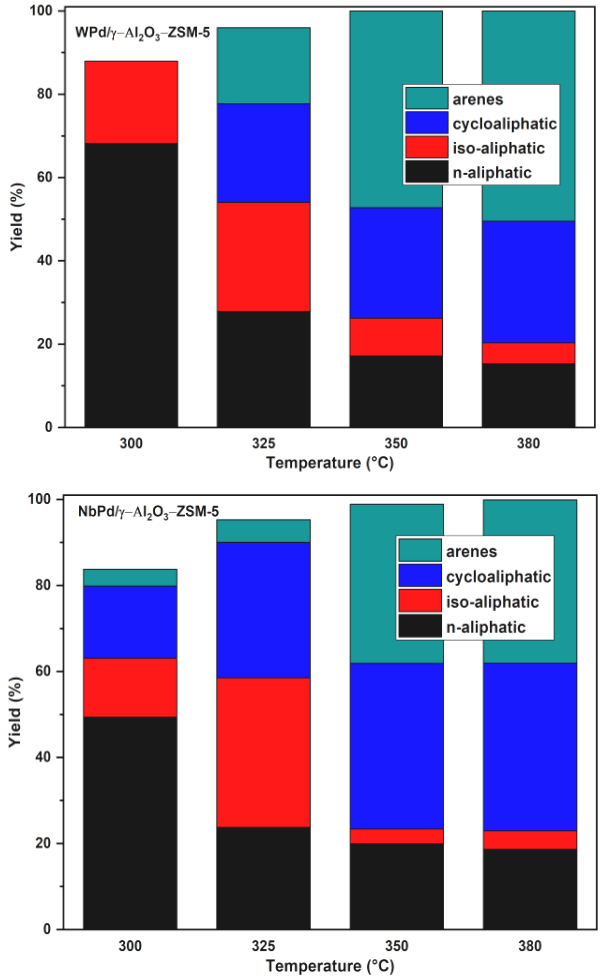

Figure 9. The yield in hydrocarbons with temperature, at pressure 20 bar, LHSV 0.5 h^{-1} for both catalysts

The yield of arenes reached values of up to 51% within the studied temperature and pressure range. On the W/Pd/γ-Al_2O_3-ZnZSM5 catalyst, arenes were not obtained at a pressure of 20 bar and lower temperature values (300°C), indicating that arenes are formed through the dehydrogenation of cycloaliphatic hydrocarbons (which were also not obtained at these parameter values). Increasing the temperature favored an increase in the yield of arenes, reaching up to 50.5% at a temperature of 380°C.

Similarly, for the Nb/Pd/γ-Al_2O_3-ZnZSM5 catalyst, the yield of arenes increased with increasing temperature within the studied temperature range, and the increase became less pronounced at higher temperatures (380°C), similar to the behavior observed for the W/Pd/γ-Al_2O_3-ZnZSM5 catalyst. This behavior is due to the dehydrogenation reactions of cyclic intermediates obtained through pericyclic reactions, such as the Diels-Alder 4+2 cycloaddition reactions of dienes with activated dienes. The tendency of decreasing slopes in the yield variation curves of arenes at temperatures of 350-380°C is attributed to the exothermic nature of the dehydrogenation reaction of alkyl-cyclohexadiene intermediates obtained through Diels-Alder reactions, which becomes unfavorable with increasing temperature.

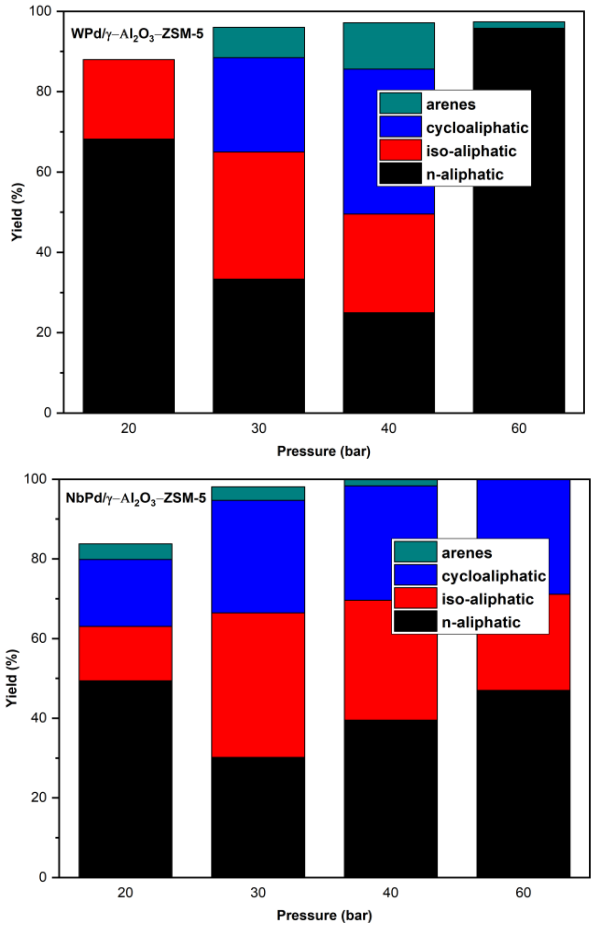

Figure 10. The yield in hydrocarbons with pressure, at 300°C, LHSV 0.5h^{-1} for both catalysts

For the Nb/Pd/γ-Al_2O_3-ZnZSM5 catalyst, at a temperature of 300°C, the yield of arenes decreased with increasing pressure, and the decrease became more pronounced at pressures above 30 bar, with the yield of arenes reaching zero at 60 bar. On the W/Pd/γ-Al_2O_3-ZnZSM5 catalyst, the yield of arenes varied following a curve with a maximum located at a pressure of 40 bar, so at a pressure of 20 bar, no arenes were identified, and at 60 bar, the yield of arenes was approximately 7 times lower than at 40 bar.

The absence of arenes on the W/Pd/γ-Al_2O_3-ZnZSM5 catalyst at a pressure of 20 bar and a temperature of 300°C is most likely due to the absence of cycloaliphatic hydrocarbons. The absence or reduced concentration of arenes at high pressures is due to the unfavorable dehydrogenation process with increasing pressure (a process that proceeds with an increase in the number of moles). The higher yields of arenes on the W/Pd/γ-Al_2O_3-ZnZSM5 catalyst compared to the Nb/Pd/γ-Al_2O_3-ZnZSM5 catalyst at pressures of 30-40 bar highlight the contribution of acid centers in the dehydrogenation process of cycloaliphatic hydrocarbons.

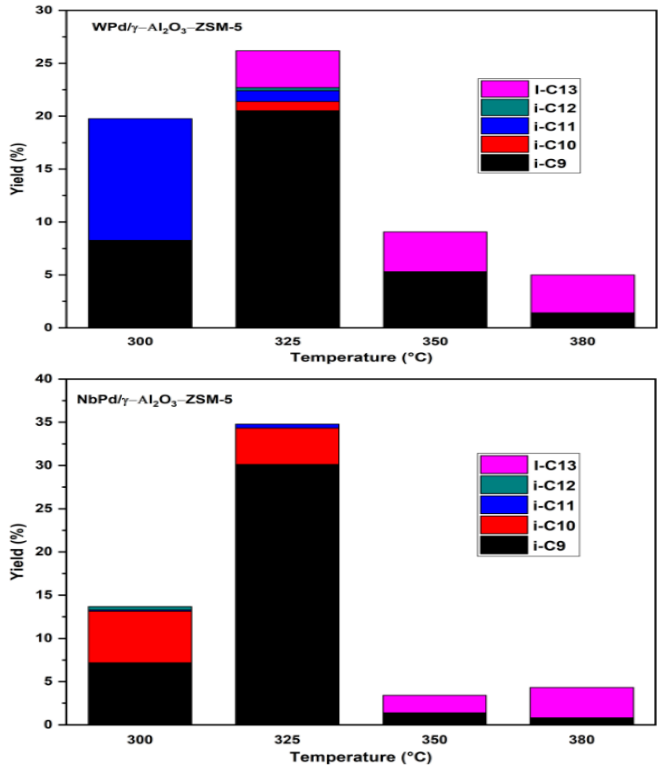

Figure 11. The yield in iso-aliphatic hydrocarbons with temperature, at pressure 20 bar, LHSV 0.5 h^{-1} for both catalysts

The influence of pressure on the yield of n-aliphatic hydrocarbons differed for the two catalysts. For the Nb/Pd/γ-Al_2O_3-ZnZSM5 catalyst, the yield of n-C10 to n-C13 increased with pressure, while the yield of n-C15 to n-C18 decreased with increasing pressure. For the W/Pd/γ-Al_2O_3-ZnZSM5 catalyst, the yield of n-C10, n-C11, n-C15, n-C17, and n-C18 varied with pressure following a curve with a minimum. However, the yield of n-C12 and n-C13 increased with pressure, while the yield of n-C16 varied with pressure following a curve with a maximum. Additionally, the yield of n-C18 tended to approach the yield of n-C17 at pressures higher than 60 bar, demonstrating that the hydrodeoxygenation process through decarboxylation is disfavored at high pressures.

The identified aromatic hydrocarbons in the liquid reaction product were arenes-C8 and arenes-C9 for both tested catalysts. The yield of arenes-C8 was higher than that of arenes-C9 over the entire range of variation of parameters for both catalysts studied. Generally, at a pressure of 20 bar, the yield of arenes increased with temperature for the Nb/Pd/γ-Al_2O_3-ZnZSM5 catalyst. For the W/Pd/γ-Al_2O_3-ZnZSM5 catalyst, the yield of arenes-C8 increased with temperature over the temperature range of 325°C to 380°C at the same pressure, while the content of arenes-C9 varied following a curve with a maximum. Overall, the yield of arenes was higher on the W/Pd/γ-Al_2O_3-ZnZSM5 catalyst compared to the Nb/Pd/γ-Al_2O_3-ZnZSM5 catalyst.

The yield of arenes-C8 varied with pressure following a curve with a maximum for both tested catalysts at a temperature of 300°C. The low values of the yield of both arenes at high pressures are attributed to the negative influence of high pressures on processes involving an increase in the number of moles. The Nb/Pd/γ-Al_2O_3-ZnZSM5 catalyst did not produce arenes-C9 at pressures above 20 bar, while the W/Pd/γ-Al_2O_3-ZnZSM5 catalyst showed a decrease in the content of these arenes with increasing pressure.

For both tested catalysts, the identified iso-aliphatic hydrocarbons in the liquid reaction product were iso-C9 to iso-C13. Generally, at a pressure of 20 bar and lower temperatures (300°C to 325°C), higher yields of iso-C9 were obtained for both catalysts, while increasing the temperature to values above 350°C favored the formation of iso-C13 hydrocarbons. The Nb/Pd/γ-Al_2O_3-ZnZSM5 catalyst showed higher yields of iso-C9 compared to the W/Pd/γ-Al_2O_3-ZnZSM5 catalyst, likely due to an optimal distribution of acidic strength (the acidic strength of WO_3 centers diminishes in the presence of adsorbed water in the catalytic pores, while the acidic strength of Nb_2O_5 centers remains unchanged in the presence of water). The decrease in the yield of iso-aliphatic hydrocarbons with increasing temperature (except for iso-C13) can be attributed to their tendency to cyclize at temperatures above 325°C in the presence of acidic catalysts.

The yield of iso-C9 varied with pressure following a curve with a maximum for both tested catalysts at a temperature of 300°C. Increasing the pressure above 30 bar unfavorably affected the elimination reactions of carbocation intermediates and, consequently, the isomerization reactions. The yield of iso-C10 to iso-C13 was not significantly influenced by increasing pressure and generally remained below 1% over the studied pressure range for both catalysts, except for the yield of iso-C11 on the W/Pd/γ-Al_2O_3-ZnZSM5 catalyst, which ranged from 2% to 11%.

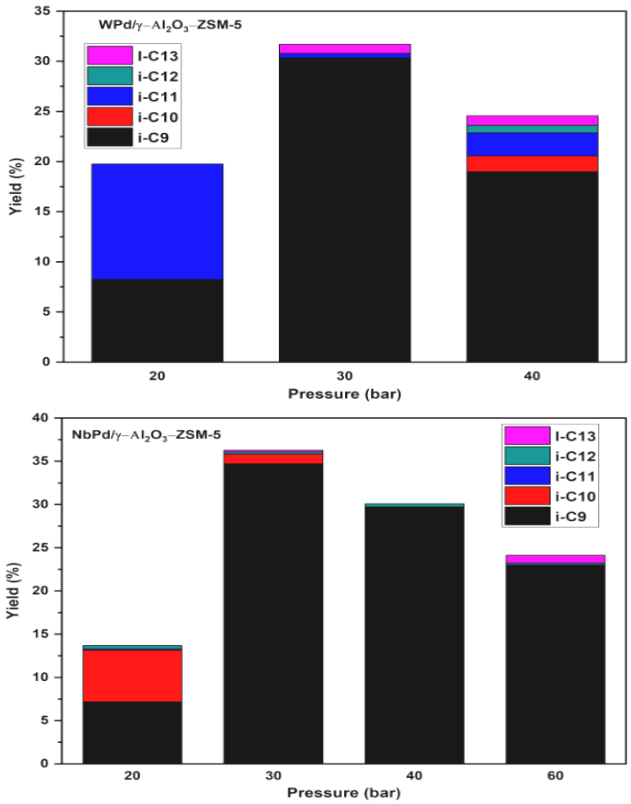

Figure 12. The yield in iso-aliphatic hydrocarbons with pressure, at 300°C, LHSV 0.5 h^{-1} for both catalysts

The cyclo-aliphatic hydrocarbons identified in the liquid reaction product were cyclo-C8 and cyclo-C9 for both tested catalysts. This information highlights the high reactivity of the ZnZSM5 zeolite in the cyclization reaction of n- and iso-C8 hydrocarbons, which were not detected in the reaction product, indicating that they cyclized instantaneously after formation. For the Nb/Pd/γ-Al_2O_3-ZnZSM5 catalyst, the yield of cyclo-C8 varied with temperature

following a curve with a maximum located at 325°C at a pressure of 20 bar. The W/Pd/γ-Al_2O_3-ZnZSM5 catalyst exhibited lower performance than the Nb/Pd/γ-Al_2O_3-ZnZSM5 catalyst at a pressure of 20 bar, and the yield of cyclo-C8 decreased with increasing temperature over the temperature range of 325°C to 380°C. On the other hand, the yield of cyclo-C9 increased with temperature over the temperature range of 300°C to 380°C for both catalysts. The porous structure of ZnZSM5 likely favors the formation of intermediates such as n- and iso-C9 hydrocarbons over n- and iso-C8 hydrocarbons.

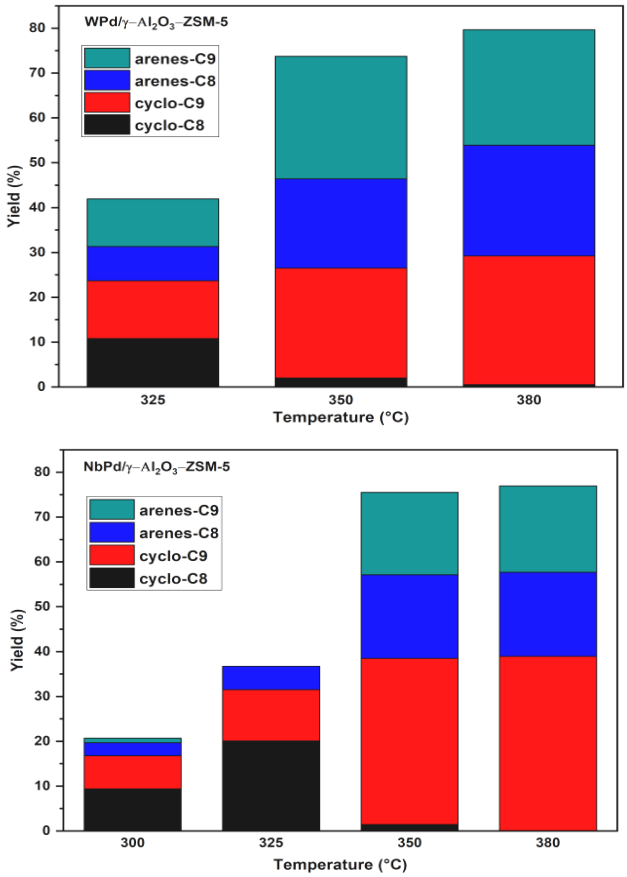

Figure 13. The yield in C8 and C9 cyclo-aliphatic hydrocarbons with temperature, at pressure 20 bar, LHSV 0.5 h^{-1} for both catalysts

The yield of cyclo-aliphatic hydrocarbons C8 varied with pressure following a curve with a maximum for both tested catalysts at a temperature of 300°C. The W/Pd/γ-Al_2O_3-ZnZSM5 catalyst exhibited a higher maximum

yield in cyclo-C8 compared to the Nb/Pd/γ-Al_2O_3-ZnZSM5 catalyst (approximately 25% compared to 17%). The abrupt decrease in the yield of cyclo-C8 and cyclo-C9 to 0% at a pressure of 60 atm in the case of the W/Pd/γ-Al_2O_3-ZnZSM5 catalyst is likely due to the decrease in Bronsted acidic strength of WO_3 centers in the presence of water resulting from the deoxygenation reaction, with water adsorption favored at high pressures. In contrast, an increase in the yield of cyclo-C9 with pressure was observed for the Nb/Pd/γ-Al_2O_3-ZnZSM5 catalyst over the entire studied pressure range.

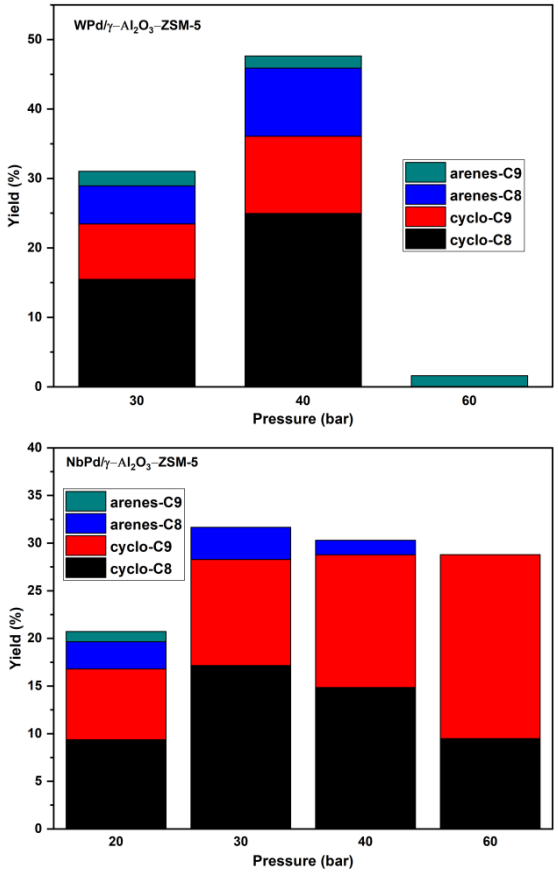

Figure 14. The yield in C8 and C9 cyclo-aliphatic hydrocarbons with pressure, at 300°C, LHSV 0.5 h^{-1} for both catalysts

The identified n-aliphatic hydrocarbons in the liquid reaction product were n-C10, n-C11, n-C12, n-C13, n-C15, n-C16, n-C17, and n-C18. Among these n-aliphatic hydrocarbons, n-C10, n-C15, n-C16, and n-C17 showed high yields at a temperature of 300°C and a pressure of 20 bar (ranging from

5% to 31% for both tested catalysts, with the W-based catalyst exhibiting higher yields for n-C10). However, with increasing temperature above 325°C, the yields of these hydrocarbons decreased rapidly, and at 380°C, except for n-C15, the yield became zero.

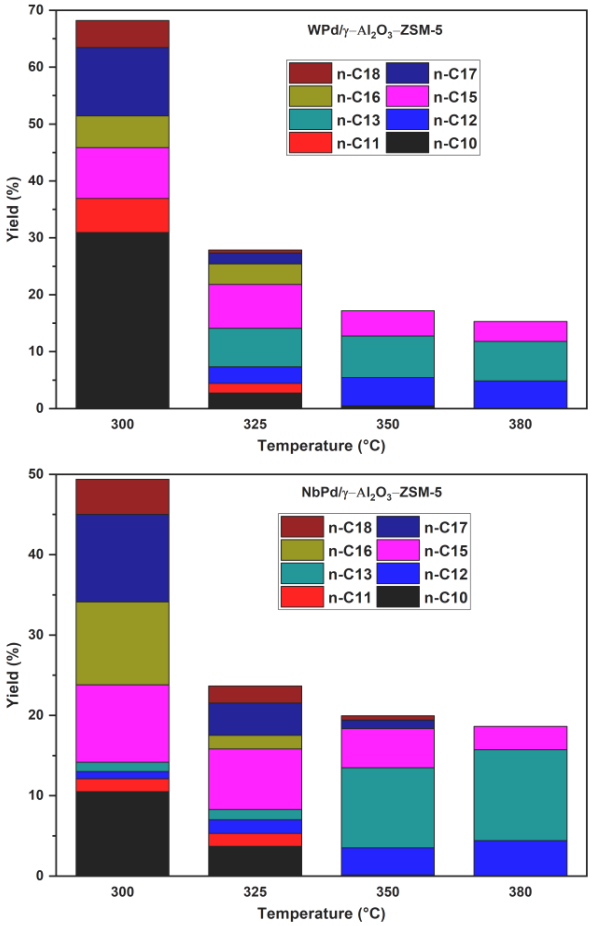

Figure 15. The yield in n-aliphatic hydrocarbons with temperature, at pressure 20 bar, LHSV 0.5 h^{-1} for both catalysts

On the other hand, n-C11, n-C12, and n-C13 exhibited lower yields at 300°C and 20 bar (ranging from 6% to 0%). But, with increasing temperature above 325°C, the yield variation for n-C11, n-C12, and n-C13 differed, resulting in relatively higher yields (4.4% and 11.3% for the Nb-based catalyst, and 4.8% and 6.9% for the W-based catalyst) at 380°C. The yield of n-C18 was approximately half of that for n-C17 throughout the studied

temperature range, indicating that deoxygenation proceeds with approximately 33% by the hydrogenation of the carboxylic bond and approximately 67% by decarboxylation. The absence of n-aliphatic hydrocarbons with less than 10 carbon atoms is likely due to their higher tendency for cyclization and dehydrogenation.

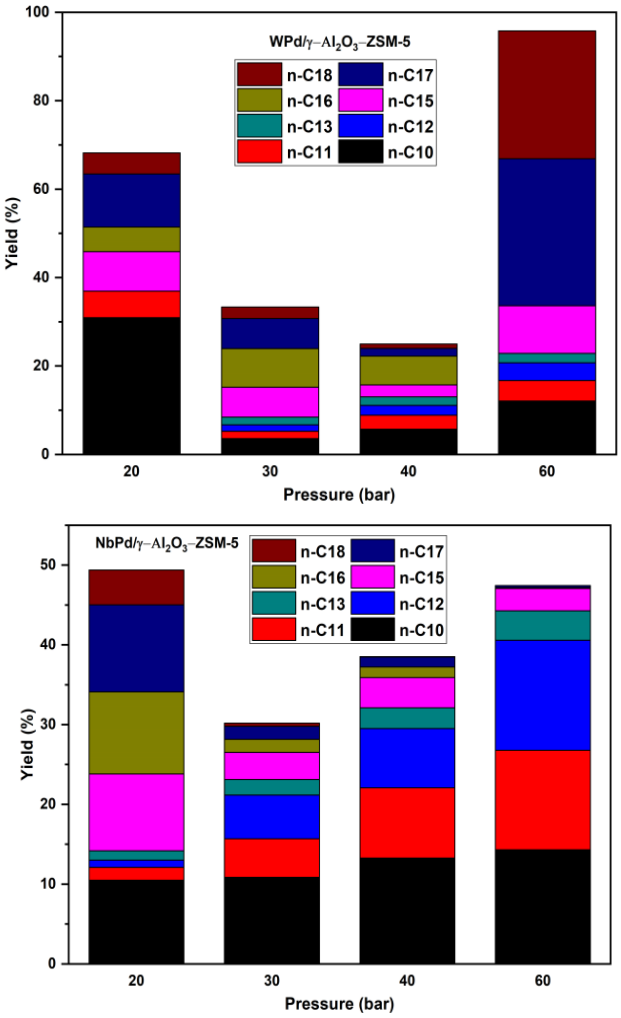

Figure 16. The yield in n-aliphatic hydrocarbons with pressure, at 300°C, LHSV 0.5 h^{-1} for both catalysts

CONCLUSIONS

The W-based catalyst exhibited higher activity than the Nb-based catalyst, attributed to a higher concentration of Lewis-type acidic centers (over 92%) and Bronsted-type acidic centers (close to 50%).

The hydrodeoxygenation-hydrocracking process of methyl esters of fatty acids on the W/Pd/γ-Al_2O_3-ZnZSM5 and Nb/Pd/γ-Al_2O_3-ZnZSM5 catalysts at 300-380°C and 20-60 bar resulted in the formation of different classes of hydrocarbons in the liquid phase, such as n-aliphatic hydrocarbons, iso-aliphatic hydrocarbons, cycloaliphatic hydrocarbons, and arenes.

Increasing the pressure to over 30-40 bar unfavorably affected the isomerization reactions by reducing the β eliminations to the intermediate carbocations, leading to a decrease in the consumption of n-aliphatic hydrocarbons. Thus, the yield of iso-aliphatic hydrocarbons, intermediates in the process of obtaining cycloaliphatic hydrocarbons, was lower compared to the yield of n-aliphatic hydrocarbons.

The high activity in the cyclization process of the catalysts tested over the range of parameters studied is probably due to the presence of the carboxyl group that can activate a nearby alkene group, favoring the occurrence of Diels-Alder reactions at relatively lower temperature values.

Over the studied temperature range at lower pressure, the yield of n-C18 remained constant, approximately half of the yield of n-C17, indicating that deoxygenation occurs to approximately 33% through the hydrogenation of the carboxylic bond and to approximately 67% through decarboxylation/ decarbonylation. Additionally, the yield of n-C18 tends to approach the yield of n-C17 at higher pressure values of over 60 bar, indicating that at high pressures, the decarboxylation process is less favored in the hydrodeoxygenation process.

EXPERIMENTAL SECTION

Characterization of palm oil fatty acids methyl esters

Synthesis of fatty acids methyl esters was described in a previous work [28]. The analysis of fatty acids methyl esters and of the reaction products was carried out using a GC–MS TRIPLE QUAD (Agilent 7890 A) with a DB-WAX capillary column (30 mL, 0.25 mm internal diameter, 0.25 μm film thickness). Helium was the carrier gas with a flow rate of 1 mL/min. The oven temperature was set at 70 °C and was increased to 230 °C with a rate of 4 °C / minute

with 5 minutes holding time. The GC injector and MS ion source temperatures were set at 250 °C and 150 °C, respectively. Transfer line temperature was set at 280 °C. The MS detector was operated in EI mode at 70 eV, with a m/z scanning range of 50–450. Peaks were identified using a NIST MS database [29]. The distribution of fatty acid methyl esters was as follows: methyl myristate (1.51 wt.%), methyl palmitate (35.72 wt.%), methyl stearate (6.68 wt.%), methyl oleate (41.82 wt.%), methyl linoleate (13.6 wt.%) and methyl icosanoate (0.66 wt.%) [16].

Catalysts preparation

The catalyst support is a mixture of 70% powdery γ-alumina (VGL-25 type, UOP Versal, Honeywell) and 30% ZnZSM-5. In the first step, 2.9 liters of deionized water, 570 grams of silica-alumina with a SiO_2/Al_2O_3 ratio of 125, 200 grams of melted hexamethylenediamine, and 20 grams of zinc acetate dissolved in 100 ml of water were added to a 10-liter stirred autoclave. The pH of the suspension was adjusted using a 50% NaOH solution to a value of 12.2, and then it was heated to 174°C under stirring for 48 hours. The pressure in the autoclave reached 9 bars. After 48 hours, the synthesized mixture was transferred to a stainless-steel autoclave with a Teflon-coated surface and dried at 120°C for 24 hours, followed by crystallization for 12 hours at 170°C. The obtained product was centrifuged, washed with distilled water until it reached a pH of 7, then dried at 120°C for 12 hours and calcined at 550°C for 10 hours. 250 grams of the obtained zeolite with MFI structure, was mixed with 2 liters of 10% ammonium nitrate solution and deionized water in a stirred vessel at 95°C for 2 hours. The operation was repeated twice. After centrifugation, the ammonium form of the zeolite was washed with 7 liters of deionized water, and the obtained suspension was centrifuged again, then the resulting zeolite was dried at 120°C for 12 hours [30].

The second stage of preparing the catalytic support involved mixing 70% γ-Al_2O_3 (type VGL-25, UOP Versal, Honeywell) and 30% ZnZSM-5 in powder form in a 1-liter capacity horizontal mixer with a heating mantle, along with a solution of nitric acid (HNO_3, 10% mass), which was gradually dosed over 60 minutes. After dosing the HNO_3 solution, mixing continued at room temperature for 4 hours. A homogeneous paste was obtained and introduced into an automatic extruder with a nozzle diameter of 1 mm. By extrusion, cylindrical granules were obtained, which were dried for 8 hours at a temperature of 150°C. After drying, the cylindrical extrudate catalytic support was calcined at a temperature of 450°C, with a heating rate of $5°C \cdot min^{-1}$ [30].

Two catalysts were prepared by impregnating the extruded catalytic support with aqueous solutions of metal precursors [18,31-33]. Thus, a W/Pd/γ-Al_2O_3-ZnZSM-5 catalyst was prepared by successive impregnation

with ammonium tungstate solution and palladium nitrate respectively at a concentration of 6.5%W and 1%Pd, and a Nb/Pd/γ-Al_2O_3-ZnZSM-5 catalyst was prepared by successive impregnation with a solution of niobium oxalate and palladium nitrate respectively at a concentration of 6.5%Nb and 1%Pd. Both catalysts were then dried at 250°C for 3 hours, following which each catalyst was impregnated with a solution of palladium nitrate (II) dihydrate (40% Pd) - $Pd(NO_3)_2 \cdot 2H_2O$ (Sigma Aldrich) in water. The impregnated catalysts were subsequently dried at 250°C for 3 hours. Before the experimental tests, the oxide precursors were reduced under a H_2 stream, at 250 °C and 5 bar for 2 hours; then, the temperature was increased to 450 °C, and the activation continued for 8 hours [16,19].

Catalysts characterization

Textural characteristics of the catalysts (surface area, pore volume, average pore diameter and pore-size-distribution) were measured by a Quantacrome NOVA 2200e instrument, by physisorption of nitrogen at -196 °C.

Thermogravimetric analyses (TGA) of the catalyst were recorded on a TGA/-IST (Thermal Analysis System TGA 2, METTLER TOLEDO, Greifensee, Switzerland) in the 30–600 °C temperature range, in a nitrogen atmosphere, with a heating rate of 10 °C/min.

The acidic properties of the catalyst (the concentrations of Brønsted and Lewis acid sites) were evaluated through the pyridine-adsorbed FT-IR spectrum analysis of pyridine adsorption by the ring vibration of pyridine detected in the frequency range of 1420–1550 cm−1 and was recorded using Tracer-100 (Shimadzu Europa GmbH) Shimadzu Fourier-Transform Infrared Spectrophotometer with KBr pellet method.

Structural morphology images of the catalysts using a Scios 2 HIVAC Dual-Beam ultra-high-resolution FIB-SEM.

Catalytic reaction

Experimental tests were carried out in a fixed bed reactor (length of 50 cm, diameter of 2.25 cm). A catalyst volume of 40 cm^3 was loaded in the middle of the reactor and the top and the bottom were filled each with 80 cm^3 inert glass beads [34,35]. The liquid samples were analyzed by GC/MS 7000 Triple Quad MS (Agilent Technologies) system equipped with HP-FFAP (30 m, 250 μm, 0.25 μm) column and He as carrier gas with volumetric flow of 1 ml/min.

REFERENCES

1. Mortensen, P.M.; Grunwaldt, J.D.; Jensen, P.A.; Knudsen, K.G.; Jensen, A.D; *Appl. Catal. A: General*, **2011**, *407*, 1-19.
2. Di Vito Nolfi, G.; Gallucci, K.; Rossi, L; I J. Environ. Res. Public Healt, **2021**, 18.
3. Jamil, F.; Al-Haj, L.; Al-Muhtaseb, A.a.H.; Al-Hinai, M.A.; Baawain, M.; Rashid, U.; Ahmad, M.N.M; *Rev. Chem. Eng* **2018**, *34*, 267-297.
4. Li, J.; Zhang, J.; Wang, S.; Xu, G.; Wang, H.; Vlachos, D.G; *ACS Catalysis*, **2019**, *9*, 1564-1577.
5. Ray, P.; Clément, M.; Martini, C.; Abdellah, I.; Beaunier, P.; Rodriguez-Lopez, J.-L.; Huc, V.; Remita, H.; Lampre, I; New J. Chem., **2018**, *42*, 14128-14137.
6. Cao, Y.; Shi, Y.; Bi, Y.; Wu, K.; Hu, S.; Wu, Y.; Huang, S; *Fuel Process. Techn*., **2018**, *172*, 29-35.
7. Jing, Z.-Y.; Zhang, T.-Q.; Shang, J.-W.; Zhai, M.-l.; Yang, H.; Qiao, C.-Z.; Ma, X.-Q; *J. Fuel Chem.Technol*.,**2018**, *46*, 427-440.
8. Konwar, L.J.; Oliani, B.; Samikannu, A.; Canu, P.; Mikkola, J.-P; *Biomass Conv. Bioref*., **2022**, *12,* 51-62.
9. Cheng, J.; Zhang, Z.; Zhang, X.; Liu, J.; Zhou, J.; Cen, K; *Fuel*, **2019**, *245*, 384-391.
10. Nepomniashchii, A.A.; Buluchevskiy, E.A.; Koshevaya, Y.O.; Gulyaeva, T.I.; Lavrenov, A.V; AIP Conference Proceedings, **2020,** *2301*, 030013.
11. Hong, Y.-K.; Lee, D.-W.; Eom, H.-J.; Lee, K.-Y; *Appl. Catal. B: Environmental*, **2014**, *150-151*, 438-445.
12. Ardiyanti, A.R.; Gutierrez, A.; Honkela, M.L.; Krause, A.O.I.; Heeres, H.J; *Appl. Catal. A: General,* **2011**, *407*, 56-66.
13. Zerva, C.; Karakoulia, S.A.; Kalogiannis, K.G.; Margellou, A.; Iliopoulou, E.F.; Lappas, A.A.; Papayannakos, N.; Triantafyllidis, K.S; *Catal. Today*, **2021**, *366*, 57-67.
14. Shao, Y.; Xia, Q.; Liu, X.; Lu, G.; Wang, Y; *Chem Sus Chem*, **2015**, *8*, 1761-1767.
15. Srihanun, N.; Dujjanutat, P.; Muanruksa, P.; Kaewkannetra, P; *Catalysts*, **2020**, 10.
16. Marinescu, M.; Popovici, D.R.; Bombos, D.; Vasilievici, G.; Rosca, P.; Oprescu, E.-E.; Bolocan, I; Reaction Kinetics, *Mecha Catalysis*, **2021**, 133, 1013-1026.
17. Doukeh, R.; Bombos, M.; Bombos, D.; Vasilievici, G.; Radu, E.; Oprescu, E.-E; *React. Kinet., Mech. Catal.*, **2021**, *132*, 829-838.
18. Doukeh, R.; Leostean, C.; Bolocan, I.; Trifoi, A.R.; Banu, I; *Chem Select*, **2021**, *6*, 3858-3868.
19. Doukeh, R.; Bombos, D.; Bombos, M.; Oprescu, E.-E.; Dumitrascu, G.; Vasilievici, G.; Calin, C.; *Sci. Rep.*, **2021**, *11*, 6176.
20. Doukeh, R.; Juganaru, T.; Bolocan, I, *Revista de chimie*, **2019**, *70*, 3132-3135.
21. Zhang, X.; Lin, T.; Li, R.; Bai, T.; Zhang, G; *Ind. Eng. Chem. Res*., **2012**, *51*, 3541-3549.

22. Doukeh, R.; Râpă, M.; Matei, E.; Prodan, D.; Győrgy, R.; Trifoi, A.; Banu, I; *Catalysts*, **2023**, 13.
23. Aryee, E.; Dalai, A.K.; Adjaye, J; *Front. Chem. Eng*., **2022**, 3.
24. Kim, Y.; Moon, D; *Cat. Surveys Asia*, **2019**, 23.
25. Kristiani, A.; Sudiyarmanto, S.; Aulia, F.; Hidayati, L.; Abimanyu, H; MATEC Web of Conferences, **2017**, *101*, 01001.
26. Dippong, T.; Goga, F.; Avram, A; *Studia UBB Chemia*, **2017**, 62, 165-176.
27. Hermida, L.; *Journal of Materials and Environmental Sciences*, **2018**, *9*, 2328-2333.
28. Stepan, E.; Enascuta, C.-E.; Oprescu, E.-E.; Radu, E.; Radu, A.; Galan, A.-M.; Vasilievici, G.; Lavric, V.; Velea, S; *Fuel*, **2016**, *172*, 29-36.
29. Enascuta, C.E.; Stepan, E.; Bolocan, I.; Bombos, D.; Calin, C.; Oprescu, E.-E.; Lavric, V.; *Waste Management,* **2018**, *75*, 205-214.
30. Matei. V., Juganaru.T., Bombos. D., Borcea A. F., Marinescu C., Ganea R., Bombos M. M., OSIM, **2010**, RO 126664 A2.
31. Calin, C.; Leostean, C.; Trifoi, A.R.; Oprescu, E.-E.; Wiita, E.; Banu, I.; Doukeh, R., Scientific Reports **2021**, 11, 19053.
32. Doukeh, R.; Trifoi, A.; Bombos, M.; Banu, I.; Pasare, M.; Bolocan, I.O.N, *Rev. Chim*., **2018**, *69*, 396-399.
33. Dan, M.; Mihet, M.; Lazar, D.; Muresan, L. *Studia UBB Chemia*, **2016**, *61*, 137-154.
34. Oprescu, E.-E.; Enascuta, C.-E.; Doukeh, R.; Calin, C.; Lavric, V.;*Renewable Energy*, **2021**, *176*, 651-662.
35. Doukeh, R.; Bombos, M.; Bolocan, I.; *Rev. Chim.*, **2019**, *70*, 2481-248.

STUDIA UBB CHEMIA, LXVIII, 3, 2023 (p. 99-114)
(RECOMMENDED CITATION)
DOI:10.24193/subbchem.2023.3.06

VALERIAN EXTRACT USED AS POTENTIAL CORROSION INHIBITOR FOR CARBON STEEL IN DIFFERENT MEDIA

George-Daniel DIMA[a], Oana-Tabita ȘERBOIU[a], Mircea Laurențiu DAN[a,*], Liviu-Virgil COSTEA[a]

ABSTRACT. The paper investigates the corrosion inhibition property of the Valerian (*Valeriana officinalis*) extract for carbon steel in acid and neutral solutions. The extracted natural compounds from plants have been reported in the literature as efficient corrosion inhibitors due to their stability to different environments, eco-friendly character, and their low cost. The usefulness of a different type of valerian species, in corrosion protection, by inhibiting the anodic oxidation reaction due to the improvement of the development of a passivating film, has been reported earlier for the *Valeriana wallichii* root extract in the corrosion of mild steel in different acidic media. Based on the latter findings, our studies have been performed in three different media, H_2SO_4, HCl and NaCl. An array of electrochemical techniques such as Tafel polarization, cyclic voltammetry, as well as chronopotentiometry have been employed to elucidate the corrosion behavior of carbon steel within the investigated media, containing various amounts of *Valeriana officinalis* extract. Quantum chemical calculations have been employed in order to assess the adsorption capacity of the mentioned extract onto the metal surface. The latter extract exhibits inhibitory effects in the studied media, even at small concentrations.

Keywords: *natural extracts; green corrosion inhibitor; Tafel linear polarization; molecular modelling, sustainability*

[a] *University Politehnica Timisoara, Faculty of Industrial Chemistry and Environmental Engineering, Laboratory of Electrochemistry, Corrosion and Electrochemical Engineering, 6 Pârvan, 300223 Timisoara, Romania*

** Corresponding author: mircea.dan@upt.ro*

INTRODUCTION

Corrosion is the deterioration of the metallic material due to the action of a corrosive environment. This causes problems of an economic nature and, from the consumer safety point of view, the destabilizing of the component materials, the durability over time of certain metallic tools and goods being seriously affected [1]. In recent times, new environmental friendly anti-corrosion protection methods have been developed based on the use of substances that adsorb themselves onto the metal surface, either physically by weak interactions, or chemically by covalent coordinative bonds between the empty orbitals of the metal and the non-participating electron pairs at the level of the heteroatoms of the component groups of the inhibitors [2].

Corrosion of steel used in the field of construction, namely that of the manufacture of fittings represents a major issue. Elements such as resistance structures of buildings or road infrastructure that interact with the sea water such as bridge piers, underwater tunnels involve huge secondary costs if a good anti-corrosion protection plan is not designed and implemented in advance [3]. One may mention examples of organic compounds that prevent mild steel from corroding in a neutral environment include some macrocyclic compounds that contain nitrogen, sulfur, and oxygen heteroatoms such as compounds with porphyrinic rings - porphyrin tetra benzoic acids and porphyrin-F-Pd [4]. In an acidic environment, heterocyclic compounds derived from the pharmaceutical field which are predominantly employed are Amoxicillin and Penicillin G [5], Cefazolin [6], diethylcarbamazine [7], active compounds from expired drugs such as Tobramycin [8], Atorvastatin [9], Nifedipine [10], amino acids containing a ring with a nitrogen heteroatom such as L-tryptophan, and its Schiff base [11, 12], respectively L-proline [13]. Recently, due to their natural availability and the relatively simple production methods, implying only a few steps of extraction and purification, starting from the raw plant, recent research has been aimed on corrosion inhibitors containing extracts from different plant components (root, stem, leaves, fruit or bark), due to their high solubility in different environments, especially in acidic ones. Each natural extract consists of a multitude of organic compounds such as amino acids, bioflavonoids, unsaturated fatty acids, which mostly have electron donor groups. Their inhibitory efficiency approaches that of many potentially toxic, synthetic organic inhibitors [14]. One of the main disadvantages regarding inhibitors based on plant extracts resides in their short shelf life. Over time and if stored in improper conditions they could be degraded by microorganisms and fungi, thus considerably reducing their inhibition efficiency [2]. The most common examples of green inhibitors for mild steel comprise extracts of *Nicotiana tabacum* in a corrosive environment of H_2SO_4 [15], the papaya

seeds extract in HCl [16], and lemon balm extract in HCl [17], respectively that of stem of pineapple extract as a mixed inhibitor for carbon steels in hydrochloric acid environment [18]. In all mentioned cases, the adsorption of substances from the extract to the metal is both physical and chemical. The main reason for the use of natural extracts as a corrosion inhibitor is the ease of patenting the method at the expense of other types of synthetic compounds, in relation to the impact on the environment or the increase in the resistance of some microorganisms in the case of use, for example of medicines. In the literature, the inhibitory properties of *Valeriana willichi* root extracts (Indian valerian) are reported [19], our research being oriented towards extracts from herbaceous plants from the Valerianaceae family, namely *Valeriana oficinalis*.

RESULTS AND DISCUSSION

Cyclic voltammetry

To gather initial information about the resistance to electrochemical oxidation/reduction of valerian tincture, as well as how the compounds present in the tincture influence the anodic and cathodic processes, a series of cyclic voltammetry tests were conducted. Figures 1a, b, and c show the results of cyclic voltammetry performed in the test solutions. The results in figure 1a, recorded in a sulfuric acid solution without valerian tincture, show typical peaks for a voltammogram in a strongly acidic environment. When the potential values become more negative than 0 V vs. $E_{Ag/AgCl}$ the cathodic process of reducing H^+ ions from the acid is observed, followed by an anodic peak indicating the oxidation of hydrogen on the platinum electrode surface. A very low intensity current level is observed in the potential range of + 0.5 V vs. $E_{Ag/AgCl}$ and + 1.50 V vs. $E_{Ag/AgCl}$, which is related to the development of the working electrode's surface's superficial layer of platinum oxides. A distinct cathodic peak can be seen around a potential value of -0.30 V vs. $E_{Ag/AgCl}$, which corresponds to the reduction process of the oxide layer's surface during its oxidation stage. Only the process of oxygen release in an acidic environment is documented at electrode potential values more positive than +0.40 V vs. $E_{Ag/AgCl}$ on cyclic curves. A modest current level of low intensity associated with the reduction of atomic oxygen or gaseous oxygen on the surface of the metal electrode can be recognized while scanning in the reverse direction of the potential range towards the starting point, the OCP value. The anodic process of oxygen formation and release on the platinum surface is inhibited by the addition of valerian tincture in the acid medium at

two concentrations, 2.5 mL L^{-1} and the highest concentration used in the experimental studies, 10 mL L^{-1}. This effect is seen by shifting the potentials associated with this process towards more positive values, while the cathodic processes corresponding to the reduction of H^+ ions and the release of hydrogen are unaffected. The pronounced anodic peak is recorded on the anodic branch at a potential value of approximately +1.75 V vs. $E_{Ag/AgCl}$ associated with the oxidation of chloride ions to atomic chlorine and their dimerization to chlorine gas on the surface of the platinum electrode on the cyclic curves in figure 1b drawn in the 0.5 M HCl solutions without and with the two additions of valerian tincture.

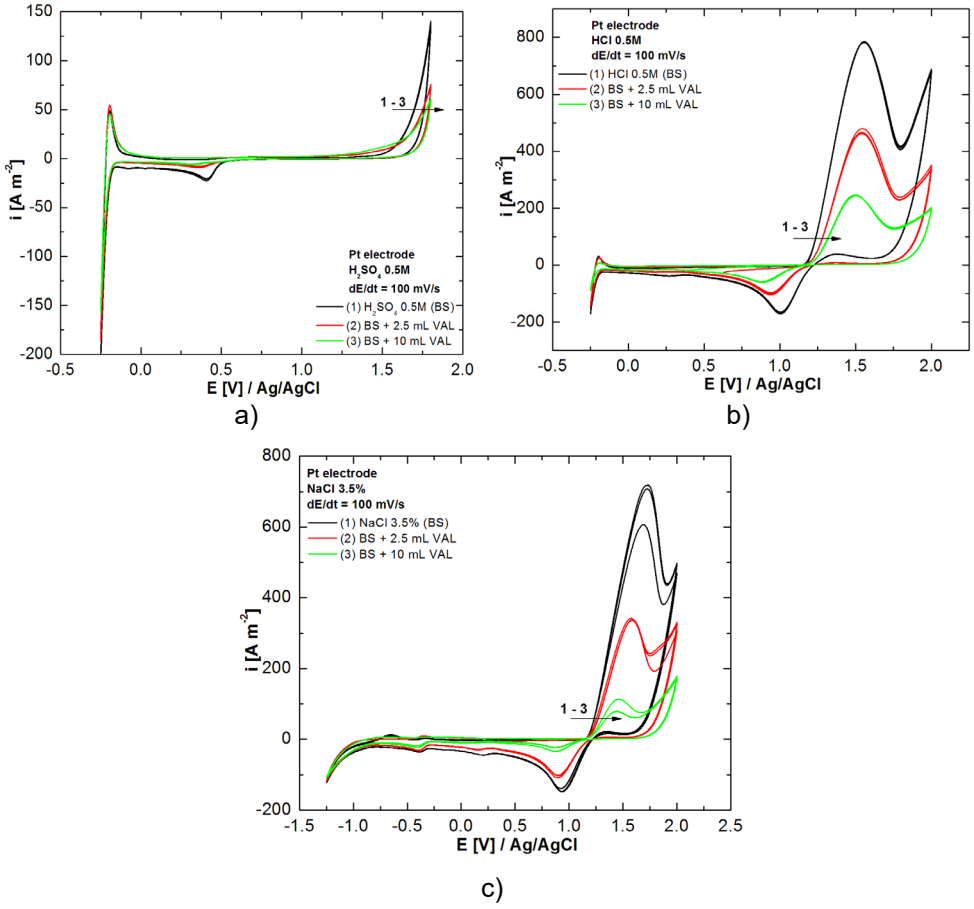

Figure 1. Cyclic voltammograms recorded on a platinum electrode in H_2SO_4 solution (a) HCl 0.5M (b) and NaCl 3.5% (c) in the absence and presence of different concentrations of valerian tincture, at a scan rate of 100 mV s^{-1}.

Because the value of the overpotential associated with the oxidation of chloride on the platinum electrode is lower than that associated with the competing process - the release of oxygen - this oxidation process occurs at potentials more negative than those corresponding to the oxidation of O^{2-} ions with the formation of atomic oxygen and then gaseous oxygen. Similar to those observed in the hydrochloric acid solutions are the cyclic voltammograms in figure 1c displayed in the 3.5% NaCl saline solutions without and with the two inhibitor concentrations of valerian tincture (2.5 and 10 mL L^{-1}). The cathodic peak at potential value -0.50 V vs. $E_{Ag/AgCl}$ which corresponds to the global initial stage in the conversion of H^+ ions to hydrogen atoms adsorbed on the platinum surface, is notable. Valerian tincture and its components are electrochemically stable over the entire potential range in which they were traced, according to the cyclic voltammetry data collected on the platinum electrode in the three corrosive environments. This means that they do not undergo electrochemical transformations (oxidation and reduction processes).

Chronopotentiometry studies – Open circuit potential determination

Figure 2 depicts the change in equilibrium potential for the working electrode in H_2SO_4 and HCl solutions of 0.5 M and 1 M, respectively. We can conclude that after 1 h, during which the electrode potential values were recorded, the electrochemical system had reached a quasi-stationary state, a state sufficient for initiating corrosion studies using the linear polarization method.

Table 1. Determination of E_{OCP} in solutions of H_2SO_4 0.5 M, HCl 0.5 M, respectively NaCl 3.5%

Electrode	$V_{Tincture}$ **[mL L^{-1}]**	**T [°C]**	E_{OCP} *[mV]/Ag/AgCl*		
			H_2SO_4 0.5 M	*HCl 0.5 M*	*NaCl 3.5%*
S355J2	0	25°C	-432	-435	-655
	1		-430	-429	-645
	2.5		-421	-427	-638
	5		-417	-422	-632
	10		-414	-418	-626

As a function of the valerian tincture concentration added to the corrosive medium, Table 1 shows the values of equilibrium potentials (open circuit potentials, or E_{OCP}) of the working electrode in the three electrolytes used as aggressive media.

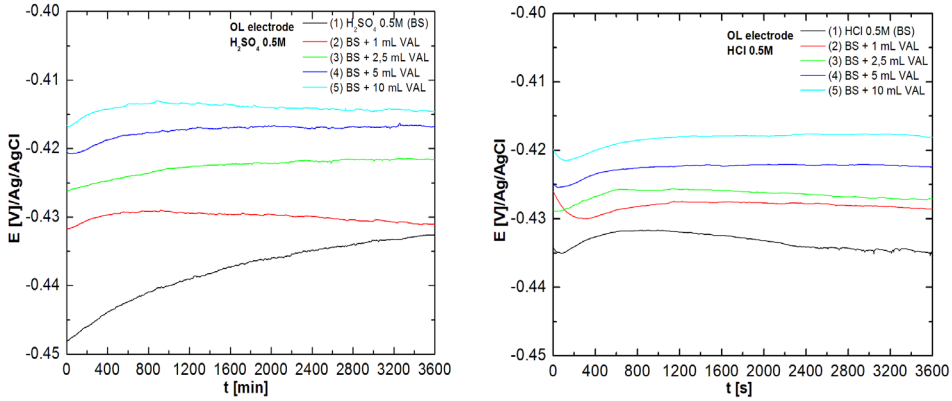

a) b)

Figure. 2. Evolution during 1 h of the equilibrium potential of the S355J2 type carbon steel electrode in solution in solution of H_2SO_4 0.5 M (a) HCl 0.5 M (b) with different inhibitor concentrations

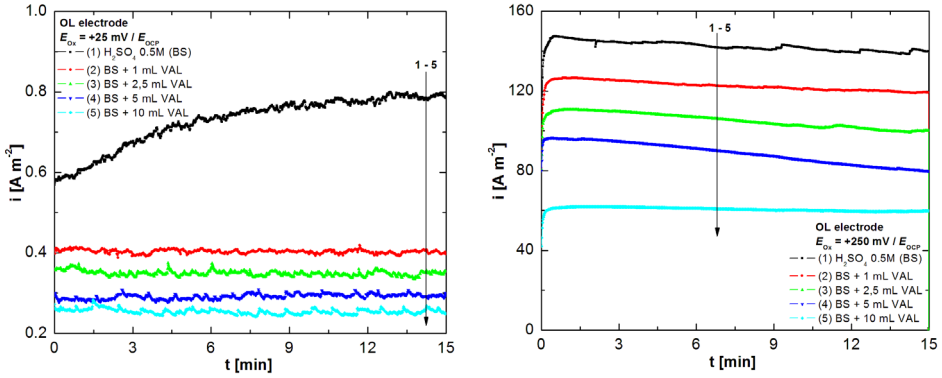

a) b)

Figure 3. Chronoamperograms in H_2SO_4 0.5 M for E_{Ox} = +25mV/E_{corr} (a), respectively for E_{Ox} = +250 mV/E_{corr} (b).

Table 2. Oxidation current density values recorded for 15 minutes in chronoamperometric determinations in H_2SO_4 0.5 M

Electrode	**Test solution**	***E*Oxidation**	
		+25 mV / E_{OCP}	+250 mV / E_{OCP}
		$i_{Oxidation}$ [A m^{-2}]	
S355J2	H_2SO_4 0.5 M (SB)	0.79	139
	SB + 1 mL L^{-1} VAL	0.40	120
	SB + 2.5 mL L^{-1} VAL	0.35	100
	SB + 5 mL L^{-1} VAL	0.29	79
	SB + 10 mL L^{-1} VAL	0.25	60

The E_{OCP} values in all three aggressive environments move towards slightly more positive values when the valerian tincture is added to the electrolyte, as the inhibitor concentration increases, as compared to the recorded carbon steel electrode potential value in solutions without valerian tincture. This variation of the E_{OCP} indicates that on the surface of the tested electrode made of carbon steel, organic molecules from the valerian tincture are adsorbed on the active sites, which form a protective layer that functions as a barrier against corrosion.

Chronoamperometry studies

Introduced as a method to study the corrosion processes of metals and alloys recently, from the perspective of the effectiveness of the use of corrosion inhibitors added in laboratory studies in various aggressive environments, the chronoamperometric method is based on the analysis of the time variation of the current under the conditions in which the electrode potential is kept at a constant value.

From the diagrams shown in Figure 3 a and b, the current density values corresponding to the oxidation of S355J2 type carbon steel samples in H_2SO_4 0.5 M solutions are shown in Table 2.

By examining the chronoamperometric data shown in the table above, one can see that as the amount of valerian tincture added to the H_2SO_4 0.5 M solutions increases, the values of the current densities corresponding to the oxidation of the S355J2 type carbon steel samples decrease. This decrease in current densities reflects a reduction in the values of corrosion rates as a result of the increased degree of adsorption of the tincture's inhibitory components on.

Corrosion studies by the linear polarization method

The three diagrams were recorded after nitrogen bubbling to remove oxygen from the test solution. In the event when the test electrolyte contains physically dissolved oxygen, this was done to avoid any possible side reactions that might occur at the electrode or on it.

Additionally, it was carried out after the electrode and the electrolyte solution had attained a particular equilibrium state.

In Figures 4a and b are showed the Tafel plots recorded on S355J2 carbon steel samples in the absence and presence of different valerian tincture concentrations added in the three corrosive environments.

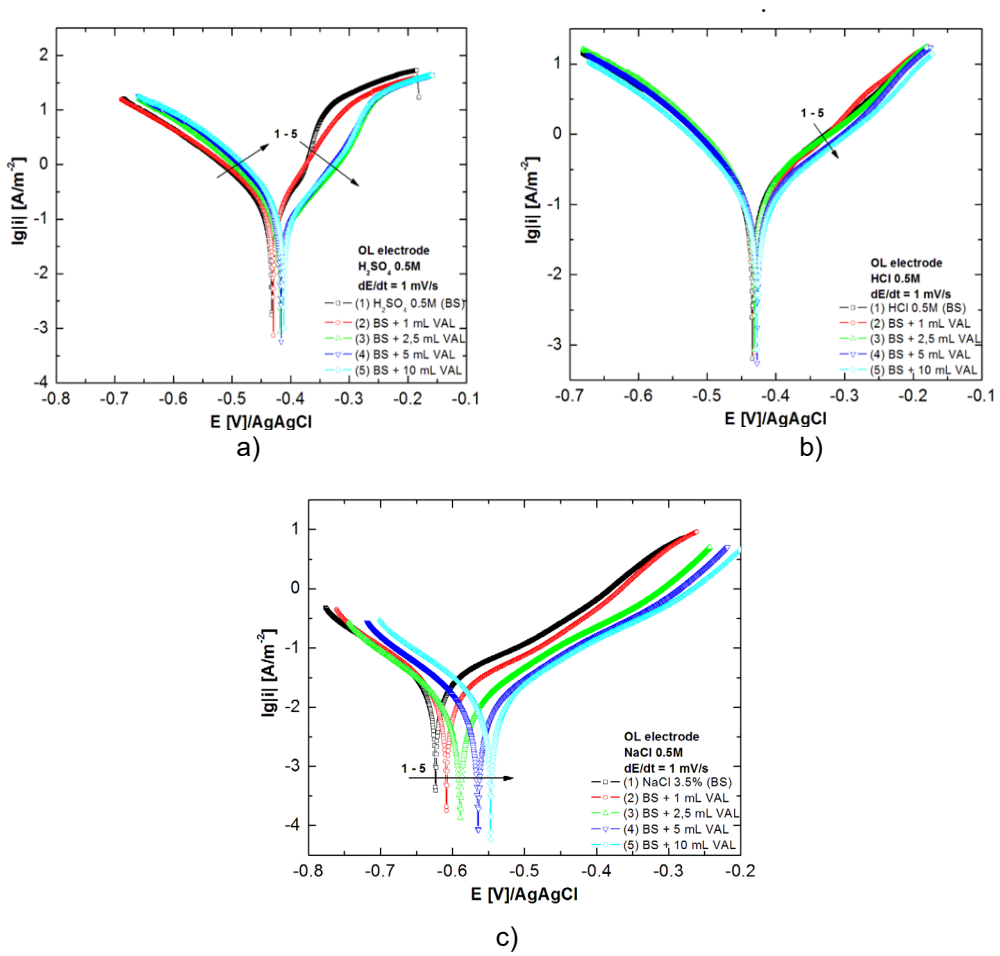

Figure. 4. Tafel polarization curves recorded, at 25°C, on S355J2 type carbon steel electrode in 0.5M H_2SO_4 (a), 0.5M HCl (b) and 0.5M NaCl (c) solutions in the absence/presence different valerian tincture concentrations.

The fitting of the linear polarization curves recorded for each determination, in order to calculate the parameters specific to the corrosion processes of the S355J2 type carbon steel samples are presented in Table 3.

Table 3. Electrochemical parameters determined by the Tafel method on S355J2 type carbon steel electrode in 0.5 M H_2SO_4, 0.5 M HCl and 3.5% NaCl solutions without and with the addition of valerian tincture, at 25°C.

Corrosion media	$V_{Tincture}$ [mL]	i_{corr} [μA cm^{-2}]	E_{corr} [mV]	$-b_c$ [mV dec^{-1}]	b_a [mV dec^{-1}]	R_p [Ω cm^2]	v_{corr} [mm y^{-1}]	IE [%]	θ
H_2SO_4 0.5 M	0	126.1	-432	118	73	155	3.62	-	-
	1	91.9	-429	98	64	183	2.14	27.12	0.27
	2.5	54.3	-422	73	60	263	1.46	56.94	0.57
	5	45.3	-418	56	55	266	1.06	64.08	0.64
	10	20.7	-412	44	49	486	0.97	83.58	0.84
HCl 0.5 M	0	128.7	-434	107	125	195	3.7	-	-
	1	93.8	-431	101	120	254	2.41	27.12	0.27
	2.5	59.3	-430	97	115	385	2.11	53.92	0.54
	5	40.4	-427	93	108	537	1.62	68.61	0.69
	10	22.5	-424	89	103	921	1.12	82.52	0.83
NaCl 3.5%	0	108.2	-658	68	85	152	0.205	-	-
	1	79.7	-623	61	69	176	0.186	26.34	0.26
	2.5	53.7	-602	54	58	226	0.161	50.37	0.50
	5	35.6	-571	49	48	296	0.138	67.10	0.67
	10	19.5	-557	48	43	505	0.115	81.98	0.82

The concentration of valerian tincture in the aggressive medium and its proportionality with the volume of tincture added are the defining factors for its inhibitory efficiency in the corrosion process of carbon steel S355J2 in H_2SO_4 medium.

Similarly, to the HCl and NaCl media, a decrease of corrosion rate is observed, followed, as is normal, by an increase in inhibitory efficiencies and an increase in inhibitor concentration.

Simultaneously, variations in polarization resistance are observed, with values ranging from a few hundred to 921 Ω in the case of the maximum inhibitor concentration.

According to the results in Table 3, valerian tincture acts as a corrosion inhibitor for the carbon steel used in the experimental studies of type S355J2 in aggressive sulfuric acid environments, HCl environments, and corrosive saline environments.

Molecular modelling

The extracts obtained from the root of the Valeriana Officinalis plant represent mixtures containing numerous compounds, their composition varying significantly depending on the obtaining method, seasonality, but especially on the geographical area of origin of the biological material. Since recent literature data reveal that the essential oils obtained from VO cultivated in the vicinity of our country are characterized by high contents of bornyl acetate ((1,7,7-trimethyl-2-bicyclo[2.2.1]heptanyl acetate)) and alpha fenchene (7,7-dimethyl-2 methylidenebicyclo[2.2.1]heptane) [22], the latter compounds have been subjected to further computational studies.

Electrochemical properties of various organic substrates are intrinsically linked to the electronic structure of their frontier orbitals, hence quantum chemical calculations of frontier orbital energies, could provide the necessary theoretical foundation to sustain the results obtained experimentally.

Quantum chemical analysis, used as a complementary technique to experimental studies, offers the possibility of elucidating the mechanisms underlying the phenomena of corrosion protection.

The energies of the frontier molecular orbitals (LUMO and HOMO respectively) as well as the energy difference (the so-called energy gap) $\Delta E = E_{LUMO} - E_{HOMO}$ have been calculated for the B3LYP optimized structures of the mentioned compounds in vacuum.

A low value of the energy of the LUMO orbital (the lowest unoccupied molecular orbital) suggests a more pronounced tendency of the organic substrate to accept electrons, while a higher energy value of the of the HOMO orbital (the occupied molecular orbital with the highest energy level) reflect the tendency of the organic molecule to lose negative electrical charges [23].

The tendency of an organic substrate to adsorb onto the metal surface (and thus to act as a corrosion inhibitor) is all the more pronounced the lower the value of the energy difference $\Delta E = E_{LUMO} - E_{HOMO}$.

Data in Table 4 shows that $E_{HOMO}(AF) > E_{HOMO}(BA)$, so alpha fenchene (AF) will present a more pronounced tendency to donate electrons to the metal.

The energies $E_{LUMO}(BA) < E_{LUMO}(AF)$ denote that bornyl acetate (BA) has a greater ability to accept electrons from the d orbital of Fe and the value $\Delta E = 0.599$ eV related to AF reflects the increased stability of the Fe-AF complex possibly formed on the metal surface.

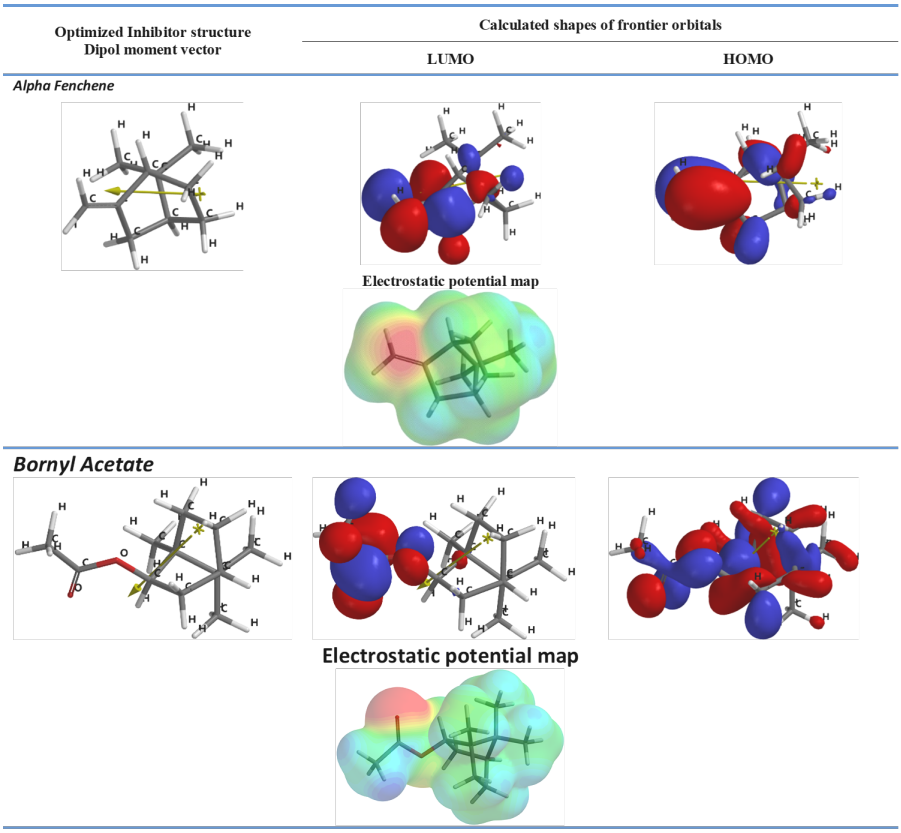

Figure 5. Frontier orbital profiles, dipole moment orientations and total charge densities mapped with electrostatic potential calculated for the optimized geometries of the two investigated main components of Valeriana officinalis extract

Given that the value of the ionization energy (IP) as well as that of the electron affinity (EA) can be estimated based on the energies of the frontier orbitals as per Koopmann's theorem (Eq. 1 and 2) [24, 25]:

$$E_{HOMO} = -IP \quad (1)$$

$$E_{LUMO} = -EA \quad (2)$$

we can calculate specific molecular descriptors, namely electronegativity (χ), chemical potential (μ), electrophilic index (ω). The higher the value of (χ), the lower the tendency of the substrate to give up electrons. The tendency to give up electrical charges to the base metal is more pronounced the higher the σ (molecular softness) parameter is, and respectively the lower the higher the η (molecular hardness) parameter is.

Table 4 Values of the parameters describing the global reactivity calculated for the main components of the valerian root extract

Global descriptors / eV	Substrate	
	Alpha Fenchene	**Bornyl Acetate**
Ionization potential (IP)	6.510	7.550
Electron affinity (EA)	0.520	0.160
Chemical potential (μ)	-3.515	-3.855
Electronegativity (χ)	3.515	3.855
Global hardness (η)	2.995	3.695
Global softness (σ)	0.167	0.135
Electrophilicity index (ω)	2.063	2.011
Electrodonating power (ω-)	4.195	4.400
$\Delta E = E_{LUMO} - E_{HOMO}$	5.990	7.390
Dipole moment (Debye)	0.930	2.660

The dipole moment of the inhibitor molecule quantifies the degree of separation of electrical charges in that molecule. Increased values of the molecular dipole moment favor adsorption phenomena on the metal surface. The anticorrosive protection capacity increases with the increase of the dipole moment of the molecule.

Data in Table 4 reveals that the polarity of BA (2.66 D) is much more pronounced, so we can conclude that the weight of BA in the anticorrosive effect exerted by the VO extract is primary [22].

CONCLUSIONS

Studies on the corrosion of S355J2 carbon steel were conducted in three environments: strong acid solutions (0.5 M H_2SO_4, 0.5 M HCl) and saline solution (3.5% NaCl). The Tafel method and linear polarization method were used to analyze the corrosion process, and the effect of valerian tincture was studied by cyclic voltammetry on a platinum electrode in these environments.

Results showed that valerian tincture significantly impacted the anodic processes of chloride ion oxidation and O^{2-} ion oxidation in all three environments but had no notable effect on the cathodic process of H^+ ion reduction. The adsorption of organic molecules from valerian tincture on the electrode suggests an electrostatic interaction between the tincture and the metal surface, contributing to the tincture's role as a corrosion inhibitor for S355J2 carbon steel in aggressive acid and saline environments.

EXPERIMENTAL SECTION

Materials

The corrosive media used in the experimental studies were prepared starting from pure reagent of high concentration by diluting with distilled water until the desired concentration was obtained, 0.5 M for the sulfuric acid solution, 0.5 M for the hydrochloric acid solution, respectively 3.5% for sodium chloride solution. Reactants used in the preparation stage were solutions of sulfuric acid (Merck 98%) and hydrochloric acid (Merck 37%) and sodium chloride p.a. (Merck). The corrosion inhibitor subjected to this study was valerian tincture – with a composition of 30% soft extract of valerian roots (Valeriana officinalis) and 70% vegetable glycerin); its inhibitory properties for the corrosion of carbon steel type S355J2 was analyzed in the three corrosive environments mentioned above.

Electrochemical methods

The electrochemical measurements were carried out in a cell with a configuration of 3 electrodes, the S355J2 steel working electrode, two graphite bars as counter electrodes and an Ag/AgCl reference electrode. The experimental determinations were recorded using the software of the BioLogics SP150N potentiostat/galvanostat, by acquiring the values of the oxidation current intensity over time at constant potential values (established according to E_{OCP}, at anodic polarization), the recorded variations being correlated with the corrosion rate of the metal sample subjected to tests in the 3 corrosive environments. The metal samples on which the corrosion tests were performed in the three aggressive environments were made of carbon steel bars (with a diameter of 1 cm) of type, the active surface of the tested samples being 0.785 cm^2. Before exposure to corrosion, the active surface of the working electrode was sanded using 800 to 2400 grit SiC paper, then washed with distilled water, subjected to ultrasonic cleaning, cleaned in acetone and then dried.

Before performing each experiment, the working electrode was stabilized for 60 minutes, following the evolution of the corrosion potential over time. In order to observe whether the valerian extract undergoes transformations in the potential window between the release of hydrogen or oxygen, cyclic voltammetry experiments were performed at valerian tincture concentrations of 2.5 mL L^{-1} and 10 mL L^{-1} respectively on the platinum electrode, starting from the open circuit potential. Next, the potentiodynamic polarization curves were obtained for inhibitor concentrations of 1; 2.5; 5 and

10 mL L^{-1}, on a potential range between -250 mV and +250 mV compared to E_{OCP}, at a polarization speed of 1 mV s^{-1}. Thus, in order to obtain more details about the kinetics of the corrosion process for the tested samples, chronoamperometric measurements were performed for 15 minutes at two different values of the oxidation potential value, +25 mV vs. E_{corr}, respectively +250 mV vs. E_{corr} in the most aggressive solution.

The corrosion parameters were obtained by fitting of the linear polarization curves recorded, using BioLogic Potentiostat SP-150 Software. Also, the polarization resistances (R_p) were calculated from the Stern-Geary equation (3) [22,27]:

$$R_p = b_a \cdot b_c / [i_{corr} \cdot 2.303 \cdot (b_a + b_c)] \quad (3)$$

where:

R_p is the polarization resistance, Ω cm^2;
b_a and b_c represents the anodic and cathodic Tafel slopes, V
i_{corr} is the corrosion current, A cm^{-2}.

In order to determine the inhibition efficiency from Tafel slope method was used the equation (4) [22,28]:

$$IE\ [\%] = [(i_{corr} - i_{corr(inh)}) / i_{corr}] \cdot 100 \quad (4)$$

where: i_{corr} and $i_{corr(inh)}$ are corrosion current densities in the absence and in the presence of the valerian tincture, A m^{-2}.

Molecular modelling

The first two most prevalent compunds present in the studied Valeriana officinalis extract (*i.e.* Bornyl acetate, BA and alpha Fenchene, AF) have been subjected to a conformational analysis and subsequent calculation of specific molecular descriptors. Geometries of *BA* and *AF* have been optimized in the gas phase. The specified molecular descriptors (frontier orbital energies, dipole moment, molecular hardness/softness, ionization energies, electron affinities, etc.) have been calculated by employing the Becke,3-parameter, Lee–Yang–Parr (B3LYP) [20,21] density functional method alonside the 6-31G* basis set.

ACKNOWLEDGMENTS

This work was supported by University Politehnica Timisoara.

REFERENCES

1. W. Kamaruzzaman, N. Nasir, N. Hamidi et al., *Arabian J. Chem.*, **2022**, 15(4), 103655.
2. H. Wei, B. Heidarshenas, L. Zhou, G. Hussain, Q. Li, K. Ostrikov, *Mat. Today Sustain.*, **2020**, 100044.
3. M. Harilal et al., *Const. Build. Mat.*, **2018**, *198*, 299-312.
4. I. Ahamad, M.A. Quraishi, *Corr. Sci.*, **2010**, *52*, 651–656.
5. G. Golestani, M. Shahidi, D. Ghazanfari, *Appl. Surf. Sci.*, **2014**, *308*, 347–362.
6. J. Aldana-González, A. Espinoza-Vázquez, M. Romero-Romo, J. Uruchurtu Chavarin, M. Palomar-Pardavé, *Arabian J. Chem.*, **2019**, *12*, 3244–3253.
7. I. Ahamad, R. Prasad, M.A. Quraishi, *J. Solid State Electrochem.,* **2010**, *14*, 2095– 2105.
8. R.G. Sundaram, G. Vengatesh, M. Sundaravadivelu, *Surf. Interf.*, **2021**, *22*, 100841.
9. P. Singh, D.S. Chauhan, K. Srivastava, V. Srivastava, M.A. Quraishi, *Int. J. Ind. Chem.*, **2017**, *8*, 363–372.
10. F. Abeng, V. Anadebe, V. Idim, M. Edim, *South African J. Chem.*, **2020**, *73*, 125–130.
11. M. Parveen, M. Mobin, S. Zehra, R. Aslam, *Sci. Rep.*, **2018**, *8*, 1–18.
12. K. Zhang, W. Yang, X. Yin, Y. Chen, Y. Liu, J. Le, B. Xu, *Carbohydrate Polym.*, **2018**, *181*, 191–199.
13. J. Haque, V. Srivastava, C. Verma, M.A. Quraishi, *J. Mol. Liq.*, **2017**, *225*, 848–855.
14. E. Berdimurodov, I. Eliboyev, K. Berdimuradov, A. Kholikov, K. Akbarov, O. Dagdag, M. Rbaa, B. El Ibrahimi, D. Kumar Verma, R. Haldhar, N. Arrousse, *Carbohydrate Polym.*, **2022**, *292*, 119719.
15. M.A. Asaad, M. Ismail, A. Khalid, *J. Teknologi*, **2018**, *80 (6)*, 53-59.
16. S. Paul, I. Koley, *J. Bio-Tribo-Corr.*, **2016**, 2, 1e.
17. A. Dehghani, G. Bahlakeh, B. Ramezanzadeh, *J. Taiwan Ins. Chem. Eng.;* **2019**, 102, 349e377.
18. Mobin M., Basik M., Aslam J. *Measurement*, **2019,** *134*, 595-605.
19. R. Haldhar, D. Prasad, A. Saxena, P. Singh, *Mat. Chem. Fron.,* **2018**, 2(6).
20. A.D. Becke, *J. Chem. Phys.*, **1993**, *98*, 5648-5652.
21. C. Lee, W. Yang, R.G. Parr., *Phys. Rev. B - Condensed Matter Mat. Phys.*, **1988**, *37*, 785-789.
22. A. Raal, E. Arak, A. Orav, T. Kailas, M. Müürisepp, *J. Essential Oil Res.*, **2008**, *20*, 524-529.
23. A. Kellenberger, D.A. Duca, M.L. Dan, M. Medeleanu, *Materials*, **2022**, *15*, 2918.
24. A. Raal, E. Arak, A. Orav, T. Kailas, M. Müürisepp, *J. Essential Oil Res.*, **2008**, *20*, 524-529.

25. R. Haldhar, D. Prasad, L.T.D. Nguyen, S. Kaya, I. Bahadur, O. Dagdag, S. Kim, *Mat. Chem. Phys.*, **2021**, *267*, 124613.
26. H.A. Kramers, C.C. Jonker, T. Koopmans, *Zeitschrift für Physik*, **1933**, *80*, 178-182.
27. M.L. Dan, A. Kellenberger, D.A. Duca, N. Vaszilcsin, C.M. Craciunescu, I. Mitelea, A. Ercuta, S. Lædre, T. Khoza, *Materials*. **2023**, *16(4)*,1501.
28. N. Vaszilcsin, A. Flueras, D.A. Duca, M.L. Dan, *Studia UBB Chem*, **2019,** *64(3)*, 17-32.

STUDIA UBB CHEMIA, LXVIII, 3, 2023 (p. 115-127)
(RECOMMENDED CITATION)
DOI:10.24193/subbchem.2023.3.07

UTILIZING PLASTIC WASTE MATERIALS IN GEOTECHNICAL ENGINEERING: A SUSTAINABLE SOLUTION FOR ENVIRONMENTAL CHALLENGES

Ana-Maria URIAN[a], Emese GÁL[b,*], Liliana-Antonela BIZO[b], Ovidiu NEMEȘ[a,*], Nicoleta Maria ILIEȘ[c], Andor Csongor NAGY[c]

ABSTRACT. This work evaluates the chemical impact of polyethylene terephthalate (PET) as plastic waste material used in clayey soil improvement. The purpose of this work is to study the behaviour of PET added in different percentages in soil, and how it affects the chemical composition of soil by applying rapid ageing cycles. The thermal stability of the clay-PET mixtures using the thermogravimetric method was studied, and the impact of PET quantity on pH was measured. To detect the migration of PET degradation products to the soil gas chromatography with mass spectrometry (GC-MS) was used. The GC-MS analysis results indicate the presence of DIBP, the concentration increased proportionally with the amount of PET added to the clay. The thermogravimetric analysis shows a thermal degradation of the polymeric chain starting from 200 °C.

Keywords: *soil, PET waste materials, thermal stability, GC-MS analysis, additives migration*

[a] *Technical University of Cluj-Napoca, Faculty of Materials and Environmental Engineering, 103-105 Muncii Ave, RO-400641 Cluj-Napoca, Romania*
[b] *Babeş-Bolyai University, Faculty of Chemistry and Chemical Engineering, 11 Arany Janos Ave, RO-400028, Cluj-Napoca, Romania*
[c] *Technical University of Cluj-Napoca, Faculty of Civil Engineering, 15 Constantin Daicoviciu Ave, RO-400020 Cluj-Napoca, Romania*
* *Corresponding authors: emese.gal@ubbcluj.ro; ovidiu.nemes@imadd.utcluj.ro*

INTRODUCTION

Finding innovative and sustainable solutions to the world's problems of plastic waste pollution and soil degradation has become a top priority. Geotechnical engineering and soil improvement present unique opportunities to address both issues simultaneously. As the world faces an escalating environmental crisis caused by plastic waste pollution, finding long-term solutions to this problem has become critical. Soil is a natural resource, providing a foundation for agriculture, infrastructure, and ecosystems. The foundation of any land-based system is critical, and it must be strong for the system to function properly. Some soils cannot withstand heavy loads due to their low bearing capacity. The utilization of various plastic waste materials to improve soil properties has gained traction as an eco-friendly and sustainable approach. In order to fix this issue, the soil must be treated with various stabilizers such as cement, furnace slag, fly ash, limestone fines, bitumen, plastic waste, and so on. It is defined as the process of improving soil properties through physical or chemical treatments, as well as the blending and mixing of other materials with the soil [1]. Plastic waste that would otherwise take hundreds of years to degrade can be given a new purpose, thereby reducing its impact on ecosystems and mitigating its contribution to climate change. By diverting plastic waste from traditional disposal methods, engineers can contribute to a cleaner environment and lower greenhouse gas emissions associated with plastic degradation [2].

Various types of plastic waste, including high-density polyethylene (HDPE) and polypropylene (PP), can be transformed into geosynthetics, such as geogrids and geotextiles. These materials provide improved engineering properties, such as increased tensile strength, soil stabilization, and improved erosion control [3]. Geosynthetics reinforce the soil structure and are especially useful in infrastructure projects like roads, embankments, and retaining walls [4]. These materials, possess advantageous engineering properties, properly processed, and mixed with soil, can improve properties like shear strength, compressibility, and permeability, making it beneficial in various geotechnical applications. Plastic waste can be used as a lightweight fill material, helping to reduce the overall weight of a structure or project. This application is especially useful when there are weight restrictions or the need to relieve stress on weak soils, minimizing settlement and the risk of soil failure in construction projects [5].

Plastic waste acts as a geogrid, reinforcing the soil matrix and preventing erosion, making it valuable for slope protection and land reclamation projects [6]. When LDPE is mixed into soil, it acts as a water reservoir, reducing

evaporation and preventing moisture loss in arid areas. This feature is useful in agriculture, landscaping, and afforestation efforts because it promotes plant growth and aids in drought resistance [7].

One of the primary concerns with using plastic waste materials in geotechnical engineering is their long-term durability. Exposure to environmental factors like UV radiation and chemical degradation can lead to a reduction in their effectiveness over time. Research is ongoing to develop methods to enhance the durability of plastic waste-based geotechnical solutions [8]. Research about the strength properties of subgrade soil reinforced by recycled Polyethylene terephthalate fibers in combination with fly ash was carried out. The optimal properties of subgrade soil were acquired at 1.2 % recycled Polyethylene terephthalate fibers and 15 % fly ash [9]. The inclusion of plastic chips of waste bottles into the sand increased the shear strength of the sand. The optimum percentage of the plastic chip was found to be 0.75% [10]. The California bearing ratio (CBR) and the shear strength of sandy soil were improved by mixing recycled polyethylene terephthalate chips in three different ratios 2%, 4%, and 8 % [10].

It has been established that using plastic waste chips as a soil stabilizing material for subgrade soil in highway subbase construction can significantly reduce the base layer thickness of flexible pavement [11].

The influence of polyethylene waste admixture or cement on the properties of soil was studied by Nicoleta-Maria Ilies et al. (2017). Several tests were carried out using 2%, 4%, 6%, and 8% polyethylene material or cement. They concluded that using waste polyethylene material in soil stabilization is an environmentally friendly method. By incorporating 4% of polyethylene waste into the soil, significant results were observed; however, the improvement was not as substantial as the results of cement admixture, however, this method results in a larger carbon footprint, making it less environmentally friendly. [12,13].

Significant increases in the soil's shear strength (SS) parameters were obtained by mixing small strips of plastic waste in the soil in 0.5%, 1%, and 2% by weight of dry soil [14].

In this paper, we aim to evaluate, using appropriate and simple methods, the effect of recycling plastic materials as reinforcement material for expansive soil stabilization in order to improve and achieve the properties required for construction works. For instance, the chemical impact of using recycled plastics, in different proportions, on soil characteristics was evaluated. The experimental tests that were carried out and the results obtained are presented.

RESULTS AND DISCUSSION

The use of plastic waste materials in geotechnical engineering is a current topic, with several specialist studies in this direction. The improvement of soil by adding various plastic waste materials (including polyethylene terephthalate), in different forms, in order to increase its physical and mechanical characteristics has been studied.

Following the encouraging results of researchers on the improvement of soils with plastic waste materials, this paper studied the behaviour of PET in different percentages used in a clayey soil, respectively how it affects the analysis of its chemical composition by applying rapid aging cycles. In order to follow the chemical degradation of PET in the soil under normal atmospheric conditions, different samples were achieved. The percentages of PET used for improvement were 2%, 4% and 6%, reported to the dry weight of the clay. For a better identification of PET degradation products in the soil, depending on the freeze-thaw cycles (Table 1), the chemical composition of PET was taken into account. PET is a high-molecular-weight thermoplastic, semi-crystalline polymer, obtained from the reaction between terephthalic acid and ethylene glycol. The acetaldehyde, formaldehyde, 2,4-di-tert-butyl-phenol (2,4-dtBP), and bis(2-hydroxyethyl) terephthalate are the main compounds released from PET due to the UV sunlight and high temperature. The phthalates, namely benzyl butyl phthalate, bis(2-ethylhexyl) phthalate (DEHP), dibutyl phthalate, and di-isobutyl phthalate, as plasticizers, can be identified as degradation compounds [15].

Thus, 4 samples named Cl, Cl_{2PET}, $Cl_{4PET,}$ and Cl_{6PET} were obtained. These were made in the laboratory, by mixing 2000 g of clay with 2%, 4%, 6% PET (reported to the dry weight of the clay). The mixtures have been brought to the optimum water content (OWC) of 18%. Cylindrical samples with a diameter of 10 cm and a height of 10 cm were collected from the Proctor apparatus. The samples have been introduced into the climatic cabinet and have been subjected to variable temperature and humidity conditions. The details of the composition, obtaining procedure and mechano-physical characteristics are given in Table 1.

In order to detect the migration of PET degradation products to the soil, gas chromatography coupled with a mass spectrometer was used. To identify potential migrants in plastic packaging materials, solvent extraction is commonly used, followed by chromatographic separations and mass spectrometric detections. Samples (plastics and clay, respectively clay mixed

with different percentages of PET) were kept in a paper bag, to exclude the contamination from the packing bag. Recycled PET materials were analyzed before and after mixing with clay. The plastic materials were chopped into small pieces (~0.5 x 0.5 cm). The extraction process is critical for determining plasticizers in polymers prior to analysis. Soxhlet extraction [16,17] and ultrasonic-assisted extraction [18] are two commonly described procedures for extracting these organic compounds from polymeric matrices. Microwave irradiation has recently been used in the field of sample preparation because it is a simple and quick methodology [19].

Table 1. Composition of clay-PET mixtures and conditions of applied rapid ageing cycles

Samples code	Composition	Freezing-thawing cycles	Temperature range
CI	Clay + 18% water	-	-
CI_{2PET}	Clay + 18% water + 2% PET	15	-10 °C ÷ +40 °C
CI_{4PET}	Clay + 18% water + 4% PET	15	-10 °C ÷ +40 °C
CI_{6PET}	Clay + 18% water + 6% PET	15	-10 °C ÷ +40 °C

PET sample (0.5 g) was weighed, placed in a 100 mL conical flask with a glass top, and extracted with dichloromethane (DCM) (2 × 10 mL) by ultrasonic assisted extraction (UAE) for 30 min at 25 °C. The extracts were combined and evaporated to dryness under 40 °C by a rotary evaporator. The concentrated mixture was redissolved in 1.5 mL DCM and subjected to GC-MS analysis. The extraction of each sample was carried out in triplicate.

Analysis of PET/ PET with clay samples by GC-MS: a volume of 2 µL of sample concentrated extract was injected in splitless mode into a gas chromatograph (GC-2010) from Shimadzu Japan, coupled with a mass spectrometer QP 2010 PLUS. The GC was equipped with a capillary column ZB5-MSplus (Phenomenex, 30 m length × 250 µm inner diameter × 0.25 µm film thickness). The carrier gas was He at 0.8 mL/min, injection temperature 220 °C. The oven temperature program began with an initial temperature of 50 °C for 10 min, and then the temperature was increased at a rate of 20°C/min to 310 °C and then maintained for 20 min. The mass spectrometer parameters used for the identification of chemical compounds were as follows: electron impact ionization; electron energy, 70 eV; with an acquisition range (m/z) from 35 to 800 in scan mode, at an acquisition rate of 500 ms, ion

source, and interface temperature 220 °C. The resultant compounds were identified by matching their mass spectra to the NIST (NIST 27, 147 libraries), WILEY library database (>90% match).

The results showed the presence of several chemical compounds in the PET samples studied, chemicals that are present in large quantities are 1,4-benzenedicarboxaldehyde, hexadecenoic acid, long alkyl chain (eicosane, tetracosane, heneicosane). Lubricants are a class of additives that are used to reduce friction between the equipment surfaces and the polymer, allowing the plastic to flow over and through the equipment and keeping it from sticking to the surfaces [20]. Carboxylic acids, their esters and amides, polyethylene waxes, paraffin, stearates, and silicones are the most common lubricants used in plastic packaging materials. Lubricants can generally be added to plastic resin or applied externally. Hexadecanoic acid and octadecanoic acid were found in all analyzed samples, indicating their widespread use as lubricant main components in the samples studied [21]. Carboxylic acids are generally recognized as safe (GRAS), and EU regulations allow them to be used as additives or polymer production aids.

Plasticizers are used to improve the flexibility, extensibility, and processability of plastic packaging materials [22]. One plasticizer was discovered in this study, 1,2-benzenedicarboxylic acid, bis(2-methylpropyl) ester (DIBP).

PET samples (PET1 and PET2) used in these tests were extracted by UAE and analyzed based on the method described above. The major compounds found were terephthalaldehyde, terephthaldehidic acid, hexadecenoic and octanoic acid (Figure 1). In further experiments, we used the mixture obtained by mixing the two PET samples.

Analysis of starting clay-PET mixture in different percentages was measured (Figure 2). It can be observed that the quantity of used PET has no or has a small influence on the chemical composition of the clay. In the chromatogram of the sample with a 6% PET - clay mixture presents of lubricants can be observed, hexadecanoic acid, octadecanoic acid, and aromatic carboxylic acids.

After applying the aging cycles, in the chromatograms of samples can be observed a higher number of peaks (Figure 3), which can be attributed to degradation products from used PET plastic wastes, respectively different additives which have been migrated to the clay. The chromatograms of the three samples are similar, but differences can be observed in the concentration of the separated compounds. The higher concentration for DIBP (retention time 20.12 min) was found in sample 6% (Figure 4).

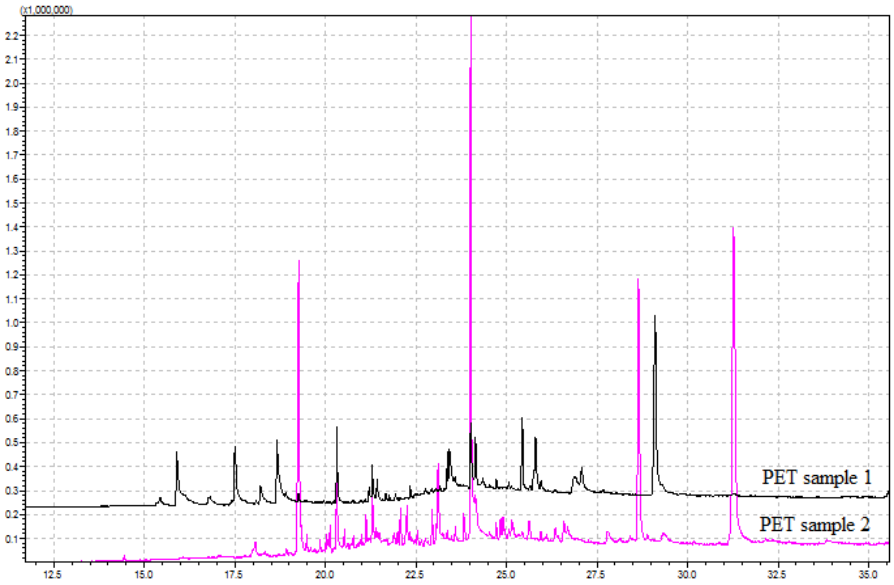

Figure 1. Gas chromatogram of used plastic waste PET (bottles used for water, soft drinks, and beer).

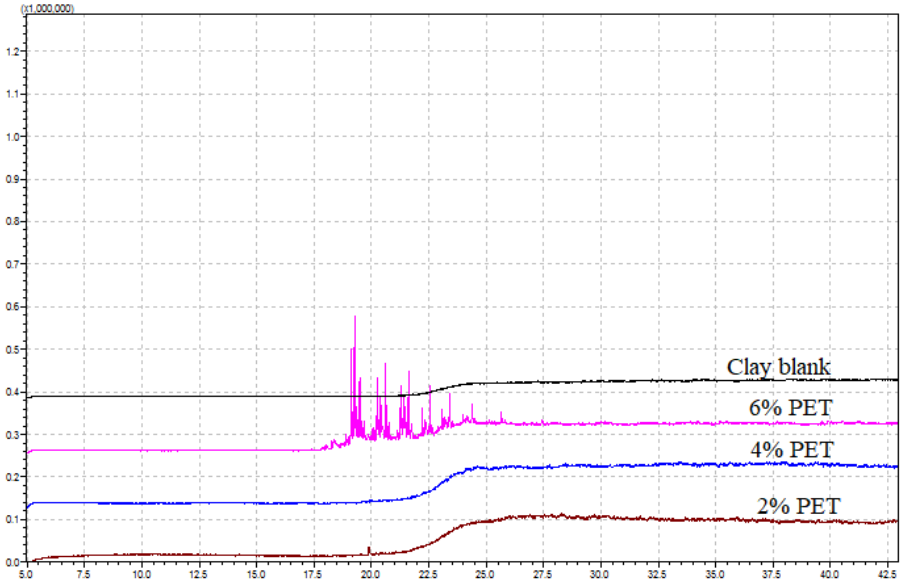

Figure 2. Gas chromatograms of clay samples with different percentages of chopped PET after mixing, before aging cycles.

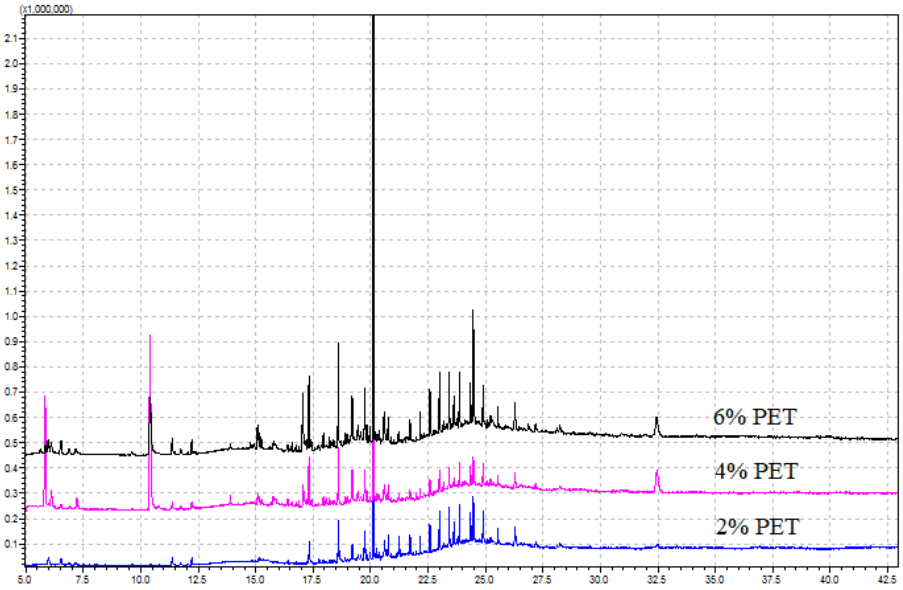

Figure 3. Gas chromatograms of the clay-PET mixtures after applying the aging cycle.

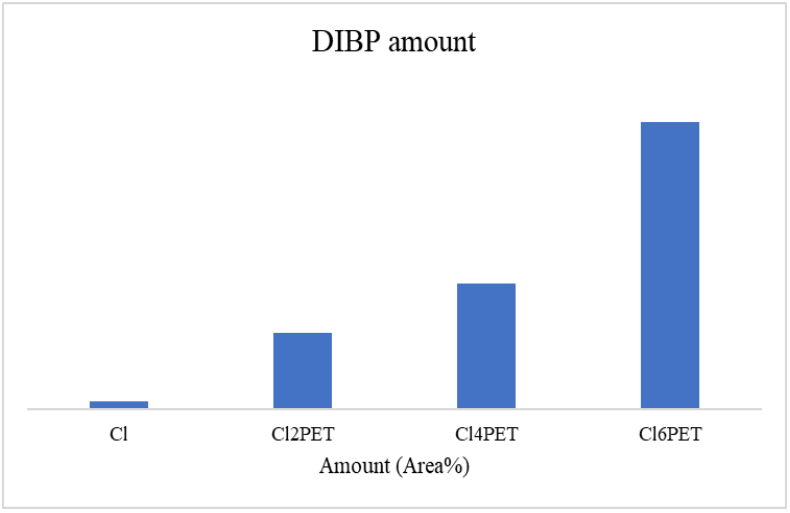

Figure 4. Graphic representation of the amount of DIBP in the aged samples, resulted from GC-MS analysis.

Also, diethylene glycol (10.39 min) can be found in higher concentrations in samples 4% and 6%. Long-chain alkanes are also present in all samples: tetradecane (17.31 min), pentadecane (18.60 min).

From a qualitative point of view, it can be mentioned that the chromatograms of the aged samples with different quantities of PET presented a higher number of peaks compared to the chromatograms of the starting clay-PET samples.

The next test determined the pH value of clayey samples. The test was conducted using the apparatus Mettler Toledo, FiveEasy20, 0 - 14 pH. The pH values can be observed in Table 2. A proportional increase in the pH value was observed, as the amount of PET added for improvement increased.

Table 2. The pH value for the clay and clay – PET samples, after applying the aging cycles

Samples code	Cl	Cl_{2PET}	Cl_{4PET}	Cl_{6PET}
pH value	6.80	6.82	7.28	7.56

To investigate the thermal stability of the PET - clay samples, thermogravimetric analysis was performed.

The TG weight loss curves and first derivative DTG curves for reference PET and the PET from PET-clay matrix samples are presented in Figure 5.

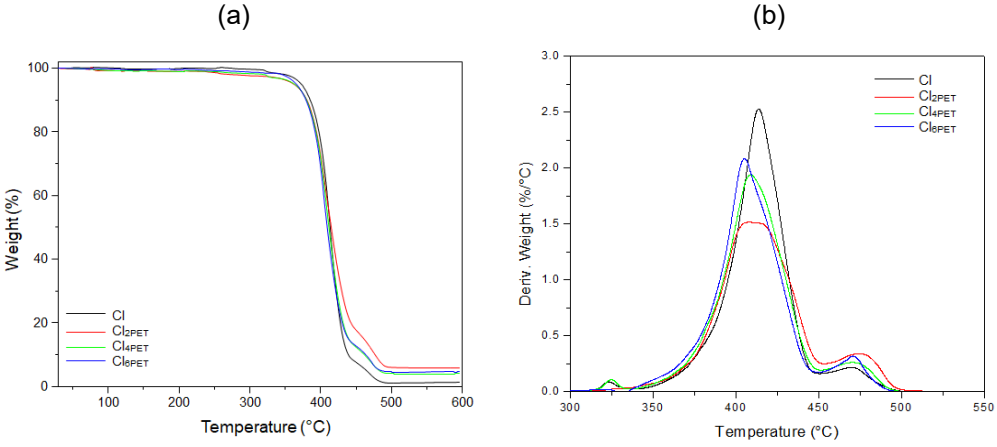

Figure 3. (a) Thermogravimetry (TG) and (b) its derivative (DTG) curves of PET, analysed from matrix clay-PET.

The curves present variations in the thermal stability among the samples. As seen from the figure the samples exhibit a two-step decomposition during TG analysis. The first step of decomposition for reference PET is due to the overlapping of two decomposition processes: the first process (30-430 °C) is mainly due to the degradation of the polymer chain through the end group-initiated mechanism and the second degradation process is due to the thermal degradation of the products formed during first decomposition process [23,24]. The second degradation step for reference PET (P3) in the temperature range 430-550 °C is due to the decomposition of thermally stable species formed during the first degradation step which could be cross-linked carbonaceous structures. In the case of PET-clay samples, the first step of decomposition took place similar to reference PET. The DTG curves revealed that complete thermal degradation occurs in two steps for all samples, with a small difference if compared to pure PET. The common step from 350 °C to 450 °C is attributed to the decomposition and carbonization of PET chains, while the second step for PET over 450 °C might be caused by the decomposition of thermolabile fragments produced in the first step. It can be stated that no significant difference in mass loss, ~ 5%, was observed between reference PET and PET analysed from 2, 4 and 6% PET-clay mixture. The TGA weight loss curves and first derivative TGA curves for reference clay and the clay analyzed from the PET-clay mixture are presented in Figure 6.

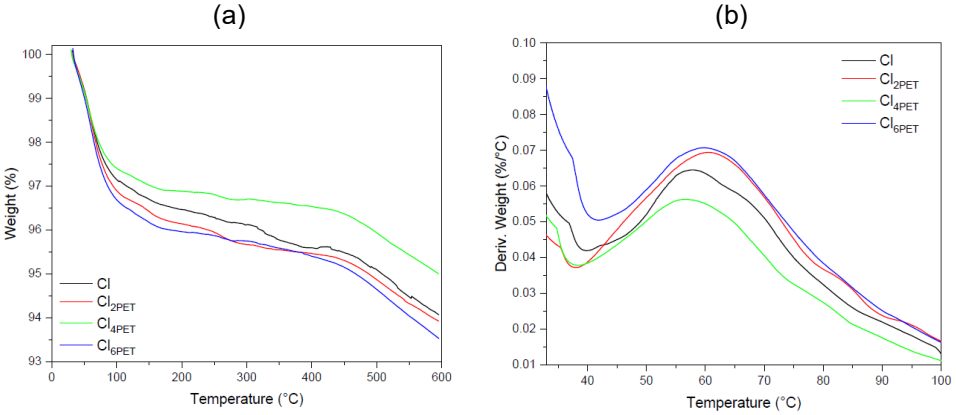

Figure 4. (a) Thermogravimetry (TG) and (b) its derivative (DTG) curves of clay, analysed from matrix clay-PET.

The mass loss of ~ 4 wt% corresponding to surface water can be observed in the temperature range 30-100 ºC, and the chemical water mass loss (400-600 ºC) was around ~ 2 wt%.

CONCLUSIONS

Improving soil with plastic waste materials is a topic that is increasingly capturing the attention of researchers. This method attempts to solve a part of the plastic waste pollution problem by reusing plastic waste materials in soil improvement.

This study investigated the migration of the chemical components from PET degradation in a clay improved with different percentages.

The clay - PET samples were subjected to variable humidity and temperature conditions in a climatic cabinet, similar to those in situ. GC-MS analysis was carried out on natural state clay and clay improved with 2%, 4%, and 6% PET. The results indicated the presence of DIBP in all four samples analysed. The presence of DIBP increased proportionally with the amount of PET added to the clay. As the percentage of PET added to the clay increased, the quantity of phthalate in the soil also increased, lubricants were also detected in the sample with higher PET quantity.

The thermogravimetric results highlight thermal stability of clay- PET mixture in the normal atmospheric conditions. The thermal degradation of polymeric chain was observed starting from 200 °C.

In conclusion, soil improved with plastic waste materials can be used, from a chemical point of view to increase the geotechnical properties of soil. This is a positive aspect that solves the problem of soils with unsuitable characteristics for foundation. Moreover, this improvement also solves a small part of the plastic waste pollution problem.

EXPERIMENTAL SECTION

The clayey-PET samples were made in the laboratory at the optimum water content (OWC) of 18%. Cylindrical samples with a diameter of 10 cm and a height of 10 cm were collected from the Proctor apparatus. These were introduced into the climatic cabinet (CONTROLS / 10-D1428/A) and subjected to 15 freezing-thawing cycles (-10 °C to +40 °C) in variable humidity conditions (up to 90%).

After the freezing-thawing cycles, approximately 10 grams of soil were collected from the unimproved clay and from each clay-PET sample. The amount of soil was ground and sieved to separate the PET from the soil and then weighed in Erlenmeyer glasses.

Over each sample was added 5 mL of dichloromethane. The samples were left in the ultrasound apparatus for 15 min. The organic solution was gravitationally filtered, and then evaporated in a rotary evaporator under vacuum at a temperature of 35 °C.

The samples were taken up in 200 µL of dichloromethane and were subjected to GC-MS analysis.

GC-MS analysis was carried out with a Shimadzu QP2010 Plus apparatus with an automatic injector AOC-20i, a ZB5MS Plus column, 30m x 0.25mm, 0.25µm, injection temperature – 220 °C, split injection mode, split ratio 20, injection volume 1 µL. The gas flow was 0.8 mL/min (He gas, 6.0), the initial temperature of the column was 50 °C. This temperature was maintained for 10 min, after which the column was heated to 310°C at 20°C/min. The column was left at this temperature for 20 minutes. The temperature of the ion source of the mass spectrometer was 220 °C and the interface temperature was also 220 °C. The analysis time was 43 minutes, the recording being made with the scan method (scanned between 35-800 m/z).

The thermogravimetric measurements were conducted on an SDT Q600 (USA) device from T.A. Instruments. Data on thermogravimetry (TG), and its derivative (DTG) curves, were simultaneously acquired under the following measurement conditions: heating from laboratory temperature to 600 °C, at a heating rate of 10 °C/min, under normal air atmosphere, using alumina crucibles.

ACKNOWLEDGMENTS

Financial support from the Project “Network of excellence in applied research and innovation for doctoral and postdoctoral programs / InoHubDoc”, project co-funded by the European Social Fund financing agreement no. POCU/993/6/13/153437 is greatly acknowledged by the author A. M. Urian.

REFERENCES

[1] W. Abu Jadayil, M. R. N. M. Qureshi, R. Ajaj, E. Aqil, G. Shawahin, H. Anver, S. Aljeawi, *Sustain*. **2022**, *14* (24), 16719.
[2] S. A. Al-Haddad, F. H. Al-Ani, M. Y. Fattah, *Appl. Sci*. **2022**, *12* (23), 12304.
[3] G. L. S. Babu, S. K. Chouksey, *Waste Manag*. **2011**, *31* (3), 481–488.
[4] F. Tanasa, M. Nechifor, M.-E. Ignat, C.-A. Teaca, *Text*. **2022**, *2(2)*, 189–208.

[5] A. I. Almohana, M. Y. Abdulwahid, I. Galobardes, J. Mushtaq, S. F. Almojil, *Environ. Ch.* **2022**, *9*, 100626.
[6] K. Malicki, J. Górszczyk, Z. Dimitrovová, *Mat*. **2021**, *14* (23), 7264.
[7] M. Abukhettala, M. Fall, *Transport. Geot*. **2021**, *27*, 100472.
[8] N. Taghavi, W.-Q. Zhuang, S. Baroutian, *J. Environ. Chem. Eng*. **2021**, *9* (6), 106464.
[9] B. Mishra, M. Kumar Gupta, *Constr. and Buil. Mat*. **2018**, *190*, 95–107.
[10] R. E. Farah, Z. Nalbantoglu, *SN Appl. Sci.* **2019**, *1* (11), 1340.
[11] B. A. Mir, in *Sust. Ci. Eng. Prac.* (Eds: V. S. Kanwar, S. K. Shukla), Vol. 72, Springer Singapore, Singapore **2020**.
[12] N.-M. Ilieş, A.-P. Cîrcu, A.-C. Nagy, V.-C. Ciubotaru, Z. Kisfaludi-Bak, *Proc. Eng*. **2017**, *181*, 444–451.
[13] A.-M. Trimbitas (Urian), O. Nemes, N. M. Ilies, A. C. Nagy, *Proc. of the 17th Danube Europ. Conf. on Geot. Eng. (17DECGE), Bucharest, România*. **2023**, *2*, 675–681.
[14] R. B. Kassa, T. Workie, A. Abdela, M. Fekade, M. Saleh, Y. Dejene, *OJCE*. **2020**, *10* (01), 55–68.
[15] L. Sørensen, A. S. Groven, I. A. Hovsbakken, O. Del Puerto, D. F. Krause, A. Sarno, A. M. Booth, *Sci. Total Environ.***2021**, 755 (2), 143170.
[16] M. Gawlik-Jędrysiak, *J. Anal. Chem*. **2013**, *68* (11), 959–960.
[17] M. Bonini, E. Errani, G. Zerbinati, E. Ferri, S. Girotti, *Microch. J*. **2008**, *90* (1), 31–36.
[18] P. Otero, S. K. Saha, S. Moane, J. Barron, G. Clancy, P. Murray, *J. Cromat. B*. **2015**, *997*, 229–235.
[19] P. Liang, L. Zhang, L. Peng, Q. Li, E. Zhao, *Bul.l Environ. Contam. Toxicol*. **2010**, *85* (2), 147–151.
[20] S. E. M. Selke, J. D. Culter, *Plastics Packaging: Properties, Processing, Applications, and Regulations*, 3rd ed., Vol. 1, Hanser Verlag GmbH Co. KG: Munich, Germany **2016**.
[21] H. Kim, S. G. Gilbert, J. B. Johnson, *Pharm. Res*. **1990**, *7* (176–179).
[22] J. N. Hahladakis, C. A. Velis, R. Weber, E. Iacovidou, P. Purnell, *J. Haz. Mat*. **2018**, *344*, 179–199.
[23] X.-S. Wang, X.-G. Li, D. Yan, *Pol. Degr. and Stab*. **2000**, *69* (3), 361–372.
[24] R. R. Chowreddy, K. Nord-Varhaug, F. Rapp, *J. Polym. Environ*. **2019**, *27* (1), 37–49.

STUDIA UBB CHEMIA, LXVIII, 3, 2023 (p. 129-139)
(RECOMMENDED CITATION)
DOI:10.24193/subbchem.2023.3.08

ENTRAPMENT OF LIPASE B FROM CANDIDA ANTARCTICA IN TAILORED SOL-GEL MATRICES FOR THE SYNTHESIS OF BENZYL DECANOATE – IMPORTANCE OF USING AN ADDITIVE

Larisa STELEA[a], Anna Maria TĂRTĂREANU[a], Adrian-Ioan DUDU[a,*]

ABSTRACT. Benzyl decanoate was successfully synthesized by the direct esterification of decanoic acid with benzyl alcohol mediated by lipase B from *Candida antarctica* immobilized by entrapment in a sol-gel matrix in a solvent-free system, using a ternary mixture of silane precursors and glycerol as additive. The most active (LS-6, 92.1% conversion after 90 minutes) and stable biocatalyst (95% of the initial activity after 7 reaction cycles) yielded 2.2 g of benzyl decanoate in a scaled-up process (91% isolation yield).

Keywords: *benzyl decanoate, esterification, solvent free system, lipase, additive, sol-gel, biocatalysis, aroma ester*

INTRODUCTION

Preparation of natural flavors starting from natural substrates through bioprocesses is industrially applied for their marketing as natural products in the European Union and US. Many flavors and fragrances esters can be enzymatically obtained using lipases that catalyze esterification or transesterification reactions. Nowadays, flavors have an important place in the world market for food additives produced *via* chemical synthesis. Aromatic esters are flavor esters obtained *via* direct extraction from plants or fruits,

[a] *Babeş-Bolyai University, Faculty of Chemistry and Chemical Engineering, 11 Arany Janos str., RO-400028, Cluj-Napoca, Romania*
** Corresponding author: adrian.dudu@ubbcluj.ro*

however, disadvantages like low product yield or purity make this technique expensive and difficult to apply industrially [1-4]. Enzymatic synthesis is an alternative because of milder reaction conditions and high chemo-, regio- and stereoselectivity [5]. Since different enantiomers or regioisomers could present different sensorial properties, enzymes are good tools, suitable to obtain the desired compound at industrial level as well [6]. Furthermore, in order to improve the control of the reactions and significantly reduce the risk of product contamination with proteins, enzyme immobilization can be employed [7]. There are many known techniques that can improve lipases' activity and stability, including adsorption to solid supports, covalent attachment, or entrapment in polymeric materials. Silica-based carries are used for enzyme immobilization by covalent attachment to solid supports, encapsulation or even by adsorption [7]. Moreover, in sol-gel entrapment of enzymes, some compounds could be used as additives (for example crown ethers, ionic liquids, deep eutectic solvents, glycerol, polyvinyl alcohol, etc.) for maintaining lipase activity, mainly in esterification reactions and/ or for protecting the enzyme structure during the immobilization process from harsh pH conditions and from alcohols resulted during sol-gel matrix formation. The advantages of this immobilization method are larger surface-to-volume *ratio*, high porosity of the obtained carriers, and high mass transfer [6, 8-10].

Lipases belong to the hydrolase family, enzymes responsible for hydrolyzing ester bonds. Because of their versatility, strong regio- and enantioselectivity, high stability in various conditions and extensive specificity for multiple substrates, these biocatalysts are frequently used in biochemical processes [2]. Lipases are appropriate for a wide range of industrial applications, including biodiesel manufacturing, pharmaceutical, food, and cosmetic technologies [10]. One recent study shows the synthesis of thymol octanoate, a promising hybrid molecule with various biological activities, mediated by lipase B from *Candida antarctica* [11].

Lipase B from *Candida antarctica* (CaL-B) is one of the most known versatile lipases. With an isoelectric point of 6.0 and a molecular weight of 33 kDa [10], the enzyme catalyzes esterification reactions through its active site which contains the catalytic triad Ser-His-Asp/Glu [2]. An essential structural feature of CaL-B is the presence of a "lid" composed of two flexible polypeptide helices which allows the enzyme to have an open and closed conformation. The lid plays a crucial role in interfacial activation mechanism and promotes the enzyme susceptibility to esterification reactions while allowing immobilization on hydrophobic supports [10].

Due to their biotechnological applications, lipases require a high degree of recovery and increased stability under the process conditions (pH, temperature, pressure, organic solvent) [6]. In this regard, immobilization techniques like adsorption, covalent attachment, cross-linking, inclusion, sol-

gel encapsulation or affinity-tag binding on supports can be used [1]. All these techniques exceed the limitations of soluble enzymes by potentially increasing catalytic activity and selectivity while lowering the production cost and allowing the automation of the process.

For this study the sol-gel encapsulation method was chosen for CaL-B immobilization, considering that the technique potentially enhances the enzyme's properties such as mechanical resistance, operation and long-term stability, thermostability and tolerance to various solvents [10]. Sol-gel encapsulation involves the use of silica-based carriers to attach enzymes through covalent binding or adsorption and presumes the formation of a silane matrix through a polymerization process that involves acidic or basic hydrolysis of silane compounds such as tetraethoxysilane (TEOS) or tetramethoxysilane (TMOS) [5].

In this work, we report the lipase catalyzed solvent-free preparation of benzyl decanoate mediated by sol-gel entrapped lipase B from *Candida antarctica*. Six biocatalysts were prepared with and without glycerol as additive and tested in the direct esterification of benzyl alcohol with decanoic acid and compared with the commercially available Novozym 435. The obtained biocatalysts were characterized by their synthetic and hydrolytic activities and recyclability in order to study the effect of additives during the encapsulation process and to prove their potential for an industrial scale-up. The optimum biocatalyst was used in a scale-up reaction (starting from 1 g of benzyl alcohol) for obtaining benzyl decanoate in order to further prove the novel biocatalysts' suitability for a potential industrial application.

RESULTS AND DISCUSSION

Lipase immobilization by sol-gel entrapment. Hydrolytic and synthetic activity assays

Six biocatalysts (LS-1 - LS-6) were successfully prepared by entrapping lipase B from *Candida antarctica* (CaL-B) *via* sol-gel method. Tetraethoxysilane and *n*-propyltriethoxysilane were used for all biocatalysts in the same molar *ratio* while three silane precursors with different hydrophobic groups (octyltriethoxysilane, *n*-hexyltriethoxysilane and phenyltriethoxysilane, all were added in a 1.6 molar *ratio*). Three catalysts were prepared without the addition of any additive (LS-1, LS-2 and LS-3), whilst for three biocatalysts glycerol was added as an additive (LS-4, LS-5 and LS-6). For the novel biocatalysts the hydrolytic and synthetic activities were evaluated and presented in **Table 1**.

As indicated in **Table 1**, the amount of biocatalyst obtained is improved when glycerol was added as additive during the immobilization step, as higher quantities were obtained for LS-4, LS-5 and LS-6 compared to their counterparts

obtained without glycerol addition (LS-1, LS-2 and LS-3), whereas the enzyme loading decreases for all biocatalysts when glycerol was added. This was to be expected, since the starting enzyme solution had the same concentration for all biocatalysts and the quantity of biocatalyst is higher for LS-4-6 than LS-1-3, therefore the *ratio* between the starting amount of enzyme and total mass of biocatalyst will be smaller.

The addition of glycerol led to an increased hydrolytic activity of LS-4-6. It can be seen that LS-5, formed from HTEOS, *n*-PTEOS and TEOS as silane precursors and glycerol as additive (4% aqueous solution, 100 µL) showed the highest hydrolytic activity, which makes the biocatalyst the most suitable for application in aqueous reaction systems. On the other hand, the synthetic activity of biocatalysts LS-4 and LS-5 was negatively influenced by the addition of glycerol, since LS-1 and LS-2 presented higher values for the synthetic activity. The only biocatalyst showing an increased synthetic activity when using glycerol was LS-6 (approximately 60% higher than its counterpart LS-3). However, LS-1, formed from OTEOS, *n*-PTEOS and TEOS as silane precursors without glycerol, showed the highest synthetic activity, making it the most suitable to be used in hydrophobic media, which was to be expected due to highly hydrophobic octyl chain on the support's surface.

Table 1. Enzyme loading, hydrolytic and synthetic activity assays for the novel biocatalysts

Sol-gel code	Silane precursors [1.6:0.4:1 molar *ratio*]	Additive	Quantity obtained [mg]	Enzyme loading [μg_{enzyme}/ $mg_{biocatalyst}$]	Hydrolytic activity [U]	Synthetic activity [mmol/min*g_{enzyme}]
LS-1	OTEOS: *n*-PTEOS:TEOS	No	36.3	0.31	12.55	8.14
LS-2	PhTEOS: *n*-PTEOS:TEOS	No	10.2	1.10	15.68	6.35
LS-3	HTEOS: *n*-PTEOS:TEOS	No	59.1	0.19	18.81	2.08
LS-4	OTEOS: *n*-PTEOS:TEOS	Yes	51.2	0.22	21.94	1.64
LS-5	PhTEOS: *n*-PTEOS:TEOS	Yes	13.6	0.82	25.07	4.75
LS-6	HTEOS: *n*-PTEOS:TEOS	Yes	61.9	0.18	28.2	3.32

To conclude, the addition of glycerol during the CaL-B entrapment *via* the sol-gel method enhances the enzymes' activity in aqueous media, whereas in hydrophobic media the enzymes' activity is negatively influenced, probably due to the increased viscosity around the entrapped enzyme.

Biocatalyst screening for the synthesis of benzyl decanoate

Experiments were performed in duplicate with the media results and standard deviations being presented. All six prepared biocatalysts (LS-1 - LS-6) were tested for the synthesis of benzyl decanoate by direct esterification of decanoic acid with benzyl alcohol in a solvent-free system. A commercially available form of CaL-B (Novozym 435) was also used as biocatalyst in order to evaluate the performances of the novel biocatalysts (**Figure 1**).

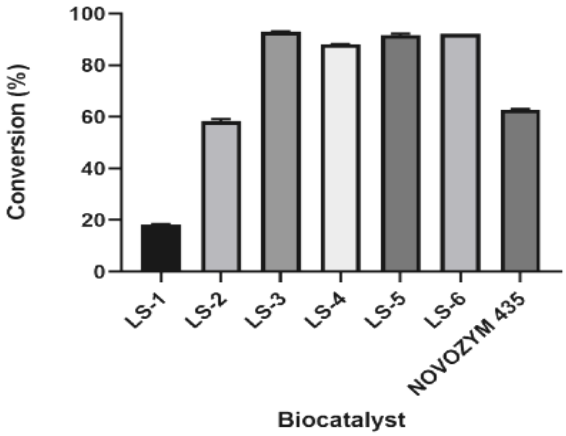

Figure 1. Results obtained for the enzymatic synthesis of benzyl decanoate, mediated by the six novel biocatalysts, in comparison with Novozym 435. Reaction conditions: 20 mg benzyl alcohol, 2 equiv. decanoic acid, 2 mg CaL-B, 30 °C, 600 rpm, 90 minutes.

The results obtained in this part of the study show that LS-1 performed poorly in the biosynthesis of benzyl decanoate with a conversion value of only 18.1% after 90 minutes. LS-2 and Novozym 435 delivered satisfactory results (58.9% and 62.8% conversion values, respectively). LS-4 and LS-5 showed excellent activity since conversion values of 88.2% and 91.1%, respectively, were obtained. The highest conversion values were registered when LS-3 and LS-6 were used as biocatalysts as they yielded the desired aroma ester with 92.9% and 92.1% conversion values, respectively. The beneficial effect of using HTEOS as one of the silane precursors in the silane matrix can be seen, since CaL-B shows great activity towards benzyl decanoate formation (in the presence or absence of glycerol).

Reusability studies

In order for a biocatalyst to be considered for a potential industrial application it should be cheap, stable, easy to recover and reusable. For this, the reusability grade of the newly prepared biocatalysts was evaluated for the production of benzyl decanoate and the obtained results can be seen in **Figure 2**.

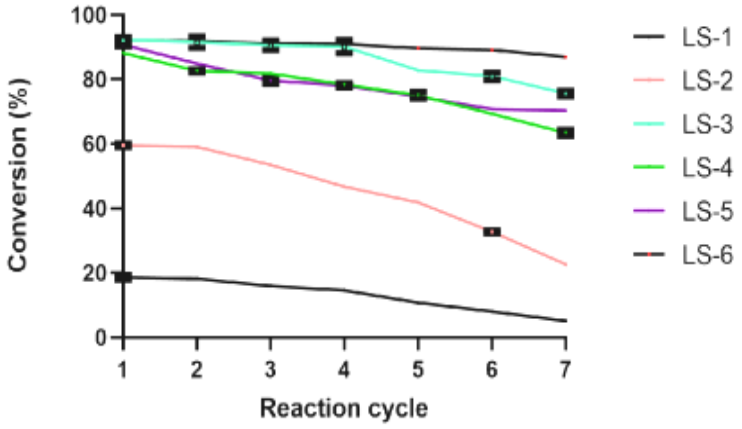

Figure 2. Evaluation of the recyclability of the newly developed biocatalysts. Reaction conditions: 20 mg benzyl alcohol, 2 equiv. decanoic acid, 2 mg CaL-B, 30 °C, 600 rpm, 90 minutes per reaction cycle.

LS-1 showed poor activity towards benzyl decanoate formation and lost almost 50% of its initial activity after the 7th reaction cycle. LS-2 also registered a relatively low conversion value for the synthesis of benzyl decanoate and also lost more than half of its initial activity after the 7th reaction cycle. LS-4 and LS-5 were more active than LS-1 and LS-2 (similar compositions, LS-4 and LS-5 contain also glycerol as additive) and also registered a loss of initial activity, initially a 5% loss of initial activity after the 1st reaction cycle and reaching ~25% loss of initial enzymatic activity after the 7th reaction cycle, however, it wasn't as significant as for the two previously mentioned biocatalysts.

LS-3 maintained all its initial activity even after the 4th reaction cycle, but the conversion value suffered a drop after the 5th reaction cycle and reached a value of 75% after the 7th reaction cycle. On the other hand, LS-6 maintained almost all its initial activity even after the 6th reaction cycle, before reaching a conversion value of 86.9% after the 7th reaction cycle. Even though both biocatalysts, LS-3 and LS-6, delivered excellent results towards

benzyl decanoate formation, the biocatalyst containing glycerol as additive (LS-6) proved to be more stable, as it maintained almost 95% of its initial activity even after the 7th reaction cycle, therefore making it suitable for a potential industrial application.

CONCLUSIONS

Benzyl decanoate was successfully synthesized *via* an enzymatic approach with lipase B from *Candida antarctica* immobilized in a sol-gel matrix starting from benzyl alcohol and decanoic acid. The sol-gel matrix obtained from hexyltriethoxysilane: *n*-propyltriethoxysilane and tetraethoxysilane (in a 1.6:0.4:1 molar *ratio*) gave the most active biocatalyst. The benefits of glycerol as additive in the immobilization step were proven, since by using the LS-6 biocatalyst (containing glycerol as additive) yielded benzyl decanoate with a conversion value of 92.1% and lost approximately only 5% of its initial activity after the 7th reaction cycle. The scale-up of the proposed process yielded 2.2 g of benzyl decanoate (η=91%) in just 90 minutes of reaction time. Benzyl decanoate obtained by this enzymatic method can be considered a natural aroma ester, since the reactants can be found in nature and an enzyme is used as catalyst, as per Regulation No. 1334/2008 of the European Parliament and of the Council and LS-6 can be considered a viable candidate for a potential industrial application.

EXPERIMENTAL SECTION

Materials

CaL-B as lyophilized powder and Novozym 435 were purchased from Novozymes (Denmark). Isopropylic alcohol, *n*-hexyltriethoxysilane (HTEOS), tetraethoxysilane (TEOS), *n*-propyltriethoxysilane (*n*-PTEOS), *n*-octyltriethoxysilane (OTEOS), phenyltriethoxysilane (PhTEOS), glycerol, decanoic acid, 3-methyl-2-benzothiazolinone hydrazine hydrochloride hydrate (MBTH), sodium sulfate, benzyl alcohol and HPLC grade methanol and water were purchased from Merck (Germany). 4-Nitrophenylpalmitate and 4-nitrophenol were products of Fluka (Switzerland). Sodium sulfate, bovine serine albumin (BSA), ammonium iron(III) sulfate, arabic gum and sodium deoxycholate were purchased from Alfa Aesar (USA). Benzyl decanoate was previously synthesized at the Enzymology and Applied Biocatalysis Research Centre. All solvents and reagents were freshly distilled and dried by standard methods before use.

The mixture of benzyl alcohol and benzyl decanoate was analyzed by reverse phase HPLC (RP-HPLC) with an Agilent 1260 Infinity series (USA) equipped with a UV-Vis detector using a Phenomenex Gemini NX-C18 (150 x 4.5 mm; 5 µm) chromatographic column and methanol: water 80:20 (v/v %) at 1 mL/min flow as eluent. For the rigorous evaluation of the conversion values, a relative response factor (RF=0.8549) was determined by analyzing samples of known concentration (for both benzyl alcohol and benzyl decanoate).

For the quantitative spectrophotometric determination of enzyme load through BCA method, using the Pierce® BCA Protein Assay Kit (Thermo Fisher Scientific Inc., USA) and for the evaluation of the novel biocatalysts synthetic and hydrolytic activities an Agilent 8453 UV-Vis spectrophotometer equipped with thermostat was used.

The enzymatic reactions were perfected using IKA C-MAG HS 7 (Germany) magnetic stirrers equipped with temperature controllers. The vacuum needed for the removal of the water formed in the system was ensured by using a Heidolph (Germany) vacuum pump.

Lipase immobilization by sol–gel entrapment

CaL-B was immobilized in sol-gel according to the recipe previously described [10]. Six samples were prepared using lyophilized enzyme powder to prepare 0.5 mL enzymatic solution (22.4 mg enzyme/mL), which was mixed with 0.1 mL *iso*-propanol and 0.05 mL NaF 1M solution. The additive (100 µL glycerol, 4% aqueous solution) was added to three of these samples (LS-4, LS-5 and LS-6) while the other three biocatalysts (LS-1, LS-2 and LS-3) were prepared without any additive. After stirring, silane precursors (OTEOS, PhTEOS, and HTEOS) were added keeping the silane precursors OTEOS, PhTEOS, HTEOS: *n*-propyltriethoxysilane: tetraethoxysilane molar *ratio*s of 1.6:0.4:1, the detailed components for each of the prepared biocatalysts can be found in **Table 1**. Each mixture was added in 4 mL glass vials, stirred and left for 24 hours at room temperature. The obtained gels were washed and vacuum filtered with 7 mL *iso*-propyl alcohol, 5 mL distilled water, 5 mL *iso*-propyl alcohol and 2.5 mL of *n*-hexane. The obtained biocatalysts were dried under advanced vacuum (17 mbar) for 1 hour and left at room temperature for 24 hours. After drying, the resulted products were crushed in a mortar and the biocatalysts were stored at 4 °C in glass vials.

Hydrolytic activity assay of the novel biocatalysts

The hydrolytic activity of the biocatalysts was determined using as model reaction the hydrolysis of 4-nitrophenylpalmitate (0.75 mM in *iso*-propanol). The reactions were perfected in Sorensen buffer which was prepared

by mixing 90 mL phosphate buffer solution (0.2 M, pH 8) with 207 mg sodium deoxycholate and 100 mg arabic gum. The reactions were perfected in 2 mL cuvettes in which 10 mg biocatalyst, 900 µL Sorensen buffer and 100 µL substrate solution were added, incubated at 37 °C, 800 rpm for 10 minutes. After 10 minutes, the samples were centrifuged and were analyzed at 410 nm.

Synthetic activity assay

The synthetic activity of the biocatalyst (expressed as the amount of released acetaldehyde *vs* the reaction time and the amount of enzyme) was evaluated using a fast and sensible colorimetric method [12] based on the *n*-butanol transesterification with vinyl acetate (2 equiv.) in *n*-hexane at 30 °C and 1000 rpm. The released acetaldehyde was quantified after derivatization with MBTH as hydrochloride salt, when the formed aldazine is further converted by oxidative coupling with another MBTH molecule in the presence of ammonium iron(III) sulfate into a blue tetraaza-pentamethylene cyanine with a maximum absorption at 598 nm.

Biocatalyst screening for the synthesis of benzyl decanoate

For the lipase mediated synthesis of benzyl decanoate, 20 mg benzyl alcohol, decanoic acid (2 equiv.) and 2 mg lipase (in order to respect the substrate: enzyme weight *ratio* of 10:1, the amount of each biocatalyst was determined based on the enzyme loading, see **Table 1**) were added in 5 mL round-bottom flasks. The flasks were stirred (600 rpm) for 90 minutes in an oil bath with magnetic stirring at 30 °C. Subsequently, to remove the resulted water, the flasks were connected to a vacuum line (20 mbar). A similar reaction was set-up using Novozym 435 (33.3 mg) for comparison. After 90 minutes, 1 mL ethanol was added to the reaction mixtures and homogenous samples (10 µL) were withdrawn and diluted with 990 µL ethanol, filtered and injected on HPLC in order to determine the conversion.

Reusability studies

Into magnetically stirred 5 mL round-bottom flasks, 20 mg benzyl alcohol, decanoic acid (2 equiv.) and 2 mg lipase (in order to respect the substrate: enzyme weight *ratio* of 10:1, the amount of each biocatalyst was determined based on the enzyme loading, as described in **Table 1**) were added. The flasks were connected to a vacuum line (20 mbar), stirred (600 rpm) at 30 °C for 90 minutes per reaction cycle. After 90 minutes, 1 mL ethanol was added to the reaction mixtures and homogenous samples (10 µL) were withdrawn and diluted with 990 µL ethanol, filtered and analyzed by HPLC.

After samplings, the flasks were sonicated for 5 minutes and the solvent was taken out. The procedure was repeated three times (adding 3 mL ethanol, sonication and pipetting the solvent out) and the flasks containing the biocatalysts were rotary evaporated to fully remove the solvent. The protocol was repeated seven times for each biocatalyst.

Preparative scale enzymatic synthesis of benzyl decanoate

In a 10 mL round-bottom flask, 1 g of benzyl alcohol, 2 equiv. (18 mmol, 3.18 g) decanoic acid and 100 mg lipase (amount of LS-6 was determined based on the enzyme loading, see **Table 1**) were added. The flask was magnetically stirred (600 rpm) at 30 °C for 90 minutes. In order to efficiently remove the water formed in the system, the flask was connected to a vacuum line (20 mbar). After 90 minutes, 5 mL ethanol was added and a 10 µL homogenous sample was withdrawn, diluted with 990 µL ethanol, filtered and injected on HPLC in order to establish the reaction conversion. The rest of the mass was rotary evaporated in order to completely remove the solvent. 10 mL dichloromethane was added and the organic phase was washed with sodium carbonate (Na_2CO_3, 3 x 20 mL) in order to remove the unreacted decanoic acid. The organic phase was separated and dried with sodium sulfate, evaporated under advanced vacuum, yielding 2.2 g of pure benzyl decanoate (η=91%). The products' purity was verified by ^{1}H-NMR and ^{13}C-NMR.

Benzyl decanoate:

Yield: 91% (2.2 g):^{1}H-NMR (400 MHz, $CDCl_3$): 0.88 (3 H, t), 1.26-1.33 (12 H, m), 1.66 (2 H, m), 2.32 (2 H, m), 5.2 (2 H, s), 7.33 (5 H, s);^{13}C-NMR (100 MHz, $CDCl_3$): 14.1, 22.7, 25.0, 29.0, 29.3 (2 C), 29.6, 31.9, 33.9, 66.4, 127.1-128.9 (4 C), 136.1, 173.1.

REFERENCES

1. I. C. Perdomo; S. G. A. Pinto; D. Romano; M. L. Contente; F. Paradisi; F. Molinari; *J. Agric. Food Chem.*; **2019**; *67*; 6517−6522
2. A. G. A. Sa; A. C. de Meneses; P. H. H. de Araujo; D. de Oliveira; *Trends Food Sci. Technol.*; **2017**; *69*; 95-105
3. R. Semproli; S. N. Chanquia; J. P. Bittner; S. Muller; P. D. de Maria; S. Kara; D. Ubiali; *ACS Sustainable Chem. Eng.*; **2023**; *11*; 5926-5936

4. B. Lorenzo; L. Fernandez; J. Ortega; L. Dominguez; *Processes*; **2023**; *11*; 1640
5. K. P. Dhake; D. D. Thakare; B.M. Bhanage; *Flavour Fragr. J.*; **2013**; *28*; 71-83
6. A. I. Dudu; L. C. Bencze; C. Paizs; M. I. Toșa; *React. Chem. Eng.*; **2022**; *7.* 442-449
7. M. T. Reetz; A. Zonta; J. Simpelkamp; *Biotechnol. Bioeng.*; **1996**; *49*; 527-534
8. M. E. Moisă; C. G. Spelmezan; C. Paul; J. H. Bartha-Vari; L. C. Bencze, F. D. Irimie; C. Paizs, M. I. Toșa; *RSC Adv.*; **2017**; *7*; 52977-52987
9. S. Serra; C. Fuganti; E. Brenna; *Trends Biotechnol.*; **2005**; *23*; 193-198
10. A. I. Dudu; M. A. Lăcătuș; L. C. Bencze; C. Paizs; M. I. Toșa; *ACS Sustainable Chem. Eng.*; **2021**; *9*; 5461-5469
11. D. A. Sanchez; G. M. Tonetto; M. L. Ferreira; *Catalysts*; **2023**; *13*; 473
12. J. Zheng; X. Fu; X. Ying; Y. Zhang; Z. Wang; *Anal. Biochem.*; **2014**; *452*; 13-15

STUDIA UBB CHEMIA, LXVIII, 3, 2023 (p. 141-151)
(RECOMMENDED CITATION)
DOI:10.24193/subbchem.2023.3.09

RADIOCARBON DATING OF THE VERY LARGE EGG BAOBAB FROM THE ANDOMBIRY FOREST, MADAGASCAR

Adrian PATRUT[a,b]*, Roxana T. PATRUT[a], Jean-Michel LEONG POK-TSY[c], Laszlo RAKOSY[d], Pascal DANTHU[e], Ileana Andreea RATIU[a,b], Jenő BODIS[a], Stephan WOODBOURNE[f]

ABSTRACT. The article discloses the AMS (accelerator mass spectrometry) radiocarbon dating results of the Egg baobab, a superlative Grandidier baobab (*Adansonia grandidieri*) from the Andomiry Forest, Atsimo-Andrefana region, Madagascar. The investigation of the baobab shows that it consists of 5 perfectly fused stems and exhibits a closed ring-shaped structure with a very large false cavity inside. The calculated overall wood volume of the Egg baobab is 450 m^3. Two wood samples were collected from the exterior of the stems, out of which nine tiny segments were extracted and dated by radiocarbon. The oldest sample segment had a radiocarbon date of 921 ± 24 BP, which corresponds to a calibrated age of 840 ± 25 years. According to this value the Egg baobab is 875 ± 75 years old.

Keywords: *AMS radiocarbon dating, Adansonia grandidieri, tropical trees, multiple stems, false cavity*.

[a] *Babeş-Bolyai University, Faculty of Chemistry and Chemical Engineering, 11 Arany Janos, RO-400028, Cluj-Napoca, Romania.*
[b] *Babeş-Bolyai University, Raluca Ripan Institute for Research in Chemistry, 30 Fantanele, RO-400294 Cluj-Napoca, Romania.*
[c] *Drfgrn-fofifa, Antananarivo, Madagascar.*
[d] *Babeş-Bolyai University, Faculty of Biology and Geology, 44 Republicii, RO-400015 Cluj-Napoca, Romania.*
[e] *Cirad, UPR BSEF, Montpellier, France.*
[f] *iThemba LABS, Private Bag 11, WITS 2050, South Africa.*
* *Corresponding author: apatrut@gmail.com*

INTRODUCTION

The *Adansonia* genus, which belongs to the Bombacoideae subfamily of Malvaceae, is represented by eight or nine species. One or two species are endemic to the tropical arid savanna of the African continent, six species have a natural distribution in Madagascar, while one species is found in Australia [1-5].

In 2005, we started a research project in order to elucidate several controversial aspects concerning the architecture, growth and age of the African baobab (*Adansonia digitata* L.). The research is based on an original approach, which is not limited to demised or fallen trees, but also allows to investigate live and standing individuals. This methodology consists on AMS radiocarbon dating of tiny wood samples extracted from inner cavities, incisions/entrances in the trunk, fractured stems and from the exterior of the trunk/stems of large baobabs [6-19]. We found that all very large African baobabs are multi-stemmed and most of them exhibit ring-shaped structures. The oldest individuals can live over 2,000 years [9, 10].

In 2013, we extended our research to the most emblematic three species of Madagascar, i.e., the fony (*Adansonia rubrostipa* Jum. & H. Perrier), the za (*Adansonia za* Baill.) and the Grandidier baobab (*Adansonia grandidieri* Baill.) [22-27].

The Grandidier baobab, named Reniala by natives (in Masikoro, i.e., “Mother of the Forest”), is the largest and most famous of the six Malagasy species. According to the classical description, *A. grandidieri* is represented by big trees with massive cylindrical trunks and flat-topped crowns with almost horizontal large branches [1,2,4]. However, the shape and dimensions of mature and old individuals exhibit considerable variation and the differences depend especially on their location.

According to the latest research, the total population of *A. grandidieri*, spreading over an area of 26,232 km^2 along the Mangoky river and in the western part of the Menabe region, amounts to 1.2-1.3 million mature individuals [20, 21].

The largest *A. grandidieri* can be found in the Morombe area and in particular in the so-called Andombiry Forest. The forest has a trapezoidal shape and is bounded by four villages: Belitsaka, Andombiry, Ankoabe and Isosa. In previous articles, we presented the investigation and radiocarbon dating results of several monumental *A. grandidieri* specimens, namely Tsitakakoike, the Pregnant baobab, the House baobab [22], the Big Reniala of Isosa [23], the Giant of Bevoay [24], the baobab A 257 and the baobab A 215 [25].

Here we present the investigation and AMS radiocarbon dating results of another superlative specimen, the so-called Egg baobab.

RESULTS AND DISCUSSION

The Egg baobab and its area. The very large tree that we named the Egg baobab (le baobab oeuf), due to its shape that resembles a flat-bottomed egg, is located in the dry deciduous Andombiry Forest, in the Morombe district, Atsimo-Andrefana region of southwestern Madagascar.

The Egg baobab can be found on the side of a dirt road between the villages of Isosa and Andombiry. Its GPS coordinates are 21º35.138' S, 043º30.525' E and the altitude is 18 m. The mean annual rainfall is 458 mm (Morombe station). The tree has a maximum height of 17.5 m, the circumference is 25.02 m at breast height (cbh; at 1.30 m above ground level), reaching a

Figure 1. General view of the Egg baobab taken from the north.

Figure 2. Another view of the Egg baobab taken from the west.

maximum value of 29.20 m at the height of 4.2 m (**Figures 1 and 2**). It has an overall wood volume of 450 m^3, out of which 400 m^3 belongs to the trunk and 50 m^3 to the canopy.

The Egg baobab has the third largest circumference at breast height of all live Grandidier baobabs, after Tsitakakantsa (29.05 m), which is located at 1.2 km and the A 257 baobab (25.70 m), located at only 0.3 km. But, the Egg baobab has the greatest maximum circumference of all *A. grandidieri* individuals. Its shape is similar to that of the famous Pregnant baobab (le baobab enceinte), located at a distance of 1.5 km, which we presented previously [22] and which is currently in a state of decline.

Five large primary branches, with diametres up to 2.5 m, emerge quasi-horizontally from the trunk, at heights of 7.2 – 9.0 m. Other branches emerge somewhat vertically from the top of the trunk, which is 10.5 m tall.

The horizontal dimensions of the canopy are 33.5 (WE) x 26.2 m (NS) (**Figure 3**). According to the on-site visual inspection and to the digital photograph analysis, the trunk consists of 5 perfectly fused stems (**Figure 4**). Due to its old age, the Egg baobab no longer produces pods.

Figure 3. The image shows the impressive canopy of the Egg baobab.

Figure 4. The trunk is covered by burls and traces of wounds.

Wood samples. Two wood samples were collected from two different stems using an increment borer. The longest sample, labelled Eb-1, with the length of 0.86 m, was collected from the exterior of a stem facing north, at the height of 1.60 m. A number of six tiny segments, each 10^{-3} m long (marked a to f), were extracted from determined positions of sample Eb-1. Another sample, labelled Eb-2, with the length of 0.62 m, was collected from an opposite stem facing south, at the height of 1.61 m. Three tiny segments (marked a to c) were extracted from this sample.

AMS results and calibrated ages. Radiocarbon dates of the nine sample segments are presented in Table 1. The radiocarbon dates are expressed in ^{14}C yr BP (radiocarbon years before present, i.e., before the reference year 1950). Radiocarbon dates and errors were rounded to the nearest year.

Calibrated (cal) ages, expressed in calendar years CE (CE, i.e., common era), are also listed in Table 1. The 1σ probability distribution (68.3%) was selected to derive calibrated age ranges. For one sample segment (1e), the 1σ distribution is consistent with one range of calendar years. For four segments

Table 1. AMS Radiocarbon dating results and calibrated ages of samples collected from the Egg baobab

Sample/ segment code	Depth[1] [height[2]] (m)	Radiocarbon date [error] (^{14}C yr BP)	Cal CE range 1σ [confidence interval]	Assigned year [error] (cal CE)	Sample age [error] (cal CE)
Eb-1a	0.10 [1.60]	-	-	-	>Modern
Eb-1b	0.25 [1.60]	209 [± 22]	1670-1687 [14.2%] **1731-1782 [45.5%]** 1796-1806 [8.6%]	1756 [± 25]	265 [± 25]
Eb-1c	0.40 [1.60]	360 [± 24]	1506-1519 [9.3%] **1524-1591 [51.7%]** 1618-1628 [5.0%]	1557 [± 35]	465 [± 35]
Eb-1d	0.60 [1.60]	694 [± 26]	1297-1320 [29.7%] **1354-1386 [38.5%]**	1370 [± 15]	655 [± 15]
Eb-1e	0.75 [1.60]	921 [± 24]	**1156-1211 [68.3%]**	1183 [± 25]	840 [± 25]
Eb-1f	0.86 [1.60]	700 [± 25]	1295-1318 [30.8%] **1355-1385 [37.5%]**	1370 [± 15]	655 [± 15]
Eb-2a	0.20 [1.61]	129 [± 21]	1710-1719 [6.5%] 1813-1836 [18.7%] 1855-1866 [7.0%] **1881-1925 [36.1%]**	1903 [± 20]	120 [± 20]
Eb-2b	0.40 [1.61]	348 [± 24]	**1510-1583 [61.2%]** 1623-1631 [7.0%]	1545 [± 35]	480 [± 35]
Eb-2c	0.62 [1.61]	660 [± 23]	**1316-1358 [53.7%]** 1383-1394 [14.6%]	1337 [± 20]	685 [± 20]

[1] Depth in the wood from the sampling point.
[2] Height above ground level.

(1d, 1f, 2b, 2c), the 1σ distribution corresponds to two ranges of calendar years, while for two segments (1b, 1c) it is consistent with three ranges and for another segment (2a) with four ranges. In these cases, the confidence interval of one range is considerably greater than that of the other(s); therefore, it was selected as the cal CE range of the segment for the purpose of this discussion. For obtaining single calendar age values of sample segments, we derived a mean calendar age of each segment from the selected range (marked in bold).

For obtaining single calendar age values of sample segments, we derived a mean calendar age of each sample segment, called assigned year, from the selected range (marked in bold). Sample/segment ages represent the difference between the current year 2023 CE and the assigned year, with the corresponding error. Sample ages and errors were rounded to the nearest 5 yr.

For one sample segment (1a), the age falls after the year 1950 CE, i.e. the ^{14}C activity, expressed by the ratio $^{14}C/^{12}C$, is greater than the standard activity in the reference year 1950. Such values, which correspond to negative radiocarbon dates, are termed greater than Modern (>Modern). In such cases, the dated wood is young, being formed after 1950 CE.

We used this approach for selecting calibrated age ranges and single values for sample ages in all our previous articles on AMS radiocarbon dating of large and old angiosperm trees [6-19, 22-27].

Dating results of sample segments. The circumference of the Egg baobab at the sampling height is 25.71 m, which translates to a diametre of 8.18 m and a radius of 4.09 m. This value also represents the distance from the exterior of both sampled stems to their theoretical pith.

For the segments extracted from the longest sample Eb-1 which was collected from the exterior, the age values of the dated segments increase with the depth in the wood from Eb-1a to Eb-1e, after which the ages decrease to Eb-1f. The oldest dated sample, i.e., Eb-1e, has a radiocarbon date of 921 ± 24 BP, which translates to a calibrated age of 840 ± 25 calendar yr.

This anomalous age sequence is characteristic to baobabs that exhibit a closed ring-shaped structure with a false cavity inside. In this architecture, for wood samples collected from the exterior of the trunk, as well as for samples collected from the inner cavity walls (if the false cavity has an accessible opening), the age sequence increases from the sampling point up to a point of maximum age, after which it decreases in the opposite direction [11, 14]. For sample Eb-1, segment ages show that the point of maximum age is located between the segments Eb-1d and Eb-1f, i.e., between 0.60 and 0.86 m from the sampling point, closer to segment Eb-1e, i.e. 0.75 m. Therefore, the maximum age in the direction of sample Eb-1 is around 875 ± 75 calendar yr. The walls of the false cavity, which is defined by 5 fused stems and is completely closed toward the exterior, have a depth of 0.70-0.80 m.

In the case of the shorter sample Eb-2, ages of all dated sample segments increase with the depth in the wood, thus showing that the point of maximum age was not reached.

Architecture of the Egg baobab. Our research has revealed that all large baobabs, including the *A. grandidieri* specimens, are multi-stemmed. We also found that superlative baobabs exhibit preferentially a novel architecture, in which the multiple stems define at ground level a circle or an ellipse, with an empty space between them. We called it ring-shaped structure (RSS). The most frequent is the closed RSS, in which the fused stems are disposed in a ring with a natural empty space inside, that we named false cavity. In the case of baobabs with a closed RSS, for long samples collected from the exterior toward the false cavity, as well as for samples collected from the false cavity walls toward the exterior of the trunk segment ages show a continuous increase from the sampling point up to a certain distance into the wood, after which they decrease toward the opposite part [9,11].

The segments which originate from sample Eb-1 show such an anomalous age sequence, which demonstrates that the Egg baobab possesses a closed RSS with a false cavity inside. The dating values also suggest that, at the height of 1.60 m, the diametre of the false cavity is around 6.70 m.

Age of the Egg baobab. The dating results of segments extracted from sample Eb-1 indicate that the age of the respective stem, which corresponds to the area (point) of maximum age, is 875 ± 75 calendar yr, i.e., 800 – 950 yr. The Egg baobab consists of five perfectly fused stems and its shape is highly symmetrical. This indicates that the ages of the five stems are identical. One can state that the stems of the Egg baobab started growing quasi-simultaneously around the year 1150 CE.

CONCLUSIONS

The research discloses the AMS radiocarbon dating results of a superlative Grandidier baobab, namely the Egg baobab from the Andombiry Forest, Morombe district, Atsimo-Andrefana region, Madagascar. The Egg baobab is composed of 5 perfectly fused stems and has a closed ring-shaped structure with a very large false cavity inside. Two wood samples were collected from the outer part of the trunk. The oldest dated sample has a radiocarbon date of 921 ± 24 BP, corresponding to a calibrated age of 840 ± 25 years. This value indicates that the Egg baobab is 875 ± 75 years old.

EXPERIMENTAL SECTION

Sample collection. The two investigated wood samples were collected with a Haglöf CH 900 increment borer (0.90 m long, 0.0108 m inner diametre). A number of nine tiny segments of the length of 10^{-3} m were extracted from predetermined positions along the samples. The segments were processed and investigated by AMS radiocarbon dating.

Sample preparation. The α-cellulose pretreatment method was used for removing soluble and mobile organic components [28]. The resulting samples were combusted to CO_2, which was next reduced to graphite on iron catalyst [29,30]. The resulting graphite samples were analysed by AMS.

AMS measurements. The radiocarbon measurements were performed at the AMS Facility of the iThemba LABS, Johannesburg, Gauteng, South Africa, using the 6 MV Tandem AMS system [31]. The obtained fraction modern values were finally converted to a radiocarbon date. The radiocarbon dates and errors were rounded to the nearest year.

Calibration. Radiocarbon dates were calibrated and converted into calendar ages with the OxCal v4.4 for Windows [32], by using the SHCal20 atmospheric data set [33].

ACKNOWLEDGMENTS

The investigation of the baobab was authorised by the Forestry Direction of the Ministry of Environment, Ecology and Forestry of Madagascar and by the Madagascar National Parks.

The research was funded by the Romanian Ministry of Education CNCS-UEFISCDI under grant PN-III-P4-ID-PCE-2020-2567, Nr. 145/2021.

REFERENCES

1. D.A. Baum, *Annals of the Missouri Botanical Garden*, **1995**, *82*, 440-471.
2. G.E. Wickens, P. Lowe, “The Baobabs: Pachycauls of Africa, Madagascar and Australia”, Springer, Dordrecht, **2008**, pp. 232-234, 256-257, 295-296.
3. J.D. Pettigrew, L.K. Bell, A. Bhagwandin, E. Grinan, N. Jillani, J. Meyer, E. Wabuyele, C.E. Vickers, *Taxon*, **2013**, *61*,1240-1250.

4. A. Petignat, L. Jasper, “Baobabs of the world: The upside down trees of Madagascar, Africa and Australia”, Struik Nature, Cape Town, **2015**, pp. 16-86.
5. G.V. Cron, N. Karimi, K.L. Glennon, C.A. Udeh, E.T.F. Witkowski, S.M. Venter, A.E. Assobadjo, D.H. Mayne, D.A. Baum, *Taxon*, **2016**, *65*, 1037-1049.
6. A. Patrut, K.F. von Reden, D.A. Lowy, A.H. Alberts, J.W. Pohlman, R. Wittmann, D. Gerlach, L. Xu, C.S. Mitchell, *Tree Physiology*, **2007**, *27*, 1569-1574.
7. A. Patrut, D.H. Mayne, K.F. von Reden, D.A. Lowy, R. Van Pelt, A.P. McNichol, M.L. Roberts, D. Margineanu, *Radiocarbon*, **2010**, *52(2-3)*, 717-726.
8. A. Patrut, K.F. von Reden, R. Van Pelt, D.H. Mayne, D.A. Lowy, D. Margineanu, *Annals of Forest Science*, **2011**, *68*, 93-103.
9. A. Patrut, S. Woodborne, R.T. Patrut, L. Rakosy, D.A. Lowy, G. Hall, K.F. von Reden, *Nature Plants*, **2018**, *4(7),* 423-426.
10. A. Patrut, K.F. von Reden, D.H. Mayne, D.A. Lowy, R.T. Patrut, *Nucl. Instrum. Methods Phys. Res. Sect. B*, **2013**, *294*, 622-626.
11. A. Patrut, S. Woodborne, K.F. von Reden, G. Hall, M. Hofmeyr, D.A. Lowy, R.T. Patrut, *PLOS One*, **2015**, *10(1)*, *e0117193.*
12. A. Patrut, L. Rakosy, R.T. Patrut, I.A. Ratiu, E. Forizs, D.A. Lowy, D. Margineanu, K.F. von Reden, *Studia UBB Chemia*, **2016**, *LXI*, *4*, 7-20.
13. A. Patrut, R.T. Patrut, L. Rakosy, D.A. Lowy, D. Margineanu, K.F. von Reden, *Studia UBB Chemia*, **2019**, *LXIV*, *2 (II)*, 411-419.
14. A. Patrut, S. Woodborne, K. F. von Reden, G. Hall, R.T. Patrut, L. Rakosy, P. Danthu, J-M. Leong Pock-Tsy, D.A. Lowy, D. Margineanu, *Radiocarbon*, **2017**, *59(2)*, 435-448.
15. A. Patrut, S. Woodborne, R.T. Patrut, G. Hall, L. Rakosy, C. Winterbach, K.F. von Reden, *Forests*, **2019**, *10*, 983-994.
16. A. Patrut, R.T. Patrut, M.J. Slater, L. Rakosy, D.A. Lowy, K.F. von Reden, *Studia UBB Chemia*, **2020**, *LXV*, *3*, 149-156.
17. A. Patrut, A. Garg, S. Woodborne, R.T. Patrut, L. Rakosy, I.A. Ratiu, D.A. Lowy, *PLOS One*, **2020**, *15(1)*, e0227352.
18. A. Patrut, R.T. Patrut, L. Rakosy, I.A. Ratiu, D.A. Lowy, K.F. von Reden, *Dendrochronologia* **2021**, *70*, 125898.
19. A. Patrut, R.T. Patrut, W. Oliver, I.A. Ratiu, D.A. Lowy, G. Shiimbi, L. Rakosy, D. Rakosy, S. Woodborne; K.F. von Reden, *Forests*, **2022**, *13*, 1899.
20. G. Vieilledent, C. Cornu, A. Cuni Sanchez, J-M. Leong Pock-Tsy, P. Danthu, *Biological Conservation*, **2013**, *166*, 11-22.
21. H. Ravaomanalina, J. Razafimanahaka, “2016. *Adansonia grandidieri*.” *The IUCN Red List of Threatened Species 2016: e.T30388A64007143*.
22. A. Patrut, K.F. von Reden, P. Danthu, J-M. Leong Pock-Tsy, R.T. Patrut, D.A. Lowy, *PLOS One*, **2015**, *10(3)*, *e0121170*.
23. R.T. Patrut, A. Patrut, J-M Leong Pock-Tsy, S. Woodborne, L. Rakosy, P. Danthu, I.A. Ratiu, J. Bodis, K.F. von Reden, *Studia UBB Chemia*, **2019**, *LXIV*, *4*, 131-39.
24. A. Patrut, R.T. Patrut, J-M. Leong Pock-Tsy, S. Woodborne, L. Rakosy, I.A. Ratiu, J. Bodis, P. Danthu, *Studia UBB Chemia*, **2020**, *LXV*, *4*, 151-158.

25. A. Patrut, R.T. Patrut, J-M. Leong Pock-Tsy, P. Danthu, S. Woodborne, L. Rakosy, I.A. Ratiu, *Forests*, **2021**, *12*, 1258.
26. A. Patrut, K.F. von Reden, P. Danthu, J-M. Leong Pock-Tsy, R.T. Patrut, D.A. Lowy, *PLoS ONE*, **2015**, *10(3)*, e0121170.
27. A. Patrut, R.T. Patrut, P. Danthu, J-M. Leong Pock-Tsy, L. Rakosy, D.A. Lowy, K.F. von Reden, *PLOS One*, **2016**, *11(1)*, *e146977*.
28. N.J. Loader, I. Robertson, A.C. Barker, V.R. Switsur, J.S. Waterhouse, *Chem. Geol.*,**1997**, *136(3)*, 313–317.
29. Z. Sofer, *Anal. Chem.*, **1980**, *52(8)*, 1389-1391.
30. J.S. Vogel, J.R. Southon, D.E. Nelson, T.A. Brown, *Nucl. Instrum. Methods Phys. Res. Sect. B*, **1984**, *5*, 289-293.
31. V.L. Mbele, S.M. Mullins, S.R. Winkler, S. Woodborne, *Phys. Procedia*, **2017**, *90*, 10-16.
32. C. Bronk Ramsey, *Radiocarbon, **2009**, 51,* 337-360.
33. A.G. Hogg, T.J. Heaton, Q. Hua, J.G. Palmer, C.S.M. Turney, J. Southon, A. Bayliss, P.G. Blackwell, G. Boswijk, C.B. Ramsey, C. Pearson, F. Petchey, P.J. Reimer, R.W. Reimer, L. Wacher, *Radiocarbon*, **2020**, *62(4)*, 759-778.

STUDIA UBB CHEMIA, LXVIII, 3, 2023 (p. 153-160)
(RECOMMENDED CITATION)
DOI:10.24193/subbchem.2023.3.10

TOXICITY OF HEMOGLOBIN DERIVATIZED WITH OXIDIZED ADENOSINE TRIPHOSPHATE AGAINST TUMORAL HUMAN CELLS

Eva FISCHER-FODOR[a], Kinga SZABO[b], Florina SCURTU[b], Maria LEHENE[b], Radu SILAGHI-DUMITRESCU[b]*

ABSTRACT. Adenosine triphosphate (ATP) has a high affinity for the organic phosphate binding site of hemoglobin (Hb), affecting the affinity for oxygen. Periodate-oxidized-ATP (oATP) behaves as an affinity tag for several enzymes that use ATP as a substrate and has the ability to form intermolecular aldimine bonds by reaction with free amino groups on proteins. Due to its unique structure, oATP has been used to produce structural and functional modifications of Hb to obtain a compound with a low affinity for oxygen that could be used as a blood substitute. However, the oATP-Hb derivative was shown to present a notable increase in pro-oxidative reactivity compared to Hb *in vitro*, and accordingly exhibited toxicity in *in vivo* studies. This pro-oxidant reactivity was alleviated by crosslinking Hb with bovine serum albumin (BSA) in an oATP-Hb-BSA copolymer. We now show that oATP and oATP-Hb-BSA display high-affinity toxicity towards cancer cells, and may hence deserve further investigation as adjuvants in anti-cancer therapy.

Keywords: *hemoglobin, cells, oATP, blood substitute, cancer*

INTRODUCTION

Red blood cells (erythrocytes) are uniquely suited to the task of oxygen transport for several important reasons. Firstly, these cells contain a high concentration of hemoglobin (35 g/dL), capable of transporting 47 mL O_2 /100 mL

[a] *Tumor Biology Department, Institute of Oncology "Prof. Dr. Ion Chiricuta", RO-400015, Cluj-Napoca, Romania*
[b] *Babeş-Bolyai University, Faculty of Chemistry and Chemical Engineering, 11 Arany Janos str., RO-400028, Cluj-Napoca, Romania*
* *Corresponding author: radu.silaghi@ubbcluj.ro*

of red cells [1]. The resulting overall oxygen binding capacity of the erythrocytes is about 18 mL/dL [2]. Secondly, erythrocytes are deformable; they can therefore efficiently diffuse through capillary vessels, thus providing a reasonable diffusion distance of oxygen from the alveolar space of the lung to hemoglobin, or from hemoglobin to cells. Thirdly, hemoglobin binds oxygen cooperatively and is under the control of the Bohr effect: local pH conditions and carbon dioxide affect the oxygen-binding behavior of hemoglobin in ways favorable for oxygen transport [3].

Hemoglobin (Hb) is a tetrameric protein with a diameter of 5.5 nm containing four prosthetic heme groups. Adult hemoglobin contains two types of subunits - two α-chains (consisting of 141 amino acids each) and two β-chains (consisting of 146 amino acids each) [4]. The three-dimensional structures of the two subunits are very similar, and the quaternary structure shows strong interactions between the subunits [2]. Hemoglobin must efficiently bind oxygen in the lungs, where pO_2 is around 13.3 kPa, and release oxygen to the tissues, where pO_2 is 4 kPa. Oxygen binding to the heme Fe in human Hb is modulated by the effector BPG (2,3-bisphosphoglycerate). In addition to BPG, the ability of Hb to release O_2 is also determined by other metabolites or anions in the intercellular compartment: H^+ , NO, adenosine triphosphate (ATP), Cl^- , CO_2 [5].

The development of a synthetic or semi-synthetic blood substitute has for decades been an active research area, aiming to reduce the shortage of blood needed for transfusions. Blood substitutes would have advantages over human blood such as accessibility, validity and are free of risk of infection. There are currently two main categories of blood substitutes under development: protein (especially hemoglobin, but also hemerythrin)-based oxygen carrier molecules (HBOCs) and fluorocarbonate-based carrier molecules [6].

Free hemoglobin is lethal because of redox activity, filtration in the kidneys, affinity for oxygen or NO dioxygenase reactivity; if reactivity of this type is controlled or reduced, Hb becomes the ideal candidate for a blood substitute. In order to achieve this function Hb undergoes a series of modifications/transformations such as: intra- and intermolecular cross- linking, polyethylene glycol derivatization, genetic modification, or encapsulation [7]. The first generation of polymers (Hb polymerized with glutaraldehyde, conjugated Hb or Hb cross-linked with oxidized adenosine triphosphate, oATP) exhibit renal toxicity, as well as other side-effects. Clinical studies have shown toxicity to the body, and these substitutes are no longer used - except for the glutaraldehyde-polycondensed Hb currently approved for human use in South Africa and Russia. The second generation of products (substitutes obtained by recombination and genetic modification) are based on a better understanding of vasoconstriction and have lower toxicity [8,9].

One of the crosslinking agents previously employed for Hb derivatization is the dialdehyde obtained by oxidation of adenosine triphosphate (ATP) with periodate, cf. Scheme 1. The two aldehyde groups allow condensation with amino groups on the surface of Hb.

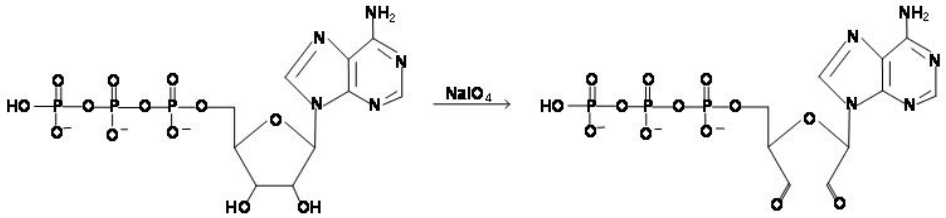

Scheme 1. Oxidation of adenosine triphosphate (ATP) by treatment with periodate.

The oATP-Hb derivative of hemoglobin was previously shown to present a notable increase in pro-oxidative reactivity compared to Hb *in vitro*, and accordingly exhibited toxicity in *in vivo* studies. This pro-oxidant reactivity was alleviated by crosslinking Hb with bovine serum albumin (BSA) in an oATP-Hb-BSA copolymer. Better performance *in vivo* was seen for the Hb-BSA copolymer when glutaraldehyde was employed as crosslinker instead of oATP. As a result, neither oATP-Hb nor oATP-Hb-BSA are currently pursued as viable blood substitute candidates [10–12]. We now report that oATP and oATP-Hb-BSA in fact display high-affinity toxicity towards cancer cells, and may hence deserve further investigation as adjuvants in anti-cancer therapy.

RESULTS AND DISCUSSION

The pro-oxidant reactivity of Hb has been argued to be a key factor responsible not only for a number of physio-pathological conditions, but also for the biological side-effects of Hb-based blood substitute candidates [4,12,21–27,13–20]. Such reactivity is enhanced under low-oxygen conditions [28–30]. Such hypoxic conditions are typical for tumors; the question may then be asked, whether the inherent pro-oxidative capacity of Hb-based blood substitute candidates may be turned into an advantage by deploying such molecules against tumors. To this, end, Hb derivatized with oATP (Hb-oATP) and the corresponding copolymer with BSA (Hb-BSA-oATP) are tested here against two lines of tumoral cells.

The cells used for these tests are DLD-1 and HT-29 - human colon tumour cells. As shown in Figure 1, he IC_{50} (half inhibitory concentration) for DLD-1 cells treated with Hb-oATP is 9.5 μM, while that for Hb-BSA-oATP is

26.0 μM. These values reflect a clear inhibitory activity on DLD-1 tumor cell growth.

As shown in Figure 2, the IC_{50} on the HT-29 cell line for Hb-oATP is 11.8 μM, while that of Hb-BSA-oATP is 16.7 μM. These values may be interpreted to reflect an efficient inhibitory activity on the growth of HT-29 tumor cells.

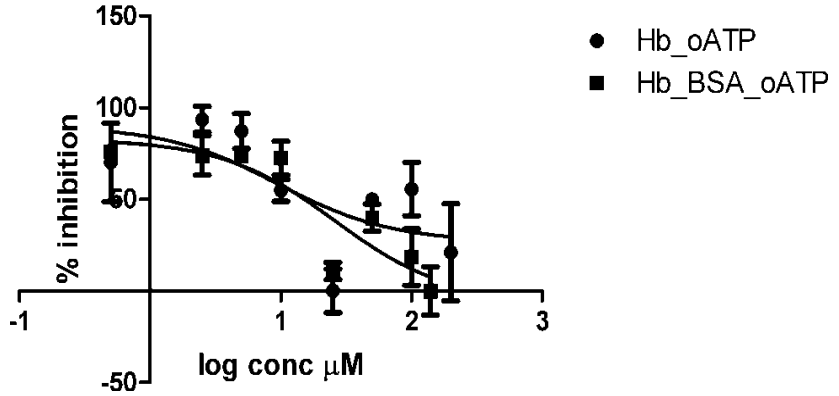

Figure 1. Sigmoidal dose-response curves representing DLD-1 tumor cell viability 24 hours after treatment with Hb-oATP and Hb-BSA-oATP.

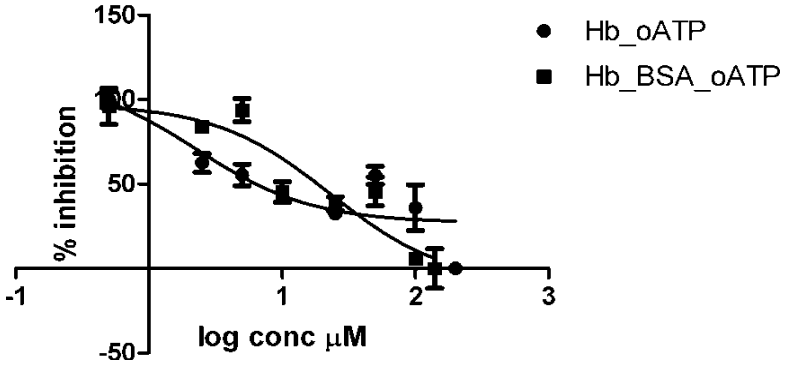

Figure 2. Sigmoidal dose-response curves representing the viability of HT-29 tumor cells 24 h after treatment with Hb-oATP and Hb-BSA-oATP.

In both of the tested tumoral cell lines the IC_{50} values suggest that Hb-oATP has a slightly better cytotoxicity. Concentrations close to the IC_{50}, or even ten times higher, can easily be achieved in a patient by injecting relatively small amounts of oATP-derived hemoglobin - i.e. concentrations that

would not invoke the side reactions otherwise known in some blood substitute candidates [4,12,21–27,13–20]. This suggests a possible utility of Hb-oATP as an active component for anti-tumor therapy. Although at 100 μM both Hb derivatives display an almost 100 % degree of inhibition, it is not expected that they would be efficient as anti-tumoral agents on their own / alone.

Of the two candidates examined here, further tests were performed using the BSA copolymer on normal / healthy human cells, since (as detailed above) this substance was previously shown to elicit less side-effects during *in vivo* experiments. These additional tests were performed on healthy isolated peripheral human blood lymphocytes using Ficoll-Paque tubes. Several cell types were used for testing: CD4 positive and CD8 positive T lymphocytes, CD19 positive B lymphocytes and CD14 positive monocytes. These cells were treated with Hb-BSA-oATP at a concentration of 100 μM in cell medium and cell survival was assessed 24 h after treatment using the MTT viability assay. As shown in Figure 3, after treatment with Hb-BSA-oATP, lymphocyte cell viability was slightly altered, in CD4+ and CD14+ cells cell viability decreased, while in CD19+ B cells it was observed that treated cells had better viability than untreated ones (Anova test, Bonferroni post-test, $p<0.05$). No influence was detected on the CD8+ population. Notably, overall these effects were minor and far smaller than the degrees of magnitude seen in Figures 1 and 2 for tumoral cells.

Measurements on cytokine signaling molecules in cells shown in Figure 3 after exposure to Hb-BSA-oATP treatment did reveal measurable changes, with pro- as well as anti-inflammatory potential. This suggests a possible practical utility in further exploring the molecular immunology responses behind the interaction of oATP-derived Hb with tumoral as well as with healthy cells.

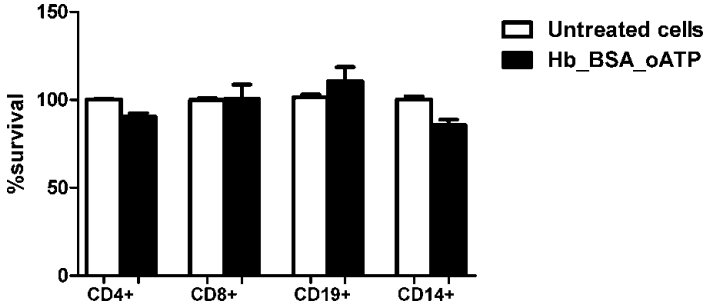

Figure 3. Influence of Hb-BSA-oATP on human cells *in vitro* after 24 h post exposure: survival of CD4 positive and CD8 positive T lymphocytes, CD19 positive B lymphocytes and CD14 positive monocytes monitored 24 h post treatment was followed.

CONCLUSIONS

Following tests on two colon tumor cell lines, it can be stated that Hb-oATP as well as Hb-BSA-oATP display cytotoxicity (slightly stronger for the former than for the latter) against tumoral cell lines. Following treatment of peripheral mononuclear cell subpopulations with oATP-derived hemoglobin in the presence of antioxidant (BSA), cell viability was followed with the MTT assay. In T lymphocytes and monocytes viability was maintained, the reduction being statistically insignificant, and in B lymphocytes the treatment induced a slight increase in viability. These findings may warrant further investigations on possible therapeutic perspectives of oATP-derivatives of Hb in antitumor therapy, as well as further investigation of the cellular response mechanisms towards these and other Hb derivatives previously proposed as blood substitute candidates.

EXPERIMENTAL SECTION

The following substances were used to conduct the experiments: bovine hemoglobin (Hb), purified as previously described [1], adenosine triphosphate (ATP), sodium periodate, glutaraldehyde, sodium borohydride were obtained from Sigma-Aldrich (Munich, Germany) and used as received. The human cell lines were manipulated and treated as previously described (including the respective ethical visas) [18,22,27,31–33]. The Hb-oATP polymer and Hb-BSA-oATP copolymer stock solutions were produced as previously described [16,34]. A Hanna pH 212 pH meter (Hanna Instruments, Italy) was used to monitor and correct the pH value of the solutions, generally adjusted with 20% hydrochloric acid or sodium hydroxide. The concentrations of Hb solutions were determined using a Cary 50 UV-vis spectrophotometer (Varian, Inc., Foster City, CA, USA).

ACKNOWLEDGMENTS

Prof. Dr. Mihai Cenariu (USAMV Cluj), dr. Denisa Hathazi (UBB) and Mariann Arkosi (UBB) are thanked for technical assistance with experiments and helpful discussions.

REFERENCES

1. B. Giardina; I. Binotti; G. Amiconi; E. Antonini; M. Brunori; C. H. Mcmurray; *Eur. J. Biochem.* **1971**, *22***,** 327–330.
2. A. G. Greenburg; H. W. Kim; *Crit. Care* **2004**, *8***,** 61–64.
3. F. Deac; B. Iacob; E. Fischer-Fodor; G. Damian; R. Silaghi-Dumitrescu; *J. Biochem.* **2011**, *149***,** 75–82.
4. V.-F. Scurtu; A. C. Moţ; R. Silaghi-Dumitrescu; *Pharmaceuticals* **2013**, *6***,** 867–880.
5. D. M. Kurtz Jr.; D. P. Ballou; D. M. Kurtz Jr.; D. P. Ballou; *Essays Biochem.* **1999**, 55–80.
6. E. Alomari; L. Ronda; S. Bruno; G. Paredi; M. Marchetti; S. Bettati; D. Olivari; F. Fumagalli; D. Novelli; G. Ristagno; R. Latini; C. E. Cooper; B. J. Reeder; A. Mozzarelli; *Free Radic. Biol. Med.* **2018**, *124*, 299–310.
7. T. M. S. Chang; *Crit. Care Clin.* **2009**, *25***,** 373–382.
8. T. M. Chang; *Artif Organs* **2004**, *28***,** 789–794.
9. R. M. Winslow; *Vox Sang.* **2006**, *91***,** 102–110.
10. A. D. Stoica; V.-A. Toma; I. Roman; B. Sevastre; F. Scurtu; R. Silaghi-Dumitrescu; *Bioinorg. Chem. Appl.* **2022**, *2022***,** 1–6.
11. A. D. Farcas; V. A. Toma; I. Roman; B. Sevastre; F. Scurtu; R. Silaghi-Dumitrescu; *Bioinorg. Chem. Appl.* **2020**, *2020***,** 1096573.
12. V. A. Toma; A. D. A. D. Farcas; I. Roman; B. Sevastre; D. Hathazi; F. Scurtu; G. Damian; R. Silaghi-Dumitrescu; *Int J Biol Macromol.* **2017**, *107***,** 1422–1427.
13. A. Mot; A. Roman; R. Silaghi-Dumitrescu; in *Metal Elements in Environment, Medicine and Biology Tome IX* (eds. Silaghi-Dumitrescu R. & Garban G.) (Cluj University Press, **2009**). 122–125.
14. F. V Deac; A. M. Bolfa; C. Magdas; B. Sevastre; S. Turc; R. Silaghi-Dumitrescu; *Rom. J. Biochem.* **2010**, *47*, 135–141.
15. D. Hathazi; F. Scurtu; C. Bischin; A. Mot; A. A. A. Attia; J. Kongsted; R. Silaghi-Dumitrescu; *Molecules* **2018**, *23***,** E350.
16. F. Deac; B. Iacob; E. Fischer-Fodor; G. Damian; R. Silaghi-Dumitrescu; *J. Biochem.* **2011**, *149***,** 75–82.
17. F. Scurtu; O. Zolog; B. Iacob; R. Silaghi-Dumitrescu; *Artif. Cells, Nanomedicine, Biotechnol.* **2014**, *42***,** 13–17.
18. E. Fischer-Fodor; A. Mot; F. Deac; M. Arkosi; R. Silaghi-Dumitrescu; *J. Biosci.* **2011**, *36***,** 215–221.
19. M. Arkosi; F. Scurtu; A. Vulpoi; R. Silaghi-Dumitrescu; D. Kurtz; *Artif. Cells, Nanomedicine, Biotechnol.* **2017**, *45***,** 218–223.
20. B. J. Reeder; M. Grey; R.-L. Silaghi-Dumitrescu; D. A. Svistunenko; L. Bülow; C. E. Cooper; M. T. Wilson; *J. Biol. Chem.* **2008**, *283***,** 30780–30787.
21. A. C. Mot; A. Roman; I. Lupan; D. M. Kurtz; R. Silaghi-Dumitrescu; *Protein J.* **2010**, *29***,** 387–393.
22. D. Hathazi; A. C. Mot; A. Vaida; F. Scurtu; I. Lupan; E. Fischer-Fodor; G. Damian; D. M. Kurtz Jr.; R. Silaghi-Dumitescu; *Biomacromolecules* **2014**, *15***,** 1920–1927.

23. F. Scurtu; B. Tebrean; M. K. Árkosi; A. Ionele; R. Silaghi-Dumitrescua; *Stud. Univ. Babeș-Bolyai Chem.* **2019**, *64***,** 421–434.
24. M. Arkosi; A. C. Mot; I. Lupan; M. G. G. Tegla; R. Silaghi-Dumitrescu; *Protein J.* **2023**, *42***,** 374–382.
25. C. E. Cooper; R. Silaghi-Dumitrescu; M. Rukengwa; A. I. Alayash; P. W. Buehler; *Biochim. Biophys. Acta - Proteins Proteomics* **2008**, *1784***,** 1415–1420.
26. F. Scurtu; A. Popa; R. Silaghi-Dumitrescu; *Stud. Univ. Babes-Bolyai Chem.* **2017**, *62***,** 59–66.
27. O. Zolog; A. Mot; F. Deac; A. Roman; E. Fischer-Fodor; R. Silaghi-Dumitrescu; *Protein J.* **2011**, *30***,** 27–31.
28. B. J. Reeder; D. A. Svistunenko; C. E. Cooper; M. T. Wilson; *Antioxid. Redox Signal.* **2004**, *6***,** 954–966.
29. K. P. Moore; S. G. Holt; R. P. Patel; D. A. Svistunenko; W. Zackert; D. Goodier; B. J. Reeder; M. Clozel; R. Anand; C. E. Cooper; J. D. Morrow; M. T. Wilson; V. M. DarleyUsmar; L. J. Roberts; V. Darley-Usmar; L. J. Roberts 2nd; L. J. Roberts 2nd; V. M. DarleyUsmar; L. J. Roberts; *J. Biol. Chem.* **1998**, *273***,** 31731–31737.
30. M. Lehene; E. Fischer-Fodor; F. Scurtu; N. D. Hădade; E. Gal; A. C. Mot; A. Matei; R. Silaghi-Dumitrescu; *Pharmaceuticals* **2020**, *13***,** 107.
31. R. Silaghi-Dumitrescu; C. Gruian; C. Puscas; A. Simon; E. Fisher-Fodor; V. Al Toma; A. Farcas; I. Roman; V.-F. Scurtu; A. A. A. Attia; G. Damian; *Stud. Univ. Babeș-Bolyai Chem.* **2020**, *65***,** 121–132.
32. B. Mureşan; C. Cimpoiu; A. Hosu; C. Bischin; E. Gal; G. Damian; E. Fischer-Fodor; R. Silaghi-Dumitrescu; *Stud. Univ. Babes-Bolyai Chem.* **2015**, *60***,** 355–370.
33. D. Tamokou Jde; J. R. R. Chouna; E. Fischer-Fodor; G. Chereches; O. Barbos; G. Damian; D. Benedec; M. Duma; A. P. N. P. Efouet; H. K. K. Wabo; J. R. R. Kuiate; A. Mot; R. Silaghi-Dumitrescu; *PLoS One* **2013**, *8***,** e55880.
34. B. Iacob; F. Deac; D. Cioloboc; G. Damian; R. Silaghi-Dumitrescu; *Artif. Cells Blood Substitutes Biotechnol.* **2011**, *39*, 293–297.

STUDIA UBB CHEMIA, LXVIII, 3, 2023 (p. 161-178)
(RECOMMENDED CITATION)
DOI:10.24193/subbchem.2023.3.11

DETERMINATION OF THE CHEMICAL COMPOSITION IN DİFFERENT PLANT PARTS OF *S. MOLLIS* TAXA

Emine YURTERI[a*], Serdar MAKBUL[b], Mutlu GÜLTEPE[c], Fatih SEYIS[a]

ABSTRACT. The volatile oil composition and secondary metabolite content in different parts of *S. mollis* ssp*. mollis* and *S. mollis* ssp. *szowitzii* were investigated in this study. Based on their chemical composition, the components of the *S. mollis* ssp*. mollis* and *S. mollis* ssp. *szowitzii* plant species could be distinguished in the current study. Using GC-MS analysis, 70 distinct volatile oil components could be found in various plant sections of this species*.* Avicularin, Biapigenin, and Hyperoside were found in the highest concentrations in all plant parts of both species. Further, Catechine and Chlorogenic acid could be detected in all plant parts of *S. mollis* ssp*. mollis*.The volatile oil composition and secondary metabolite content of different parts of this investigated two species revealed high variability, displayed by Biplot Analysis. Different components of medicinal importance could be detected in different parts of this species. These compounds could be isolated and used for further basic investigations.

Keywords: *Scorzonera mollis, volatile oil, secondary metabolites, Türkiye*

INTRODUCTION

Several plants are still used in Turkish folk medicine to treat a variety of disorders since they are widely known for their therapeutic properties in Turkish culture. One of the world's significant gene hubs for plant diversity is

[a] *Recep Tayyip Erdogan University, Faculty of Agriculture, Field Crops Department, Academy Street, 53300, Pazar-Rize, Türkiye*
[b] *Recep Tayyip Erdogan University, Faculty of Science, Biology Department, Zihni Derin Campus, 53100, Rize, Türkiye*
[c] *Giresun University, Vocational High School, Forestry Department, Yayla Street, 28902, Dereli -Giresun, Türkiye*
* *Corresponding author: emine.yurteri@erdogan.edu.tr*

Turkey. Turkey is projected to have 10.000 flowering plant taxa, which is almost as many as all of Europe [1-3]. The number of plant species utilized as folk remedies in Turkey has lately been estimated to be approximately 1,500, up from earlier estimate of 500 [4]. Traditional Greco-Arabic (Unani) medicine is still commonly used in the south and southeast of Turkey.

The largest and name-giving genus of the Cichorieae subtribe Scorzonerinae is Scorzonera L., which has 180–190 species [5]. Members of the genus are mostly found in the dry and mountainous Irano-Turanian region, although they are also widely distributed in temperate and subtropical regions of Eurasia and N Africa. The genus is represented by perennial herbs, frequently with a caudex or tuber, and infrequently by biennials or dwarf subshrubs with linear to oblong, whole to pinnatisect leaves. [6]. *Scorzonera* is represented by 59 taxa, 31 of them endemic to Türkiye, in Türkiye [7]. Several species of *Scorzonera* were utilized in Anatolian folk medicine [8-13]. These species are distinguished with a rich latex component. Further, flavonoids [14], bibenzyl derivatives [15], benzyl phthalates [16], coumarins [17], dihydroisocoumarins [18], phenolic acid derivatives [19], lignans – neolignans [20], sesquiterpenes [21] and triterpenes [22] were determined in the genus.

Scorzonera mollis is represented with two subspecies named as *Scorzonera mollis* ssp*. mollis* and *Scorzonera mollis* ssp*. szowitzii* in Türkiye. These taxa which belongs to the Iranian-Turanian phytogeographic region, usually grows in all over the Anatolia, Türkiye. [7]. These plants grow in rocky places, gypsum soils, meadows, and clearance of *Quercus sp* and *Pinus sp*. [7].

When we examine the medicinal applications of various civilizations, plants with medicinal value always come to the forefront. Medicinal plants have been used to treat health problems, enhance the flavor of food, and preserve it [23]. Furthermore, such plants were widely used in the prevention of disease epidemics. Furthermore, plants with medicinal value comprise a large group of plants that are of great interest due to their pharmaceutical, cosmetic, and nutritional properties [24].

Volatile oils exhibit a variety of biological activities, such as antibacterial, antioxidant, antiviral, insecticidal etc. [25]. They are also used in cancer treatment, food preservation, aromatherapy, perfumery industries [26] wound healing [27], treatment of various infectious diseases, and as natural organic compounds and medicines [26,28]. Volatile oils are becoming increasingly important as they are used in the beverage and food industries, cosmetics and fragrance industries to create valuable perfumes with a variety of biological activities [29].

To date, it appears that the volatile oil composition and polar metabolites of *S. mollis* ssp. *szowitzii* have not been thoroughly studied in Turkey. *S. undulata*

spp. *deliciosa* [17], *S. undulata* [30], *S. sandrasica* [31], and *S. calyculata* [32] have all been studied. The current study aims to present for the first time in Turkey the findings about the volatile oil composition and secondary metabolite content of *S. mollis* ssp. *szowitzii*. The obtained results will provide additional insight into the chemical composition of plant parts in this species and reveal the species' potential value.

Phenolic content analyses for *S. cinerea*, *S. eriophora*, *S. incia*, *S. laianiata*, *S. parviflora*, *S. cana* (C.A. Meyer) Hoffm. var. a*lpina*, *S. cana* (C.A. Meyer) Hoffm. var. j*acquiniana*, *S. cana* (C.A. Meyer) Hoffm was published earlier [33]. Furthermore, chemosystematic studies were conducted on S. aristata, S. austriaca, S. boetica, S. crispatula, S. hispanica, *S. trachysp*. and *S. villosa*, respectively [34]. The phenolic components and in vitro antioxidant, anti-inflammatory, and antibacterial properties of *S. hieraciifolia* Hayek were investigated [19]. The phenolic compounds from *S. tomentosa* and *S. judaica* were studied moreover by [18, 20, 35]. Also the phytochemical composition and antioxidant activity of *S. suberosa*, *S. laciniata* and *S. latifolia* was screened [36].

Chemical composition using GC-MS was determined in *S. sandrasica* [31], *S. undulata* [30], *S. undulata* ssp. *deliciosa* (Guiss) [17] and *S. hispanica* [37]. Antioxidant and antihyperglycemic activity of *S. cinerea* [38], chemical composition (GC-MS), antioxidant, antibacterial and anticancer activities of *S. calyculata* Boiss. [39] and prospective neurobiolocal effects of different plants [40] were topics of Scorzonera research.

Also, information on the anti-antinociceptive action of *S. latifolia*, *S. mollis* ssp. *szowitsii*, *S. suberosa*, and *S. tomentosa* as well as natural compounds derived from *S. aristata* [41] was presented. Biologically active natural compounds from *S. divaricata* and S*. pseudodiaricata* in Mongolia were published by [42]. Two novel phenolic compounds and certain biological activities of *S. pygmaea* were identified [43]. The anti-diabetic effects of extracts from the aerial portions of *S. tomentosa*, *S. mollis* ssp. *szowitsii*, *S. suberosa* ssp. *suberosa*, *S. eriophora*, *S. acuminata*, *S. sublanata*, and *S. cana* var. *jacquiniana* were also assessed [44].

A pharmacognostic, antibacterial, and laxative investigation of *S. undulata* was reported [45]. In *S. aristata*, *S. austriaca*, *S. boetica*, *S. crispatula*, *S. hispanica*, *S. trachysperma*, and *S. villosa*, phenolic compounds were identified by [31]. The inulin form in *S. hispanica* was described [46]. *S. mackmeliana*'s antibacterial and antibiofilm activity were also identified [47].

S. undulata's antibacterial potential was published by [48]. *S. cinerea* Boiss., S*. latifolia* (Fisch Mey.) DC., *S. incisa* DC., *S. mollis S. parviflora* Jocq., Bieb. ssp. *szowitzii* (DC.) Chamb., S*. tomentosa* L were examined [49] *S. acuminata* Boiss., *S. cana* (C.A: Meyer) Hoffm. var. *alpina* (Boiss.) Chamberlain,

S. cana (C.A. Meyer) Hoffm. var. *jacquiniana* (W. Koch) Chamberlain, *S. cana* (C.A Meyer) Hoffm. var. *radicosa* (Boiss. -) Chamberlain, *S. eriophora* DC., *S. suberosa* C. Koch ssp. *suberosa* and *S. sublanata* were investigated regarding their capacity for wound healing [50]. *S. paradoxa* Fisch and C.A. Mey was assessed regarding fatty acid compositions, chemical content, and antioxidant activity [51].

In general, studies on *S. mollis* taxa chemical profile are rarely. The current study's objective is to give information regarding the volatile oil and phenolic makeup of various *S. mollis* parts. Results will provide additional insight into the chemical profile of plant parts in this species and highlight the species' potential worth.

RESULTS AND DISCUSSION

Table 1 shows the volatile compounds of various *S. mollis* ssp. *mollis* and *S. mollis* ssp. *szowitzii* plant parts. The root, stem, and leaf parts of this species' contained 70 different volatile oil components. It is obvious that the volatile oil composition of different plant parts of these two *Scorzonera* species varies. Some volatile oil components were detected only in the root, others only in the stem and leaves of *S. mollis* ssp. *mollis* and *S. mollis* ssp. *szowitzii*, and their percentages varied.

Table 1. Percentage of volatile oil composition of *S. mollis* ssp. *szowitzii* and *S. mollis* ssp. *mollis* plant parts (Values are given as mean of three parallel analysis)

No	RI*	Component	*S. mollis* ssp. *szowitzii*			*S. mollis* ssp. *mollis*		
			Root	Stem	Leaf	Root	Stem	Leaf
		Monoterpene Hydrocarbons						
1	933	α-Pinene	1.67	0	0	0	1.19	0
2	975	β-Pinene	3.66	1.19	0	0	0	0
3	1393	Neodene	1.36	0	0	0	0	0
	Total		6.69	1.19	0	0	1.19	0
		Oxygenated Monoterpenes						
4	1032	Eucalyptol	0	0	0	0.56	0	0
5	1165	Isoborneol	0	0	0	1	0	0
6	1267	Piperitone	0	0	0	0.88	0	0
7	1406	Eugenol	0	0	1.73			
8	Total		0	0	1.73	2.44	0	0
9		**Oxygenated Sesquiterpenes**						
10	1458	Sesquicineole	0	0	2.11	0	0	0
11	1589	Caryophyllene oxide	1.38	8.16	6.81	0	7.49	4.38
12	1693	Bergamotol	0	0	0	0.63	0	0
	Total		1,38	8.16	8.92	0.63	7.49	4.38

No	RI*	Component	*S. mollis* ssp. *szowitzii*			*S. mollis* ssp. *mollis*		
			Root	Stem	Leaf	Root	Stem	Leaf
		Sesquiterpene Hydrocarbons						
13	1367	Cyclosativene	1.52	1.14	0	1.46	0	0
14	1375	α-Copaene	0.92	0	0	3.65	1.14	1.6
15	1391	β-Patchoulene	2.32	20.68	12.31	0	0	0
16	1404	α-Gurjunene	0	0.99	1.65	0	0	0
17	1424	β-Caryophyllene	0	1.12	0	0	11.82	12.02
18	1435	Thujopsene	0	1.06	0	0	0	0
19	1449	α-Himachelene	0	0	3.88	0	0	0
20	1458	α-Humulene	0	1.84	1.28	0	1.41	0.96
21	1473	α-Ionone	1.07	0	0	0	0	0
	1480	α-Curcumene	0	0	0	2.74	0	0
22	1485	Germacrene D	0	0	2.01	0	0	1.1
23	1489	β-Chamigrene	0	1.31	0	0	0	0
24	1490	β-Ionone	4.39	0	0.79	0	3.17	4.73
25	1497	α-Muurolene	1.52	0	0	0	0	0
26	1498	Valencene	1.52	1.14	0	0	0	0
27	1528	Δ-Cadinene	0.92	0	0	0	0	0
28	1367	Cyclosativene	2.32	20.68	12.31	0	0	0
	Total		23,92	32.17	23.72	7.85	17.54	20.41
		Alcohols, Ketones, Aldehydes, Furans						
29	790	Ethyl n-propyl ketone	1.27	2.02	0	0	0	0
30	792	Pentanol	0	0	0	0	0.95	1.89
31	801	Capronaldehyde	5.15	5.12	1.69	0	0	0
32	902	Enanthaldehyde	0	1.03	0	0	0	0
33	958	Benzaldehyde	0	0	0	0	1.23	0
34	1003	Caprylaldehyde	0	1.25	0	0	0	0
35	1034	Benzyl alcohol	0	0	0	0	1.09	0
36	1042	Phenylacetaldehyde	0	0	0	0	0.95	1.03
37	1107	Pelargonaldehyde	0	2.55	8.65	0	0.94	0
38	1163	Nonenal	0	0	0	0.53	0	0
39	1206	Capraldehyde	0	0.93	0	0	0	0
40	1231	Caprylyl acetate	1.41	1.67	0	0	0	0
41	1305	Dihydrocarvyl acetate	0	1.04	0	0	0	0
42	1366	Neryl acetate	0	0	0	0.9	0	0
43	1394	Undecyl alcohol	0	0	0	0.69	0	0
44	1493	Lauryl alcohol	0	1.87	0	0.63	0	0.99
45	1500	Pentadecane	6.62	2.33	1.55	2.02	1.37	2.31
46	1573	Tridecenal	1.7	0.94	0	0	0	1.17
47	1580	Tridecyl alcohol	1.71	0.97	1.48	0	0	1.27
48	1614	Tetradecanal	0	0	1.23	0.63	0	0
49	1680	Myristic alcohol	2.62	1.56	0.9	0	2.49	2.2
50	1691	Tridecyl methyl ketone	0	0	0	0	0	0.79
51	1753	Farnesal	3.52	0	0	4	0	0
52	1784	Pentadecanol	0	0	0	0	0	1.06
53	1881	Cetyl alcohol	0	0	1.4	0.68	0	0
54	1922	Hexadecenoic acid	0	0	1.05	0	1.23	0
55	2115	Phytol	0	0	0	6.03	10.26	12.08
56	Total		24,00	23.28	17.95	17.41	22.87	24.79

No	RI*	Component	*S. mollis* ssp. *szowitzii*			*S. mollis* ssp. *mollis*		
			Root	Stem	Leaf	Root	Stem	Leaf
57		**Alkanes, Alkenes, Alkynes, Arenes**						
58	1040	Octenone	1.08	1.42	0	0	0	0
59	1072	Octenol	0	0	1.02	0	0	0
60	1108	Hendecane	0	0	0	0	0	0.92
61	1196	Myrtenal	0.9	0	0			
62	1301	Tridecane	1.4	1	0	0	0	0.81
63	1400	Tetradecane	3.73	3.23	2.04	1.19	1.21	1.66
64	1600	Hexadecane	16.42	9.15	5.73	7.12	5.71	7.86
47	1700	Heptadecane	7.24	4.43	3.31	5.5	4.32	4.9
48	1800	Octadecane	1.39	2.27	1.89	1.86	3.2	3.16
49	1901	Nonadecane	0	1.44	0	3.27	4.07	5.61
50	2001	Eicosane	0	0	0	1	2.33	0
51	2018	Civetone	3.85	0	0	42.62	0	0
52	2100	Heneicosane	0	2.25	9.93	2.26	1.33	2.78
	Total		36,01	25.19	23.92	64.82	22.17	27.7
		Ethers, Carboxylic acids, Esters						
53	796	Lactate ethyl	0	2.1	0	0	0	0
54	797	Lactate	0	0	0	0	1.08	0
55	991	Furan	0.96	0	0	0.54	0	0
56	1454	Geranyl acetone	1.34	1.3	0.85	0.9	2.19	1.12
57	1532	Citonellyl butyrate	0	0	2.02	0	3.51	5.2
58	1577	Undecalactone	2.23	0	0	0	0	0
59	1649	Furan-2-carboxylic	0	0	0	0	0	2.31
60	1656	Citronellyl tiglate	0	0	0.96	0	0	0
61	1657	Dihydrojasmonate	0	1.00	0	0	1.41	1.76
62	1658	Hedione	0	0	0	1.4	0	0
63	1671	Jasmonate methyl	0	0	0	2.01	0	0
64	1672	Dodecalactone	0	0	1.49	1.23	0	2.06
65	1683	Apiole	0	1.15	0	0	0	0
66	1841	Phytone	0	0	6.24	0	10.7	8.76
67	1925	methyl Palmitate	3.45	3.52	5.84	0.75	8.43	1.51
68	1996	Palmitate ethyl	0	0.94	0	0	1.44	0
69	2115	Phytol	0	0	4.77	0	0	0
	Total		7,98	10.01	22.17	6.83	28.76	22.72
		Others						
70	1392	Thiazole	0	0	1.61	0	0	0
	Total		0	0	1.61	0	0	0
		Chemical classes						
		Monoterpene Hydrocarbons	6.69	0	0	0	0	0
		Oxygenated Monoterpenes	0	1.48	0	2.44	0	0
		Oxygenated Sesquiterpenes	1.38	8.16	8.92	0.63	7.49	4.38
		Sesquiterpene hydrocarbons	23.92	32.17	23.72	7.85	17.54	20.41
		Alcohols, Ketones, Aldehydes, Furans	24.00	23.28	17.95	17.41	22.87	24.79
		Alkanes, Alkenes, Alkynes Arenes	36.01	25.19	23.92	64.82	22.17	27.7
		Ethers, Carboxylic acids, Esters	7.98	10.01	22.17	6.83	28.76	22.72
		Others	0	0	1.61	0	0	0
		Totally	99.98	100	100	99.98	100	100

*Kovats Retention Index (RI)

In *S. mollis* ssp. *mollis*, Eucalyptol, Isoborneol, Piperitone, Bergamotol, α-Curcumene, Tetradecanal, Cetyl alcohol, Civetone, Furan, Hedione and Methyl Jasmonate were present only in root parts. If we consider the other species, *S. mollis* ssp. *szowitzii* α-Pinene, Neodene, α-Copaene, α-Ionone, α-Muurolene, γ-Cadinene, Farnesal, Myrtenal, Civetone and Furan were detected only in roots of this species.

Stem parts of *S. mollis* ssp. *mollis* contained 8 components: α-Pinene, Benzaldehyde, Benzyl alcohol, Pelargonaldehyde, Hexadecenoic acid, Lactate and Dihydrojasmonate. On the other hand, there were 12 components that were only found in stem parts *S. mollis* ssp. *szowitzii*: β-Caryophyllene, Thujopsene, β-Chamigrene, Enanthaldehyde, Caprylaldehyde, Capraldehyde, Dihydrocarvyl acetate, Lauryl alcohol, Nonadecane, Dihydrojasmonate, Apiole and Ethyl Palmitate.

The leaves of *S. mollis* ssp. *mollis* displayed 8 volatile oil components, namely Germacrene D, Tridecenal, Trideceyl alcohol, Tridecyl methyl ketone, Pentadecanol, Hendecane, Tridecane and Furan-2-carboylic acid. If we examine further, the leaves of *S. mollis* ssp. *szowitzii*, we find substances that are exclusively found in this section of the plant: Eugenol, Sesquicineole, α-Himachalene, Germacrene D, Tetradecanal, Cetyl alcohol, Hexadecenoic acid, Myrtenal, Citonellyl butyrate, Citronellyl tiglate, Dodecalactone, Phytone and Phytol.

Caryophyllene oxide, β-Patchoulene, Cyclosativene, Capronaldehyde, Pentadecane, Tetradecane, Hexadecane, Heptadecane, Octadecane, Nonadecane and Methyl Palmitate were detected in all plant parts of *S. mollis* ssp*. szowitzii.* Further, in all parts of *S. mollis* ssp. *szowitzii* α-Copaene, Phytol, Tetradecane, Hexadecane, Heptadecane, Octadecane, Nonadeacane, Heneicosane nd mthyl Palmitate were identified.

Volatile oil components detected in high amounts in of *S. mollis* ssp. *mollis* were Civetone with 42.62 % in root, β-Caryophyllene with 11.82 % in stem and Phytol with 12.08 % in leaf.

Besides, in *S. mollis* ssp*. szowitzii* highest values were obtained with 16.42 % for Hexadecane in root, with 20.68 % for Cyclosativene in stem and 12.31 % for β-Patchoulene and Cyclosativene in leaf parts.

Obviously, plant parts of *S. mollis* ssp. *mollis* and *S. mollis* ssp*. szowitzii* differed in their volatile oil composition.

Table 1 lists the chemical classes of *S. mollis* ssp. *mollis* and *S. mollis* ssp*. szowitzii* ‘s volatile oil composition. In fact, based on their examined chemical content, *S. mollis* ssp. *mollis* and *S. mollis* ssp*. szowitzii* plant parts could be distinguished from one another clearly (Table 1 and Fig. 1, 2 and 3). Seven chemical classes could be determined based on the volatile oil components present in plant parts: monoterpene hydrocarbons, oxygenated monoterpenes, oxygenated sesquiterpenes, sesquiterpene hydrocarbons,

the group of alcohols, ketones, aldehydes, and furans and the group of alkanes, alkenes, alkynes, and arenes; as well as the group of ethers, carboxylic acids, and esters.

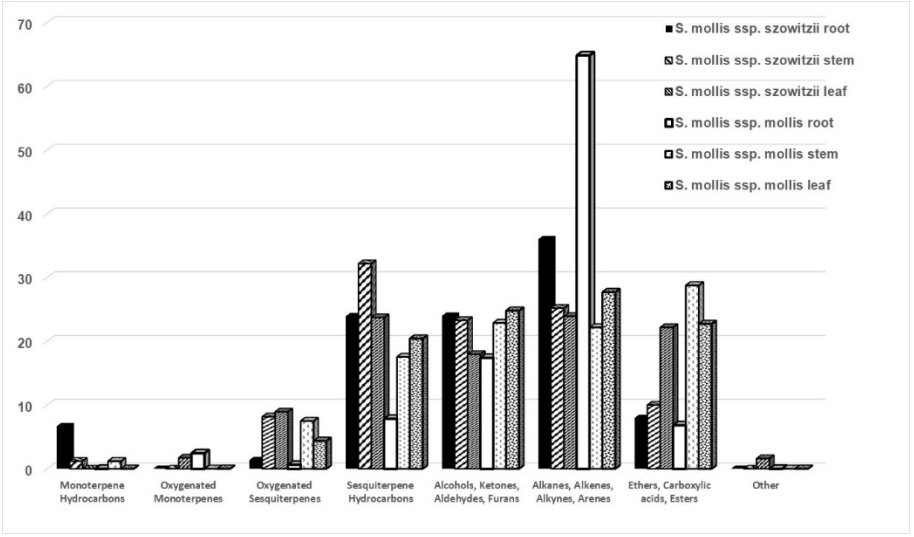

Figure 1. Distribution of chemical classes in *S. mollis* ssp. *mollis and S. mollis* ssp. *szowitzii* plant parts

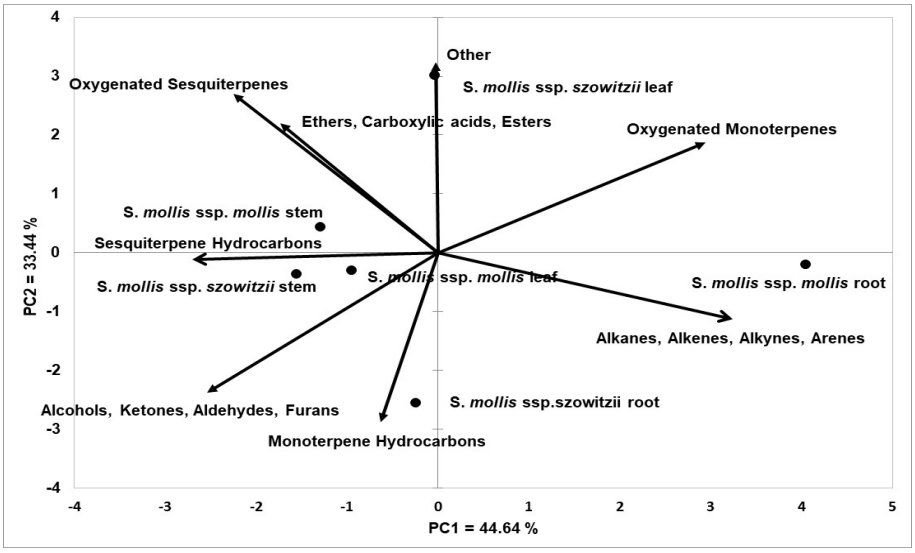

Figure 2. Biplot Analysis of *S. mollis* ssp. *mollis* and *S. mollis* ssp. *szowitzii* plant parts based on determined volatile oil composition

Particularly, the volatile oil composition of all plant parts (root, stem and leaf) of these two *Scorzonera* species was dominated by the Sesquiterpene Hydrocarbons, the group of Alcohols, Ketones, Aldehydes and Furans and the group of Alkanes, Alkenes, Alkynes and Arenes (Table 1).

In Fig. 2 and Fig. 3 we can see that root parts of *S. mollis* ssp. *mollis* were clearly different based on Biplot analysis 78.07 % of present variation could be explained (Fig. 3). Specially, Oxygenated Monoterpenes and the group of the group of Alkanes, Alkenes, Alkynes and Arenes were responsible for this clear differentiation.

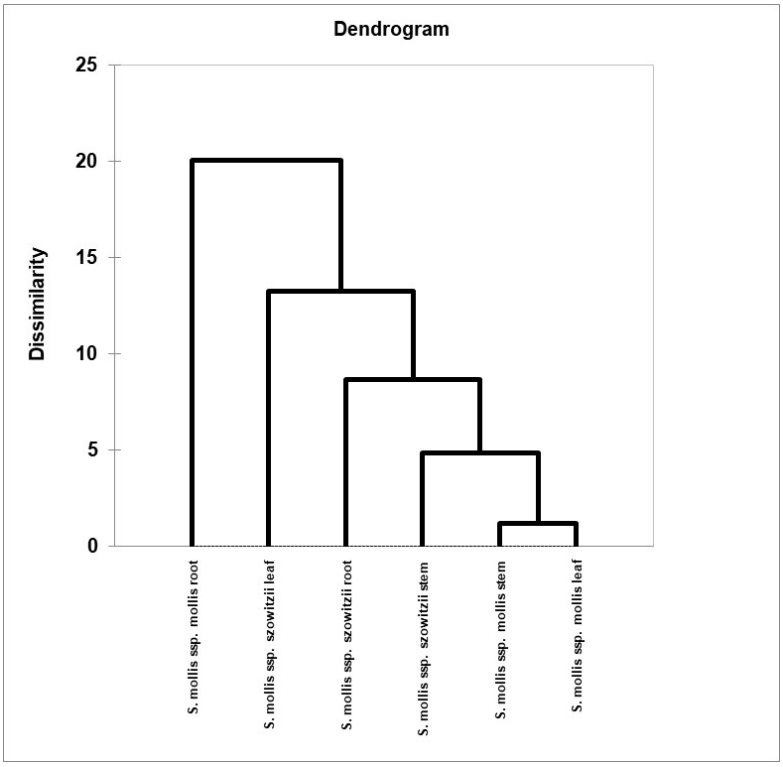

Figure 3. Cluster Analysis of *S. mollis* ssp. *mollis* and *S. mollis* ssp. *szowitzii* plant parts based on determined volatile oil composition

Table 2 lists the secondary metabolites found in different plant parts of *S. mollis* ssp. *mollis* and *S. mollis* ssp. *szowitzii*. Avicularin, Biapigenin, and Hyperoside were found in the highest concentrations in all plant parts of both species. Further, Catechine and Chlorogenic acid could be detected in all plant parts of of *S. mollis* ssp. *mollis*.

Table 2. Phenolic compounds detected *S. mollis subsp. szowitzii* using HPLC Analysis (Values and standard deviation were calculated three parallel analysis)

Compound	*S. mollis* ssp. *sweetie* root (mg/g DW)	*S. mollis* ssp. *szowitzii* stem (mg/g DW)	*S. mollis* ssp. *szowitzii* leaf (mg/g DW)	*S. mollis* ssp. *mollis* root (mg/g DW)	*S. mollis* ssp. *mollis* stem (mg/g DW)	*S. mollis* ssp. *mollis* leaf (mg/g DW)
Apigenin	0.012 ± 0.00028	0.051± 0.00168	0.015± 0.00106	0		0.006± 0.00010
Avicularin	6.552± 0.00636	6.719± 0.04779	8.488± 0.01230	5.786± 0.01539	6.753± 0.01081	6.898± 0.03600
Biapigenin	60.005± 0.00282	6.282± 0.00678	6.046± 0.05256	0	6.101± 0.00233	6.212± 0.02600
Caffeic acid	0.229± 0.00063	0.363± 0.00378	0.084± 0.00335	2.239± 0.00300	0.679± 0.00435	0.552± 0.00916
Catechin	1.423± 0.00212	0.413± 0.00314	1.161± 0.00360	17.931± 0.04454	14.658± 0.02957	15.631± 0.01447
Carvacrol	0	0	0.228± 0.00351	0	0	0
Chlorogenic acid	2.002± 0.00495	0.699± 0.02228	2.071± 0.00458	24.48± 0.04582	19.869± 0.02800	21.364± 0.06410
Epicathechin	0.721± 0.00565	0.247± 0.00295	1.169± 0.00360	0	0	0
Gallocatechin	0.397± 0.00283	0.08± 0.00132	0.434± 0.00451	0.125± 0.00265	1.325± 0.00351	1.1± 0.01682
Hyperoside	11.267± 0.01626	11.157± 0.00168	6.009± 0.00650	6.786± 0.01113	5.441± 0.02081	1.454± 0.00916
Isoquercitrin	0.049± 0.00367	0.05± 0.00150	0	0.093± 0.00147	1.633± 0.00700	1.145± 0.00229
Luteolin	0.468± 0.00636	0.514± 0.00550	0.606± 0.00557	0.519± 0.00666	0.529± 0.01115	0.507± 0.00275
P-Coumaric acid	0.04± 0.00495	0.032± 0.00047	0.395± 0.0010	0	0.078± 0.00489	0.068± 0.00200
Quercetin	0.538± 0.00283	0.405± 0.00874	0.279± 0.00808	0.278± 0.00557	0.249± 0.00351	0.143± 0.00305
Quercitrin	5.794± 0.00141	1.26± 0.0378	0.314± 0.00700	4.677± 0.02200	3.387± 0.03802	2.076± 0.00208
Rosmarinic acid	0	0	0.08± 0.00709	0	0.054± 0.00305	0
Rutin	0.024± 0.00085	0.066± 0.00360	1.631± 0.00656	0.098± 0.00259	6.13± 0.00700	9.75± 0.09452
Thymol	0.447± 0.00283	0.614± 0.00529	0.362± 0.00737	0	0.347± 0.01750	0.35± 0.00473

These two *Scorzonera* species contained significant phenolic compounds such as Caffeic acid, Epicatechin, Gallocatechin, Isoquercitrin, Luteolin, p-Coumaric acid, Quercetin, Rutin, and Thymol.

Figure 4 shows the Biplot of determined secondary metabolites found in various plant parts of *S. mollis* ssp. *mollis* and *S. mollis* ssp. *szowitzii*. The

calculated first two principal components accounted for 72.58% of the total variation. The plant parts of both species could be seperated clearly based on their secondary metabolite content (Fig. 4 and Fig. 5).

Quercitrin, Caffeic acid, Catechine, Chlorogenic acid Isoquercitrin, Rutin and Gallocatechine were effective in distinguishing of *c* plant parts from *S. mollis* ssp. *szowitzii* plant parts. Fig. 6 shows the dendogramme obtained using phenolic compound data.

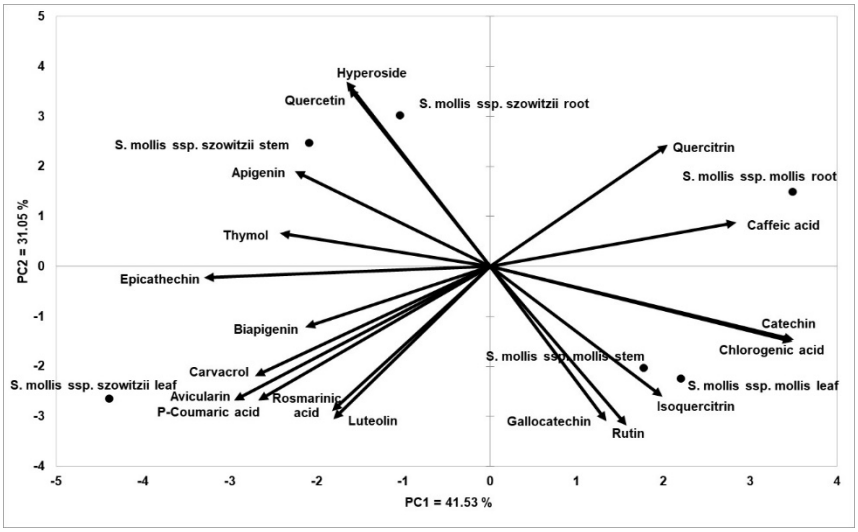

Figure 4. Biplot Analysis of HPLC data of *S. mollis* ssp. *mollis* and *S. mollis* ssp. *szowitzii*

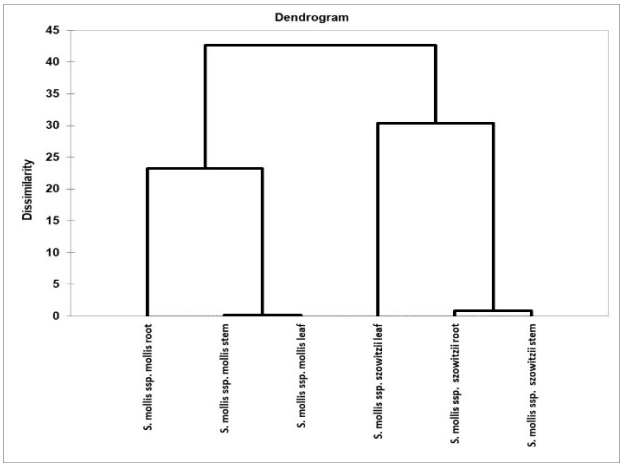

Figure 5. Dendogram of *S. mollis* ssp. *mollis* and *S. mollis* ssp. *szowitzii* plant parts based on secondary metabolite content

Principal Component Analysis (PCA) and Biplot is a helpful statistical technique for differentiating plant materials, and the findings can reveal the similarities and differences across diverse species in terms of their chemical profile [52-53]. Based on volatile oil composition, PC1 contributed 44.64 % and PC2 contributed 33.44 % (totally 78.08 %) to the current variation, which was highly helpful in differentiating the tested materials (Fig. 3).

Differentiating plant parts of *S. mollis* ssp*. mollis* and *S. mollis* ssp*. szowitzii* based on the content of their volatile oils was accomplished using the Biplot and Cluster Analysis Methods. As shown in the produced Biplot (Fig. 3) and Dendogram (Fig. 4), plant parts of both species could be separated clearly from each other based on the data acquired.

The chemical composition of volatile oils is influenced by exogenous variables (plant anatomy and physiology) and environmental regulators (light, precipitation, growing environment, and soil). Different plant sections have different chemical compositions as a result [54].

In the plant parts of both species 70 distinct volatile oil components could be detected, although the proportion and distribution of these components varied. In our situation, it was possible to clearly differentiate the volatile oil composition of the investigated plant parts of both species (Fig. 2, 3 and 4).

There have been few studies on the volatile oil composition of *Scorzonera* species, but in *S. mollis* ssp*. mollis* and *S. mollis* ssp*. szowitzii* there are lacking. Hexadecanoic acid (20.3%) was the one and only substance that was abundant in *S. hispanica*, followed by Octane (7.5%), Hexane (4.8%), and Octadecanoic acid (3%) [8]. Hexadecanoic acid (42.2%), n-Tetradecanoic acid (16.1%), Octadecanoic acid (7.7%), and Hexadecenoic acid (4.5%) were the primary components of the roots of *S. undulata* ssp. *deliciosa* (Guiss) Maire. The principal chemical components of the roots of *S. undulata* ssp. *deliciosa* (Guiss) Maire were also identified as Methyl hexadecanoate (30.4%), Methyl linoleate (23.9%), Heneicosane (12.2%), and Octadecane (4.4%) [30]

Trimethyl Pentadecanone (27.73%), Caryophyllene oxide (16.84%), Neophytadiene (7.68%), and (E)—Ionone was found in oil extracted from the leaves and flowers of *S. calyculata* (6.77 %). Oxygenated sesquiterpenes accounted for 20.68% of the total essential oil, followed by diterpenes (8.34), monoterpene hydrocarbons (4.75%), sesquiterpene hydrocarbons (1.88%), and oxygenated monoterpenes (1.04%) [39].

The most abundant compounds in *S. sandrasica* were Caryophyllene Oxide (19.7%), Manoyl Oxide (16.05%), Manool (11.3%), 2-Oxo-Manoyloxide (8.9%), Sclareol (7.7%), and β-Caryophyllene (7.6%) (Ugur et al., 2012). Carvacrol made up 2.7% of total oil.

In Türkiye, there is a scarcity of HPLC data on the phenolic composition of S. mollis ssp. mollis and S. mollis ssp. szowitzii. The main phenolic compounds in leaf extracts of *S. cinaerea* [38] were Chlorogenic acid (6560.0 mgkg-1),

Gallic acid (2286.3 mgkg-1), Rutin (779.5 mgkg-1), Protocatetechuic acid (512.2 mgkg-1) and P-coumaric acid (mgkg-1). S. aristata Ramond sx DC aerial parts were tested for Quercetin, 3-O-Glucoside, Rutin, Isooorientin, Chlorogenic, 4,5-d, Caffeoyl Quinic Acid, and 3,5-Dicaffeolyl Quinic Acid. The same species' subarial parts contained Caffeic acid methyl ester and 3,5-Daicaffeoyl Quinic Acid [41]. S. hieraciifolia Hayek roots were found to contain chlorogenic methyl acid ester and caffeic acid [19].

Additionally, Kaempferol, Rutin, Caffeic Acid, and Rosmarinic Acid were found in the aerial parts and roots of *S. tomentosa* [35]. In the aerial portions and roots of S. hispanica L., Caffeine, Rosmarinic acid, Apigenin and Quercetin were found. The presence of Rutin, Muricetin, Quercetin, and Myricetin in *S. suberosa*, as well as Myricetin, Quercetin, Quercetin, and Kaempferol in *S. laciniata* and *S. latifolia*, was reported [36].

Tools like Principal Component Analysis (PCA) and Cluster Analysis are useful for identifying genotypes and related grouping that is based on resemblance [55-56]. Plant materials can be differentiated using PCA analysis, and differentiating several species based on their chemical profile could be accomplished [52-53]. Characters that are crucial for the genetic variability in crops can be analyzed if these two approaches are combined [57]. A subsequent phase in PCA is called a Biplot, where factors that help distinguish one variant from another can be grouped and identified [58]

The various parts of the *S. mollis* ssp*. mollis* and *S. mollis* ssp*. szowitzii* plant that were under investigation may be easily separated from one another based on their volatile oil composition and polar metabolite content. The root, stem, and leaf sections of these two plant species differed most in case of the leaf parts in terms of volatile oil composition. The current study evaluated the volatile oil composition and secondary metabolite content of *S. mollis* ssp*. mollis* and *S. mollis* ssp*. szowitzii* plant sections using statistical methods in addition to chemical content analyses.

CONCLUSIONS

Research has been done on the aerial and subaerial sections of the *Scorzonera* genus to learn more about their phytochemical profile and therapeutic potential. Since *Scorzonera* species are frequently used in folk medicine in many European and Asian countries, contemporary phytoanalyses and biological studies have been conducted to confirm the bioactive properties of these plants. *Scorzonera* species are regarded as a possible source of antioxidant agents because they contain a variety of bioactive substances, such as flavonoid aglycones and glycosides, triterpenoids, sesquiterpenoids, quinic acid, and caffeic acid derivatives.

In conclusion, the volatile oil composition and polar metabolite content of *S.* taxa were investigated together for the first time as far we know. The present results indicate differences in the volatile oil composition and polar metabolite content of different plant parts of this species. Data presented here could also be useful in determining the forthcoming goals for further wide-ranging studies on this species as well as enriching our current knowledge about *S. mollis* taxa chemistry.

We now know more about the systematics of the species *Scorzonera* thanks to caryological, ethnobotanical, chemical, and phenetic research on this plant. The chance to gain a detailed understanding of the chemical profile of this species will be made possible by the results that have been presented and by additional chemical screening of *S. mollis* taxa. Different elements that appear to be medicinally significant have been found in all sections of this species. Regarding the isolation and use of these significant detected components, the acquired data provides insightful information that will be useful for further research.

EXPERIMENTAL SECTION

Collection of plant material

S. mollis ssp. *mollis* and were collected from Mürefte (Tekirdağ), Ganos Mountain, meadows at heights of ~900 - 1000 m in the northwest part of Türkiye on 06 June 2011 and *S. mollis* ssp. *szowitzii* from Gümüşhane, Köse Mountain, at 1900 - 2000 m in the north part of Türkiye on 27 June 2011, respectively. The plant photos taken from the distribution area are presented in Figure 6. Voucher specimens (Makbul 289 and Makbul 296) was deposited in the Herbarium of the Department of Biology, Recep Tayyip Erdogan University (RUB), Rize, Türkiye. The plant materials were identified immediately after collection and air-dried at room temperature for later analysis.

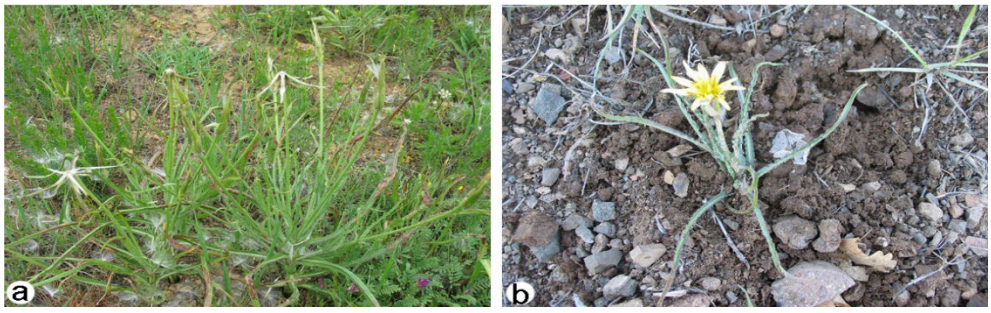

Figure 6: a. *Scorzonera mollis* ssp. *mollis* (Makbul 289);
b. *Scorzonera mollis* ssp. *mollis* (Makbul 296)

Sample preparation and volatile oil analysis

The plant materials (1.00 g, each) were powdered and placed in a 10 mL vial sealed with a silicone-rubber septum cap. The fiber was pre-conditioned according to the manufacturer instructions. At equilibrium, the fiber was exposed to the headspace for 1 min at room temperature. Once sampling was finished, the fiber was withdrawn into the needle and transferred to the injection port of GC or GC–MS system [59]..

GC-FID analysis GC analyses were accomplished by an Shimadzu GC-MS instrument equipped with HP-WAX and HP-5 capillary columns (30 m × 0.25 mm, 0.25 µm film thickness), working with the following temperature program: 60 ◦C for 10 min, ramp of 5 ◦C/min up to 220 ◦C; injector and detector temperatures 250 ◦C; carrier gas nitrogen (2 mL/min); detector dual FID; split ratio 1:30; injection of 0.5 µL. Identification of the components was performed, for both columns, by comparison of their retention times with those of pure authentic samples and by means of their linear retention indices (LRIs) relative to a series of n-hydrocarbons. The length of alkane series was C8–C24. 2.5. GC-MS analysis Volatile components were analyzed by gas chromatography-mass spectrometry (GC-MS) system. The GC-MS analyses were performed using a Shimadzu GC-MS-QP 2010a GC-MS system operating on electro spray ionization (EI) mode (equipped with a CP 5MS (30 m × 0.25 mm i. d., film thickness 0.25 µm), using Helium (1 mL/min) as the carrier gas. Oven temperature was programmed from 40 ◦C to 240 ◦C at 2 ◦C/min, then isothermal at 220 ◦C for 20 min. The temperature of injector and detector was 240 ◦C. Mass spectra were taken on 70 eV. Area normalization was used for determination of composition percentage. After compounds in gas chromatography column were separated, each individual ion-mass spectrum was taken. Compounds were detected using Shimadzu FFNSC (Flavour & Fragrance Natural & Synthetic Compounds GC/MS Library) library.

Plant extract preparation and quantification for HPLC analyses

To obtain a homogenous drug powder, air-dried plant material (from 10 plants) were mechanically ground in a laboratory mill. Ultrasonication at 40°C for 60 minutes in an ultrasonic bath extracted 0.1 g samples (weighed with 0.0001 g precision) in 10 mL of 100% methanol. The prepared extracts were filtered through a 0.22 mm pore size membrane filter (Carl Roth GmbH, Karlsruhe, Germany) and stored at 4°C until analysis. The extraction and drying processes were carried out in complete darkness.

The flavanoids and phenolic acids were separated using a Shimadzu LC-2030C-3D HPLC device equipped with a DAD detector and an RP-18 (5 mm, 250 mm X 4.0) column. For the detection of corresponding compounds,

the binary gradient elution method was used. The mobile phase A was made up of water that had been acidified with 0.3% phosphoric acid as eluent A and acetonitrile that had been acidified with 0.3% phosphoric acid as eluent B. The following elution profiles were used: 0:10 min 10% B, 10:30 min% 25 B, 30:38 min 60% B, 3845 60% B, and 4545.01 min 10% B. At a column temperature of 25°C, the flow rate was 0.6 mL/min. The injection volume of the extract was 10 µl. Identification was performed in a range of 200–400 nm wavelengths by comparing UV/Vis spectral data and retention times to those of standard compounds.

Data Analysis

Biplot Analysis were performed using the XLSTAT 2021 Statistical Program to visualize present variation in *S. mollis* ssp. *mollis* and *S. mollis* ssp. *szowitzii* plant parts investigated for chemical variability. Scatter plot diagrams were created using current data [60]. Based on GC-MS and HPLC analysis data separate Biplot and Cluster Diagrams were also created.

REFERENCES

1. P.H. Davis; *Flora of Turkey and the East Aegean Islands*, Edinburgh, Edinburgh University Press, **1965–1968**.
2. P.H. Davis; R.R. Mill; K. Tan; *Flora of Turkey and the East Aegean Islands Islands*, Vol. 10 (Supplement 1), Edinburgh University Press, **1988**.
3. A. Guner, N. Ozhatay; T. Ekim; K.C.H. Baser; Flora of Turkey and the East Aegean Islands, Edinburgh University Press, **2000**.
4. T. Baytop; *Healing with Plants in Turkey. In the past and today*, Istanbul, Turkey, Nobel Medical Verlag, **1999**.
5. R.V. Kamelin; I.U. Tagaev; *Bot. J.*, **1986**, *71*, 1672–1682.
6. M.A. Zaika; N. Kilian; K. Jones; A.A. Krinitsina; M.V. Nilova; A.S. Speranskaya; A.P. Sukhorukov; *PhytoKeys*, **2020**, *137*, 1–85.
7. K. Coşkunçelebi; S. Makbul; M. Gültepe; S. Okur; M.E. Güzel; *Turkish Journal of Bot.*, **2015**, *39*, 76-87.
8. C. Zidorn; E.P. Ellmerer-Müller, H. Stuppner; *Pharmazie.*, **2000a**, *55*, 550-551.
9. C. Zidorn; E.P. Ellmerer; S. Sturm; H. Stuppner; *Phytochem.*, **2003**, 63, 61 – 67.
10. S. Paraschos, P. Magiatis, E. Kalpoutzakis; C. Harvala, A.L. Skaltsounis, *Journal Natural Prod.*, **2001**, *64*, 1585-1587.
11. Y. Zhu; Q. Wu, P. Hu; W. Wu; *Food Chem.,* **2009**, *114*, 1316-1320.
12. N. Tsevegsuren; Edrada N., Lin R.A.; R. Ebel; C.Torre; S. Ortlepp; V. Wray; P. Proksch; *Planta Medica*, **2006**, *72*, 967.

13. Y. Wang; R.A. Edrada-Ebel, N. Tsevegsuren, J. Sendker; M. Braun; Journal of Natural Prod., **2009**, *72*, 671–675.
14. Ö.B., Acıkara; Ö.B. Ergene; F. Bakar; Ç.G. Saltan; S. Nebioğlu; *The Turkish J. of Pharmac. Sci.*, **2017**, *14(2)*, 179–184.
15. C. Zidorn; E.P. Ellmerer-Müller; H. Stuppner; H., *Helvetica Chimica Acta*, **2000b**, *83*, 2920–2925.
16. A. Sarı; *Natural Product Res.*, **2010**, *24(1)*, 56–62.
17. B. Harkati; S. Akkal; M.G.D. Franca; *Green Sustainable Chem.* **2012**, *(2)*, 59-61.
18. A. Sarı; C. Zidorn; E.P. Ellmerer; F. Özgökce; K.H. Ongania; H. Stuppner; *Helvetica Chimica Acta,* **2007**, *90*, 311-317.
19. A. Sarı; H. Şahin; N. Özsoy; Ç.B. Özbek; *South African Journal of Bot.*, **2019**, *125*, 116–119.
20. A. Bader; N. De Tommasi; R. Cotugno; A. Braca; *Journal of Natural Prod.*, **2011**, *74 (6)*, 1421–1426.
21. Y.J. Yang; X. Liu; H.R. Wu; X.F. He; Y.R. Bi; Y. Zhu; Z.L. Liu; *Food Chem.***, 2013**, *138(2-3)*, 2057–2063.
22. O.B. Acıkara; G.S. Çitoglu; S. Dall'Acqua; K. Smejkal; J. Cvacka, M. Zemlicka; *Natural Product Res.*, **2012**, *26 (20)*, 1892–1897.
23. R.A. Dar; M. Shahnawaz; P.H. Qazi; *The Journal of Phytopharmac.,* **2017**, *6(6)*, 349-351.
24. A.R. Hassan; *Pharmaceutical Analytica Acta*, **2012**, *3*, 10.
25. B. Abu-Shanab; G.M. Adwan; D. Abu Safiya; N. Jarrar; K. Adwan; Turkish J. of Biol., **2005**, *28 (2-4)*, 99-102.
26. M. Kelen, B. Tepe; *Bioresource Technol,* **2008**, 99 (10), 4096-4104.
27. M.S. Lee; J. Choi; P. Posadzki; E. Ernst; *Maturitas,* **2012**, *71 (3)*, 257-260.
28. B. Tepe; D. Daferera; A.S. Tepe, M. Polissiou; A. Sokmen; *Food Chem.*, **2007**, *103 (4)*, 1358-136429. J.L. Rios; M.C. Recio; *Journal of Ethnopharmac*., **2005**, *100 (1-2),* 80-84.
30. O. Boussaada, S.; S. Ammar; D. Saidana; J. Chriaa; I. Chraif; M. Daami; *Microbiol. Res.*, **2008**, *163*, 87-95.
31. A. Ugur; N. Sarac; O. Ceylan; M.E. Duru; Y. Beyatlı; *Journal of Medicinal Food.,* **2010**, *13 (3)*, 635–639.
32. A. Ayromlou; S. Masoud; A. Mirzaie; A., *J. of Reports in Pharmaceutical Sci.*, **2019**, *79*, 118-127.
33. Ö.B. Acıkara; G.S. Citoglu; T. Coban; *Turkish J. of Pharmaceutical Sci.*, **2013**, *10 (3)*, 453-462.
34. S. Granica; C. Zidorn; *Biochemical Systematics and Ecol*., **2015**, 25, 102-113.
35. S. Dall'Acqua; G. Ak; S. Sut; I. Ferrerese; G. Zengin; E. Yıldıztugay, M.F. Mahomoodally; K.I. Sinan; D. Lobine; *Industrial Crops and Prod.*, **2020**, *154*, 112751.
36. Y. Erden; S. Kırbag; Ö. Yılmaz; *Proceedings of the National Academy of Sciences India Section B Biological Sci.*, **2013**, *83 (2)*, 271-276.
37. G. MacLeod, J. Ames; *Phytochem.*, **1991**, *3*, 833-8898.
38. M.A. Temiz; *Acta Pharmac.,* **2021**, *71*, 603-617.

39. A. Ayromlou; S. Masoudi; A. Mirzale; *J. of Reports in Pharmaceutical Sci.*, **2020**, *9*, 118.
40. F.S. Senol, O.B. Acikara; G.S: Citoglu; İ.E. Orhan, S. Dall'Acqua; F. Özgökce; *Pharmaceutical Biol.*, **2014**, *52 (7)*, 873-888.
41. M. Jehle, J. Bano; E.P. Ellmerer, C. Zidorn; *Natural Product Communic.,* **2010**, *55*, 725-727.
42. N. Tsevegsuren; R.A. Edrada; W. Lin; R. Ebel; C. Torre, S. Ortlepp; V. Wray; P. Proksch; *Journal of Natural Prod.*, **2007**, **70**, 962 - 967.
43. H. Sahin; A. Sarı; N. Özsoy; B.Ö. Celik; O. Koyuncu, O., *Istanbul Journal of Pharmacy*, **2020**, *50(3)*, 294-299.
44. A.A. Sakul; E. Kurtul; H. Ozbek, N.İ. Kirmizi; B.C. Bahtiyar; G.S. İscan; O.B. Acikara; *Clinical and Experimental Health Sci.* **2021**, *11*, 74-80.
45. H.S. Kargol; H.M. Elgadi; M.T. Gadamsi; H.M. Shubar; A.M. Geroushi; İnt. Research J. of Pharmacy; **2013**, 4(4), 96-99.
46. N. Petkova; *Asian J. of Pharmaceutical and Clinical Res.* **2018**, 11: 221-225.
47. A. Sweidan; M. El-Mestrah, H. Kanaan; I. Dandache; F. Merhi; A. Chokr; *Pakistan Journal of Pharmaceutical Sci.,* **2020**, 33 (1), 199-206.
48. H.B. Abdelkader; K.B.H Salah; K. Liouane; O. Boussasa; K. Gafsi; M.A. Mahjoub; M. Aouni; A.N. Hella; Z. Mighri; *J. of Microb. Res*., **2010**, *4 (19)*, 1954-1958.
49. E.K. Akkol; B. Acıkara; I., Süntar; S.G. Çitoglu; H. Keles; B. Ergene; *J. of Ethnopharmac.*; **2011**, *137*, 1018–1027.
50. İ. Süntar; Ö.B. Acıkara; G.S. Citoglu; H. Keles; B. Eregene; E.K. Akkol; *Current Pharmaceutical Design*, **2012**, 18, 1421-1433.
51. M.A. Nasseri; S.S. Bigy; A. Allahresani; M. Malekaneh; *J. of Natural Pharmaceutical Prod.*, **2014**, *10 (4)*, 19781.
52. A. Smelcerovic; S. Zuehlke; M. Spiteller; N. Raabe, T. Ozen; *Biochemical. Systematics and Ecol.*, **2008**, *36*, 316–319.
53. A. Bertoli; C. Cirak; M. Leonardi; F. Seyis; L. Pistelli; *Pharmaceutical Biol.*, **2011**, *49*, 741–751.
54. A. Barra; *Natural Product Communic.*, **2009**, *4(8)*, 1147-1154.
55. S.A. Mohammadi; B.N. Prasanna; *Crop Sci.*, **2003**, *43*, 1235-1248.
56. J.P. Peeters; J.A. Martinelli; *Theoretical and Applied Genet.*, **1989**, *78*, 42-48.
57. G. Rachovska; D. Dimova; B. Bojinov; B., *Proceedings of the Scientific* 58. M. Aghaee; R. Mohammadi; S. Nabovati; *Australian J. of Plant Sci.*, **2010**, *4*, 505-514.
59. E. Yurteri; S. Makbul; K. Coskuncelebi; M. Gültepe; F. Seyis; *Fresenius Envir. Bulletin*, **2022**, 31 (3), 346-3468.
60. K. Backhaus; B. Erichson; W. Plinke; R. Weiber; *Multivariate Analysis Methods*, Heidelberg, Germany, Springer Verlag, **1989**, pp. 453-516.

STUDIA UBB CHEMIA, LXVIII, 3, 2023 (p. 179-189)
(RECOMMENDED CITATION)
DOI:10.24193/subbchem.2023.3.12

DETAILED KINETICS OF A DIFFUSION DRIVEN ADSORPTION PROCESS

Alexandra Ana CSAVDARI[a,*]

ABSTRACT. The present work completes information reported previously on Chrystal violet adsorption from aqueous solutions onto *Salvinia natans* powder. It identifies intraparticle diffusion as the rate determining step within the sequence of four individual stages of the adsorption mechanism. It also demonstrates, that even is somewhat faster, the film diffusion at the solid-liquid boundary is also slow enough to contribute to the overall process rate. The novel use of a simple kinetic model, consisting of two parallel and competing first-order steps, as well as of an algorithm familiar to pharmacokinetics (the method of residuals), individual rate coefficients of both the film and the intraparticle diffusion were calculated simultaneously from the same kinetic curves. The dependence of their values with employed operating conditions consolidates previous findings and conclusions.

Keywords: *Adsorption; Rate determining diffusion; Method of residuals; Competing first-order processes*

INTRODUCTION

Adsorption of various organic and inorganic chemical species from gases or wastewaters onto the surface of specially designed solid adsorbents has proved to be highly efficient as well as cost effective. Hence, it has gained increased significance in recent research [1-4]. Within this context, overall process kinetics and mechanism are of outmost importance in the design of any adsorption equipment, which operates either continuously or discontinuously [5-13].

[a] *Babeş-Bolyai University, Faculty of Chemistry and Chemical Engineering, 11 Arany Janos Street, RO-400028, Cluj-Napoca, Romania*
* *alexandra.csavdari@ubbcluj.ro*

Adsorption experiments follow the process during non-equilibrium, by monitoring its extent as a function of total fluid – solid contact time. The registered parameter is usually an adsorption yield, expressed as a percentage of removed pollutant quantity from its initial amount, or as an adsorption capacity ***q***, expressed in mg pollutant adsorbed by 1g of adsorbent until a certain moment after process initiation. Values are dependent on temperature, pollutant/ adsorbent mass ratio [5-13], quality of mixing, pH (for example in dye adsorption [6,8,14]), and of course on the nature of adsorbed as well as adsorbent species. As such, kinetic adsorption models shed light on the rate determining step of the process, hence process mechanism, as well as on the optimum conditions to be employed in order to obtain the desired overall performance. Moreover, adsorption/desorption dynamics knowledge also contribute to the better understanding of catalysis and corrosion phenomena [11].

Dedicated literature [4-5,8-11] usually mentions a succession of four main stages of mass transfer. Each might affect the overall process rate. The first involves the bulk movement of the adsorptive (chemical species to be removed from the fluid) from the bulk phase of the fluid, liquid or gas, to the vicinity of the external surface of the solid adsorbent. This is usually a fast transport that is not taken into consideration when describing adsorption dynamics. On the other hand, the second stage, that of the film diffusion (FD), involving the solute species' crossing of the fluid boundary layer to the actual solid surface, can be much slower and might influence the overall process' rate. The following intraparticle (pore) diffusion stage (IPD), of solute's transport from the surface of the adsorbent into the inner space of its pores, is often mentioned as the rate determining step. The last stage involves the actual adsorption (attachment) of the adsorptive species onto the adsorbent's surface by means of either chemi- or physisorption. This is generally described as happening fast, and hence not affecting the overall adsorption rate.

If the solute's molecule size as well as its initial concentration in the fluid are fairly small, and moreover the mixing quality is low, then the film diffusion is controlling the overall rate. Otherwise, it is usually the intraparticle diffusion [5,9].

Proposed models [5,8-9] describe pseudo-first order or pseudo-second order overall kinetics, take into account only the adsorption or both the adsorption–desorption ensemble of reversible processes, consider diffusion as rate controlling or propose combined diffusion–adsorption control, as well as introduce various non-linear models in order to best fit the experimental data and explain process mechanism [5,9].

Yet, none differentiates between the characteristics (such as rate coefficients) of the film and intraparticle diffusion, nor puts forward values of

both obtained from a single kinetic curve. Moreover, the fact that FD and IPD occur not only successively, but also in parallel (competing), is usually ignored by scientists striving for adsorption dynamics elucidation.

Hence, the main aim of this work is to demonstrate that a simple kinetic model, composed of two parallel and competing first order processes, can be used to describe overall adsorption kinetics in diffusion controlled situations. This implies both rapid bulk movement and chemi-/physisorption, situation easily achieved when toxic organic species (dyes, pesticides, biocides, etc.) are removed from their diluted aqueous solutions by solid high-value inner surface adsorbents [8,12-13]. The model assumes that time resolved non-equilibrium measurements describe in a single kinetic curve both film (FD) as well as intraparticle diffusion (IPD), and hence can be used to determine simultaneously the first-order rate coefficients of both by using the method of residuals (also called Feathering or Peeling method). This is a consecrated data processing procedure, which uses a biexponential equation to describe administrated drug pharmacokinetics, when distributed between the central and the peripheral compartments [15-16].

Experimental data used to demonstrate this novel approach were provided by the authors of a previous study [14]. This compared the phytoremediation performances of living and powder *Salvinia natans* (SN) in the removal of Crystal violet (CV) from its aqueous synthetic solutions. In both cases, dynamic behavior was described by an overall second-order process and cumulative corresponding rate coefficients have been calculated.

Yet, no distinction has been presented among the individual stages in the case of powder *S. natans*, a process which matches a usual S-L adsorption. In other words, no explanation has been given about the identity of the rate determining process as well as about the values of its rate coefficients. Final conclusions mentioned that adsorption of CV on powder SN proved to be physical in nature, but did not prove whether it is slow or fast as compared to the diffusion driven film and intraparticle steps.

Therefore, this work also aims to complete the conclusions of the former study for the case of Crystal violet adsorption on powder *Salvinia natans*, by: (1) identifying the rate determining step, (2) putting forward values for the rate coefficients of individual stages of the process, and (3) completing and consolidating the previous study's conclusions by interpreting the newly found rate coefficients' dependence on employed experimental conditions. A stated above, goal (2) is achieved by using an ensemble of two parallel (competing) first-order processes and the method of residuals to calculate both FD and IPD rate coefficients from kinetic curves describing the overall residual CV concentration *versus* total S-L contact time.

RESULTS AND DISCUSSION

Validity of the rate determining intraparticle diffusion assumption

Published experimental results describing Crystal violet adsorption from its aqueous solution on *Salvinia natans* powder [14] rely on kinetic curves representing the adsorption capacity ***q*** (mg CV / g SN powder) as a function of total contact time ***t*** (min, h). Data were collected at various temperatures (10, 23, 35 and 40°C, respectively) and at variable initial concentration of CV, in the range of 20 to 90 mg/L. Hence, by keeping the same amount of solid SN powder, the adsorptive/adsorbent mass ratio has been varied. The effects of rotation speed and aqueous environment pH value on the process were also assessed.

Since the possibility of the IPD to be the rate determining step has not been explored, the linearity of adsorption capacities at a given time (q_t) plots *versus* the square root of total contact time ($t^{0.5}$) has been checked. According to literature [8-11], a linear dependence - such as the one described by equation (1) - demonstrates that pore diffusion is the slowest stage of the entire adsorption process.

The slope $\mathbf{k_{IDP}}$ ($mg.g^{-1}.h^{-0.5}$) stands for the intraparticle diffusion rate coefficient. Such plots may present multi-linearity [6-7], which indicates that two or more rate controlling steps occur during the course of the overall process. In these cases, each slope stands for a different $\mathbf{k_{IDP}}$ value, characterizing pores of different diameters. Smaller pores are described by lower $\mathbf{k_{IDP}}$ values, since the path available for diffusion also becomes smaller [6-7,17].

The **intercept** in equation (1) also helps in the assessment of the diffusion's role in the overall process. It is correlated with the thickness of the boundary layer, and as such with the importance/significance of film diffusion [7]. If the plot is linear and the intercept is equal to zero (the plot passes through the origin), then only IPD is significant. If the intercept differs from zero (the plot does not pass trough the origin), then FD plays an observable role in the overall process, and its contribution to the overall adsorption rate cannot be ignored. The higher the intercept's value, the more significant the FD gets.

$$q_t = k_{IPD}\, t^{0.5} + \text{intercept} \qquad (1)$$

Figure 1 illustrates an example of q_t *vs* $t^{0.5}$ plot, for the data presented by Mânzatu *et al.* [14]. The linearity is proven by the good correlation coefficient. Moreover, there is no observable multilinearity and the line does not pass through the origin. Hence: (*i*) IPD is rate determining, but (*ii*) FD cannot be ignored in the overall rate, and (*iii*) the pore size of the SN powder appears to be uniform.

Similar results were obtained for all employed experimental conditions described in [14]. Variation of the initial CV concentration of the aqueous media, $[CV]_0$, between 30-90 mg/L, but by keeping all other experimental conditions unchanged (see Figure 1), causes no significant change in the rate constant $\mathbf{k_{IPD}}$. Its value remains 4.83±0.93 $mg.g^{-1}.h^{-0.5}$, suggesting that IPD occurs in similar sized pores. The rate coefficient of IPD does not change with increasing $[CV]_0$, yet the overall rate does, because the FD gets to be more significant in the sum of both. This is suggested by the fact that the intercept of equation (1) increases proportionally with the value of $[CV]_0$, from 2.48 mg/g to 19.53 mg/g. In other words, internal diffusion is rate determining within the overall process, yet a higher dye concentration in the bulk will amplify the driving force of diffusion, hence its rate, but not its rate coefficient.

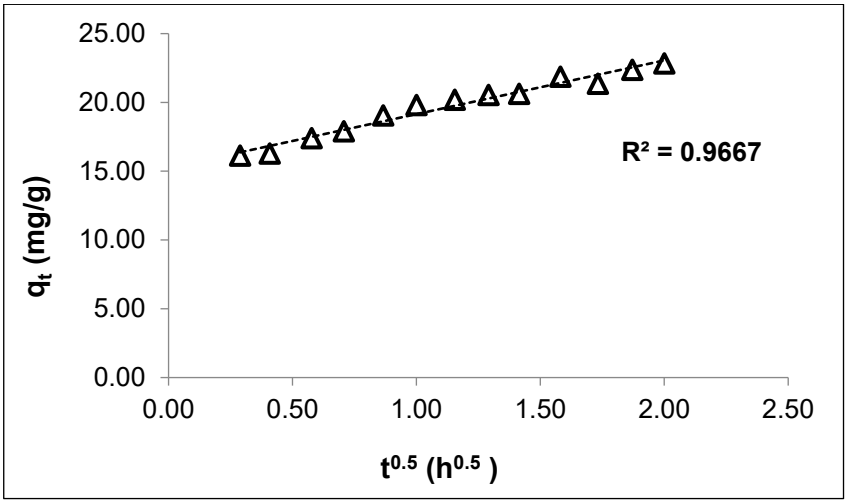

Figure 1. Testing the validity of rate determining IPD assumption, by means of the q_t *vs* $t^{0.5}$ plot. ($[CV]_0$ = 50 mg/L; m_{SN} = 0.40 g; pH = 5.4; 23°C; 9000 rot/h)

By changing the temperature between 10 and 40°C under the same operating conditions (see Figure 1), the values of $\mathbf{k_{IPD}}$ average around 11.94±1.54 $mg.g^{-1}.h^{-0.5}$ with some minor deviation. The thickness of the boundary layer, correlated to the intercept of equation (1), will result in a value of 3.11±1.38 mg/g. Variability of these values is low and exhibits no trend; thus it may be due to measurement errors. Hence, temperature does not affect significantly the diffusion driven processes, at least not within this narrow variation domain.

The same conclusions may be drawn for variable pH, within the range of 3.35 to 10.00 units. $\mathbf{k_{IPD}}$ averages around 11.25±1.41 $mg.g^{-1}.h^{-0.5}$, while the intercept around 3.25±0.93 mg/g. Both values are very close to the ones calculated for the temperature dependence. Thus, neither parameter affects the rates of FD and IPD.

It may be concluded that rate determining intraparticle diffusion has been proved. Film diffusion may not be ignored, yet it is somewhat faster. Even though equation (1) is able to offer some information related to the contribution of diffusion to the overall process rate, it cannot provide the individual rate coefficients of FD and IPD, respectively.

Simultaneous determination of individual rate constants for both film and intraparticle diffusion steps

In order to overcome this shortcoming, this paper proposes the following:

- The overall process is described by an ensemble of two competing, rate determining, first-order steps (**I** and **II**, respectively), namely the FD and the IPD, as shown in Figure 2. ED stands for the "external" film diffusion and IPD for the "internal" pore diffusion. $\mathbf{k_1}$ and $\mathbf{k_2}$, respectively, stand for the first order rate coefficients of the two parallel competing stages.
- Even though IPD is succeeding ED, it is much slower, hence the bulk of the CV transport in step **I** is carried out *via* ED.
- ED is faster than IPD ($\mathbf{k_1} > \mathbf{k_2}$)
- The overall adsorption rate may be written as the disappearance rate of CV form the aqueous bulk phase, and further as the sum of the rates of steps **I** and **II**, as it is expressed by equation (2).
- The adsorption is occurring immediately as the CV molecule reaches the adsorption's active site.

$$r = - d[CV]/dt = r_I + r_{II} = \mathbf{k_1}\,[CV] + \mathbf{k_2}\,[CV] \qquad (2)$$

Simple chemical kinetics formalism will transform equation (2) into a sum of two exponential terms:

$$[CV] = A \exp(-\mathbf{k_1}\, t) + B \exp(-\mathbf{k_2}\, t) \qquad (3)$$

In equation (3), A and B represent the amount of initial CV quantity theoretically corresponding to removal solely by film or intraparticle diffusion, respectively. Their sum should ideally be equal to $[CV]_0$.

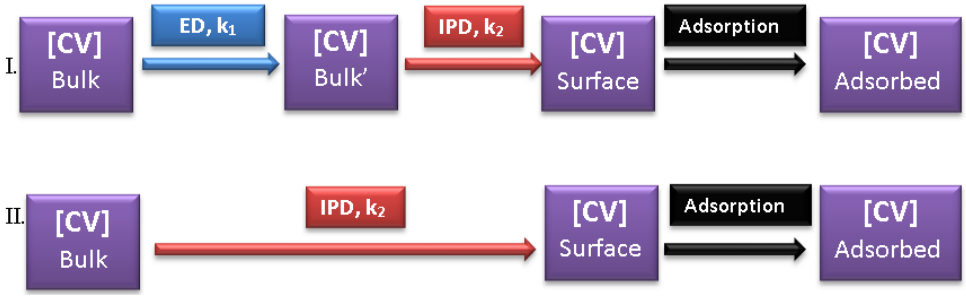

Figure 2. Kinetic model proposed to determine the individual rate coefficients of film and intraparticle diffusion, respectively.

At the initiation of the process when total contact times are short and $t \rightarrow 0$, the rate r_I of the ED is significantly higher than the rate r_{II} of IPD, thus r_{II} may be neglected in equation (2). Hence,

$$[CV] \approx A \exp(-\mathbf{k_1} t) \qquad (4)$$

In advanced phases of the process when $t \rightarrow \infty$, the situation reverses and r_I may be neglected. Hence,

$$[CV] \approx B \exp(-\mathbf{k_2} t) \qquad (5)$$

The method of residuals [15-16] is designed to enable the calculus of both $\mathbf{k_1}$ and $\mathbf{k_2}$ values from a single kinetic curve, provided that: (*i*) there is a sufficient difference between their values, so that the assumptions in equations (4) and (5) are true, and (*ii*) there are sufficient [CV] *vs* **t** experimental data pairs. Both conditions are satisfied in this case. The calculus algorithm is detailed in the experimental section.

Table 1 summarizes the results. It may be concluded that both $\mathbf{k_1}$ and $\mathbf{k_2}$ increase gradually with temperature. This may indicate a slight endothermic behaviour [8]. Also, the solubility of the CV dye decreases with increasing temperature, hence minimizing the effect of desorption [14].

The activation energy of both film and intraparticle diffusion may be calculated by means of Arrhenius linearization ln(k) *vs* 1/T. In both cases good correlation coefficient lines were obtained: $R^2 = 0.9354$ for $\mathbf{k_1}$ values and $R^2 = 0.9007$ for $\mathbf{k_2}$ values, respectively. The slopes generated activation energies of 10.35 and 2.86 KJ/mole for the FD and IPD processes. These values are in agreement with those generally listed for physical phenomena, IPD being usually less sensitive to temperature changes.

Table 1. Values of the individual film (k_1) and intraparticle (k_2) diffusion process rate coefficients, as a function of operating parameters

Temperature (°C)	$[CV]_0$ (mg/L)	Mixing rate (rot/h)	pH	k_1 (1/h)	k_2 (1/h)
10	50	9000	5.40	0.962	0.343
23				1.052	0.375
35				1.313	0.378
40				1.468	0.390
23	30	9000	5.40	1.561	0.147
	40			3.909	0.176
	50			3.377	0.279
	70			3.142	0.148
	90			2.891	0.233
23	30	9000	5.40	3.122	0.115
		15000		3.041	0.115
		18000		2.188	0.106
23	50	9000	3.35	-	0.300
			5.40		0.286
			7.30		0.461
			8.62		0.448
			10.00		0.305

Altering the dye's initial concentration should not affect the rate constants of diffusion, but alters the rates *via* modifying the value of its driving force: the concentration difference between the bulk and the surface values, respectively. Values in Table 1 show however a certain scattering, probably due to experimental and calculus errors (only a few concentration *vs* time data are available for the determination of each rate coefficient value). Averages of $k_1 = 2.975 \pm 0.876$ h^{-1} and $k_2 = 0.197 \pm 0.058$ h^{-1} have been calculated.

Table 1 suggests that high mixing rates result in a slight lowering of both k_1 and k_2. This might be caused by the mechanical instability of the solid adsorbent (dried and milled plant leaves). At high speed, the stirrer crushes most probably the adsorbent, hence lowers somewhat its pore dimensions. As a result, diffusion slows down.

In case of experiments carried out at various pH of the aqueous media, the data enabled only the calculus of k_1. The highest value corresponds to 7.3 pH. Crystal violet is a basic dye; consequently under acidic conditions

hydrogen ions inhibit the binding of positively charged Crystal violet ions to the surface of the sorbent [8,14].

CONCLUSIONS

This work completes the conclusions of a previously reported study on Crystal violet adsorption dynamics onto powder *Salvinia natans*. Although the authors propose a pseudo-second order rate law which fits well the experimental data, this does not provide information regarding the process mechanism, since it treats it as a single generic process.

Hence, by looking at the individual stages of the process, by identifying the rate determining step as being the intraparticle diffusion, and by also demonstrating that the film diffusion's contribution to the overall rate is not negligible, the present paper sheds more light upon the removal mechanism of various organic dyes form their aqueous solutions by means of adsorption.

Moreover, the treatment of the process as an ensemble of two competing first-order processes (the film and the intraparticular diffusion respectively), as well as the novel use of a time-resolved data processing approach, borrowed from the field of pharmacokinetics, enabled the simultaneous determination of both slow diffusion process rate coefficients. Their dependence as a function of operating conditions (temperature, initial CV concentration, mixing rate and pH) is in agreement with previous conclusions [14], yet completes and consolidates them.

EXPERIMENTAL SECTION

Calculus was carried out by using *Microsoft Excel*. Experimental data Chrystal violet concentration *versus* total S-L contact time, under various operating conditions, were provided by the authors of work described in reference [14].

The calculus algorithm of the method of residuals contains the steps below [15]. The principle of the method is also illustrated in Figure 3.

- Logarithm values of [CV] are plotted against the contact time **t**.
- At high contact times the graph reaches linearity. The slope of this line gives the value of $\mathbf{k_2}$. The value of B in equation (5) corresponds to its intercept.
- The equation of this line (corresponding to the linearized form of equation 5) is further used to calculate the differences between y-coordinate values on the Crystal violet concentration-time plot and

the y-coordinate values from the extrapolated line. These values correspond to the residuals – see Figure 3.

- The logarithm values of residuals are plotted versus their corresponding contact time (close to the beginning of the process).
- A new line is generated that corresponds to the linearized form of equation 4. Its slope stands for $\mathbf{k_1}$ and its intercept for A in equation (4), respectively.

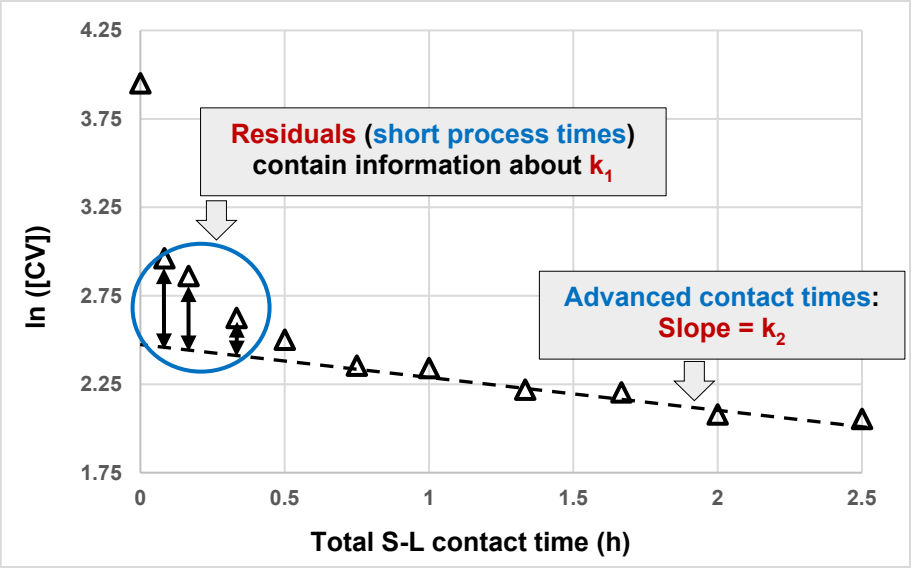

Figure 3. Illustration of the method of residuals for the calculus of both individual film ($\mathbf{k_1}$) and intraparticle ($\mathbf{k_2}$) diffusion process rate coefficients from a single kinetic curve. Experimental conditions are those listed for Figure 1.

REFERENCES

1. V. Krstić; Role of zeolite adsorbent in water treatment. In *Handbook of Nanomaterials for Wastewater Treatment: Fundamentals and Scale up Issues*, Bh. Bhanvase, Sh. Sonawane, V. Pawade, A. Pandit (Eds.); Elsevier, Amsterdam, The Netherlands, **2021**, Chapter 14, pp. 417-481.
2. T. R. Sahoo, B. Prelot; Adsorption processes for the removal of contaminants from wastewater: the perspective role of nanomaterials and nanotechnology. In *Nanomaterials for the Detection and Removal of Wastewater Pollutants*, B. Bonelli, F. S. Freyria, I. Rossetti, R. Sethi, (Eds.); Elsevier, Amsterdam, The Netherlands, **2021**, Chapter 7, pp. 161-222.

3. H. K. Agbovi, L. D. Wilson; Adsorption processes in biopolymer systems: fundamentals to practical applications. In *Natural Polymer-Based Green Adsorbent for Water Treatment*, Elsevier, S. Kalia (Ed.), Amsterdam, The Netherlands, **2021**, Chapter 1, pp. 1-51.
4. T. A. Saleh; *Kinetic models and thermodynamics of adsorption processes: Classification*. In *Surface Science of Adsorbent and Nanoadsorbents*, T. A. Saleh (Ed.), Elsevier, Amsterdam, The Netherlands, **2022**, Chapter 3, pp. 65-97; Series *Interface Science and Technology*, **2022**, *34*, 65-97.
5. K. L. Tan, B. H. Hameed, *J. Taiwan Inst. Chem. Eng*., **2017**, *74*, 25-48.
6. G. F. Malash, M. I. El-Khaiary, *J. Colloid Interface Sci*., **2010**, *348*, 537-545.
7. R. Ocampo-Pérez, J. Rivera-Utrilla, C. Gómez-Pacheco, M, Sánchez-Polo, J. J. López-Penalver, *Chem. Eng. J.*, **2012**, *213*, 88-96.
8. M. T. Yagub, T. K, Sen, Sh. Afroze, H. M. Ang, *Adv. Colloid Interface Sci*., **2014**, *209*, 172-184.
9. H. Qiu, L. Lv, B-C. Pan, Q-J. Zhang, W-M. Zhang, Q-X. Zhang, *Zhejiang Univ. Sci. A*., **2009**, *10(5)*, 716-724.
10. L. Largitte, R. Pasquier, *Chem. Eng. Res. Des*., **2016**, *109*, 495-504.
11. S. Azizian, *J. Colloid Interface Sci.*, **2004**, *276*, 47-52.
12. A-M. Danciu, A. Csavdari, *II. International Agricultural, Biological & Life Science Conference*, Edirne, Turkey, **2020**, Abstract Book, pp. 288.
13. A-M. Danciu, A. A. Csavdari, *5th International Conference on Chemical Engineering*, ICCE, Iaşi, Romania, **2020**, Abstract Book, pp. 95.
14. C. Mânzatu, B. Nagy, A. Török, L. Silgahi-Dumitrescu, C. Majdik, *Studia UBB Chemia*, **2015**, *60(4)*, 289-304.
15. S. E. Leucuța, *Biofarmacie și Farmacocinetică*, Editura Dacia, Cluj-Napoca, **2010**, pp. 171-235.
16. https://www.intechopen.com/chapters/63161
17. F-Ch. Wu, W-R. Tseng, R-Sh. Juang, *Chem. Eng. J*., **2009**, *153*, 1-8.